



OTTO VON GUERICKE  
UNIVERSITÄT  
MAGDEBURG

VST

FAKULTÄT FÜR VERFAHRENS-  
UND SYSTEMTECHNIK

# Direct Numerical Simulations of Gaseous Combustion in Complex Geometry

Dissertation  
for the award of the degree

**Doktoringenieur (Dr.-Ing.)**

by M.Sc. Cheng Chi

Date of birth: 04, Dec, 1990

in: Xiaogan, China

accepted by the Faculty of Process and Systems Engineering  
of the Otto-von-Guericke-University of Magdeburg

Reviewer: Prof. Dr.-Ing. Dominique Thévenin

Prof. Dr.-Ing. Christian Hasse

Prof. Dr. Hong G. Im

Dr.-Ing. Peter Janas

submitted on: 28.09.2020

Graduation Colloquium on: 16.03.2021



# Declaration

I hereby declare that I prepared the submitted work without inadmissible assistance and without the use of any aids other than those indicated. Facts or ideas taken from other sources, either directly or indirectly have been marked as such.

In particular, I did not use the services of a commercial graduation consultation. Furthermore, I have not made payments to third parties either directly or indirectly for any work connected with the content of the submitted dissertation.

This work has so far not been submitted either in Germany or abroad in same or similar form as a dissertation and has also not yet been published as a whole.

Magdeburg,  
28.09.2020

Cheng Chi

# ABSTRACT

This dissertation aims at investigating turbulent combustion and flows associated with complex geometries. Direct numerical simulations (DNS) have been done using the in-house, low Mach combustion solver DINO, for all the simulations in the dissertation. Detailed physicochemical models are used so that the coupling between chemical reactions, turbulent transport, and heat exchange are solved accurately.

In the first chapter, a general introduction to the scope of this study is given.

In the second chapter, the fundamentals on DNS have been explained. The governing equations solved in DINO are listed. The numerical algorithms and models are clarified.

The third chapter is focused on the immersed boundary method (IBM), which is used to deal with the complex geometries. The background of IBM is introduced. The drawbacks of the conventional ghost-cell IBM are discussed and finally a novel, efficient ghost-cell IBM is developed. Different benchmarks ranging from the flow around a cylinder in two dimensions to the pulsating flow inside a patient-specific, three-dimensional cerebral aneurysm have been checked and compared.

The fourth and fifth chapters investigate different gaseous combustion applications in simple geometry by DNS. In the fourth chapter, the heat release rate markers for turbulent premixed syngas flame, hydrogen flame, and methane flame are investigated in detail. Systematic DNS results concerning spherically expanding flames are analyzed. Optimal chemical markers are finally found, corresponding to different ranges of mixture conditions. In the next chapter, the hotspot ignition issue in turbulence has been discussed. The relationship



between ignition probability, ignition delay time and turbulence intensity has been studied. Many cases are systematically simulated by DNS to get a statistically correct relationship, due to the randomness of the turbulence.

The sixth chapter presents turbulent combustion simulations in complex geometries, such as a simplified internal combustion engine (ICE). The coupling equation between the temperature and pressure in a closed domain has been explained. A simplified pre-chamber/main chamber system is first studied for analyzing ignition by a hot jet. The characteristics of the pre-chamber hot jet and its contribution to the ignition event in main chamber has been investigated in detail. Then, a simplified ICE geometry is simulated for the intake stroke. Finally, a real industrial pre-chamber geometry has been simulated, for a selected range of crank angles.

Conclusions and outlook of this dissertation are presented in the last section.

**Novelties and significance:**

1. A novel, efficient immersed boundary method has been developed to solve by DNS turbulent reacting flows in complex geometries;
2. Optimal heat release markers for syngas flames, hydrogen flames, and methane flames have been found by analyzing the DNS results. This is relevant for experimental measurements of flame fronts;
3. Using DNS, safety-related hotspot ignition probability has been found to be strongly influenced by the turbulence intensity. The relationship between ignition probability, ignition delay, and turbulence intensity has been found;
4. Large-scale DNS has been enabled in realistic, engine-related geometries. The results are useful to guide industrial design and increase engine efficiency.

# Zusammenfassung

Ziel dieser Dissertation ist es, die turbulente Verbrennung und Strömung komplexer Geometrien zu untersuchen. Für alle Simulationen in der Dissertation wurden Direkte Numerische Simulationen (DNS) mit dem internen Verbrennungslöser DINO mit niedriger Mach-Zahl durchgeführt. Die detaillierten physikochemischen Modelle werden verwendet, um die Kopplung zwischen chemischen Reaktionen, turbulentem Transport und Wärmeaustausch genau zu lösen.

Im ersten Kapitel wird eine allgemeine Einführung in den Umfang dieser Studie gegeben.

Im zweiten Kapitel wurden die Grundlagen zu DNS erläutert. Die in DINO gelösten maßgeblichen Gleichungen sind aufgelistet. Die numerischen Algorithmen und Modelle werden geklärt.

Das dritte Kapitel konzentriert sich auf die Immersed Boundary-Methode (IBM), mit der die komplexen Geometrien behandelt werden. Der Hintergrund der IBM wird vorgestellt. Die Nachteile der herkömmlichen Geisterzellen-IBM werden diskutiert und schließlich eine neuartige, effiziente Geisterzellen-IBM entwickelt. Verschiedene Benchmarks, die vom Fluss um einen Zylinder in zwei Dimensionen bis zum pulsierenden Fluss innerhalb eines patientenspezifischen dreidimensionalen zerebralen Aneurysmas reichen, wurden überprüft und verglichen.

Das vierte und fünfte Kapitel untersuchen verschiedene Gasverbrennungsanwendungen in einfacher Geometrie mittels DNS. Im vierten Kapitel werden die Wärmefreisetzungsratenmarker für turbulente vorgemischte Synthesegasflammen, Wasserstoffflammen und Methanflammen im Detail untersucht. Systematische DNS-Ergebnisse bezüglich sphärisch expandierender Flammen werden analysiert. Schließlich werden optimale chemische Marker gefunden, die verschiedenen Bereichen der Mischungsbedingungen entsprechen. Im nächsten Kapitel wurde das Problem der Hotspot-Zündung bei Turbulenzen

erörtert. Die Beziehung zwischen Zündwahrscheinlichkeit, Zündverzögerungszeit und Turbulenzintensität wurde untersucht. Viele Fälle werden von DNS systematisch simuliert, um aufgrund der Zufälligkeit der Turbulenzen eine statistisch korrekte Beziehung zu erhalten.

Im sechsten Kapitel werden turbulente Verbrennungssimulationen in komplexen Geometrien vorgestellt, beispielsweise ein vereinfachter Verbrennungsmotor (ICE). Die Kopplungsgleichung zwischen Temperatur und Druck im geschlossenen Bereich wurde erläutert. Zunächst wird ein vereinfachtes Vorkammer/Hauptkammersystem zur Analyse des Problems der Heißstrahlzündung vor der Kammer untersucht. Die Eigenschaften des Vorkammer-Heißstrahls und sein Beitrag zum Zündereignis in der Hauptkammer wurden eingehend untersucht. Anschließend wird eine vereinfachte ICE-Geometrie für den Einlasshub simuliert. Schließlich wurde eine reale industrielle Vorkammergeometrie für einen ausgewählten Bereich von Kurbelwinkeln simuliert.

Schlussfolgerungen und Ausblick dieser Dissertation werden im letzten Abschnitt vorgestellt.

### **Neuheiten und Bedeutung:**

1. Eine neuartige, effiziente Methode mit eingetauchten Grenzen wurde entwickelt, um turbulente DNS-Reaktionsströmungen in komplexen Geometrien zu lösen;
2. Durch Analyse der DNS-Ergebnisse wurden optimale Wärmefreisetzungsmarker für Synthesegasflammen, Wasserstoffflammen und Methanflammen gefunden. Dies ist relevant für die experimentellen Messungen der Flammenfronten;
3. Bei Verwendung von DNS wurde festgestellt, dass die sicherheitsrelevante Hotspot-Zündwahrscheinlichkeit stark von der Turbulenzintensität beeinflusst wird. Die Beziehung zwischen Zündwahrscheinlichkeit, Zündverzögerung und Turbulenzintensität wurde gefunden;

4. Großformatiges DNS wurde in realistischen, motorbezogenen Geometrien aktiviert. Die Ergebnisse sind nützlich, um das Industriedesign zu steuern und den Motorwirkungsgrad zu erhöhen.

# TABLE OF CONTENTS

<b>Abstract</b>	<b>i</b>
<b>List of Figures</b>	<b>ix</b>
<b>List of Tables</b>	<b>xviii</b>
<b>1 Introduction</b>	<b>1</b>
1.1 Background and motivation . . . . .	1
1.2 Aim of the dissertation . . . . .	4
1.3 Structure of the dissertation . . . . .	5
<b>2 Fundamentals on Direct Numerical Simulations of Reacting Gas Flows</b>	<b>7</b>
2.1 Governing equations . . . . .	8
2.1.1 Low Mach formulation . . . . .	8
2.1.2 Incompressible formulation . . . . .	11
2.2 Numerical algorithms . . . . .	11
2.2.1 Spatial discretization . . . . .	11
2.2.2 Time integration . . . . .	12
2.2.3 Solving the Poisson equation . . . . .	13
2.2.4 Boundary conditions and initial conditions . . . . .	14
2.2.5 Parallelization . . . . .	14
<b>3 Immersed Boundary Method Implementation</b>	<b>17</b>
3.1 Introduction . . . . .	17
3.2 Formulation and Numerical Method . . . . .	20
3.2.1 Governing equations . . . . .	20
3.2.2 Discretization scheme . . . . .	21
3.2.3 Conventional ghost-cell IBM . . . . .	22

3.2.4	A novel ghost-cell IBM implementation . . . . .	25
3.2.5	Method summary . . . . .	31
3.2.6	Geometry representation and boundary motion . . . . .	34
3.2.7	Efficient implementation and parallelization . . . . .	34
3.3	Benchmark Simulations . . . . .	35
3.3.1	Tilted planar Poiseuille flow . . . . .	36
3.3.2	Uniform flow past a fixed circular cylinder . . . . .	38
3.3.3	Oscillating circular cylinder in a fluid at rest . . . . .	41
3.3.4	Flow around a flapping wing . . . . .	43
3.3.5	Flow past a 3D sphere . . . . .	49
3.3.6	Flow in an intracranial aneurysm . . . . .	53
3.4	Extension to low Mach reacting flows . . . . .	58
3.5	Novelty of the present IBM . . . . .	59
3.6	Conclusions . . . . .	60
<b>4</b>	<b>Gaseous Combustion Simulations: Assessing Heat Release</b>	<b>62</b>
4.1	Optimal Heat Release Rate Marker in Premixed Syngas Flames . . . . .	63
4.1.1	Introduction . . . . .	63
4.1.2	Numerical setups . . . . .	66
4.1.3	Identifying markers of heat release . . . . .	68
4.1.4	Results and discussion . . . . .	72
4.1.5	Conclusions for syngas flames . . . . .	83
4.2	Application to Premixed Hydrogen Flames . . . . .	84
4.2.1	Introduction . . . . .	84
4.2.2	Numerical setups . . . . .	85
4.2.3	Results and discussion . . . . .	87
4.2.4	Conclusions for hydrogen flames . . . . .	93
4.3	Application to Premixed Methane Flames . . . . .	95
4.3.1	Introduction . . . . .	95
4.3.2	Numerical setups . . . . .	96
4.3.3	Identifying markers of heat release . . . . .	98
4.3.4	Results and discussion . . . . .	100
4.3.5	Conclusions for methane flames . . . . .	108
4.4	Conclusions . . . . .	109

<b>5</b>	<b>Hotspot Ignition of a Turbulent Gas Flame</b>	<b>111</b>
5.1	Introduction . . . . .	111
5.2	Problem configuration and initialization . . . . .	114
5.2.1	Direct numerical simulations . . . . .	114
5.2.2	Flame configurations and initialization . . . . .	115
5.2.3	Postprocessing and particle tracking . . . . .	119
5.3	Numerical results and discussion . . . . .	121
5.3.1	Ignition/misfire events under laminar conditions . . . . .	122
5.3.2	Ignition or misfire events under turbulent conditions . . . . .	126
5.3.3	Ignition point tracking and analysis . . . . .	132
5.4	Concluding remarks . . . . .	135
<b>6</b>	<b>Simulations of turbulent reacting flows in complex geometry</b>	<b>137</b>
6.1	General introduction . . . . .	137
6.2	Pre-chamber hot jet ignition . . . . .	138
6.2.1	Introduction . . . . .	138
6.2.2	Numerical simulations and configurations . . . . .	141
6.2.3	Results and Discussion . . . . .	146
6.2.4	Intermediate conclusions . . . . .	169
6.3	DNS simulation in generic internal combustion engine without combustion .	171
6.3.1	Introduction . . . . .	171
6.3.2	Incompressible simulation of the intake stroke . . . . .	172
6.3.3	Low Mach simulation of the intake stroke . . . . .	174
6.3.4	Conclusions and perspectives . . . . .	179
6.4	DNS simulations in real pre-chamber geometry . . . . .	179
6.4.1	Numerical setup . . . . .	180
6.4.2	Engine operating conditions . . . . .	180
6.4.3	Fuel injection phase . . . . .	180
6.4.4	Back-flow phase . . . . .	186
6.4.5	Spark ignition phase . . . . .	192
6.4.6	Conclusions and perspectives . . . . .	193
<b>7</b>	<b>Conclusions and Outlook</b>	<b>197</b>
7.1	Conclusions . . . . .	197

7.2 Outlook . . . . .	199
<b>Bibliography</b>	<b>200</b>



# LIST OF FIGURES

1.1	Single cylinder engine with pre-chamber hot jet ignition [4]. . . . .	2
2.1	Strong scaling of DINO on SuperMUC-NG. Three cases with three different grid points are tested: 0.5, 1, and 4 billion grid points. . . . .	15
3.1	Conventional ghost-cell IBM: sketch for a one-dimensional case. . . . .	24
3.2	Conventional ghost-cell IBM: sketch for a two-dimensional case. . . . .	25
3.3	Computational domain for the tilted planar Poiseuille flow (all lengths are in cm). . . . .	36
3.4	Convergence of the $L_1$ , $L_2$ and $L_\infty$ norm errors of $u$ and $v$ velocity components when refining the computational grid. . . . .	38
3.5	Streamlines of the flow around a fixed circular cylinder at $Re = 40$ . . . . .	40
3.6	Convergence of the $L_1$ , $L_2$ and $L_\infty$ norm errors of the streamwise ( $u$ ) and spanwise ( $v$ ) velocity with the computational grid size. . . . .	41
3.7	Instantaneous vorticity contours plot for the flow at $Re = 100$ around the fixed circular cylinder at (a) $t = 30T$ (b) $t = 60T$ , with $T = D/U_\infty$ . . . . .	42
3.8	Velocity profiles in streamwise $u$ (left), and spanwise direction $v$ (right), at 4 different stream-wise cross-sections ( $x = -0.6D, 0D, 0.6D$ and $1.2D$ ) for 3 different phase positions: (A) $\phi = 180^\circ$ ; (B) $\phi = 210^\circ$ and (C) $\phi = 330^\circ$ . The symbols are experimental results from [70]. The lines denote the present results. . . . .	44
3.9	Time history of the in-line force acting on the cylinder. Symbols: experimental results from [70]; solid line: present simulation results. . . . .	45
3.10	Snapshots of the vorticity fields near a flapping wing at $Re = 157$ at 4 different time instants during one flapping period $T$ : (a) $t = 0.25T$ ; (b) $t = 0.44T$ ; (c) $t = 0.74T$ ; and (d) $t = 0.99T$ . . . . .	47

3.11	Time history of (a) drag coefficient and (b) lift coefficient for the flow around the flapping wing at $Re = 157$ . — novel ghost-cell immersed boundary method; ---- body-conforming mesh method of [72]; ..... moving immersed boundary method of [71]; --- immersed interface method of [73]. . . . .	48
3.12	$L_2$ norm error for the continuity equation concerning the flow around a fixed 3D sphere at a Reynolds number of 10. The • symbols represent results of the novel ghost-cell IBM. The + symbols represent the IBM results in [57] with ghost velocity included in the pressure correction equation, while the * represents the IBM results in [57] with ghost velocity excluded from the pressure correction equation. . . . .	50
3.13	Instantaneous pseudo-streamlines of the velocity field around the sphere within the $x - y$ plane (A) for flow at $Re_d = 100$ ; (B) for flow at $Re_d = 300$ . . . . .	51
3.14	Comparison of the (averaged) drag coefficients with results from the literature.	53
3.15	Patient-specific inflow velocity used during each cardiac cycle (duration of 0.925 s). . . . .	54
3.16	Measured parallel efficiency of the overall numerical solution and of the IBM procedure on SuperMUC. . . . .	55
3.17	Geometry of the patient-specific cerebral aneurysm with inlet/outlets, and locations of two orthogonal cut-planes used to analyze the results. The color plots on the planes show the peak-systolic velocity magnitude. . . . .	56
3.18	Comparison of the peak-systolic velocity magnitude along the two cut-planes (P1: top; P2: bottom) using the novel ghost-cell IBM and various adapted unstructured meshes (Cases C, E, I, K, and X in [83]). . . . .	57
4.1	Parity plot between the normalized heat release and the reconstruction based on $\bar{c}_{HCO}^{1.46} \times \bar{c}_{OH}^{0.71}$ (black points), or $\bar{c}_{CH_2O}^{0.3} \times \bar{c}_{OH}^{0.65}$ (gray points). . . . .	77
4.2	Example of instantaneous (a) normalized heat release distribution $\bar{H}_r$ at dimensionless time $\tau = 1.5$ ; (b) normalized heat release distribution reconstructed by $\bar{c}_{HCO} \times \bar{c}_{OH}$ ; (c) normalized heat release distribution reconstructed by $\bar{c}_{HCO}^{1.5} \times \bar{c}_{OH}^{0.75}$ and (d) normalized heat release distribution reconstructed by $\bar{c}_{CH_2O}^{0.32} \times \bar{c}_{OH}^{0.8}$ at dimensionless time $\tau = 1.5$ . All these results correspond to Case G. . . . .	78

4.3	Example of instantaneous (a) normalized heat release distribution $\overline{H}_r$ at dimensionless time $\tau = 1.5$ ; (b) binarized heat release distribution after thresholding (a) at half of the peak value (black pixels corresponding to $0.5 \leq \overline{H}_r \leq 1$ ); (c) binarized heat release distribution after thresholding normalized heat release distribution reconstructed by $\overline{c}_{\text{HCO}}^{1.5} \times \overline{c}_{\text{OH}}^{0.75}$ at half of the peak value and (d) binarized heat release distribution after thresholding normalized heat release distribution reconstructed by $\overline{c}_{\text{CH}_2\text{O}}^{0.32} \times \overline{c}_{\text{OH}}^{0.8}$ at half of the peak value. All these results correspond to Case H. . . . .	80
4.4	Case F (3D DNS): (a) normalized heat release and (b) reconstruction using $\overline{c}_{\text{HCO}}^{1.5} \times \overline{c}_{\text{OH}}^{0.75}$ . . . . .	81
4.5	(a) Parity plot of flame thickness, showing the comparison between the values derived from the actual heat release profile, and from the proposed heat release reconstruction marker $\overline{c}_{\text{HCO}}^{1.5} \times \overline{c}_{\text{OH}}^{0.75}$ and (b) Parity plot of flame curvature, showing the comparison between the values derived from the actual heat release profile, and from the proposed heat release reconstruction marker, $\overline{c}_{\text{HCO}}^{1.5} \times \overline{c}_{\text{OH}}^{0.75}$ . . . . .	82
4.6	Example of instantaneous (a) binarized heat release distribution (black pixels corresponding to $0.5 \leq \overline{H}_r \leq 1$ ) and (b) binarized heat release distribution reconstructed by $\overline{c}_{\text{O}_2}^{0.46} \times \overline{c}_{\text{OH}}^{0.4}$ at dimensionless time $\tau = 1.5$ in Case A. . . . .	87
4.7	Example of instantaneous (a) normalized heat release distribution $\overline{H}_r$ at dimensionless time $\tau = 1.5$ ; (b) normalized heat release distribution reconstructed by $\overline{c}_{\text{OH}}$ ; (c) normalized heat release distribution reconstructed by $\overline{c}_{\text{H}_2}^{0.43} \times \overline{c}_{\text{OH}}^{0.5}$ and (d) normalized heat release distribution reconstructed by $\overline{c}_{\text{O}_2}^{0.46} \times \overline{c}_{\text{OH}}^{0.4}$ at dimensionless time $\tau = 1.5$ . All these results correspond to Case A. . . . .	92
4.8	Case G (3D DNS): Clipped iso-surface of (a) normalized heat release; (b) conventional reconstruction by OH only; (c) reconstruction by $\overline{c}_{\text{O}_2}^{0.46} \times \overline{c}_{\text{OH}}^{0.40}$ . . . . .	94
4.9	Objective function $q$ evaluated for $\text{OH} \times \text{CH}_2\text{O}$ with all possible exponents in Case F (for HHRR). Note that the $z$ -axis is inverted, so that the best possible reconstruction (minimizing $q$ ) appears as a peak. . . . .	101

4.10	Objective function $q$ evaluated for conventional HRR markers with unity or with optimal exponents for Cases A to I (for HHRR). Note that the $z$ -axis is inverted, so that the best possible reconstruction (minimizing $q$ ) appears as a peak. The optimal exponents (denoted “opt”) are always those found for a specific equivalence ratio, and may thus vary from point to point. . . . .	102
4.11	Normalized HRR vs. reconstruction from (a) $[\text{OH}] \times [\text{CH}_2\text{O}]$ and (b) $[\text{H}] \times [\text{CH}_2\text{O}]$ , with unity or with optimal exponents for laminar flames at different equivalence ratios. . . . .	104
4.12	Joint PDF of the correlation between normalized HRR and (a) reconstruction from $([\text{OH}] \times [\text{CH}_2\text{O}])$ ; (b) reconstruction from $([\text{OH}]^{1.07} \times [\text{CH}_2\text{O}]^{1.17})$ ; (c) reconstruction from $([\text{H}] \times [\text{CH}_2\text{O}])$ or (d) reconstruction from $([\text{H}]^{1.11} \times [\text{CH}_2\text{O}]^{0.86})$ . . . . .	106
4.13	Case M (3D DNS): Clipped iso-surface of (a) normalized heat release; (b) conventional reconstruction by $([\text{OH}] \times [\text{CH}_2\text{O}])$ with unity exponents; (c) reconstruction by $([\text{OH}]^{1.07} \times [\text{CH}_2\text{O}]^{1.17})$ ; (d) reconstruction by $([\text{H}]^{1.11} \times [\text{CH}_2\text{O}]^{0.86})$ . The iso-surfaces are clipped with 3 cut-planes normal to $x$ , $y$ and $z$ directions respectively. . . . .	107
5.1	Typical computational domain and flame configuration showing $S1D$ case – one-dimensional hotspot (initial configuration). . . . .	116
5.2	All the considered cases in the Borghi-Peters turbulent premixed combustion diagram [137]. . . . .	118
5.3	Ignition delay ( $\tau$ ) versus (a) initial temperature $T_0$ for $\Phi = 1.0$ (and $R_0 = 1$ mm for setups $S1D$ , $S2D$ , $S3D$ ) and (b) mixture equivalence ratio ( $0.1 \leq \Phi \leq 1.0$ for setup $S0D$ ) of $\text{H}_2$ -air mixtures under laminar conditions, with corresponding experimental data from the literature [146, 178]. . . . .	123
5.4	Hotspot ignition delay versus initial radius of hot kernel $R_0$ for stoichiometric $\text{H}_2$ -air mixtures in setup $S2D$ . . . . .	124
5.5	Hotspot-induced ignition diagram as a function of $(T_0, R_0)$ for stoichiometric $\text{H}_2$ -air mixtures under laminar conditions in setup $S2D$ . Successful ignition is shown with circle, misfire with dot. . . . .	125

5.6	Exemplary temporal evolution of the temperature field during a successful (left column: $u'/s_L = 0.78$ ) and misfire (right column: $u'/s_L = 1.13$ ) event in a hotspot-induced ignition simulation of stoichiometric H <sub>2</sub> -air pre-mixtures under turbulent conditions for $T_0 = 1000$ K and $R_0 = 1.2$ mm. (a) $t/\tau_f = 0.0$ , (b) $t/\tau_f = 0.3$ and (c) $t/\tau_f = 0.6$ . The color scale is always a min-max scale and is therefore different for each subfigure. . . . .	127
5.7	Hotspot-induced ignition: (a) ignition delay $\tau_{mean}$ and (b) ignition probability, $P_i$ versus turbulence intensity ( $u'/s_L$ ) of atmospheric stoichiometric H <sub>2</sub> -air pre-mixtures computed for $T_0 = 1000$ K, $R_0 = 1.2$ mm. . . . .	129
5.8	Hotspot ignition delay $\tau$ versus turbulence intensity ( $u'/s_L$ ) of atmospheric stoichiometric H <sub>2</sub> -air pre-mixtures computed for both 2D and 3D configurations. The hot kernel has an initial radius $R_0 = 1.2$ mm and initial temperature $T_0 = 1100$ K. . . . .	131
5.9	Temporal evolution of (a) the relevant contributions in the temperature transport equation and (b) the mass fractions of all intermediate species at the ignition point for one realization of Case 6, tracked in a Lagrangian frame, and leading to successful ignition. . . . .	133
5.10	Temporal evolution of (a) the relevant contributions in the temperature transport equation and (b) the mass fractions of all intermediate species at the point that will reach highest temperature at the end of the simulation for one realization of Case 8, tracked in a Lagrangian frame, and leading to misfire. . . . .	134
6.1	Schematic of the computational domain: (a) 2D domain showing also the three points $M_1$ , $M_2$ , $M_3$ used for a quantitative analysis of the process as well as the location of the orifice outlet used to compute mass fluxes (white dashed line); (b) 3D domain showing the iso-surface of $Q$ -criterion at $3 \times 10^{10}$ (1/s <sup>2</sup> ) colored by velocity magnitude and iso-surface of temperature at 800 K colored by heat release rate at $t = 0.5$ ms. . . . .	143
6.2	Comparison of the normalized power spectrum density of the initial turbulence as a function of frequency in Case G and Case B3D. . . . .	145
6.3	Time evolution of the normalized progress variable $\bar{c}$ at point $M_1$ , $M_2$ and $M_3$ (solid lines) and mass flow rate of CH <sub>2</sub> O, CH <sub>3</sub> , HO <sub>2</sub> and OH (dashed lines) through the orifice outlet for Case A. A positive mass flux is from pre-chamber to main chamber. . . . .	147

6.4	(a) Velocity field (gray colour scale) with single temperature isovalue (red, 1500 K) at 0.13 ms, corresponding to the end of Phase 1; (b) Heat release rate (gray colour scale) at 0.58 ms, close to the end of Phase 2; (c) OH mass fraction (gray colour scale) with single temperature isovalue (red, 1500 K) at 1.0 ms, Phase 3; and (d) OH mass fraction (gray colour scale) with isovalues of normalized progress variable $\bar{c}$ (solid coloured lines) and velocity vectors (scaled proportional to magnitude, peak velocity 6.15 m/s) at 1.7 ms, Phase 4. All these results correspond to Case A. . . . .	148
6.5	(a) Temperature, (b) axial velocity, (c) mass fraction of OH and (d) heat release rate profile across the orifice at the level of point M <sub>3</sub> at t = 0.13 ms, 0.58 ms, 1.00 ms and 1.70 ms in Case A. . . . .	151
6.6	Time-evolution of relative heat release $H_i$ associated to different species at ignition spot (point shown in Fig. 6.4(b)) until ignition by the hot jet, exemplarily for Case A. Species with negligible contributions are not shown. . . .	153
6.7	Scatter plot (black dots) of CH <sub>4</sub> mass fraction (a and b), HO <sub>2</sub> mass fraction (c and d) and CH <sub>3</sub> mass fraction (e and f) vs. temperature in the whole main chamber at time $t = 0.52$ ms for Case A (a, c and e) and at time $t = 0.7$ ms for Case C (b, d and f). Corresponding premixed 1D flames under the same conditions (the same initial temperature and pressure as the main chamber in the 2D DNS) for different mixtures equivalence ratios $\phi$ are also plotted for comparison (coloured solid lines). The scatter plots show all the grid points in the main chamber. . . . .	155
6.8	Time evolution of maximum OH mass fraction along all vertical cross-sections (from left – pre-chamber – to right – main chamber –, the two vertical dashed lines marking the position of the orifice), exemplarily for (a) Case A and (b) Case G. For a better visibility, the beginning of the process is not shown, and the time-scales vary. . . . .	159
6.9	Time evolution of the different terms controlling heat balance in the orifice (left scale, lines with markers), together with (right scale) axial velocity at points M <sub>3</sub> (red) and M <sub>1</sub> (blue) as well as pressure difference between M <sub>3</sub> and M <sub>1</sub> (black). The different phases are labelled on the top. All these results are shown exemplarily for Case A. . . . .	161

6.10	Time evolution of the progress variable $\bar{c}$ at points $M_1, M_2, M_3$ and contribution of reaction to heat balance within the orifice for Case H. The different phases are labelled on the top. . . . .	162
6.11	Time evolution of the maximum OH mass fraction in the main chamber for Case A - G. For each curve, the time is normalized by the characteristic time-scale of the jet ( $\tau_{c_j} + \tau_{h_j}$ ), so that normalized time 1 corresponds to the end of the jet flow from pre-chamber to main chamber. . . . .	162
6.12	Scatter plot of (a) mass fraction of $\text{CH}_3$ vs. progress variable and (b) mass fraction of $\text{HO}_2$ vs. progress variable in the main chamber for Case A (red circles) at $t = 0.52$ ms and Case A3D (black dots) at $t = 0.545$ ms. . . . .	165
6.13	Iso-surface of OH mass fraction at 0.001 colored by heat release rate for Case B3D at 3 different time instants (a) $t = 0.545$ ms, (b) $t = 0.755$ ms, and (c) $t = 0.864$ ms. . . . .	166
6.14	Scatter plot of (a) mass fraction of $\text{HO}_2$ vs. temperature and (b) local equivalence ratio vs. temperature in the main chamber for Case A3D (red circles) and Case B3D (black dots) at $t = 0.545$ ms. . . . .	167
6.15	Time evolution of the volume in the main chamber where OH mass fraction is larger than 0.001 in Case A3D and Case B3D. . . . .	168
6.16	(a) PDFs of the most extensive and most compressive strain rates ( $s_1$ and $s_3$ ) and strain rate tensor norm ( $ s_N $ ) in Case A3D at $t = 0.9$ ms; (b) PDFs of the extensive strain rate eigenvector alignment with the flame normal unit vector at the flame front in Case A3D and Case B3D at $t = 0.9$ ms. . . . .	170
6.17	Schematic of the geometry (in mm, left) and mesh structure near the valve part (right). . . . .	173
6.18	Instantaneous velocity magnitude (top) and vorticity magnitude (bottom) profile at different time instants (36 °CA, 77 °CA, 90 °CA, 135 °CA from left to right) for the 2D simulation. . . . .	175
6.19	Comparison of $V_x/V_{p,mean}$ between experiment and the 3D DNS at 36 °CA at different axial locations below the cylinder head (solid line: DNS, symbols: experiment). $X_{60}, X_{70}$ and $X_{80}$ represents 10 mm, 20 mm, and 30 mm below the cylinder head, respectively. . . . .	176
6.20	3D profiles of the velocity magnitude at 45 °CA, 90 °CA, 135 °CA, 180 °CA. . . . .	177

6.21	Velocity magnitude (top), temperature (middle) and O <sub>2</sub> mass fraction (bottom) profile at 16 °CA, 63 °CA, 90 °CA, 120 °CA and 180 °CA (from left to right). . . . .	178
6.22	Iso-surface of methane mass fraction ( $Y_{CH_4} = 0.01$ ) at 270 °CA, 276 °CA, 282 °CA, and 295 °CA (from left to right). . . . .	182
6.23	Iso-surface of methane mass fraction ( $Y_{CH_4} = 0.01$ ) at 272.7 °CA, 275.5 °CA, 278.2 °CA, and 281.8 °CA: comparison between DNS (left) and URANS (right). . . . .	183
6.24	Vertical cut plane showing the methane mass fraction distribution with iso-surface of the methane mass fraction at 0.01: comparison between DNS (top) and URANS (bottom) at 278 °CA (left) and 282 °CA (right). . . . .	184
6.25	2D central cut plane showing the contribution of (a) convection and (b) diffusion at 282 °CA regarding methane mass fraction. . . . .	185
6.26	2D central cut plane showing the velocity magnitude profile for DNS (top) and URANS (bottom) at 277 °CA, 282 °CA, and 290 °CA. . . . .	187
6.27	Temporal evolution of inlet velocity and thermodynamic pressure in the pre-chamber, as obtained in a partner group (V. Sazonov, Prof. H. Rottengruber) from 1D simulation. . . . .	188
6.28	Iso-surface of methane mass fraction ( $Y_{CH_4} = 0.6$ ) at 645 °CA, 650 °CA, 657 °CA, and 663 °CA (from left to right). . . . .	189
6.29	2D central cut profile of velocity magnitude at 680 °CA (a) using DNS and (b) using URANS. . . . .	189
6.30	2D central cut profile of temperature at 680 °CA (a) using DNS and (b) using URANS. . . . .	190
6.31	(a) Mean velocity profile (in m/s); (b) absolute velocity fluctuations (in m/s) and (c) relative velocity fluctuations in the 2D pre-chamber central cut plane at 710 °CA. . . . .	191
6.32	Peak Reynolds number vs. time (a) in the whole pre-chamber and (b) in the central gap connecting both parts of the pre-chamber. . . . .	191
6.33	Turbulent velocity profile in the compression simulation at 710 °CA (left), and derived initial profile for ignition simulation (right). . . . .	192
6.34	OH mass fraction (color plot) and temperature contours (isolines) at the 2D central cut plane through the initial spark location at $t = 0.011$ ms, $t = 0.031$ ms, and $t = 0.0465$ ms revealing the progress of ignition below the central gap in the pre-chamber. . . . .	194



# LIST OF TABLES

3.1	Magnitude of the absolute error and computed convergence order for the planar Poiseuille flow simulation using the novel IBM compared to the simulation using the IBM from [38]. . . . .	37
3.2	Comparison between the current study and previous works concerning recirculation length $L_W$ , drag coefficient $C_D$ , and Strouhal number $St=fD/U_\infty$ , where $f$ is the frequency of vortex shedding. . . . .	39
3.3	Magnitude of the absolute error and computed convergence order for the flow past a circular cylinder at $Re = 40$ using the novel IBM in comparison with the IBM from [38]. . . . .	40
3.4	Comparison of the computed flow characteristics with other experimental and numerical studies. . . . .	52
4.1	Considered DNS cases (composition in molar percentages) for syngas flames. An appropriate nitrogen complement (corresponding to oxygen/nitrogen ratio of air) is added before starting simulation. . . . .	67
4.2	Objective function $q$ (to be minimized) for all possible species combinations in Case A; lower-left when using unity exponents, upper-right when using optimal exponents. The symbol - indicates no acceptable solution. . . . .	72
4.3	Four best correlations in Case A, B, C and D, followed by best results for LIF-measurable species. . . . .	73
4.4	Best LIF-measurable correlations in Case E. . . . .	74
4.5	Obtained correlations for the best LIF-measurable species combination, $HCO \times OH$ . . . . .	75
4.6	Best LIF-measurable correlations in Case G. . . . .	75
4.7	Best correlations in Case H, I and J for LIF-measurable species. . . . .	79
4.8	Considered DNS cases for hydrogen flames. . . . .	86

4.9	Objective function $q$ (to be minimized) for all possible species combinations in Case A; lower-left when using unity exponents, upper-right when using optimal exponents. The symbol – indicates no acceptable solution (value of $q$ above 1000%). Along the diagonal, the resulting objective function for a single species with optimal exponent is listed. . . . .	88
4.10	Four best correlations for Cases A, B and C (from top to bottom), followed by best results for experimentally-measurable correlations. . . . .	89
4.11	Best experimentally-measurable correlations in Case D. . . . .	89
4.12	Best experimentally-measurable correlations in Cases E and F. . . . .	90
4.13	Best experimentally-measurable correlations in Cases H, I and J. . . . .	91
4.14	Investigated DNS cases for methane flames. . . . .	97
5.1	Initial turbulence parameters for all simulated cases. . . . .	118
5.2	Really obtained $Re_t$ for all runs of all simulated cases. . . . .	119
5.3	Hotspot ignition times (in ms) of atmospheric, stoichiometric $H_2$ -air mixtures with initially $T_0 = 1000$ K, $R_0 = 1.2$ mm for nine of the thirteen different turbulent conditions. Fifteen realizations are presented for each turbulence intensity. Entries with a hyphen (–) refer to a misfire event. . . . .	128
6.1	The investigated DNS cases . . . . .	144
6.2	Time-scales and global Damköhler number for Cases A - G considered in this study. The value of $Da$ is computed at $t = \tau_{cj} + \tau$ for ignition cases and at $t = \tau_{cj} + \tau_{hj}$ for misfire cases at the exit of the orifice (white dashed line in Fig. ??). Remember that the ignition delay is computed after the end of the cold-jet phase, so that ignition takes place indeed at $\tau_{cj} + \tau$ . . . . .	158

# Chapter 1

## Introduction

### 1.1 Background and motivation

Combustion, still being the most important supply (80% according to [1]) for the energy demand worldwide, is important for fundamental research and industrial applications. Over the last decades, the fundamental knowledge and principles of the gaseous combustion process have been investigated intensively. A well structured system for the combustion process has been developed and clarified (concerning laminar flame and turbulent flame, premixed flame and diffusion flame, turbulent flame regime...). The combustion research of today is more focused on the process related to industrial applications, where the problem is more realistic and complicated (both in temporal scale and spatial scale). Among these processes, ignition (safety-related ignition, pre-chamber assisted ignition ...) is particularly interesting. Understanding the ignition and following combustion process in realistic, complicated geometry is critical for real applications (eg. pre-chamber hot jet ignition system as shown in Fig. 1.1). While most of the previous studies concerning industrial applications rely on experiments, it is usually impossible to obtain all the details of the flow and flame in the experimental measurements. As an alternative, numerical simulation provides all the details concerning the physics and chemistry and helps better understanding of the complicated

process in realistic applications. Due to the rapid advancing of the computing powers in recent years, high fidelity simulations (DNS and high fidelity LES) of turbulent flames in realistic geometries become possible. Ignition and combustion process can be well resolved in the detailed simulations. This builds up the main foundation of this thesis.

Ignition is an important and complex process. Previous studies on ignition for safety analysis mostly rely on experimental measurements and simplified theoretical models [2]. Since chemical kinetics, turbulent transport and heat exchange are fully coupled in the ignition process, numerical investigations need to take all aspects into account simultaneously. Main challenges for chemical kinetics are the poorly known chemical pathways and the large number of individual reactions for complex fuels. The challenge for turbulent transport is the intrinsic complexity of turbulence and the poor predictions of different turbulence models. The challenge for heat exchange is to model accurately all relevant paths (convection, diffusion, radiation). To meet these challenges, DNS using detailed chemical mechanisms for hydrogen flames (for which accurate and validated physicochemical data are available [3]) involving full heat convection and diffusion processes have been considered as discussed in Chapter 5. This chapter validates the numerical methods in the present thesis for ignition study and provides insights on the complex process involved in ignition in turbulence.

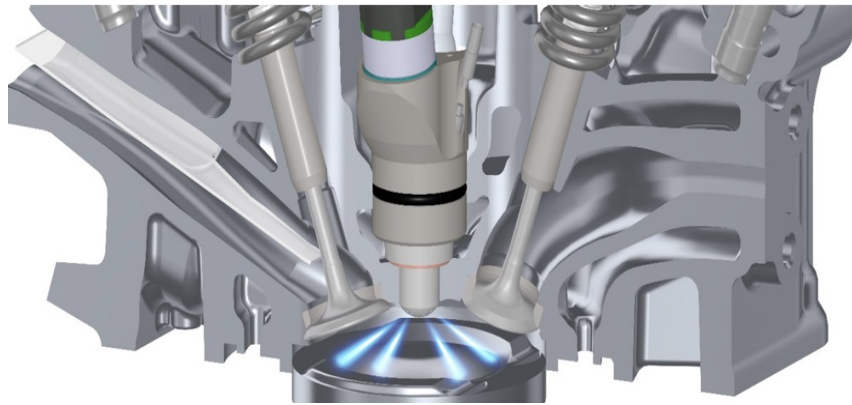


FIGURE 1.1. Single cylinder engine with pre-chamber hot jet ignition [4].

Pre-chamber turbulent hot jet ignition systems are becoming popular for modern lean gas engines, since they lead to an increase in thermal and fuel efficiency [5]. Previous studies rely mostly on experiments or simplified numerical simulations (Reynolds-averaged Navier-Stokes (RANS) or Large Eddy Simulation (LES)), because of the complex processes involved. Different configuration parameters influence the final ignition probability. A variety of practical pre-chamber/main chamber configurations have been tested in experiments. The underlying physicochemical connections between these effects are still unknown. DNS is thus performed in this dissertation to investigate in detail the hot jet characteristics and the ignition probability. The detailed discussion of the results is presented in Chapter 6.

To investigate combustion phenomena in such a complex geometry, such as the pre-chamber geometry, most existing numerical methods rely on body-conforming grids to represent the geometry boundaries. Though these methods give an accurate representation of the boundary walls, they are often difficult to implement for high-order DNS studies. Instead, Cartesian grid methods are much more efficient and CPU time saving for high-fidelity, high-order DNS simulations. Among all the Cartesian grid methods, the ghost-cell immersed boundary method has become popular due to its easy implementation and good accuracy [6]. In this dissertation, a novel, efficient ghost-cell immersed boundary method will be introduced to describe complex geometries. The detailed background of the method is described in Chapter 3.

For practical combustion applications, heat release is the most important quantity, and would be very interesting to compare between DNS and experiments. However, experimental techniques to measure directly heat release are barely available. For this reason, heat release rate markers are usually used to indirectly represent heat release in experiments. For different fuel flames, different heat release rate markers have been employed, which are usually combination of species and radicals. However, such conventional flame markers are not so

accurate in case of detailed comparison in numerical simulations. Thus, Chapter 4 provides a DNS analysis leading to a more accurate determination of heat release using optimized species combinations as markers.

## 1.2 Aim of the dissertation

The final aim of this dissertation is to find a way to accurately represent an arbitrary complex geometry in DNS while keeping high accuracy and computational efficiency. The first step was to develop an efficient immersed boundary method (IBM) for incompressible non-reacting flows based on the DNS solver DINO [7]. The efficiency, convergence, accuracy and robustness of this IBM have been validated through various benchmarks, including 3D complex geometries and moving geometries. Then, this IBM technique has been extended to low-Mach reacting flows to allow for large-scale combustion simulations in complex geometries.

The central application pertains to combustion and ignition phenomena. To understand such complex processes, the interactions between thermodynamics, turbulent transport and detailed chemistry kinetics must be properly taken into account, first for simple cases.

For better comparison with experiments, accurate heat release markers are identified for different fuels.

Finally, this dissertation investigates ignition and combustion phenomena in complex geometries (relevant for internal combustion engines) by large-scale DNS. Thanks to the developed tools, such simulations become possible. An improved understanding of the complex flow and combustion process has been obtained.

## **1.3 Structure of the dissertation**

The dissertation is organized as follows. First, the fundamentals of DNS, including the governing equations and generic numerical algorithms are introduced in Chapter 2. A novel ghost-cell IBM to take into account a complex geometry is presented in Chapter 3. Chapter 4 identifies suitable flame front markers of heat release for premixed flames by analyzing systematic DNS results. The safety-related hotspot ignition in turbulence is investigated in Chapter 5. Chapter 6 discusses DNS in an internal combustion engine and an industrial pre-chamber geometry, revealing the details of pre-chamber hot jet ignition. Finally, concluding remarks and outlooks are provided in Chapter 7.





## Chapter 2

# Fundamentals on Direct Numerical Simulations of Reacting Gas Flows

Direct numerical simulation, also called "numerical experiment", is the most accurate numerical method for simulating turbulent flows and combustion. It involves detailed physico-chemical models and resolves the turbulence without introducing any turbulence models. To achieve that, a fine mesh resolution is always necessary, to resolve both the Kolmogorov length scale and the reaction length scale. Due to the rapid advancement of computing resources in recent years, DNS in real geometries with a large physical domain become increasingly possible. The simulation results are extremely useful for fundamental studies of turbulent flows and flames. It also provides a practical reference for model developments in Large Eddy Simulation (LES) and Reynolds-averaged Navier-Stokes equations (RANS).

DINO [7] is an in-house, parallel combustion DNS solver developed in our group in Magdeburg. It solves the incompressible and low Mach formulation of the Navier-Stokes equations, since most applications involving chemical reactions and combustion take place at low Mach numbers [8]. Such a low Mach formulation gives a large speed-up in the simulation compared to the fully compressible formulation [9]. Since DINO has been developed further during several PhD theses of our group, only the most important information are retained

in this dissertation. Interested readers are referred to the PhD thesis of Gordon Fru [10] and Abouelmagd Abdelsamie [11] for additional details regarding DINO. In the following, the governing equations and numerical algorithms implemented in DINO will be clarified.

## 2.1 Governing equations

There are two systems of governing equations for 1) low Mach formulation and 2) fully incompressible formulation. They can be used to describe reacting or non-reacting mixtures.

### 2.1.1 Low Mach formulation

The low Mach formulation in DINO is originally based on the study in [12]. Pressure is composed of a homogeneous thermodynamic pressure  $p(t)$  and a dynamic fluctuating pressure  $\tilde{p}(x, t)$ , where  $\tilde{p}(x, t) \ll p(t)$ . Thus, the vorticity and entropy waves are kept, while the acoustic waves are removed. The time step limitation by the acoustic times is no longer needed, resulting in a large speed-up of the code.

The conservation equations can be summarized as follows:

$$\frac{\partial \rho}{\partial t} = -\frac{\partial(\rho u_i)}{\partial x_i}, \quad (2.1)$$

$$\frac{\partial(\rho u_i)}{\partial t} = -\frac{\partial \tilde{p}}{\partial x_i} + R_{m,i}, \quad (i = 1, 2, 3) \quad (2.2)$$

$$\frac{\partial T}{\partial t} = -\frac{1}{\rho C_p} \sum_{k=1}^{N_s} h_k \dot{\omega}_k + R_T, \quad (2.3)$$

$$\frac{\partial Y_k}{\partial t} = -\frac{\partial \dot{\omega}_k}{\partial \rho} + R_{Y_k}, \quad (k = 1, \dots, N_s) \quad (2.4)$$

using the ideal gas approximation

$$\rho = \frac{pW}{RT}, \quad (2.5)$$

and considering the species mass conservation

$$\sum_{k=1}^{N_s} Y_k = 1, \quad (2.6)$$

where  $\rho$ ,  $u_i$ ,  $\tilde{p}$ ,  $p$ ,  $T$ ,  $Y_k$ ,  $N_s$ ,  $R$ ,  $W$ ,  $C_p$ ,  $h_k$  and  $\dot{\omega}_k$  are the mixture density,  $i^{th}$  component of velocity, fluctuation pressure, thermodynamic pressure, temperature,  $k^{th}$  species mass fraction, number of species, ideal gas constant, mixture mean molecular weight, specific heat capacity at constant pressure, specific enthalpy, and mass reaction rate, respectively. The right-hand-side of the momentum equation Eq. 2.2 is obtained as:

$$R_{m,i} = -\frac{\partial(\rho u_j u_i)}{\partial x_j} + \frac{\partial}{\partial x_j} \left[ \mu \left( \frac{\partial u_i}{\partial x_j} + \frac{\partial u_j}{\partial x_i} \right) \right] + \frac{\partial}{\partial x_j} \left[ \left( \kappa - \frac{2}{3}\mu \right) \frac{\partial u_l}{\partial x_l} \right] \delta_{ij} + \rho \sum_{k=1}^{N_s} Y_k f_{k,i}, \quad (2.7)$$

where  $\delta_{ij}$ ,  $f_{k,i}$ ,  $\mu$  and  $\kappa$  are the Kronecker delta, components of the specific volume force acting on species  $k$ , dynamic and volume viscosity, respectively. The right-hand-side of the temperature equation Eq. 2.3 is obtained as:

$$R_T = -u_j \frac{\partial T}{\partial x_j} + \frac{1}{\rho C_p} \left[ \frac{\partial}{\partial x_j} \left( \lambda \frac{\partial T}{\partial x_j} \right) - \frac{\partial T}{\partial x_j} \sum_{k=1}^{N_s} \rho C_{p,k} Y_k V_{k,j} + \sum_{k=1}^{N_s} \rho Y_k V_{k,j} f_{k,j} \right], \quad (2.8)$$

where  $\lambda$  and  $V_{k,j}$  represent heat diffusion coefficient and  $j^{th}$  component of the species molecular diffusion velocity, respectively. The right-hand-side of the species equation Eq. 2.4 is obtained as:

$$R_{Y_k} = -u_j \frac{\partial Y_k}{\partial x_j} - \frac{1}{\rho} \frac{\partial(\rho Y_k V_{k,j})}{\partial x_j}. \quad (2.9)$$

To compute the molecular diffusion velocity of species  $k$ ,  $\mathbf{V}_k$ , the mixture-averaged dif-

fusion velocity and multicomponent diffusion velocity approach [13] have been used in this dissertation. Note that unity or constant Lewis numbers are also implemented in DINO.

For mixture-averaged diffusion, a diffusion coefficient  $D_k$  is first computed:

$$D_k = \frac{1 - Y_k}{\sum_{j \neq k} X_j / \xi_{jk}}, \quad (2.10)$$

where  $\xi_{jk}$  are the binary diffusion coefficients. The diffusion velocity is then computed as:

$$\mathbf{V}_k = -D_k \frac{\nabla X_k}{X_k} + \sum_{k=1}^{N_s} D_k \nabla X_k \frac{W_k}{W}. \quad (2.11)$$

The last term is the correction velocity needed to ensure mass conservation ( $\sum_{k=1}^{N_s} Y_k \mathbf{V}_k = 0$ ).

For multicomponent diffusion, the process is computed by inverting the species linear transport system [14],

$$F = L^{00,00^{-1}}, \quad (2.12)$$

with

$$L_{ij}^{00,00} = \frac{16T}{25p} \sum_{k=1}^{N_s} \frac{X_k}{W_i \xi_{ik}} (W_j X_j (1 - \delta_{ik}) - W_i X_j (\delta_{ij} - \delta_{jk})) \quad (2.13)$$

The diffusion coefficients are computed by

$$D_{ij} = X_i \frac{16TW}{25pW_j} (F_{ij} - F_{ii}), \quad (2.14)$$

with  $F_{ij} = L_{ij}^{00,00^{-1}}$ . Thus, the species diffusion velocity is

$$\mathbf{V}_k = -\frac{1}{X_k W} \sum_{j=1}^{N_s} W_j D_{kj} \nabla X_j. \quad (2.15)$$

Thermal diffusion (Soret effect) is also included in DINO and is switched on for hydrogen

flames in this dissertation. The corresponding diffusion velocity reads

$$\mathbf{V}_{kT} = -D_{kT} \frac{\nabla T}{T} \quad (2.16)$$

Other thermal, transport coefficients and all chemical source terms are computed using the open-source library Cantera [15].

### 2.1.2 Incompressible formulation

For non-reacting flows, the incompressible formulation is used instead of the low Mach formulation for faster integration. Then, the mass conservation equation Eq. 2.1 and the right-hand-side of the momentum equation Eq. 2.7 are reduced to

$$\frac{\partial u_i}{\partial x_i} = 0, \quad (2.17)$$

$$R_{m,i} = -\frac{\partial(\rho u_j u_i)}{\partial x_j} + \mu \frac{\partial^2 u_i}{\partial x_j^2} + \rho f_i, \quad (2.18)$$

where the dynamic viscosity  $\mu$  is constant and  $f$  is the specific volume force.

## 2.2 Numerical algorithms

In this part, the main numerical algorithms for solving the above governing equations are introduced.

### 2.2.1 Spatial discretization

Cartesian grids with uniform size have been used in the whole study. The partial derivatives (first and second) in space in the governing equations are discretized using the centered,

sixth-order finite difference schemes as follows:

$$\frac{\partial u_i}{\partial x} = \frac{1}{60} (u_{i+3} - u_{i-3} - 9(u_{i+2} - u_{i-2}) + 45(u_{i+1} - u_{i-1})) / \Delta x, \quad (2.19)$$

$$\frac{\partial^2 u_i}{\partial x^2} = \frac{1}{180} (2(u_{i+3} + u_{i-3}) - 27(u_{i+2} + u_{i-2}) + 270(u_{i+1} + u_{i-1}) - 490u_i) / \Delta x^2. \quad (2.20)$$

The schemes are stepwisely reduced down to third-order near real domain boundaries.

## 2.2.2 Time integration

There are different time integration algorithms implemented in DINO for flexibility. In the simulations of this dissertation, two algorithms are mainly used.

The first algorithm is a fully explicit, low-storage, fourth-order Runge-Kutta method [16]. This algorithm is computationally efficient but may suffer from stability issue for stiff applications. It can handle most of the simulation cases in this dissertation. The numerical procedure is

$$T^{n+1} = T^n + \Delta t \left( \left( -\frac{1}{\rho C_p} \sum_{k=1}^{N_s} h_k \dot{\omega}_k \right)^n + R_T^n \right), \quad (2.21)$$

$$Y_k^{n+1} = Y_k^n + \Delta t \left( \left( -\frac{\partial \dot{\omega}_k}{\partial \rho} \right)^n + R_{Y_k}^n \right), \quad (2.22)$$

$$\rho^{n+1} = \frac{pW^{n+1}}{RT^{n+1}}, \quad (2.23)$$

$$(\rho u_i)^* = (\rho u_i)^n + \Delta t R_{m,i}^n, \quad (2.24)$$

$$\nabla^2 \tilde{p}^{n+1/2} = \frac{1}{\Delta t} \left[ \frac{\partial \rho^{n+1}}{\partial t} + \frac{\partial (\rho u_j)}{\partial x_j} \right], \quad (2.25)$$

$$(\rho u_i)^{n+1} = (\rho u_i)^* - \Delta t \frac{\partial \tilde{p}^{n+1/2}}{\partial x_i}. \quad (2.26)$$

In this procedure, the pressure-free projection method [17–19] has been used.

The second algorithm is the implicit Williamson third-order Runge-Kutta method with analytic Jacobian inversion (PyJAC [20]). This algorithm is much more stable for stiff applications. The stiff combustion cases in the dissertation are simulated using this procedure:

$$T^* = T^n + \alpha_j \Delta t R_T^n, \quad (2.27)$$

$$Y_k^* = Y_k^n + \alpha_j \Delta t R_{Y_k}^n, \quad (2.28)$$

$$\rho^* = \frac{pW^*}{RT^*}. \quad (2.29)$$

The stiff terms are solved by the analytic Jacobian inversion, resulting in updated  $\left(-\frac{\partial \dot{\omega}_k}{\partial \rho}\right)^{n+1}$  and  $\left(-\frac{1}{\rho C_p} \sum_{k=1}^{N_s} h_k \dot{\omega}_k\right)^{n+1}$ . Then

$$T^{n+1} = T^* + \alpha_j \Delta t \left(-\frac{1}{\rho C_p} \sum_{k=1}^{N_s} h_k \dot{\omega}_k\right)^{n+1}, \quad (2.30)$$

$$Y_k^{n+1} = Y_k^* + \alpha_j \Delta t \left(-\frac{\partial \dot{\omega}_k}{\partial \rho}\right)^{n+1}, \quad (2.31)$$

$$\rho^{n+1} = \frac{pW^{n+1}}{RT^{n+1}}. \quad (2.32)$$

The momentum equations and Poisson equation are integrated in the same way as the explicit fourth-order Runge-Kutta method. The parameter  $\alpha_j$  ( $= 1/3, 5/12, 1/4$  for  $j = 1, 2, 3$  respectively) is the sub-integration parameter (3 sub-integrations for the third-order method).

### 2.2.3 Solving the Poisson equation

One of the most CPU-time consuming part is solving the Poisson equation (Eq. 2.25). An efficient way to solve this equation is necessary for fast computations. In DINO, the Poisson

equation is solved by Fast Fourier Transform (FFT). The developed approach is an extension of that described in [21–24], where pre- and post-processing were applied both in physical and in wave space. Suitable pre- and post-processing steps are applied to the corresponding array before and after calling the FFT subroutine in the 2DECOMP&FFT library [25] for different boundary conditions. This approach is computationally very efficient and gives a very high order of accuracy (comparable to spectral accuracy).

### 2.2.4 Boundary conditions and initial conditions

Boundary conditions for the low-Mach formulation or the incompressible formulation are straightforward [26]. Standard Dirichlet and Neumann boundary conditions perform well and stable.

For initial conditions, the concern is to generate a suitable initial turbulence for the simulation. In DINO, there are four different algorithms for generating an initial turbulence. In this dissertation, an Inverse Fast Fourier Transform (IFFT) relying on the Von Karman spectrum with Pao correction [27] is always used.

### 2.2.5 Parallelization

The parallelization in DINO relies on the open-source library 2DECOMP&FFT [25]. This library is built on top of standard MPI and MPI-I/O libraries and supports large-scale parallel applications on distributed memory systems [21, 22]. DINO has been written with the x-pencil orientation in order to minimize the computational time needed for transposing the data as required for non-periodic boundary conditions.

The resulting parallel efficiency has been tested on SuperMUC-NG at Leibniz super-computing center in Munich, ranging from 1024 to 65536 processors. The tested cases are reactive 3D Taylor-Green vortex benchmark as mentioned in [28]. Figure 2.1 shows the scal-



ing curve. The obtained parallel efficiency is quite high for a low-Mach DNS code, ensuring efficient computations for up to  $O(10^4)$  cores.

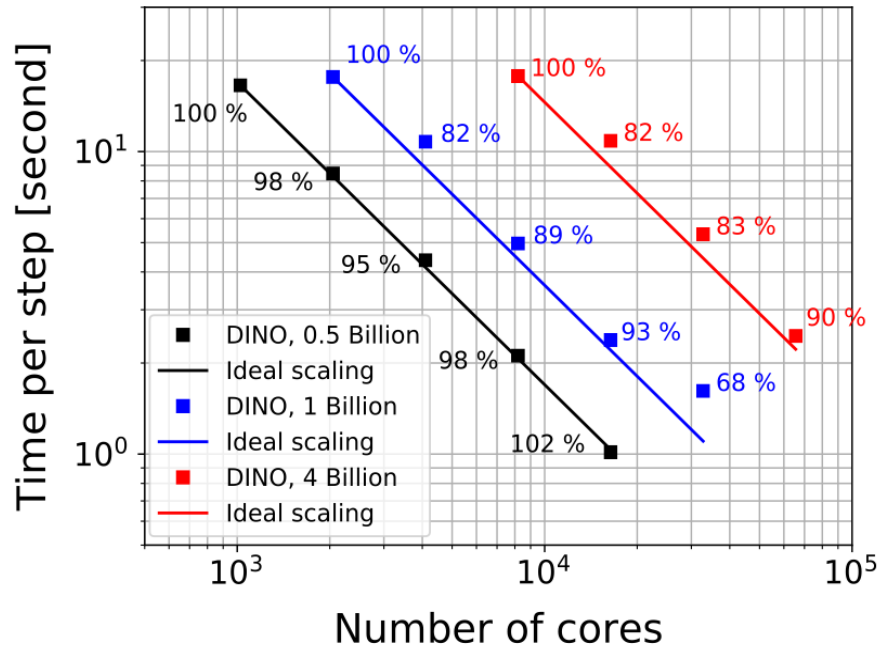


FIGURE 2.1. Strong scaling of DINO on SuperMUC-NG. Three cases with three different grid points are tested: 0.5, 1, and 4 billion grid points.



# Chapter 3

## Immersed Boundary Method

### Implementation

Parts of the results presented in this chapter have been published in the Journal of Computational Physics [29].

#### 3.1 Introduction

For computational fluid dynamics (CFD) simulations with complex geometries, Cartesian grids show many advantages over body-fitted methods, in particular easy mesh generation, memory and CPU savings, easy parallelization and possible benefit from adaptive mesh refinement. These advantages open the door for high-fidelity CFD simulations, explaining the numerous investigations on Cartesian grids in recent years.

As one of the most popular Cartesian grid methods, the immersed boundary method (IBM) has been introduced at the turn of the century [30, 31] and has been considerably extended since then [32, 33]. The underlying physics of IBM is to enforce the boundary conditions by modifying the momentum forces near the solid boundary, either continuously or discretely. The immersed boundary method is thus categorized as either continuous forcing

approach or discrete forcing approach [32, 34].

Compared to the continuous forcing approach [35, 36], where the forcing function is computed on the boundary and then spread over the vicinity of the immersed surface [37], the discrete forcing approach is more flexible and allows for a sharper representation of the immersed boundary [38]. In earlier discrete forcing methods [39–41], the discrete momentum forcing was computed on the body surface and inside the body; then, an explicit mass source/sink was required to maintain the conservation of mass near the boundary. To improve this point, an alternative discrete forcing method implicitly involves the momentum forcing in the discrete spatial operators, by introducing ghost cells. This approach is called ghost-cell immersed boundary method, and is considered in the present work.

Ghost-cell IBM was first introduced in [42, 43]. It has been later widely used and extended, see for instance [38, 44, 45]. Compared to other immersed boundary methods, such as cut-cell methods [46–49], ghost-cell IBM is more efficient and easier to implement in parallel, while showing comparable accuracy [6]. The ghost cell is identified as the grid cell (for a finite-volume discretization) or grid point (for a finite-difference discretization) in the solid phase near the solid boundary with at least one neighbor grid cell (respectively point) in the fluid. The conventional idea for ghost-cell IBM is to impose implicitly the boundary condition at the interface by including the variable values at the ghost cells in the governing equations. The ghost cell values are usually extrapolated from the values at the nearby fluid cells and at the boundary points.

As the boundary interface is only implicitly enforced, the accuracy of the ghost-cell IBM is a critical issue. Tseng and Ferziger [44] computed the values of the ghost cells with a quadratic extrapolation and obtained second-order accuracy for their ghost-cell IBM. Gao et al. [50] used a second-order Taylor series expansion for the ghost values, later eliminating numerical instabilities by matrix inversion [44]. Then, Mittal et al. [38] and Ghias et al.

[45] used well-conditioned extrapolation/interpolation stencils for the values of the variables at the ghost cells and also obtained second-order accuracy. Pan and Shen [51] and Chi et al. [6] introduced a simplified but still stable extrapolation/interpolation scheme involving a farther image point for the ghost cell values, delivering second-order accuracy for  $L_2$  and  $L_1$  norms.

All the previous studies tried to improve the accuracy of the ghost-cell IBM by introducing higher-order extrapolation/interpolation schemes for the ghost cell values. However, the convergence rate of the truncation error with the conventional ghost-cell IBM is not persistent, for reasons that we will describe in Section 3.2.3. Additionally, high-order extrapolation/interpolation methods are always sensitive to numerical instabilities [52]. Finally, for IBM coupled with a finite-difference discretization, as considered in the present work, high-order methods often lead to discrete conservation issues [41, 45, 49, 53, 54]. To solve these problems regarding convergence, stability, and conservation, an improved ghost-cell IBM is introduced in the present work.

First, some limitations of the conventional ghost-cell IBM are analyzed. Then, a stable, second-order ghost-cell IBM is introduced and implemented in a finite-difference solver. The method involves multiple ghost values at the ghost cells, one for each discretization direction. The developed approach is compatible with different discretization schemes in the interior of the fluid domain. In the present case, the IBM is implemented in a high-order finite-difference solver; the order is reduced progressively near the immersed boundary. In contrast to conventional ghost-cell methods, where ghost-cell variables are involved in the Navier-Stokes equations and boundary forces are implicitly enforced, the present approach involves instead explicit discrete forces near the boundary. The fictitious ghost cell values are only used to compute these discrete forces and are not directly considered in the continuity equation any more, resulting in improved mass conservation at the boundary. The present

approach leads to a straightforward parallel implementation, and the following test cases have been computed in parallel.

This chapter is organized as follows: Section 3.2 introduces the governing equations and the numerical methods, including discretization. In a second step, limitations of the conventional ghost-cell methods and proposed improvements are discussed. Then, simulation results from various test cases are shown in Section 3.3. Finally, Section 3.4 discusses the extension of the method for low Mach flows, followed by the conclusion in Section 3.6.

## 3.2 Formulation and Numerical Method

In this part, the governing equations for incompressible flows and the numerical method are explained. The main drawbacks of the conventional ghost-cell immersed boundary method are analyzed. In an effort to solve these issues, a novel ghost-cell IBM is proposed.

### 3.2.1 Governing equations

The incompressible formulation of the Navier-Stokes equations is considered in this first part. The conservation equations for mass and momentum are thus re-written from Eq. 2.17 and Eq. 2.2 as:

$$\nabla \cdot \mathbf{u} = 0, \quad (3.1)$$

$$\frac{\partial \mathbf{u}}{\partial t} + (\mathbf{u} \cdot \nabla) \mathbf{u} - \nu \nabla^2 \mathbf{u} + \nabla P \mathbf{I} = \mathbf{f} \quad (3.2)$$

Here,  $\mathbf{f}$  is the boundary forcing term,  $P$  is the pressure divided by (constant) density  $\rho$ ,  $\nu = \mu/\rho$  is the kinematic viscosity with  $\mu$  the dynamic viscosity, and  $\mathbf{u}$  is the velocity vector with components  $u$ ,  $v$  and  $w$ , i.e.  $\mathbf{u} = u\mathbf{i} + v\mathbf{j} + w\mathbf{k}$ .

### 3.2.2 Discretization scheme

Following the numerical schemes in the in-house direct numerical simulation solver DINO [7], the momentum equation (Eq. 3.2) is discretized spatially using a centered, sixth-order finite difference scheme, progressively reduced down to third order near real domain boundaries (meaning here the actual boundaries of the numerical domain, and not the additional immersed boundaries). For the example shown in what follows, the iteration in time uses a fully explicit, low-storage fourth-order Runge-Kutta method [16]. As explained in [7], implicit solvers are available as well, and could be also combined with the proposed IBM approach after minor changes.

For pressure/velocity coupling, the fractional step reads

$$\mathbf{u}^* = \mathbf{u}^n + \Delta t \mathbf{R}^n, \quad (3.3)$$

$$\nabla^2 P^{n+1/2} = \frac{1}{\Delta t} \nabla \cdot \mathbf{u}^*, \quad (3.4)$$

$$\mathbf{u}^{n+1} = \mathbf{u}^* - \Delta t \nabla P^{n+1/2}, \quad (3.5)$$

with  $\mathbf{R}$  the right-hand side term including convective term, diffusive term, and the boundary forcing term

$$\mathbf{R} = -(\mathbf{u} \cdot \nabla) \mathbf{u} + \nu \nabla^2 \mathbf{u} + \mathbf{f}. \quad (3.6)$$

Here,  $\mathbf{u}^*$  is the intermediate velocity. In this fractional step, the continuity and momentum equation are coupled together using the pressure-free projection method [17, 18]. The continuity constraint is ensured in Eq. (3.4), which is obtained from Eq. (3.5) by applying the divergence operator.

### 3.2.3 Conventional ghost-cell IBM

In the conventional ghost-cell immersed boundary method the boundary forcing term  $\mathbf{f}$  is implemented implicitly in the momentum equation in order to enforce the boundary condition at each time step [44]. Hence,  $\mathbf{f}$  is not evaluated explicitly and is set to 0 in the computation. Instead, the boundary forcing is implicitly coupled to the convective and diffusive terms in Eq. (3.6) and to the pressure gradient term in Eq. (3.5). By extrapolating the velocity and pressure at the ghost cells from the nearby fluid cells, and incorporating the boundary conditions, the convective, diffusive and pressure gradient terms at the fluid points near the boundary are modified. Equations (3.3) and (3.5) are transformed into:

$$\frac{\mathbf{u}^* - \mathbf{u}^n}{\Delta t} = \mathbf{R}^n + (\mathbf{R}^n|_{ghost} - \mathbf{R}^n), \quad (3.7)$$

$$\frac{\mathbf{u}^{n+1} - \mathbf{u}^*}{\Delta t} = -\nabla P^{n+1/2} + (\nabla P^{n+1/2} - \nabla P^{n+1/2}|_{ghost}), \quad (3.8)$$

where  $\mathbf{R}^n$  and  $\nabla P^{n+1/2}$  are the terms computed when assuming that there is no immersed boundary in the computational domain, while  $\mathbf{R}^n|_{ghost}$  and  $\nabla P^{n+1/2}|_{ghost}$  are the terms obtained when the values at the ghost cells are included in the computations. Thus,  $(\mathbf{R}^n|_{ghost} - \mathbf{R}^n)$  and  $(\nabla P^{n+1/2} - \nabla P^{n+1/2}|_{ghost})$  represent the action of the boundary forces on the fluid points. If  $(\mathbf{R}^n|_{ghost} - \mathbf{R}^n)$  and  $(\nabla P^{n+1/2} - \nabla P^{n+1/2}|_{ghost})$  are evaluated at the fluid points which are far away from the immersed boundary, these two values are equal to 0, recovering the standard solution. The range of influence of the immersed boundary at a fixed time step is determined by the discretization scheme employed to compute the partial derivatives.

In the present study, a sixth-order central difference scheme is used to discretize the spatial derivatives in the internal fluid domain. This high-order approach is particularly useful for simple turbulence studies, for instance in a periodic box. But it must be compatible



with the developed IBM method. The discretization scheme (denoted here as  $f_c(a, b, n)$  where  $a$  is the discretized variable,  $b$  is the discretization direction, and  $n$  is the order of the derivative) is as follows:

$$f_c(u_i, x, 1) = \frac{\partial u_i}{\partial x} = \frac{1}{60} (u_{i+3} - u_{i-3} - 9(u_{i+2} - u_{i-2}) + 45(u_{i+1} - u_{i-1})) / \Delta x; \quad (3.9)$$

$$f_c(u_i, x, 2) = \frac{\partial^2 u_i}{\partial x^2} = \frac{1}{180} (2(u_{i+3} + u_{i-3}) - 27(u_{i+2} + u_{i-2}) + 270(u_{i+1} + u_{i-1}) - 490u_i) / \Delta x^2. \quad (3.10)$$

As there are 3 points involved on either side of the discretization point  $i$ , this specific discretization involves three layers of fluid points near the immersed boundary, as shown in Fig. 3.1. As a consequence, three layers of ghost points are necessary to get correct derivatives at the fluid points near the immersed boundary. For instance, for the 1D case shown exemplarily in Fig. 3.1, the values at ghost points  $i + 1$ ,  $i + 2$  and  $i + 3$  are extrapolated from the fluid points and the boundary point P in the conventional ghost-cell IBM. The boundary force is discretely and implicitly applied at the fluid points  $i$ ,  $i - 1$  and  $i - 2$ .

In the conventional approach, the extrapolation for the ghost values takes place along the direction normal to the solid boundary, leading to the image point (IP) shown in Fig. 3.2. This procedure is straightforward and has been used to develop different high-order reconstruction schemes. However, some problems concerning accuracy, stability, and conservation are often encountered using the conventional approach. The main bottlenecks of the conventional ghost-cell IBM are as follows:

Drawback 1: In previous studies, different attempts have been documented concerning a higher order computation of the ghost cell values, in order to improve the order of accuracy of the IBM representation. However, most of those computations rely on the assumption that the order of  $\Delta l$  is of the same order as the grid size  $\Delta x$ , i.e.  $\Delta l = O(\Delta x)$ , where  $\Delta l$  is

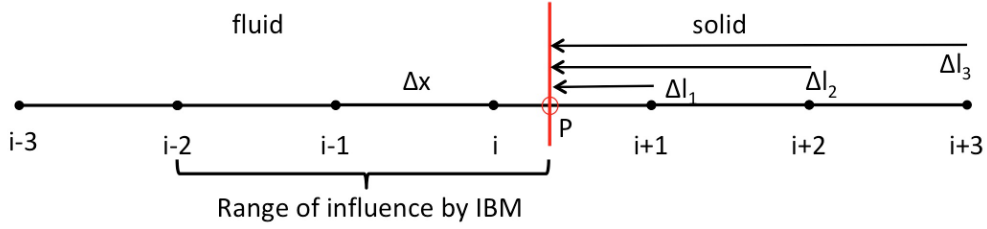


FIGURE 3.1. Conventional ghost-cell IBM: sketch for a one-dimensional case.

the distance from the ghost point to the boundary [34, 38, 50, 55]. Since  $\Delta l$  is not linearly related to  $\Delta x$ , the error term based on  $O(\Delta l)$  does not necessarily converge like  $\Delta x$ . The convergence rate of the truncation error is fluctuating and not persistent. It is believed that the error term based on  $O(\Delta l)$  will statistically converge at the desired order. However, to ensure a clean (persistent) convergence rate is still important, especially when a coarser simulation result is not good enough and a better result is expected by refining the mesh resolution.

Drawback 2: For multi-dimensional simulations, as explained in Fig. 3.2, the intersection point P with the solid body along the normal direction is the implicitly enforced boundary point when extrapolating the values at the ghost point  $(i + 1, j)$ . However, the points naturally relevant for the employed numerical discretization stencil are the boundary points X and Y (Fig. 3.2); those are not enforced at all.

Drawback 3: When considering high-order spatial discretization schemes in the fluid solver, as is here the case, multiple layers of ghost points become necessary. As shown in Eqs. (3.9) and (3.10), to compute the spatial derivatives at fluid point  $i$ , the ghost values at points  $i + 1$ ,  $i + 2$  and  $i + 3$  are required, which means that the distances  $\Delta l_1$ ,  $\Delta l_2$  and  $\Delta l_3$  must be taken into account simultaneously to enforce the boundary conditions. Looking back at Drawback 1, the relationship between  $\Delta l_1$ ,  $\Delta l_2$ ,  $\Delta l_3$ , and  $\Delta x$  is even more complex. Practically, this leads to a complex implementation. Multiple layers of ghost points hinder

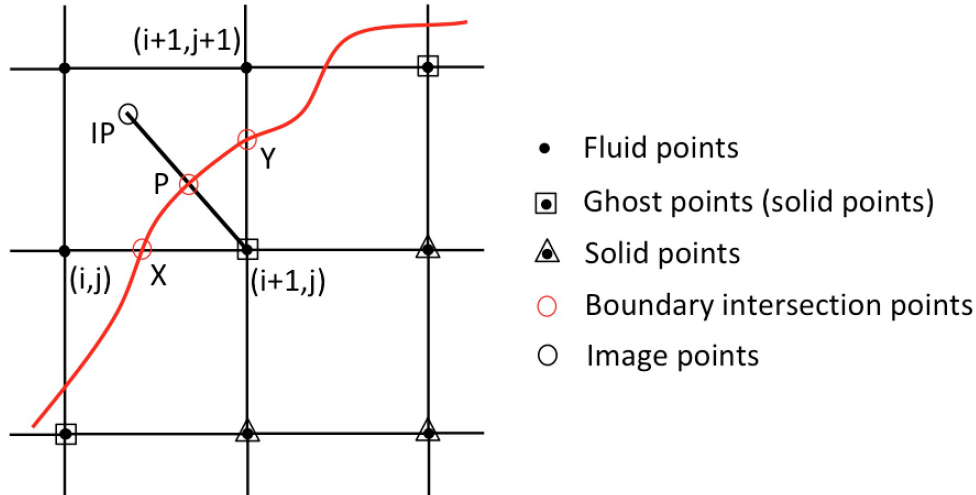


FIGURE 3.2. Conventional ghost-cell IBM: sketch for a two-dimensional case.

parallelization efficiency and make it more difficult to accurately capture the boundary layer at sharp corners.

### 3.2.4 A novel ghost-cell IBM implementation

In order to release the previously discussed bottlenecks, an improved ghost-cell IBM method is now introduced.

Drawback 2 is related to the representation of the immersed boundary, impacting the magnitude of the absolute error. Drawbacks 1 and 3 concern the convergence rate of the truncation error, determining the order of accuracy of the ghost-cell IBM. The magnitude of the absolute error is most important for DNS at higher Reynolds numbers, so that Drawback 2 is considered first.

In conventional methods, for instance in a two-dimensional case (Fig. 3.2), the values computed at the ghost point  $(i+1, j)$  will be used in both  $x$  and  $y$  directions for reconstructing the fictitious boundary force at fluid points  $(i, j)$  and  $(i+1, j+1)$ , respectively. Following the previous discussion, the fictitious momentum force at point  $(i, j)$  in  $x$  direction and at

point  $(i+1, j+1)$  in  $y$  direction can be formulated from Eq. (3.6) and Eq. (3.7) respectively as:

$$f_x(i, j) = - \left( \frac{\partial(u_{i,j}u_{i,j})}{\partial x} + \frac{\partial(u_{i,j}v_{i,j})}{\partial y} \right)_{ghost} + \nu \left( \frac{\partial^2 u_{i,j}}{\partial y^2} + \frac{\partial^2 u_{i,j}}{\partial x^2} \right)_{ghost} + \left( \frac{\partial(u_{i,j}u_{i,j})}{\partial x} + \frac{\partial(u_{i,j}v_{i,j})}{\partial y} \right) - \nu \left( \frac{\partial^2 u_{i,j}}{\partial y^2} + \frac{\partial^2 u_{i,j}}{\partial x^2} \right), \quad (3.11)$$

$$f_y(i+1, j+1) = - \left( \frac{\partial(v_{i+1,j+1}u_{i+1,j+1})}{\partial x} + \frac{\partial(v_{i+1,j+1}v_{i+1,j+1})}{\partial y} \right)_{ghost} + \nu \left( \frac{\partial^2 v_{i+1,j+1}}{\partial y^2} + \frac{\partial^2 v_{i+1,j+1}}{\partial x^2} \right)_{ghost} + \left( \frac{\partial(v_{i+1,j+1}u_{i+1,j+1})}{\partial x} + \frac{\partial(v_{i+1,j+1}v_{i+1,j+1})}{\partial y} \right) - \nu \left( \frac{\partial^2 v_{i+1,j+1}}{\partial y^2} + \frac{\partial^2 v_{i+1,j+1}}{\partial x^2} \right). \quad (3.12)$$

In Eq. (3.11) and Eq. (3.12), the partial derivatives with notation "ghost" are functions of the variables at the nearby fluid points and ghost points, depending on the employed discretization schemes (DCT):

$$\left( \frac{\partial \mathbf{u}_{i,j}}{\partial x} \right)_{ghost} = \text{DCT}(\mathbf{u}_{i+1,j}, \mathbf{u}_{i,j}, \mathbf{u}_{i-1,j} \dots), \quad (3.13)$$

$$\left( \frac{\partial \mathbf{u}_{i+1,j+1}}{\partial y} \right)_{ghost} = \text{DCT}(\mathbf{u}_{i+1,j}, \mathbf{u}_{i+1,j+1}, \mathbf{u}_{i+1,j+2} \dots). \quad (3.14)$$

To implicitly enforce the immersed boundary condition and get a proper boundary force, most conventional methods compute the ghost values  $\mathbf{u}_{i+1,j}$  by bilinear interpolation using the surrounding fluid points or boundary interception points. It is obvious that the two boundary points X and Y cannot be accurately represented simultaneously by using just one ghost value, no matter which reconstruction method is used for the ghost values. Therefore, two different sets of independent ghost values ( $\mathbf{u}_{i+1,j}|_x$  and  $\mathbf{u}_{i+1,j}|_y$ ) are necessary at the same ghost point  $(i+1, j)$  in order to fulfill the boundary conditions in both computational direc-

tions; similarly, three ghost values are employed for a 3D problem. Then, Equations (3.13) and (3.14) become

$$\left(\frac{\partial \mathbf{u}_{i,j}}{\partial x}\right)_{ghost} = \text{DCT}(\mathbf{u}_{i+1,j}|_x, \mathbf{u}_{i,j}, \mathbf{u}_{i-1,j}\dots), \quad (3.15)$$

$$\left(\frac{\partial \mathbf{u}_{i+1,j+1}}{\partial y}\right)_{ghost} = \text{DCT}(\mathbf{u}_{i+1,j}|_y, \mathbf{u}_{i+1,j+1}, \mathbf{u}_{i+1,j+2}\dots). \quad (3.16)$$

In this manner, both fictitious momentum forces  $f_x(i, j)$  and  $f_y(i + 1, j + 1)$  are computed correctly and account for the presence of the two boundary points X and Y simultaneously. In this way, the boundary is represented more accurately from the numerical point of view. A similar treatment has been proposed for incompressible viscous flows in [52] and for compressible Euler flows in [56]. These different ghost values are only used to reconstruct the fictitious boundary force in a discrete sense, and will not be used in the continuity equation.

For multi-dimensional simulations, the ghost values are now computed along the discretization directions instead of the boundary-normal direction. One disadvantage of this treatment would be for slip-wall boundary conditions, where curvature information of the boundary at the point where it is intersected by the grid is required. However, all the cases considered in what follows and in our research involve no-slip wall boundary conditions, leading to a straightforward computation of the ghost values along the grid directions. The algorithm for extrapolating the ghost values is introduced later.

Concerning now drawback 3, reducing progressively the discretization scheme near the immersed boundary reduces the number of required layers of ghost points. The same is already done at the real boundaries. In the present ghost-cell IBM, the original sixth-order finite-difference algorithm is reduced step-by-step to 1) fifth order at the second layer of fluid points near the immersed boundary, and 2) fourth order at the first layer, leading to following equations for the first derivatives in the one-dimensional case exemplified in Fig.

3.1:

$$\begin{aligned} \frac{\partial u_{i-1}}{\partial x} \Big|_{5th} = & \frac{1}{60} (2(u_{i-3} - u_{i-4}) - 13(u_{i-2} - u_{i-3}) + 20(u_{i-1} - u_{i-2}) \\ & + 27(u_i - u_{i-2}) - 3(u_{i+1} - u_i)) / \Delta x; \end{aligned} \quad (3.17)$$

$$\begin{aligned} \frac{\partial u_i}{\partial x} \Big|_{4th} = & \frac{1}{12} ((u_{i+1} - u_{i-3}) + 2(u_{i+1} - u_{i-1}) + 10(u_i - u_{i-1}) \\ & - 6(u_{i-1} - u_{i-2})) / \Delta x. \end{aligned} \quad (3.18)$$

Similar to the original discretization function  $f_c$ , the above discretization with a step-wise order reduction is denoted as  $f_b$ . The employed stencils are no longer centered (as was the case for the sixth-order finite difference), but are forward/backward finite-difference schemes depending on the position of the immersed boundary. Therefore, only one layer of ghost points is finally needed to reconstruct the boundary forces. This treatment is not specific for the sixth-order central finite difference scheme employed in this study; it can be easily adjusted for other high-order finite-difference algorithms.

Provided everything has been implemented correctly, the truncation error would converge at fourth-order with the grid size. The final order of accuracy will be limited by the accuracy of the computation of the ghost point values. The truncation errors in the computations of the ghost point values involve both  $\Delta l$  and  $\Delta x$ . As there is no direct linear relationship between  $\Delta l$  and  $\Delta x$ , as discussed previously, the persistent convergence rate of the truncation error can be ensured if  $\Delta l$  is treated properly.

In the current ghost-cell IBM implementation, a third-order extrapolation scheme based

on a Taylor series expansion on a regular grid is applied for the ghost point velocities,

$$\begin{aligned}
 u_{i+1} = & u_P + \Delta l \left( \frac{u_{i-1} - u_P}{2\Delta x - \Delta l} - \frac{2(u_i - u_P)}{\Delta x - \Delta l} \right) + O(\Delta l \Delta x^2) \\
 & + O(\Delta x^4) + O\left(\frac{\Delta x^5}{2\Delta x - \Delta l}\right) + O\left(\frac{\Delta x^2(\Delta x - \Delta l)^3}{2\Delta x - \Delta l}\right),
 \end{aligned} \tag{3.19}$$

where  $u_P$  denotes the corresponding fluid variable at the boundary. This solution is equivalent to quadratic polynomial interpolation and is retained to eliminate the error terms which are dominated by  $O(\Delta l^n \Delta x^m)$ , with  $n \geq 1$  and  $m \leq 1$ .

From Eq. (3.19), it is clear that the total truncation error is dominated by  $O(\Delta l \Delta x^2)$ , which should converge in a third-order manner with grid size  $\Delta x$  (at least second-order persistent convergence rate).

To avoid stability issue of the above extrapolation scheme when the fluid point is too close to the boundary (i.e., when  $\Delta x - \Delta l$  is approaching 0), the higher order scheme is reduced down to a lower order when  $1 - \frac{\Delta l}{\Delta x} < r$ . In that case,

$$u_{i+1} = u_P + \Delta l \frac{u_P - u_{i-1}}{2\Delta x - \Delta l}. \tag{3.20}$$

Here,  $r$  is the stability threshold. Based on our experience with the test cases shown in what follows, it is recommended to choose  $r$  between 0.1 and 0.2, the solution being more stable for a higher value of  $r$  but more accurate for a lower value of  $r$ . In the examples shown in the next section,  $r = 0.2$  has been systematically retained. The 1st order fallback scheme described by Eq. (3.20) will inevitably impact in a negative manner the overall order of the proposed IBM method whenever it is activated. This is the reason why the formally second-order approach will deliver a real overall order lower than two (especially for coarser grids) in the numerical tests discussed in what follows. As suggested by one reviewer of [29], an alternative way to solve the above stability issue would be to shift the stencil in Eq. (3.19)

by  $\Delta x$  if  $(\Delta x - \Delta l) < \frac{\Delta x}{2}$ . This approach would indeed keep the order. However, it would also involve farther fluid points in the stencil, which may be a problem, for instance for very thin boundary layers.

For conventional ghost-cell IBM, a Neumann boundary condition for pressure is usually enforced [38, 43], resulting in zero pressure force over the boundary. However, an unphysical mass flux still might exist at the boundary. The drawback of the Neumann boundary condition for pressure at the immersed boundary has been discussed in [57, 58]. To explain this issue, Equations (3.4) and (3.5) are written as follows near the immersed boundary:

$$\nabla^2 P^{n+1/2} = \frac{1}{\Delta t} \nabla \mathbf{u}_{ghost}^*, \quad (3.21)$$

$$\mathbf{u}^{n+1} = \mathbf{u}_{ghost}^* - \Delta t \nabla P_{ghost}^{n+1/2}. \quad (3.22)$$

$\nabla \mathbf{u}_{ghost}^*$  is computed by involving the ghost velocity field  $\mathbf{u}_{ghost}^*$ , which contains the interpolated (fictitious) values at the ghost points. The quantity  $\nabla P_{ghost}^{n+1/2}$  takes into account the Neumann condition at the boundary. By applying the divergence operator to Eq. (3.22), and using Eq. (3.21),

$$\begin{aligned} \nabla \mathbf{u}^{n+1} &= \nabla \mathbf{u}_{ghost}^* - \Delta t \nabla^2 P_{ghost}^{n+1/2} \\ &= \Delta t \nabla^2 P^{n+1/2} - \Delta t \nabla^2 P_{ghost}^{n+1/2}. \end{aligned} \quad (3.23)$$

The pressure field  $P_{ghost}$  is modified from the field  $P$  using:

$$P_{ghost}(\mathbf{x}) = \begin{cases} P(\mathbf{x}), & \text{if } \mathbf{x} \in \text{fluid and solid region,} \\ P^*(\mathbf{x}), & \text{if } \mathbf{x} \in \text{ghost region,} \end{cases} \quad (3.24)$$

where  $\mathbf{x}$  denotes the location of the computed grid point.  $P^*(\mathbf{x})$  is usually interpolated or extrapolated from  $P(\mathbf{x})$  by incorporating the Neumann boundary condition for pressure



on the IB. By involving the ghost (unphysical) values  $\mathbf{u}_{ghost}^*$  in the above computation, the pressure correction equation (Eq. (3.22)) would generate a driving pressure force if the Neumann boundary condition is not enforced. Thus, the inter/extrapolated  $P^*(\mathbf{x})$  is not the same as  $P(\mathbf{x})$  at the ghost points. It is also obvious from Eq. (3.23) and Eq. (3.24) that  $\nabla \mathbf{u}^{n+1}$  is not equal to 0 at the fluid points near the IB, leading to an unphysical mass source or sink term there. This discussion shows that there would be an unphysical mass flux across the boundary if the Neumann boundary condition would be simply enforced for the pressure near the boundary. Therefore, as already done in [57, 58], the physical solution, instead of the fictitious velocity field, is applied at the ghost points in Eq. (3.21) and Eq. (3.22). More numerical details can be found in Section 3.2.5. In this manner, there is no driving pressure force along the IB and a Neumann boundary condition for pressure is not needed. As a result, local continuity is preserved, without any additional mass source or sink. This pressure treatment is also simpler compared to the implementation of a Neumann boundary condition.

After implementing all these features, the resulting ghost-cell IBM should deliver accurate and stable results while fulfilling the divergence-free condition, as will be shown in what follows for different test-cases of increasing complexity.

### 3.2.5 Method summary

The numerical procedure for the proposed IBM approach can be summarized as follows:

1. Compute the level set function, which is time-dependent for a moving geometry.
2. Determine the locations of the ghost points (i.e., one layer of grid points within the solid body).
3. Substitute the velocity at the ghost points and solid points with the boundary (solid

body) velocity and store it as pre-extrapolation velocity field  $\mathbf{u} = (u, v, w)$ . Extrapolate the ghost values at the ghost points using Eqs. (3.19) and (3.20). For multi-dimensional cases, extrapolate in each direction separately, and store the scalar ghost values in vectors ( $\mathbf{u}_G = (u_{gx}, u_{gy}, u_{gz})$ ,  $\mathbf{v}_G = (v_{gx}, v_{gy}, v_{gz})$  and  $\mathbf{w}_G = (w_{gx}, w_{gy}, w_{gz})$  where the indices  $gx, gy, gz$  represent the values in  $x, y, z$  directions.) After extrapolation, there are three (for 3D cases) newly generated velocity fields, denoted as  $\mathbf{u}_{gx} = (u_{gx}, v_{gx}, w_{gx})$ ,  $\mathbf{u}_{gy} = (u_{gy}, v_{gy}, w_{gy})$ , and  $\mathbf{u}_{gz} = (u_{gz}, v_{gz}, w_{gz})$ . These velocity fields keep the same values at the fluid points as the pre-extrapolation velocity field  $\mathbf{u} = (u, v, w)$ .

4. Compute the fictitious force based on the directional ghost values, using

$$\mathbf{F}(\mathbf{x}) = \begin{cases} \mathbf{R}_{b,\mathbf{x}}(\mathbf{u}_{gx}, \mathbf{u}_{gy}, \mathbf{u}_{gz}) - \mathbf{R}_{c,\mathbf{x}}(\mathbf{u}), & \text{if } \mathbf{x} \in \text{IBM influence range} \\ 0, & \text{otherwise.} \end{cases} \quad (3.25)$$

The range of IBM influence has been discussed in the previous section, and depends on the actual discretization scheme, as shown in Fig. 3.1. It is smaller if the scheme is more compact and if the discretization order is lower.  $\mathbf{R}_{c,\mathbf{x}}(\mathbf{u})$  is the right-hand-side of the momentum equation:

$$\mathbf{R}_{c,\mathbf{x}} = \mathbf{L}(f_c(u|v|w, x|y|z, 1|2)). \quad (3.26)$$

The term  $\mathbf{R}_{b,\mathbf{x}}(\mathbf{u}_{gx}, \mathbf{u}_{gy}, \mathbf{u}_{gz})$  is obtained from

$$\begin{aligned} \mathbf{R}_{b,\mathbf{x}} = & \mathbf{L}(f_b(u_{gx}|v_{gx}|w_{gx}, x, 1|2), \\ & f_b(u_{gy}|v_{gy}|w_{gy}, y, 1|2), f_b(u_{gz}|v_{gz}|w_{gz}, z, 1|2)), \end{aligned} \quad (3.27)$$

where function  $f_c$  has been presented in Eqs. (3.9) and (3.10), function  $f_b$  has been

defined in Eqs. (3.17) and (3.18). The symbol  $|$  represents "or".  $\mathbf{L}()$  is the vector function, whose output components are computed by the scalar inputs separately.

5. Add the fictitious force to the right-hand-side of the momentum equation (Eq. (3.3)) as:

$$\mathbf{u}^* = \mathbf{u}^n + \Delta t (\mathbf{R}^n + \mathbf{F}(\mathbf{x})^n). \quad (3.28)$$

Equation (3.28) is computed only in the fluid region. Then, solve the Poisson equation (Eq. (3.4)), for instance with a fast spectral approach [7, 21]:

$$\nabla^2 P^{n+1/2} = \frac{1}{\Delta t} \nabla \cdot \mathbf{u}^*. \quad (3.29)$$

Finally, update the velocity field  $\mathbf{u}^{n+1}$  using the pressure correction equation (Eq. (3.5)) and the pressure field computed from Eq. (3.29). During this process, physical solutions remain at the ghost points and solid points.

6. Continue the next Runge-Kutta sub-time step. (Go back to Step (3).)
7. Continue the next time step. (Go back to Step (3) for a stationary boundary or to Step (1) for a moving boundary.)

As the algorithm only needs to replace the partial derivatives concerning convection and diffusion terms, it is fairly independent of the actual procedures employed for spatial discretization and temporal iteration. Concerning for instance time integration, the IBM algorithm has been already successfully combined with a fully explicit, low-storage 4th-order Runge-Kutta method [16], a 3rd-order explicit Williamson method [59], and a 3rd-order semi-implicit Williamson-Runge-Kutta method with analytic Jacobian inversion (in case of reactive-flow) [20], without any major impact on the implementation.

### 3.2.6 Geometry representation and boundary motion

The present ghost-cell IBM is combined with a level-set method [60] to represent the complex geometry and the motion of the boundary. The level-set function  $\phi$  is computed at every grid point and contains the signed distance from the grid point to the immersed boundary. Therefore,  $\phi = 0$  is exactly where the boundary locates. For a moving boundary, the level-set function  $\phi$  is varying with time. To compute  $\phi$  for a given geometry, the explicit mathematical expression of the level-set function or the triangular surface mesh of the geometry should be known; then, the level-set values can be directly computed from the explicit function, or reconstructed from the surface mesh. The values of  $\phi$  at the ghost points are used to compute  $\Delta l$  and are thus necessary for an accurate reconstruction of the boundary. More details about the level-set method can be found in [61–63].

To deal with a moving boundary, one critical issue is the computation of the fluid variables such as velocity and pressure for the freshly generated fluid points that were solid points at the previous time step, i.e. for which  $(\phi_i^{n+1}\phi_i^n < 0)$ . In the present study, the fluid values at these new fluid points are interpolated from the surrounding fluid points and from the nearby boundary point, taking into account the moving boundary. Details concerning the implemented interpolation algorithm can be found in Mittal et al. [38].

### 3.2.7 Efficient implementation and parallelization

The implementation of the developed ghost-cell method is flexible. It can be combined with many different spatial discretization schemes and time integration approaches. As the extrapolation scheme always stick to the discretization directions, this method does not need to solve an interpolation matrix for the ghost values, as done for instance in [38, 41]. This avoids additional iterations involved by the matrix computation, reducing computational time.

For most conventional ghost-cell IBM methods, parallelization on large distributed-memory computers is not easy. By involving the image point [6, 38, 45, 51], which is projected normally through the boundary from the ghost point, the communication between different CPU/GPU processors becomes necessary, which is particularly challenging when the corresponding ghost point is near a domain-decomposition interface. Though it would be possible to derive a communication pattern containing directly the corner points when parallelizing the IBM procedure, this is not so straightforward for parallelization algorithms relying on the pencil decomposition. This issue disappears in the present ghost-cell IBM, since it does not involve any boundary-normal projected point. The parallelization of the new ghost-cell IBM is simple and straightforward. For the test cases shown in what follows, parallelization relies on a 2D pencil decomposition based on the open-source library 2DECOMP&FFT [25]. The communication between subdomain boundaries is handled by the halo-cell communication function integrated in the library.

### 3.3 Benchmark Simulations

In this section, the stability and accuracy of the new ghost-cell IBM method is checked in various benchmarks involving incompressible flow simulations of increasing complexity. Both stationary and moving, simple and complex geometries are taken into account. The rate of convergence is evaluated from the linear regression of the norm errors, which are denoted  $L_m$ , with  $L_m = (\sum_i^N |e_i|^m / N)^{1/m}$ . Here  $e_i$  is the error relative to the exact (baseline) solution at the  $i$ -th grid point, and  $N$  is the total number of grid points in the computational domain. The  $L_\infty$  error is defined as the largest local error ( $\max |e_i|$ ) in the whole domain.

### 3.3.1 Tilted planar Poiseuille flow

This first case is simulated to check the magnitude of the error near the immersed boundary. An exact analytical solution exists for this case. In order to activate the IBM, the planar channel has been tilted on purpose by a specific angle, so that the channel boundaries in general do not align with the actual grids. The Reynolds number for the planar Poiseuille flow is defined as  $Re = UD/\nu$ , where  $D$  is the distance between the two channel boundaries,  $U$  is the mean flow velocity,  $\nu$  is the kinematic viscosity. A laminar flow with Reynolds number  $Re = 120$  is simulated in the present case. The numerical setup of the tilted Poiseuille flow is shown in Fig. 3.3.

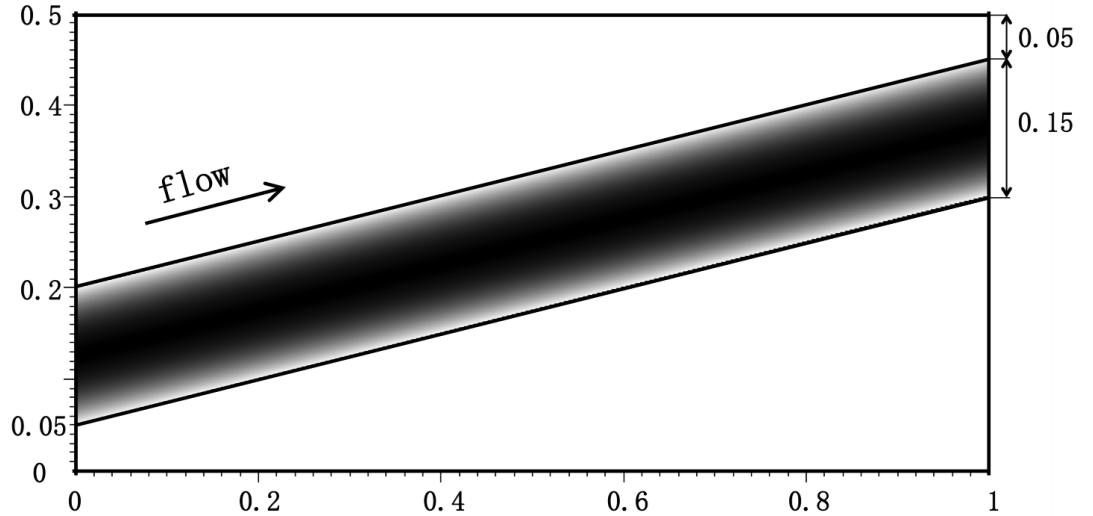


FIGURE 3.3. Computational domain for the tilted planar Poiseuille flow (all lengths are in cm).

The planar Poiseuille flow has been simulated twice using two different IBM approaches: 1) the ghost-cell IBM described in [38], and 2) the novel IBM approach described in this work. Both simulations are continued up to the same iteration with the same constant time

step  $\Delta t = 10^{-5}$  s. The absolute error is computed in a smaller domain  $[0.1:0.9]\text{cm} \times [0:0.5]\text{cm}$ , to exclude the possible influence of the inlet and outlet boundary. This choice gives a more reasonable comparison between these two methods, as we do not know the performance of the reference IBM [38] intersected with the real boundary. Table 3.1 shows the error norms computed for the two methods using the same uniform grid with  $2048 \times 1024$  points. The magnitude of the error norm is smaller using the proposed IBM method, which indicates that the representation of the domain boundaries is improved.

To quantify the convergence rate of the proposed IBM, the absolute error has been computed for different grid resolutions ( $2048 \times 1024$ ,  $1024 \times 512$ ,  $512 \times 256$ ,  $256 \times 128$ ). Table 3.1 shows the errors and the estimated convergence orders at each refinement step. Similarly, figure 3.4 shows the convergence rates of the  $L_1$ ,  $L_2$  and  $L_\infty$  norm errors for the two components ( $u$  and  $v$ ) of velocity. It can be seen that the results are approaching second-order accuracy, deviations being due to the 1st order fallback scheme described by Eq. (3.20).

Grids	$256 \times 128$	$512 \times 256$	$1024 \times 512$	$2048 \times 1024$	$2048 \times 1024$ ([38])
$L_1$ for $u$	$4.37 \times 10^{-4}$	$1.19 \times 10^{-4}$	$3.20 \times 10^{-5}$	$6.78 \times 10^{-6}$	$5.67 \times 10^{-5}$
Est. order	-	1.88	1.89	2.24	
$L_2$ for $u$	$1.09 \times 10^{-3}$	$3.12 \times 10^{-4}$	$8.83 \times 10^{-5}$	$2.03 \times 10^{-5}$	$1.51 \times 10^{-4}$
Est. order	-	1.80	1.82	2.12	
$L_\infty$ for $u$	$6.71 \times 10^{-3}$	$2.58 \times 10^{-3}$	$8.57 \times 10^{-4}$	$2.59 \times 10^{-4}$	$3.30 \times 10^{-4}$
Est. order	-	1.38	1.59	1.73	
$L_1$ for $v$	$3.74 \times 10^{-4}$	$1.05 \times 10^{-4}$	$2.89 \times 10^{-5}$	$7.12 \times 10^{-6}$	$1.40 \times 10^{-5}$
Est. order	-	1.83	1.86	2.02	
$L_2$ for $v$	$1.13 \times 10^{-3}$	$3.44 \times 10^{-4}$	$9.18 \times 10^{-5}$	$2.20 \times 10^{-5}$	$4.73 \times 10^{-5}$
Est. order	-	1.72	1.91	2.06	
$L_\infty$ for $v$	$5.22 \times 10^{-3}$	$1.92 \times 10^{-3}$	$5.93 \times 10^{-4}$	$1.65 \times 10^{-4}$	$2.35 \times 10^{-4}$
Est. order	-	1.44	1.70	1.85	

TABLE 3.1. Magnitude of the absolute error and computed convergence order for the planar Poiseuille flow simulation using the novel IBM compared to the simulation using the IBM from [38].

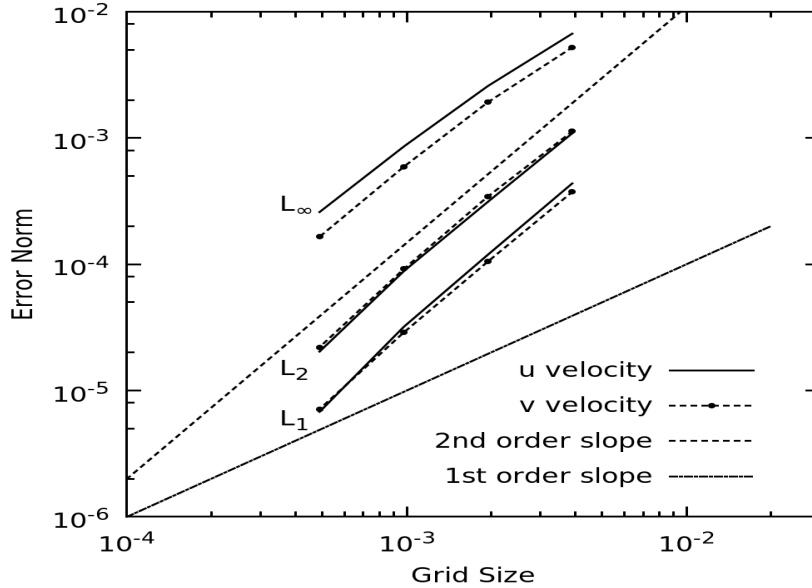


FIGURE 3.4. Convergence of the  $L_1$ ,  $L_2$  and  $L_\infty$  norm errors of  $u$  and  $v$  velocity components when refining the computational grid.

### 3.3.2 Uniform flow past a fixed circular cylinder

This case is a standard benchmark for the validation of Navier-Stokes solvers and IBM algorithms. The resulting flow shows different behaviors as a function of the Reynolds number. The Reynolds number is  $Re = U_\infty D / \nu$ , where  $D$  is the diameter of the cylinder,  $U_\infty$  is the incoming velocity of the uniform flow. The flow remains steady and symmetrical for Reynolds number lower than about 47, then becomes unsteady and generates periodic Kármán vortex streets for higher Reynolds numbers. When the Reynolds number becomes higher than about 188.5, the flow begins to intrinsically turn into a three-dimensional flow [64–66]. For the present study, flows at Reynolds number of 40 and 100 have been investigated in two-dimensional simulations.

The simulation domain is a square with side length  $40D$ , which is large enough to minimize the domain confinement effects on the development of the wake. A uniform grid with  $1024 \times 1024$  grid points is used to discretize the domain, which makes the grid resolution



near the cylinder comparable to that of [44]. The cylinder is centered at  $(16D, 20D)$  in the domain.

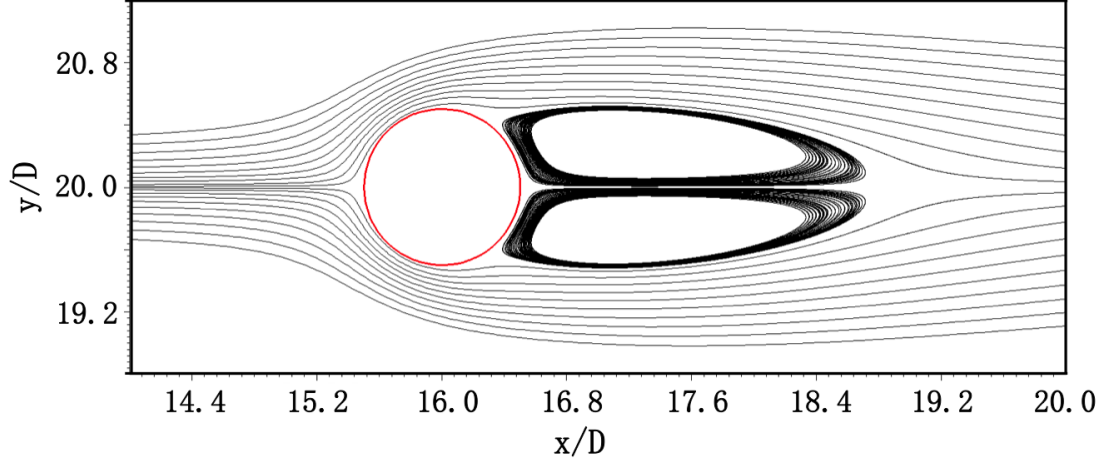
Figure 3.5 shows the streamlines around the cylinder at  $Re = 40$ . A steady solution is obtained, symmetrical about the wake centerline. The drag coefficient  $C_D = F_x / (0.5\rho U_\infty^2 D)$  has been calculated, where  $F_x$  is the drag force calculated using the domain integral method described in [67]. Then, the length of the recirculation zone  $L_W$  has been extracted. As shown in Table 3.2, the comparison with previous studies, both numerical and experimental, is very good.

	Re=40		Re=100
	$L_W/D$	$C_D$	$St=fD/U_\infty$
Current study	2.29	1.53	0.166
Tseng and Ferziger [44]	2.21	1.53	0.164
Ye et al. [48]	2.27	1.52	-
Lai and Peskin [67]	-	-	0.165
Kim et al. [40]	-	1.51	0.165
Baranyi [68]	-	-	0.163
Williamson (Exp.) [69]	-	-	0.166

TABLE 3.2. Comparison between the current study and previous works concerning recirculation length  $L_W$ , drag coefficient  $C_D$ , and Strouhal number  $St=fD/U_\infty$ , where  $f$  is the frequency of vortex shedding.

The convergence rate has been checked again in this case. The simulation results with a finer resolution  $1024 \times 1024$  are taken as baseline solution for computing the truncation errors. The  $L_1$ ,  $L_2$  and  $L_\infty$  norm errors using coarser resolutions ( $512 \times 512$ ,  $256 \times 256$ ,  $128 \times 128$ ) have been computed and tabulated in Table 3.3. The norm errors using the IBM from [38] with resolution  $512 \times 512$  is also tabulated for comparison. The proposed IBM systematically leads to a slightly smaller absolute error. Figure 3.6 shows the associated convergence rate. As it can be seen, the measured errors are again converging with the grid size at a rate close to the second-order slope.

For the flow at  $Re = 100$ , the wake becomes unstable and a Kármán vortex street is

FIGURE 3.5. Streamlines of the flow around a fixed circular cylinder at  $Re = 40$ 

Grid size (mm)	1/128	1/256	1/512	1/512 ([38])
$L_1$ for $u$	$8.62 \times 10^{-4}$	$1.59 \times 10^{-4}$	$2.88 \times 10^{-5}$	$2.04 \times 10^{-4}$
Est. order	-	2.44	2.46	
$L_2$ for $u$	$2.45 \times 10^{-3}$	$4.43 \times 10^{-4}$	$7.41 \times 10^{-5}$	$5.84 \times 10^{-4}$
Est. order	-	2.47	2.58	
$L_\infty$ for $u$	$5.17 \times 10^{-2}$	$1.41 \times 10^{-2}$	$4.12 \times 10^{-3}$	$8.14 \times 10^{-3}$
Est. order	-	1.87	1.77	
$L_1$ for $v$	$6.11 \times 10^{-4}$	$1.02 \times 10^{-4}$	$1.68 \times 10^{-5}$	$1.44 \times 10^{-4}$
Est. order	-	2.58	2.60	
$L_2$ for $v$	$1.54 \times 10^{-3}$	$2.96 \times 10^{-4}$	$5.49 \times 10^{-5}$	$4.01 \times 10^{-4}$
Est. order	-	2.38	2.43	
$L_\infty$ for $v$	$3.84 \times 10^{-2}$	$9.81 \times 10^{-3}$	$2.63 \times 10^{-3}$	$4.81 \times 10^{-3}$
Est. order	-	1.97	1.90	

TABLE 3.3. Magnitude of the absolute error and computed convergence order for the flow past a circular cylinder at  $Re = 40$  using the novel IBM in comparison with the IBM from [38].

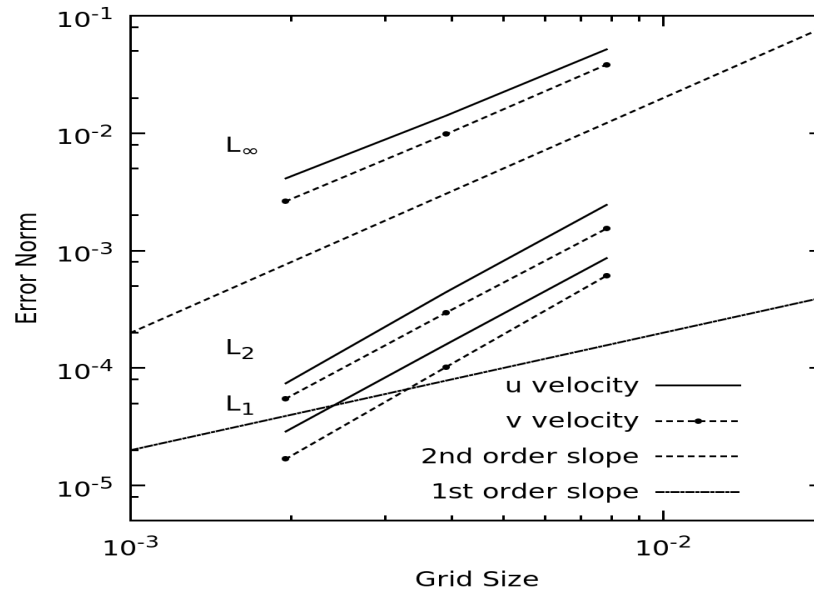


FIGURE 3.6. Convergence of the  $L_1$ ,  $L_2$  and  $L_\infty$  norm errors of the streamwise ( $u$ ) and spanwise ( $v$ ) velocity with the computational grid size.

generated, as shown in Fig. 3.7.

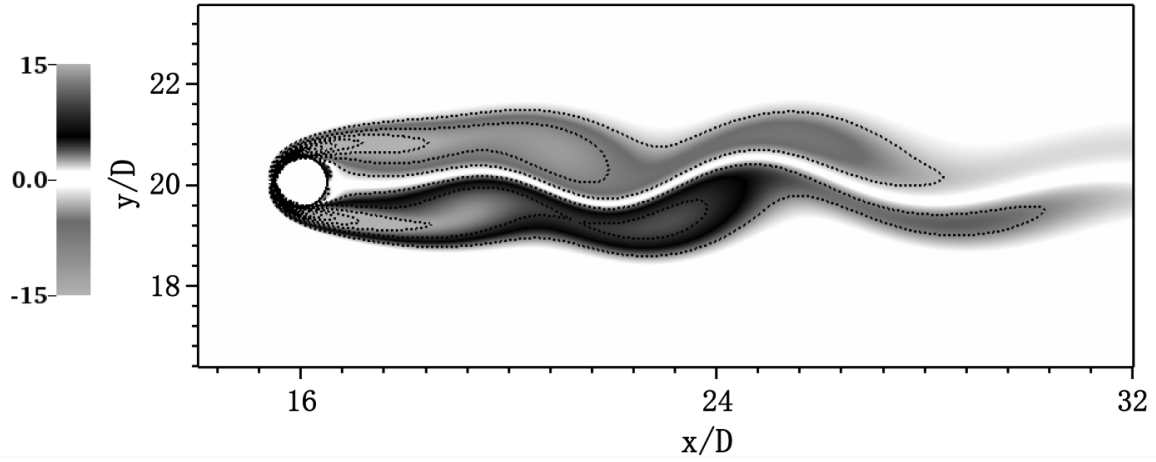
The vortex shedding frequency  $f$  can be obtained from the periodic variation of the flow. The Strouhal number  $St = fD/U_\infty$  is then calculated, and is shown in Table 3.2. The obtained results match very well with previous numerical and experimental studies.

### 3.3.3 Oscillating circular cylinder in a fluid at rest

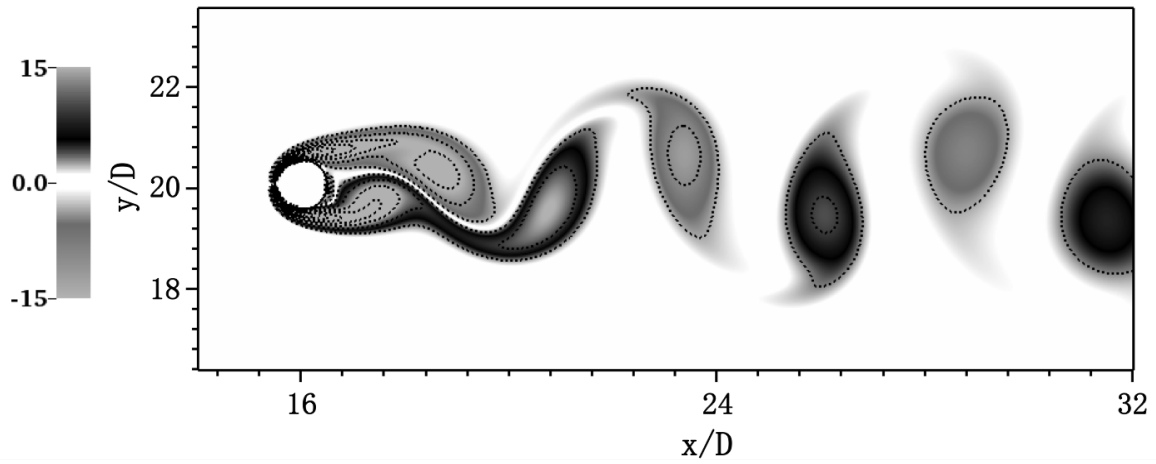
After checking the accuracy for a flow over a fixed geometry, the performance of the ghost-cell IBM for moving geometries must also be investigated. For this purpose, an oscillating circular cylinder in a fluid initially at rest is simulated using the proposed method.

The cylinder is initially located at the center of the domain. Its center oscillates in the streamwise direction as follows

$$x(t) = -A \sin(2\pi ft), \quad (3.30)$$



(a)



(b)

FIGURE 3.7. Instantaneous vorticity contours plot for the flow at  $\text{Re} = 100$  around the fixed circular cylinder at (a)  $t = 30T$  (b)  $t = 60T$ , with  $T = D/U_\infty$ .

where  $A$  is the amplitude of the oscillation and  $f$  is the oscillation frequency.

The Reynolds number is defined as  $Re = U_{max}D/\nu$ , where  $U_{max}$  is the maximum velocity of the cylinder,  $D$  is the diameter of the cylinder,  $\nu$  is the kinematic viscosity. Another important parameter is the Keulegan-Carpenter number,  $KC = U_{max}/fD$ . For the present study,  $Re = 100$  and  $KC = 5$ , keeping the values previously used by Dütsch et al. [70] for LDA experiments and a companion numerical study.

The computational domain is chosen to be  $60D \times 30D$ . All the boundaries are outflow boundary conditions with a velocity gradient equal to 0. The cylinder surface is associated to a no-slip velocity boundary condition, with a surface velocity  $u(t) = -2\pi fA \cos(2\pi ft)$ . The fluid domain is discretized by a uniform grid with  $2048 \times 1024$  points, resulting in a mesh resolution near the cylinder similar to that used in [71].

Figure 3.8 shows the normalized streamwise and spanwise velocity ( $u/u_{max}$  and  $v/v_{max}$ ) at 4 different cross-sections ( $x = -0.6D, 0D, 0.6D$  and  $1.2D$ ) for 3 different phase positions ( $\phi = 180^\circ, 210^\circ, 330^\circ$ ). The results are compared with the LDA measurements of [70]. Even if some discrepancies are observed, it is clear that the present results are overall in good agreement with the experimental data.

The in-line force  $F_x$  acting on the oscillating cylinder has been computed as a function of time and is shown in Fig. 3.9. Here, the comparison with the experimental measurements is perfect, confirming the accuracy of the present ghost-cell IBM for describing the flow around a moving geometry.

### 3.3.4 Flow around a flapping wing

The previous case considered only the translational motion of a solid body. In the present configuration, the flow induced by a flapping wing is investigated, which involves both translational and rotational motion. The velocity along the body surface points is not uniform

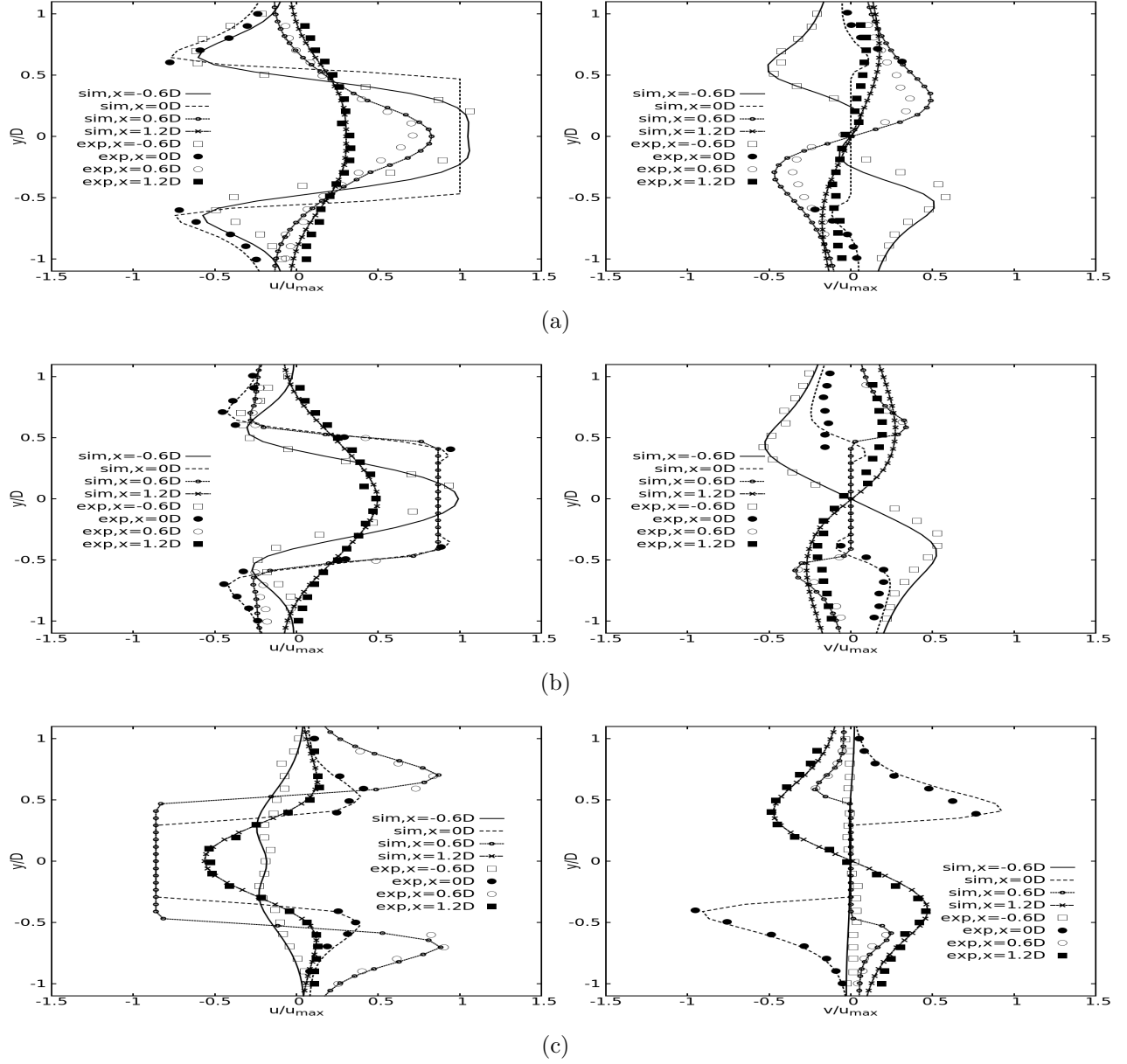


FIGURE 3.8. Velocity profiles in streamwise  $u$  (left), and spanwise direction  $v$  (right), at 4 different stream-wise cross-sections ( $x = -0.6D, 0D, 0.6D$  and  $1.2D$ ) for 3 different phase positions: (A)  $\phi = 180^\circ$ ; (B)  $\phi = 210^\circ$  and (C)  $\phi = 330^\circ$ . The symbols are experimental results from [70]. The lines denote the present results.

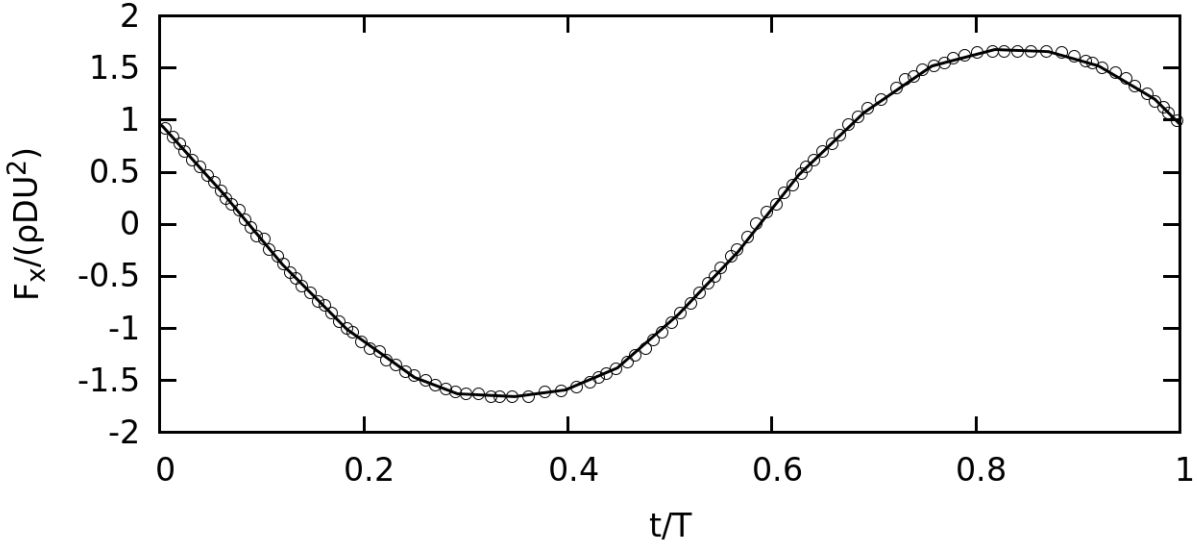


FIGURE 3.9. Time history of the in-line force acting on the cylinder. Symbols: experimental results from [70]; solid line: present simulation results.

any more, resulting in a far more complicated fluid-structure interaction. The configuration of this case follows the setup originally proposed by Wang [72]. The hovering wing is a two-dimensional ellipse with major axis  $c$  (chord length) and aspect ratio (ratio between major axis and minor axis)  $e$ . The wing moves along a stroke plane inclined at an angle of  $\beta$ . The prescribed translational and rotational motion of the hovering wing is governed by

$$A(t) = 0.5A_0(\cos(2\pi ft) + 1), \quad (3.31)$$

$$\theta(t) = \theta_0(1 - \sin(2\pi ft + \phi_0)), \quad (3.32)$$

where  $A(t)$  is the translational motion of the wing with an amplitude  $A_0$ . The flapping frequency is chosen as  $f = \frac{c}{\pi A_0}$ . The rotational motion of the wing starts from an angle of attack of  $\theta_0$  with phase difference  $\phi_0 = 0$ . The chord length  $c$  is retained as the length scale, the maximum translational velocity  $\pi A_0 f$  is taken as the velocity scale. Thus, the Reynolds number is  $\text{Re} = \pi A_0 f c / \nu$ . In the following simulation, the parameters are kept as

in previous studies [71–74]:  $c = 1$ ,  $e = 4$ ,  $A_0 = 2.5c$ ,  $\beta = \pi/3$ ,  $\theta_0 = \pi/4$ , leading to  $\text{Re} = 157$ .

The computational domain is a square with domain length  $l = 24c$ . A uniform grid of  $1024 \times 1024$  is used to discretize the domain, resulting in a grid spacing of  $0.0234c$ . This resolution is slightly finer than the grid spacing used in [73, 74], and comparable to the one employed in [71].

Figure 3.10 shows four snapshots of the vorticity fields near the wing during one flapping period. A vortex dipole is generated from the leading and trailing edge vortices and sheds right-downward, resulting in lift force for the wing. The vorticity fields shown in Fig. 3.10 are visually in good agreement with results of previous studies [71–74].

The drag and lift coefficients on the flapping wing have been calculated as a function of time and are plotted in Fig. 3.11. The results from the body-conforming mesh method in [72], the moving IBM in [71] and the immersed interface method in [73] are also plotted in this figure, allowing a direct comparison with the current ghost-cell IBM. Concerning the drag coefficient (Fig. 3.11(a)), the novel ghost-cell IBM delivers results very similar to the IBM approach described in [71]. Concerning now the lift coefficient (Fig. 3.11(b)), our approach is the closest one to the body-conforming mesh results documented in [72]. At the same time, the time step employed for the novel ghost-cell IBM is noticeably larger than that documented in [73], where small values are necessary to maintain the shape of the rigid body when using the immersed interface method. Overall, the performance of the novel ghost-cell IBM appears to be very satisfactory for such a complex fluid-structure interaction with a moving body.



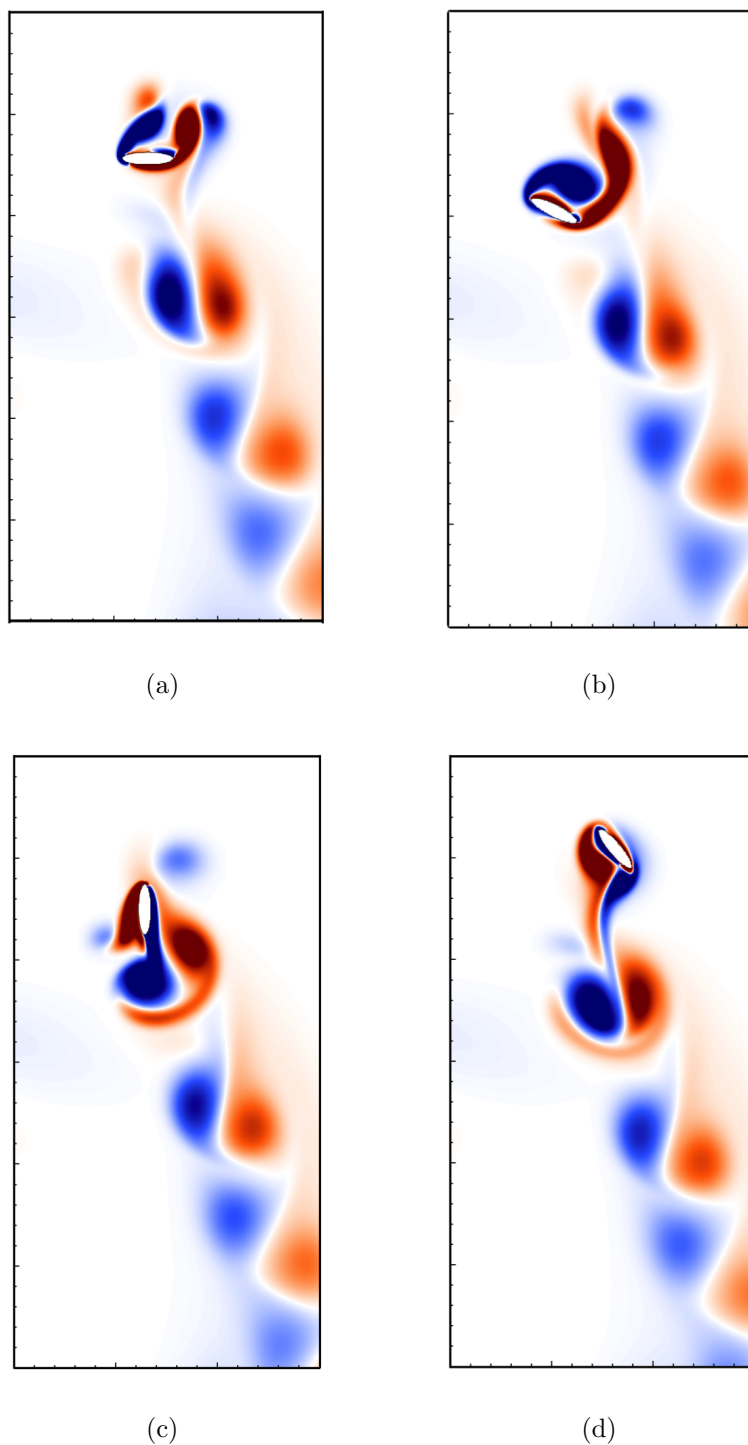
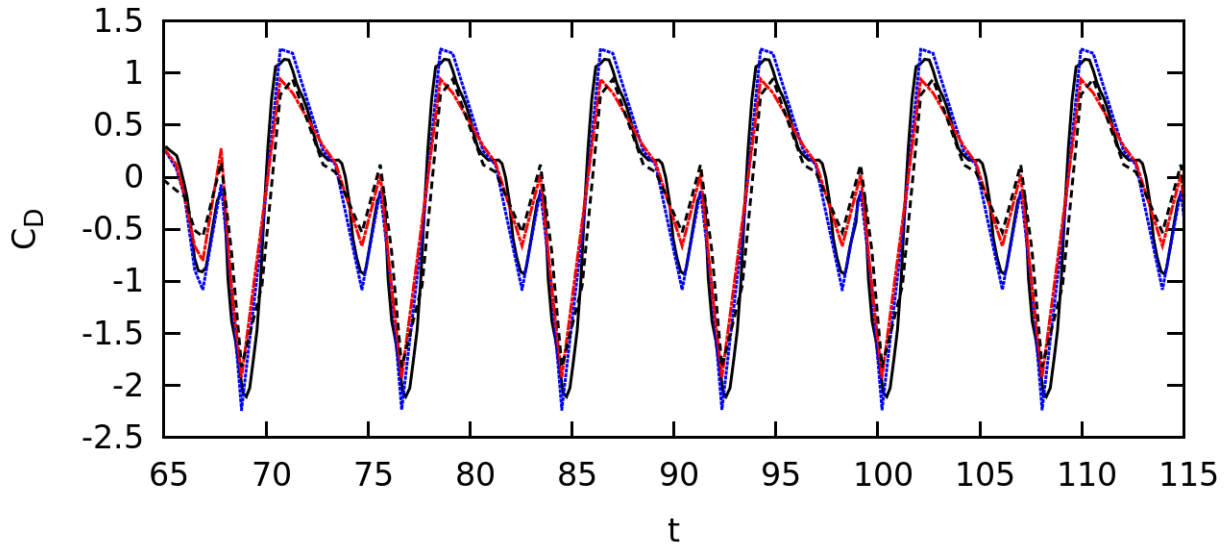
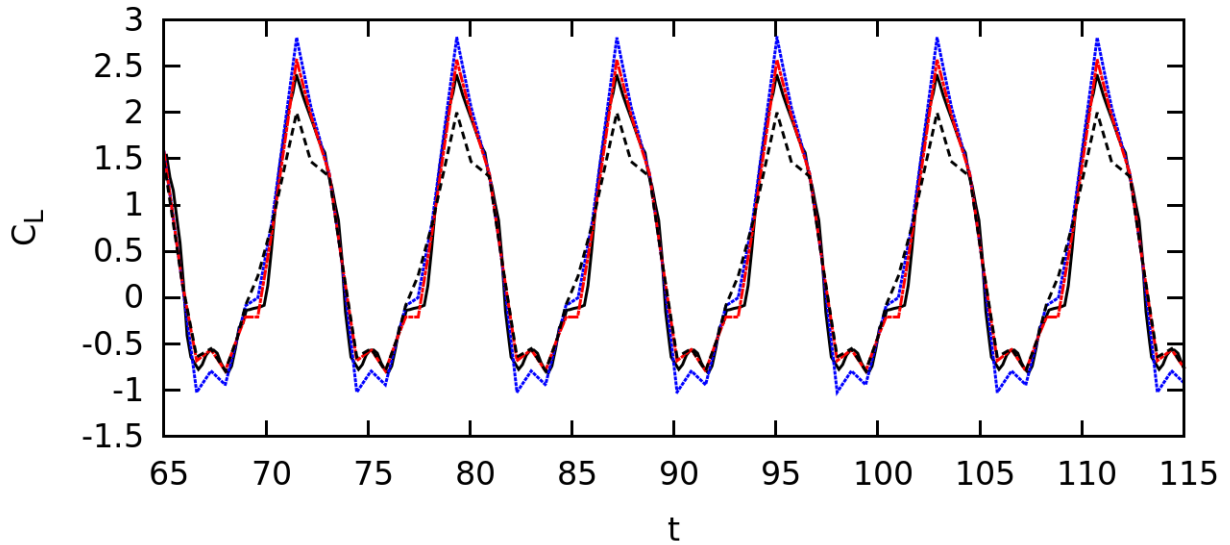


FIGURE 3.10. Snapshots of the vorticity fields near a flapping wing at  $Re = 157$  at 4 different time instants during one flapping period  $T$ : (a)  $t = 0.25T$ ; (b)  $t = 0.44T$ ; (c)  $t = 0.74T$ ; and (d)  $t = 0.99T$ .



(a)



(b)

FIGURE 3.11. Time history of (a) drag coefficient and (b) lift coefficient for the flow around the flapping wing at  $Re = 157$ . — novel ghost-cell immersed boundary method; ---- body-conforming mesh method of [72]; ..... moving immersed boundary method of [71]; -.-.- immersed interface method of [73].

### 3.3.5 Flow past a 3D sphere

All previous cases considered flows around 2D geometries. As a final step, the flow past a 3D sphere is now simulated to check the performance of the ghost-cell IBM in such configurations. This standard test case has been widely investigated in both experimental [75–77] and numerical studies [38, 78, 79], for low to moderate Reynolds numbers. It has been found that the flow is axisymmetric and steady below a Reynolds number of 210, becomes non-axisymmetric at a Reynolds number between 210 and 280, and finally unsteady at Reynolds numbers above 280 [34, 79].

In the present study, the flow past a fixed 3D sphere at a Reynolds number of 10 is first simulated to check that the novel ghost-cell IBM fulfills mass conservation (divergence-free condition). Using the same numerical setup as in [57], the computational domain has a size of  $3.5d \times 4d \times 4d$  and is discretized by a uniform Cartesian grid with  $28 \times 32 \times 32$  points. The time step is controlled by a constant CFL number of 0.01. The  $L_2$  norm error of the continuity equation has been computed for each iteration step and is compared with the results of [57] in Fig. 3.12. It can be seen that the total error of the novel IBM related to the continuity equation is kept below a very small value (lower than  $10^{-6}$ ), proving that mass conservation is satisfactorily enforced. The error converged below  $10^{-6}$  almost at the same time iteration step (iteration 14) as when using the IBM approach from [57] with ghost velocity excluded from the pressure correction equation.

Then, the same flows have been simulated at increasing Reynolds numbers of 100, 150, 300 and 350. The computational domain has a size of  $15d \times 15d \times 15d$  and is discretized by a uniform Cartesian grid with  $256 \times 256 \times 256$  grid points.

Figure 3.13(a) shows instantaneous pseudo-streamlines around the sphere within the  $x-y$  plane for the flow at  $Re_d = 100$ . In this configuration, the flow is axisymmetric and steady, as documented in the literature. The absolute distance from the center of the flow recirculation

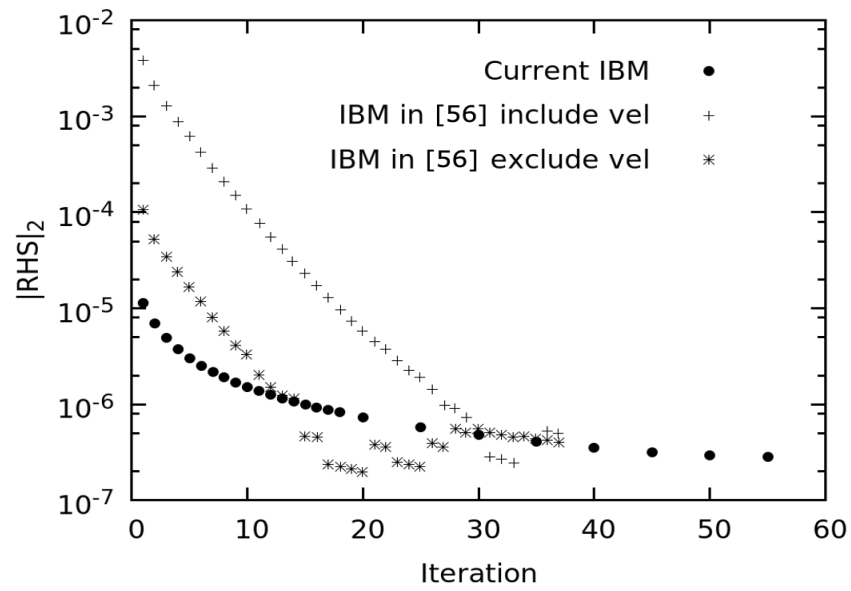
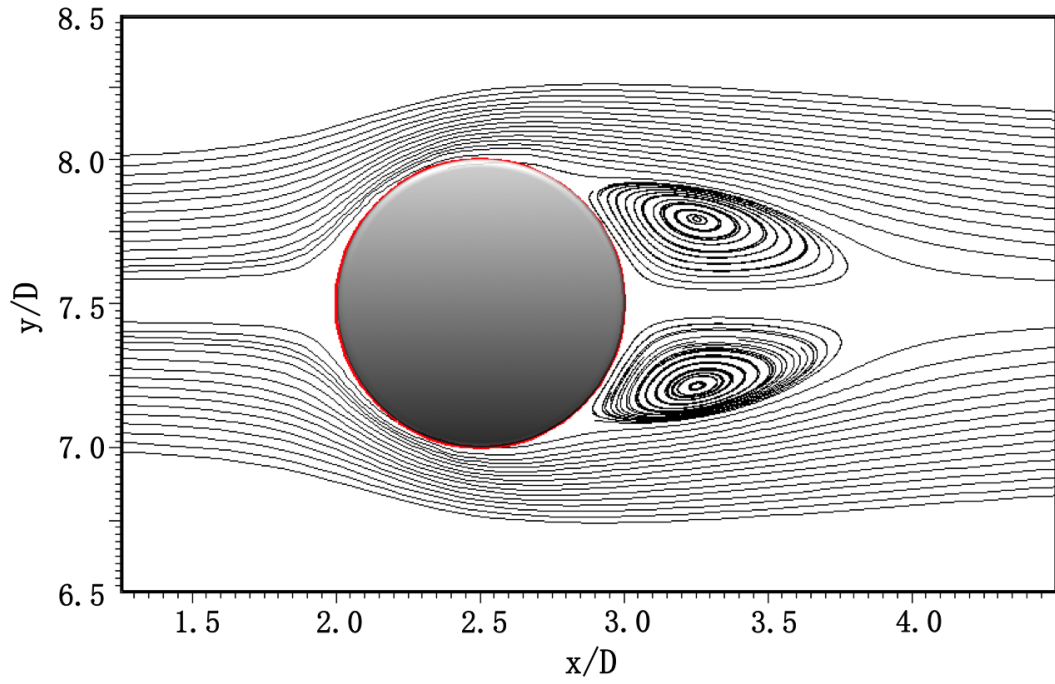
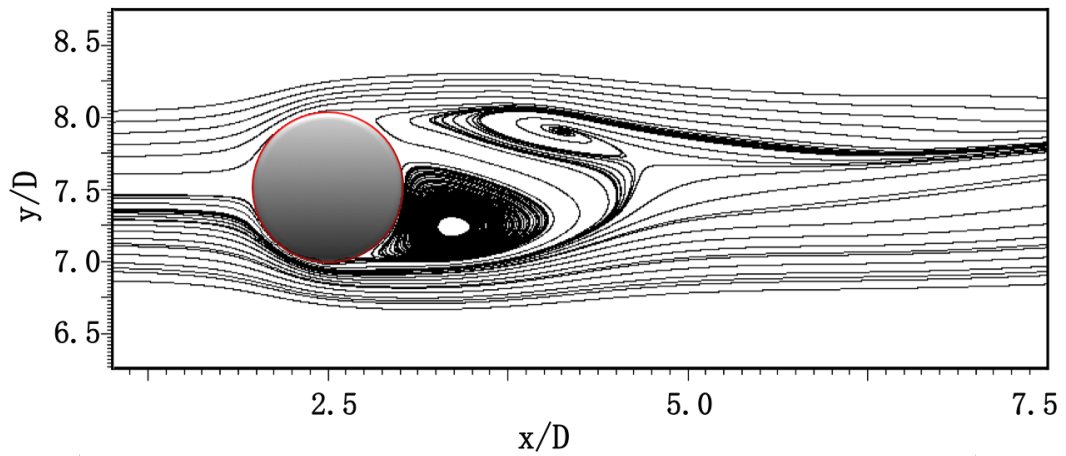


FIGURE 3.12.  $L_2$  norm error for the continuity equation concerning the flow around a fixed 3D sphere at a Reynolds number of 10. The  $\bullet$  symbols represent results of the novel ghost-cell IBM. The  $+$  symbols represent the IBM results in [57] with ghost velocity included in the pressure correction equation, while the  $*$  represents the IBM results in [57] with ghost velocity excluded from the pressure correction equation.



(a)



(b)

FIGURE 3.13. Instantaneous pseudo-streamlines of the velocity field around the sphere within the  $x - y$  plane (A) for flow at  $Re_d = 100$ ; (B) for flow at  $Re_d = 300$ .

pattern to the sphere center is denoted as  $x_c$  and  $y_c$  in  $x$  and  $y$  directions, respectively. The length of the recirculation zone is written  $L_W$ . These flow characteristics have been also calculated for flow at  $Re_d = 150$  and compared with previous studies, as documented in Table 3.4. A very good agreement is obtained.

	$Re_d=100$			$Re_d=150$			$Re_d=300$	$Re_d=350$
	$x_c/d$	$y_c/d$	$L_W/d$	$x_c/d$	$y_c/d$	$L_W/d$	St	St
Present study	0.75	0.285	0.85	0.32	0.29	1.19	0.134	0.14
Taneda [80]	0.745	0.28	0.8	0.32	0.29	1.2	-	-
Mittal [64]	-	-	0.87	-	-	-	-	0.14
Johnson and Patel [79]	0.75	0.29	0.88	0.32	0.29	1.2	0.137	-
Marella et al. [34]	-	-	0.88	-	-	1.19	0.133	-
Mittal et al. [38]	0.742	0.278	0.84	0.31	0.3	1.17	0.135	0.142

TABLE 3.4. Comparison of the computed flow characteristics with other experimental and numerical studies.

At Reynolds numbers of 300 and 350, non-axisymmetric and unsteady flows are obtained. To reach a periodic state, the simulations have been appropriately continued until a periodic signal was found for the near-wake pressure. The frequency of this periodic signal is used to estimate the Strouhal number  $St$ , as shown in Table 3.4.

Figure 3.13(b) shows pseudo-streamlines around the sphere within the  $x - y$  plane for the flow at  $Re_d = 300$  at one time instant. This time-instant has been retained to allow comparison with the same streamlines (second flow phase) in [79]. It can be seen in Fig. 3.13(b) that the upper side of the near-wake vortex is becoming unstable and starts moving downstream, while the lower side of the vortex is becoming stable.

The mean drag coefficient obtained for all these cases has been calculated and is summarized in Fig. 3.14. As the flows for  $Re_d = 300$  and 350 are unsteady, the drag coefficients for these two cases have been averaged after reaching periodic steady-state.

From the comparisons in Table 3.4 and Fig. 3.14, it is clear that the results obtained with the new method are in excellent agreement with previously published experimental and

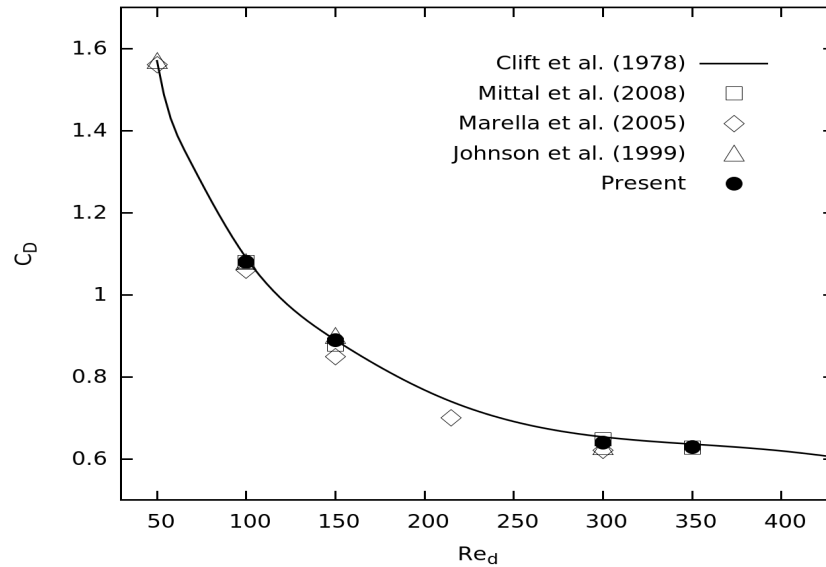


FIGURE 3.14. Comparison of the (averaged) drag coefficients with results from the literature.

numerical studies, showing that the novel ghost-cell IBM method can be used for 3D cases as well.

### 3.3.6 Flow in an intracranial aneurysm

The last benchmark involves a medical flow simulation using a patient-specific intracranial aneurysm, since this topic has been very intensively considered in our group in the last decade [81]. This case is used to check the fidelity of the novel ghost-cell IBM for highly irregular 3D geometries, as well as to measure its parallel efficiency. The employed 3D aneurysm geometry has been derived from a female patient as described in [82]. Previous numerical and experimental studies considering this same geometry are discussed in particular in [83]. Following the guidelines discussed in [83], blood is described as an incompressible fluid with density  $\rho = 1055 \text{ kg/m}^3$  and constant dynamic viscosity  $\mu = 0.004 \text{ Pa}\cdot\text{s}$ . The period of each cardiac cycle for the patient is taken constant at 0.925 s. The patient-specific inflow velocity

prescribed during each cardiac cycle is plotted in Fig. 3.15. Outflow boundaries are constant-pressure outlets. The grid resolution in this simulation is set to  $40 \mu\text{m}$ . The simulation was carried out on SuperMUC (supercomputer cluster at Leibniz Supercomputing Center in Munich) using 1024, 2048, 4096, and 8192 CPU processors with 2.6 GHz, respectively. The CPU time needed for the IBM process has been measured separately by activating appropriate counters. Figure 3.16 shows the strong scaling plot of the overall CPU time per time step. It can be seen that a good parallel efficiency (almost 80%) is obtained for this low-Mach solver. The efficiency of the proposed IBM procedure is shown separately in Fig. 3.16. Again, the parallel efficiency of the IBM method is very high, comparable to that of the overall code (70 to 80%). It can also be seen that the numerical cost associated to IBM is roughly only 7 – 9% of the total computational time.

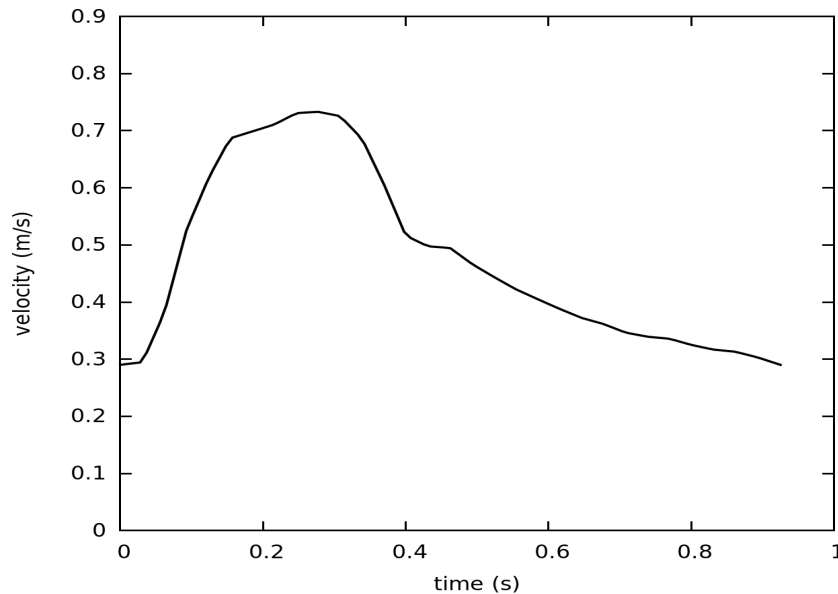


FIGURE 3.15. Patient-specific inflow velocity used during each cardiac cycle (duration of 0.925 s).

As found in [83], the simulation needs to be continued for at least 3 cardiac cycles in order to eliminate initial transients. Figure 3.17 shows the aneurysm geometry, represented as iso-



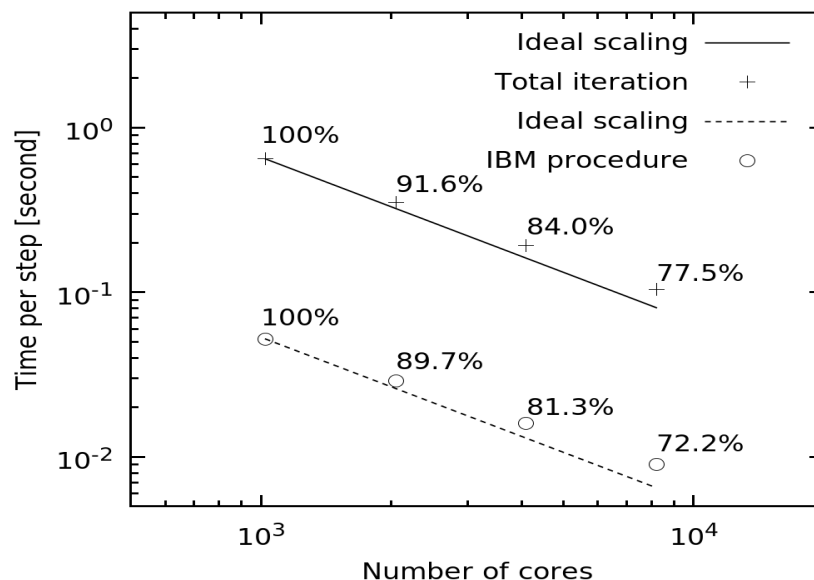


FIGURE 3.16. Measured parallel efficiency of the overall numerical solution and of the IBM procedure on SuperMUC.

surface of the level-set function,  $\phi = 0$ . Two cut-planes have been selected for comparing the results with those presented in [83]. The peak-systole velocity magnitude obtained with the novel ghost-cell IBM on these two cut-planes is shown in Fig. 3.18. Selected simulation results documented in [83] for the velocity magnitude are also shown in Fig. 3.18, allowing a direct comparison.

Compared with Cases C, E, I, K and X in [83], carried out using adapted unstructured meshes, the results obtained on a regular Cartesian grid with the novel ghost-cell IBM show an excellent agreement for plane P2. Slight discrepancies are observed on plane P1, but deviations are below 10% when comparing the present results with the solution averaged from all Cases in [83]. This last test case confirms robustness and accuracy of the proposed method.

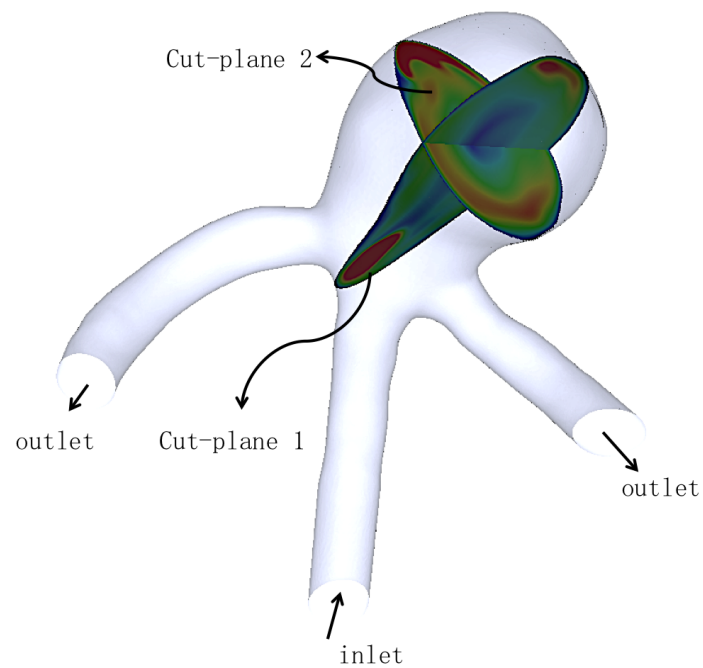


FIGURE 3.17. Geometry of the patient-specific cerebral aneurysm with inlet/outlets, and locations of two orthogonal cut-planes used to analyze the results. The color plots on the planes show the peak-systolic velocity magnitude.

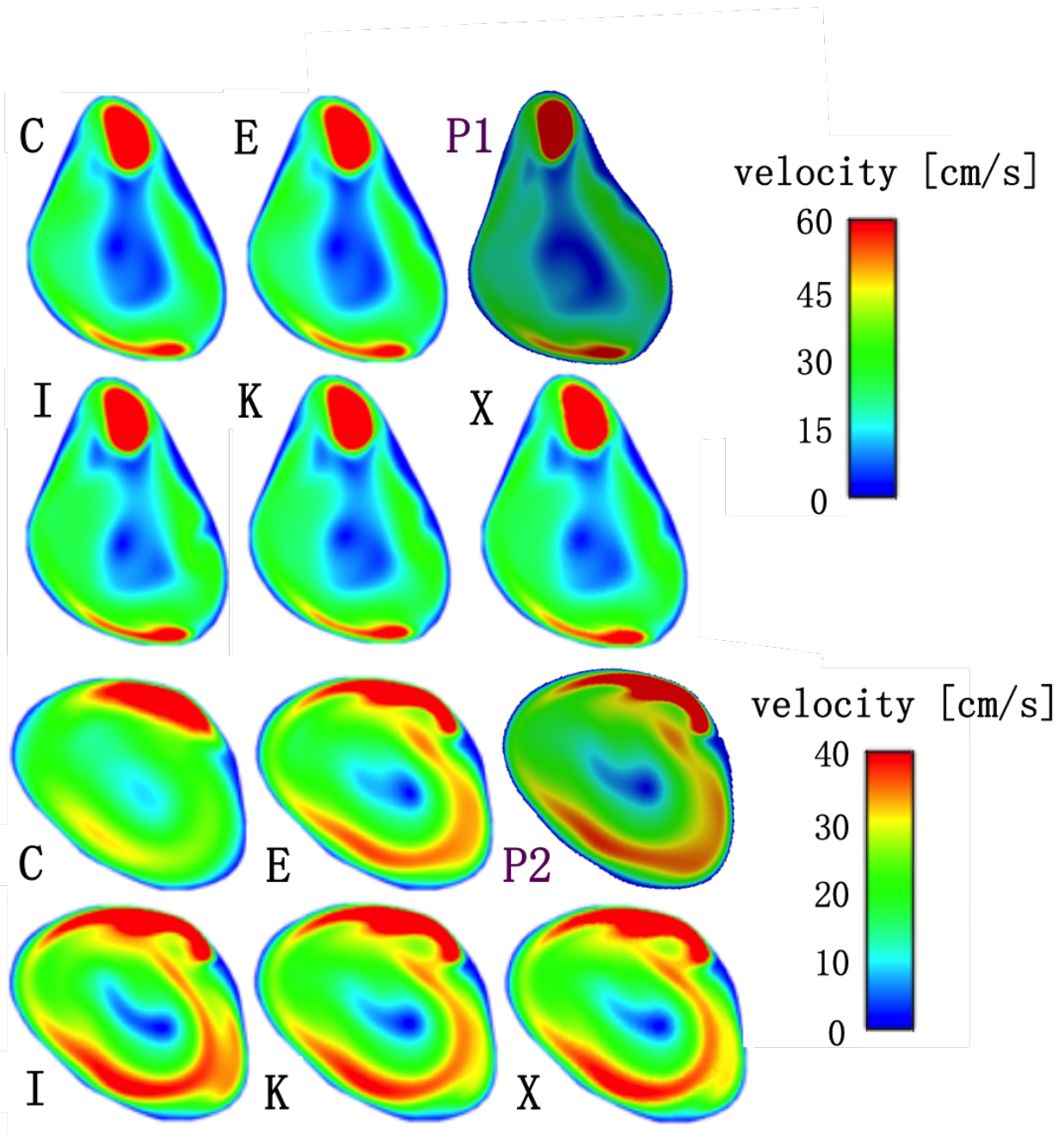


FIGURE 3.18. Comparison of the peak-systolic velocity magnitude along the two cut-planes (P1: top; P2: bottom) using the novel ghost-cell IBM and various adapted unstructured meshes (Cases C, E, I, K, and X in [83]).

### 3.4 Extension to low Mach reacting flows

The extension of the IBM for low Mach reacting flows is straightforward. Previously, we have defined the no-slip wall boundary condition with all momentums on the wall to be zero. For low Mach reacting flows, another two boundary conditions should be enforced on the wall: for temperature (Eq. 2.3) and species (Eq. 2.4).

For temperature, isothermal wall condition (Dirichlet type) and adiabatic wall condition (Neumann type) are needed. The fictitious thermal force  $F_T(\mathbf{x})$  is computed in the same way as the fictitious dynamic force  $\mathbf{F}(\mathbf{x})$ , from Eq. 3.25,

$$F_T(\mathbf{x}) = \begin{cases} R_{b,T,\mathbf{x}}(T_{gx}, T_{gy}, T_{gz}) - R_{c,T,\mathbf{x}}(T), & \text{if } \mathbf{x} \in \text{IBM influence range} \\ 0, & \text{otherwise.} \end{cases} \quad (3.33)$$

$R_{c,T,\mathbf{x}}(T)$  is the original right-hand-side of the temperature equation and  $R_{b,T,\mathbf{x}}(T_{gx}, T_{gy}, T_{gz})$  is adapted on the immersed boundary.  $T_{gx}, T_{gy}$  and  $T_{gz}$  are the fictitious temperature at the ghost point in  $x$ ,  $y$  and  $z$  direction respectively. The fictitious temperatures at the ghost points are essential for the computation of  $R_{b,T,\mathbf{x}}$ . For isothermal wall condition, such temperature can be easily inter/extrapolated from the boundary point value (constant temperature), such as Eq. 3.19. For an adiabatic wall condition, the exact temperature on the boundary is unknown. The temperature at the ghost point is computed using the boundary-normal mirror point values, computed by bilinear interpolation as mentioned in [6].

For species, a condition of zero-gradient (zero mass flux) is imposed through the wall.

The fictitious kinetic force  $F_{Y_k}(\mathbf{x})$  is computed as

$$F_{Y_k}(\mathbf{x}) = \begin{cases} R_{b,k,\mathbf{x}}(Y_k) - R_{c,k,\mathbf{x}}(Y_k), & \text{if } \mathbf{x} \in \text{IBM influence range} \\ 0, & \text{otherwise.} \end{cases} \quad (3.34)$$

$R_{c,k,\mathbf{x}}(Y_k)$  is the original right-hand-side of the species equation for species  $k$ , and  $R_{b,k,\mathbf{x}}(Y_k)$  is considering the zero-gradient species condition on the immersed boundary.  $R_{b,k,\mathbf{x}}(Y_k)$  is computed by involving the fictitious species mass fraction at the ghost points, which is computed by bilinear interpolation as in [6].

Apart from the above boundary conditions, the wall-normal component of diffusion velocity ( $\mathbf{V}_k$ ) has also to be zero on the wall. The fictitious diffusion velocities at the ghost points are inter/extrapolated from the near-wall fluid points and are involved in the computation of  $R_{b,T,\mathbf{x}}(T_{gx}, T_{gy}, T_{gz})$  and  $R_{b,k,\mathbf{x}}(Y_k)$ .

In this way, the immersed boundary method has been adapted for the low-Mach reacting flows involving temperature and species boundary conditions. The applications of the immersed boundary method for combustion problems in complex geometries are discussed later in Chapter 6.

### 3.5 Novelty of the present IBM

The novelties of the present IBM can be summarized as:

- Accuracy: the implicit boundary forces are enforced in the directions of numerical discretization, free of the ghost cell itself. The numerical boundary points are represented more precisely, ensuring lower magnitude of truncation error.
- Convergence: the conventional, poor assumption that the distance from the ghost point

to the boundary is in the order of the grid size is not used in the present IBM, ensuring the convergence rate of the truncation error.

- **Efficiency:** the interpolation procedure requires no additional iterations, saving CPU time. Communication of the projection point information between different CPU/GPU processors is not needed, improving the parallelization efficiency.
- **Stability:** the stability issue when the fluid point is too close to the boundary (stiff gradient) is solved.

## 3.6 Conclusions

An efficient, robust and accurate ghost-cell immersed boundary method has been developed for incompressible and low-Mach flow simulations involving complex geometries. It has been implemented in a high-order finite-difference DNS solver. In contrast to conventional ghost-cell methods in which ghost values are extrapolated normally through the boundary, the present method always follows the discretization directions, but involving multiple ghost values at the same ghost points in multi-dimensional simulations (3 values at each ghost point in 3D). This leads to an easier and more accurate representation of the boundary on the employed Cartesian grid. The effect of the assumption  $\Delta l = O(\Delta x)$  on the persistent convergence of the truncation error has been discussed and the error term involving  $\Delta l$  has been carefully treated. Finally, a second-order convergence is obtained for the truncation errors. Stability issues observed when one fluid point is close to the boundary have been solved by reducing progressively the local order of accuracy. To improve mass conservation near the boundary, the commonly used Neumann boundary condition for pressure is not used, avoiding an artificial pressure force over the boundary. The conservation constraint is implicitly enforced by the continuity equation, without involving the ghost velocities.

Parallelization of the developed ghost-cell IBM is straightforward, reducing communication issues compared to conventional methods.

Various test cases ranging from the flow around a cylinder in two dimensions to the pulsating flow inside a patient-specific, three-dimensional cerebral aneurysm have been considered and discussed. Both steady boundaries and moving boundaries have been employed. The simulation results have been extensively compared to previous experimental and numerical studies, showing a very good agreement. These tests have shown that the novel ghost-cell IBM is second-order accurate near the boundary, robust even for moving geometries and complex boundaries, and ensures mass conservation. Reacting flows can also be considered with this approach.

# Chapter 4

## Gaseous Combustion Simulations: Assessing Heat Release

Heat release is the central property of all combustion systems. However, it is perhaps the most difficult quantity to measure experimentally, preventing meaningful model development and validation. This is why "numerical experiments" are used here to support the identification of suitable, indirect markers of heat release.

To identify the high heat release region (indicating the flame front), optimal chemical markers are found by analyzing in a systematic manner DNS results. In the following studies, section 4.1 investigates the optimal chemical markers for premixed syngas flames, and the pixel image-based optimization technique is introduced. Section 4.2 investigates the optimal markers for premixed hydrogen flames under different pressure conditions. Section 4.3 investigates general optimal markers for premixed methane flames in either high heat release region or low heat release region. The connection between the proposed chemical markers and the fluorescence signal modeling is discussed. Since it is unclear how the markers depend on fuel composition or combustion regimes, these different studies are necessary to derive a more general picture.



## 4.1 Optimal Heat Release Rate Marker in Premixed Syngas Flames

Parts of the results presented in this section have been published in the Journal Flow, Turbulence & Combustion [84].

### 4.1.1 Introduction

In combustion, one of the critical issues consists of identifying the location of the flame front. Different concepts are used today to define this quantity, depending on the particular problem under consideration [85]. If the location of maximum heat release (ridge line in 2D, ridge surface in 3D) could be identified, it would clearly be a good candidate for defining the flame position in a general manner.

The determination of heat release profiles in laminar as well as turbulent flames is essential both from fundamental and practical points of view, heat release being one of the most important reasons why flames are so interesting for mankind. While this quantity can be easily calculated in numerical simulations, it was up to now impossible to derive an experimental methodology delivering a direct picture of heat release fields, in spite of a considerable amount of research concerning this issue. For this reason, many groups have tried over the last decades to elaborate an indirect measurement technique based on species concentrations.

A first experimental method to characterize the flame front is the detection of excited molecules such as  $\text{OH}^*$  and  $\text{CH}^*$  by chemiluminescence measurements [86, 87]. Panoutsos et al. [88] stated that the use of  $\text{OH}^*$  chemiluminescence exhibits nearly the same performance as the product of  $\text{OH}$  and  $\text{CH}_2\text{O}$  concentration measurements (see later for more details). However, one major problem of chemiluminescence is that it delivers a signal in-

tegrated along the line of view. The same applies to interferometric techniques [89]. It is hence possible to characterize heat release in simple laminar flames using this technique, as extensively discussed, e.g., in [90]. However, for turbulent conditions, it is impossible to obtain the instantaneous heat release profile for flames in this manner. Anikin et al. [91] applied computed tomography for 2D chemiluminescence measurements of  $\text{OH}^*$ . This complex technique works also for turbulent conditions. The application of computed tomography to 3D chemiluminescence measurements is discussed by Floyd et al. [92].

The use of OH-PLIF (Planar Laser-Induced Fluorescence) measurements to localize flame profiles is very common, even in industrially relevant configurations (e.g., [93–96]). However, because of the intrinsic complexity of turbulent flames, the measurement of a single species can often lead to ambiguities. Therefore, there is a growing trend towards combining several simultaneous planar imaging techniques in order to provide data that can be interpreted much more accurately and completely [97, 98].

Najm, Paul and co-workers [99, 100] have examined in two seminal papers many possible diagnostic methods to mark chemical heat release in methane-air and dimethyl ether-air flames. They finally found a good temporal and spatial correlation between the concentration of the formyl radical HCO and the heat release rate for premixed flames. Unfortunately, the fluorescence signals of HCO are quite weak, so that planar imaging measurements of its fluorescence sometimes can not provide adequate signal-to-noise levels. Single-shot LIF measurements of HCO distributions in turbulent flows remain very difficult.

In order to avoid this difficulty, Paul and Najm [100] proposed a pixel-by-pixel product of the OH and  $\text{CH}_2\text{O}$  PLIF images in order to yield an image closely related to the heat release rate in laminar premixed methane-air and dimethyl ether-air flames at  $\phi = 0.9$ . In contrast to the HCO signal, the OH and  $\text{CH}_2\text{O}$  images mostly show a satisfactory signal-to-noise ratio in turbulent flames and can be obtained rather easily. This interesting method has,

since then, been used by many different authors for numerous applications [101–108].

A study by Nikolaou and Swaminathan [109] reexamined the validity of the reaction rate of  $\text{OH} + \text{CH}_2\text{O} = \text{HCO} + \text{H}_2\text{O}$  as a reliable heat release rate marker for lean methane-air and preheated stoichiometric multicomponent mixtures ( $\text{CO}$ ,  $\text{H}_2$ ,  $\text{H}_2\text{O}$ ,  $\text{CO}_2$  and  $\text{CH}_4$ ) based on PREMIX computations complemented by DNS data at Reynolds numbers up to 230, revealing in particular that the obtained correlations may depend on stoichiometry. Mulla and co-workers [110] recently studied the product of H-atom LIF and  $\text{CH}_2\text{O}$  LIF signals and compared it with  $\text{OH} \times \text{CH}_2\text{O}$ ; the  $\text{H} \times \text{CH}_2\text{O}$  marker is shown to have weak sensitivity to variation in the stoichiometry and wider applications.

In spite of this considerable research activity, it may still be possible to find an even better combination of measurable quantities in order to estimate instantaneous heat release profiles in turbulent premixed flames. For this purpose, a systematic analysis has been implemented, so that all possible species combinations can be tested. Furthermore, exponents are introduced as additional parameters to improve the accuracy of the correlation. The optimal approximation of the heat release profile is directly quantified numerically by post-processing raw data obtained through Direct Numerical Simulations (DNS) of turbulent flames employing detailed physicochemical models. Since independent realizations are available, the generality of the findings can be checked. In order to illustrate the procedure, and due to the growing interest of syngas in practical processes (e.g., [111, 112]), synthetic gas has been used as fuel in the DNS. Syngas indeed appears to be an appropriate choice, involving part of (but not all) the kinetic complexity of higher hydrocarbons.

One major difference between this work and the previous ones is that the local thickness of the heat release profiles is taken directly into account in the analysis process. In this manner, the optimal species combinations identified by the procedure should be able to represent not only the regions of high heat release rate (HRR), but also can be used to

compute the corresponding thickness and curvature, as demonstrated in what follows.

### 4.1.2 Numerical setups

All turbulent premixed spherical syngas flames are computed in this work by Direct Numerical Simulation, solving the Navier-Stokes equations for multi-component reacting flows. Derivatives are computed using centered explicit schemes of order six. Temporal integration is realized with a semi-implicit Runge-Kutta algorithm of order three. Chemical kinetics and transport coefficients are computed using Cantera 1.8 [15]. All DNS computations are performed by our in-house low-Mach turbulent reacting code, DINO [7], presented in the previous chapters.

A homogeneous isotropic turbulent velocity field is initiated at  $t = 0$  on top of the initially laminar premixed flame configuration. The initial turbulent field is generated using a parallel turbulence generator based on an Inverse Fast Fourier Transform (IFFT) relying on an analytically prescribed turbulence spectrum following von Kármán with Pao correction (VKP spectrum). Considering that the computational requirements for DNS of turbulent reactive flows are huge, most DNS simulations in this study are conducted in 2D; it will be demonstrated that 3D and 2D results of DNS do not differ noticeably concerning the reconstruction of HRR distributions. Table 4.1 shows the employed DNS database.

Two different reaction mechanisms have been used in the DNS computations, in order to check their possible influence. First, the syngas combustion mechanism published by Davis et al. [113] is employed (Cases A, B, C, D, E and F). It involves 14 species (CO, HCO, CO<sub>2</sub>, H<sub>2</sub>O, O<sub>2</sub>, O, H, OH, HO<sub>2</sub>, H<sub>2</sub>O<sub>2</sub>, H<sub>2</sub>, N<sub>2</sub>, Ar, and He) and 38 reactions. Choosing the mechanism of Davis et al. [113] is justified by the recent benchmark of many syngas combustion mechanisms against experimental data documented in Olm et al. [114]. The authors found that, from all sixteen different mechanisms investigated, Davis et al. best

TABLE 4.1. Considered DNS cases (composition in molar percentages) for syngas flames. An appropriate nitrogen complement (corresponding to oxygen/nitrogen ratio of air) is added before starting simulation.

	Mechanism	$\Phi$	H <sub>2</sub> /CO	CO	H <sub>2</sub>	O <sub>2</sub>	$u_{rms}/s_l$	$l_{int}/\delta$	Re <sub>l</sub>	Re <sub>t</sub>	Ka
A	Davis	1.12	0.76	16.8	12.8	14.8	13.3	1.82	469	355	1632
B	Davis	1.0	1.0	14.8	14.8	14.8	10.4	2.20	611	417	1592
C	Davis	0.8	1.2	12.2	14.6	15.4	10.0	1.72	413	287	1519
D	Davis	0.8	0.76	15.2	11.5	15.4	13.0	1.95	524	395	1457
E	Davis	0.8	1.2	12.2	14.6	15.4	23.1	1.82	1009	944	6591
F	Davis	1.12	0.76	16.8	12.8	14.8	9.4	2.43	622	483	2654
G	USC II	1.0	1.0	14.8	14.8	14.8	9.5	2.04	499	339	1553
H	USC II	1.12	0.76	16.8	12.8	14.8	13.4	2.08	552	375	1801
I	USC II	0.8	1.2	12.2	14.6	15.4	10.8	1.94	513	364	1359
J	USC II	0.8	0.76	15.2	11.5	15.4	12.1	1.97	506	412	1301

reproduces the experimental flame velocity data and the measured species concentration profiles. To check the robustness of the derived indicators of heat release, another syngas reaction scheme derived from USC Mech Version II [115] with 14 species (CO, HCO, CH<sub>2</sub>O, CO<sub>2</sub>, H<sub>2</sub>O, O<sub>2</sub>, O, H, OH, HO<sub>2</sub>, H<sub>2</sub>O<sub>2</sub>, H<sub>2</sub>, N<sub>2</sub>, and Ar) and 48 individual reactions, has been used for further comparisons (Cases G, H, I and J).

For Case A, the conditions already used in [116] have been kept, with  $T_u = 300$  K and atmospheric pressure,  $p_u = 1$  bar. Cases B, C and D correspond to different equivalence ratios  $\Phi$  and H<sub>2</sub>/CO ratios, using the same reaction mechanism. Case E is proposed to investigate the influence of turbulence intensity, the turbulent Reynolds number based on the integral scale (Re<sub>l</sub> = 1009) being noticeably larger than in all the other cases (Re<sub>l</sub>  $\approx$  500). Further cases are discussed later in this paper.

All relevant turbulence parameters can be found in Table 4.1. Here, the laminar flame speed is denoted  $s_l$ , as usual. The Reynolds number is  $Re_l = u_{rms} l_{int}/\nu_r$ , where  $u_{rms}$  represents the fluctuating velocity,  $l_{int}$  the integral length scale and  $\nu_r$  the kinematic viscosity on the reactant side. The Zeldovich thickness is defined as  $\delta = \nu_r/s_l$ . Ka represents the Karlovitz number, which is  $Ka = (\delta/\eta)^2$ .  $\eta$  is the Kolmogorov length scale. To obtain proper

equilibrium between turbulence and chemistry [117], all computations have been continued up to  $t = 1.5\tau_t$ , where  $\tau_t = l_{int}/u_{rms}$  is the characteristic time-scale of the time-decaying turbulence. The analysis of the results is carried out at that final time, and  $Re_t$  is the real Reynolds number at time  $t = 1.5\tau_t$ . Due to turbulence decay,  $Re_t$  is as expected lower than  $Re_l$ .

The DNS domain under investigation is a box with the length of 1.5 cm on each side, with periodic boundary conditions. A fixed mesh is employed in each direction with a spatial resolution of 18.75  $\mu\text{m}$ , necessary to resolve correctly species like  $\text{CH}_2\text{O}$  or  $\text{H}_2\text{O}_2$ . To ignite the flame, the equilibrium conditions corresponding to the fresh gas compositions of Table 4.1 are computed using Cantera, and are initially implemented within a small kernel with radius  $r = 1.2$  mm at the center of the numerical domain.

### 4.1.3 Identifying markers of heat release

For syngas, the fuel is a mixture of CO and  $\text{H}_2$ . The H/O radicals are produced by the elementary reactions of the hydrogen–oxygen system, creating a pool of radicals H, O, OH and  $\text{HO}_2$ . The main elementary reaction for oxidation of CO is the  $\text{CO} + \text{OH} = \text{CO}_2 + \text{H}$  reaction. Radical HCO is formed in the  $\text{H} + \text{CO}$  reaction, and reactions of HCO with radicals H, O and OH contribute to the removal of HCO. The heat production at any location in the flame can be calculated using:

$$H_r^\ominus = \sum_j \Delta_r H_j^\ominus r_j = \sum_j \Delta_r H_j^\ominus k_j c_{j1} c_{j2} \quad (4.1)$$

where  $\Delta_r H_j^\ominus$ ,  $r_j$  and  $k_j$  are reaction enthalpy, rate and rate coefficient of reaction step  $j$ , respectively. To find species pair showing the highest correlation with the local heat production, one possibility is to calculate all terms of the summation in Eq. (4.1). If one term

is much larger than the others, then the corresponding species pair can be used for characterizing heat release. This approach is not straightforward, since such an analysis should be done at many locations and time points, in order to properly take into account variations in temperature and concentrations. Additionally, it will only deliver unit exponents, while the correlation might be better using non-unit exponents, as shown afterwards. Hence, looking for correlations between local concentrations and local heat release using DNS data appears to be a more efficient approach.

The aim of the present study is now to find by a suitable process:

- The best pair of reacting species ( $A_1$ ,  $A_2$ ) from all those appearing in the chemical scheme (11 for [113], 12 for [115]);
- The most suitable exponents  $s_1$  and  $s_2$  for those species;
- To minimize the difference between the real heat release profile and the reconstructed one, i.e., finding:

$$\min \left\| \bar{H}_r - \frac{\bar{c}_{A_1}^{s_1} \times \bar{c}_{A_2}^{s_2}}{\max(\bar{c}_{A_1}^{s_1} \times \bar{c}_{A_2}^{s_2})} \right\| \quad (4.2)$$

where  $\bar{c}$  denotes the normalized molar concentration, e.g.,  $\bar{c}_{A_1} = c_{A_1}/c_{A_1,\max}$  and  $\bar{H}_r$  represents the normalized heat release,  $\bar{H}_r = H_r/H_{r,\max}$ .

It must first be decided how much information concerning the heat release rate should enter the analysis. Preliminary studies have demonstrated that choosing only a single iso-surface of  $\bar{H}_r$  is not appropriate for this purpose, since it would either eliminate a large part of the active reaction zone (when choosing a value of  $\bar{H}_r$  close to 1), or it would not really coincide with the most active region (when choosing a value far below 1). Skeletonization [118], which is commonly used for example in medical imaging to extract shape features, e.g., of bones, has been tested as an alternative, but was found to predict very poorly the thickness (and sometimes even the position) of the heat release ridge line when the gradients

of  $\overline{H}_r$  are different on both sides of the local maximum. This is indeed very common in turbulent premixed flames, since the evolution toward the fresh gases is not at all symmetric to the evolution toward the burnt gases.

Finally, in order to obtain a sufficiently accurate but practicable solution to analyze DNS results, a simple thresholding approach has been used and found to work very well during all our tests. The thresholding approach is summarized as follows:

1) Normalize the heat release distribution to obtain  $\overline{H}_r$ , and normalize the possible HRR marker  $\overline{c}_{A_1}^{s_1} \times \overline{c}_{A_2}^{s_2}$  to obtain  $\overline{\overline{c}_{A_1}^{s_1} \times \overline{c}_{A_2}^{s_2}}$ .

2) A direct thresholding to half of the peak value is applied to both normalized distributions, keeping only the locations where  $\overline{H}_r \geq 0.5$  for heat release distribution and the locations where  $\overline{\overline{c}_{A_1}^{s_1} \times \overline{c}_{A_2}^{s_2}} \geq 0.5$  for HRR marker distribution. To check the sensitivity of the chosen threshold ( $\overline{H}_r = 0.5$ ), two other limit values (0.3 and 0.7) have also been tested as alternatives. They delivered exactly the same prediction concerning optimal species pairs to predict HRR. As a consequence, thresholding with  $\overline{H}_r \geq 0.5$  has been retained for what follows.

3) The final result is hence (at least part of) the embedded ridge line of heat release together with a local thickness information, corresponding to the condition  $0.5 \leq \overline{H}_r \leq 1$ . In this manner, it is possible to combine local and global information on high heat release in a suitable way. The final outcome for a two-dimensional DNS result is a binarized image (denoted as Image 1) for which all pixels with  $\overline{H}_r \geq 0.5$  are black and all other ones white. The similar binarized image (denoted as Image 2) is also obtained for which all pixels with  $\overline{\overline{c}_{A_1}^{s_1} \times \overline{c}_{A_2}^{s_2}} \geq 0.5$  are black and all other ones white. The process is illustrated later in Fig. 4.3. The extension of this local method to three-dimensional images is straightforward, delivering voxels instead of pixels.

4) Finally, the similarity of both results is quantified by counting the number of pixels



showing a different value in both images. The obtained integer value is a measure of the discrepancy between the particular species combination and the real HRR. The objective of the analysis is now to minimize this value. Note that this approach does not consider integral values at all. It is a purely local algorithm, based on pixel-counting (or voxel-counting in 3D).

To quantify the reconstruction quality, the number of black pixels in the thresholded binarized image of normalized heat release (Image 1) is counted as  $n_{pix1}$ . Then, the number of pixels with a different value in the original image of heat release (Image 1) and in the reconstruction (Image 2) are counted in the same manner, delivering  $n_{pix2}$ . An objective function is finally introduced as  $q = n_{pix2}/n_{pix1}$ , which is a non-dimensional quantity used as a measure of reconstruction quality. Clearly, the lowest possible value is  $q_{min} = 0$  and would correspond to a perfect reconstruction. On the other hand, this ratio can rapidly become larger than 100%, in particular when the thickness of the profiles differ. Indeed, a value of  $q$  below 50% already corresponds visually to a good reconstruction.

The objective is now to find both the species pair  $A_1$  and  $A_2$  and the associated exponents  $s_1$  and  $s_2$  leading to the lowest objective function value. All possible combination pairs (55 for [113], 66 for [115]) have been evaluated in the same process as stated above, together with the exponents  $s_1$  and  $s_2$ , allowed to vary freely between 0.00 and 3.00 considering two digits: 0.00 is clearly the minimum value, since negative values would lead to division-by-zero issues; 3.00 is assumed to be a sufficiently high value, as shown later by the results, since no best solution was found directly on the boundary.

### 4.1.4 Results and discussion

#### Impact of composition

In this section, the kinetic scheme of Davis et al. [113] is used. Case A corresponds to a slightly rich flame. The obtained objective function for Case A is presented in Table 4.2 for the optimal exponents (upper-right part of the table) compared to the case with unity exponents ( $s_1 = s_2 = 1$ , in the lower-left part of the table).

TABLE 4.2. Objective function  $q$  (to be minimized) for all possible species combinations in Case A; lower-left when using unity exponents, upper-right when using optimal exponents. The symbol - indicates no acceptable solution.

	CO <sub>2</sub>	H <sub>2</sub> O	O <sub>2</sub>	O	H	HO <sub>2</sub>	H <sub>2</sub> O <sub>2</sub>	H <sub>2</sub>	CO	HCO	OH
CO <sub>2</sub>	-	245%	111%	118%	222%	106%	93%	108%	111%	51%	156%
H <sub>2</sub> O	480%	-	119%	118%	167%	108%	83%	123%	132%	51%	156%
O <sub>2</sub>	133%	182%	-	31%	28%	102%	100%	-	-	48%	63%
O	447%	448%	144%	-	111%	22%	30%	46%	32%	50%	116%
H	457%	420%	112%	344%	-	26%	29%	44%	26%	49%	156%
HO <sub>2</sub>	145%	147%	132%	127%	38%	-	100%	102%	102%	48%	63%
H <sub>2</sub> O <sub>2</sub>	119%	112%	145%	56%	70%	126%	-	100%	100%	47%	58%
H <sub>2</sub>	158%	163%	-	170%	69%	130%	150%	-	-	50%	51%
CO	187%	228%	-	193%	183%	132%	146%	-	-	48%	65%
HCO	274%	184%	58%	255%	202%	78%	73%	67%	56%	-	30%
OH	386%	479%	68%	307%	463%	89%	80%	76%	66%	245%	-

Comparing the lower left and upper right parts of the table, the advantage of introducing the optimal exponents  $s_1$  and  $s_2$  becomes obvious. The reduction of the objective function obtained due to non-unity exponents is always considerable. For instance, the HCO×OH pair shows a difference of 245% for unity exponents, while this difference reduces to 30% with the optimal exponent combination.

The detailed results for the four best correlations in Case A are listed in Table 4.3. Unfortunately, these best correlations correspond to species that cannot be measured accurately at present in turbulent flames. Hence, good correlations involving species measurable by LIF

are added in the lower part of the table, and are discussed later.

TABLE 4.3. Four best correlations in Case A, B, C and D, followed by best results for LIF-measurable species.

Case A			Case B		
Species pairs	unity exponent	optimal exponent	Species pairs	unity exponent	optimal exponent
O × HO <sub>2</sub>	127%	22%	O × HO <sub>2</sub>	53%	17%
H × HO <sub>2</sub>	38%	26%	H × H <sub>2</sub> O <sub>2</sub>	83%	18%
H × CO	183%	26%	O <sub>2</sub> × O	92%	19%
O <sub>2</sub> × H	112%	28%	O × CO	125%	20%
HCO × OH	245%	30%	HCO × OH	136%	25%
CO × HCO	56%	48%	CO × HCO	61%	45%
CO × OH	66%	65%	CO × OH	73%	50%
Case C			Case D		
Species pairs	unity exponent	optimal exponent	Species pairs	unity exponent	optimal exponent
H × H <sub>2</sub> O <sub>2</sub>	84%	14%	O × HO <sub>2</sub>	214%	18%
O × HO <sub>2</sub>	46%	17%	H × HO <sub>2</sub>	27%	22%
O × CO	114%	19%	H × CO	254%	22%
H × HO <sub>2</sub>	46%	19%	H × O <sub>2</sub>	181%	25%
HCO × OH	115%	25%	HCO × OH	314%	38%
CO × HCO	58%	30%	CO × HCO	62%	43%
CO × OH	74%	42%	CO × OH	65%	59%

Let us now consider Cases B, C and D. The mixture is stoichiometric ( $\Phi = 1$ ) with H<sub>2</sub>/CO ratio of 1 in volume for Case B; Case D has the same H<sub>2</sub>/CO ratio as Case A, but for a lean flame; while Case C has the same equivalence ratio as Case D (lean), but with a large H<sub>2</sub>/CO ratio. The best correlations including the LIF-measurable correlations for Cases B, C and D are also listed in Table 4.3. Comparing results of these four cases, it is obvious that the combination O×HO<sub>2</sub> would be in general the best possible reconstruction. However, as it is up to now still impossible to measure fields of HO<sub>2</sub> and O in turbulent flames, the most accurate combination that is measurable by LIF involves HCO×OH with optimal exponents. In all cases, the objective function  $q$  for the combination HCO×OH with optimal exponents always stays below 40%, highlighting the very good reconstruction quality. This also demonstrates that the combination HCO×OH is neither sensitive to equivalence ratio nor to H<sub>2</sub>/CO ratio, at least in the range considered in this work.

### Impact of turbulence

Case E is introduced to check the possible impact of turbulence intensity, roughly doubling the Reynolds number. Results are listed in Table 4.4. The combination  $\text{HCO} \times \text{OH}$  with optimal exponents still acts as the best LIF-measurable correlation, demonstrating again the robustness of this estimator.

TABLE 4.4. Best LIF-measurable correlations in Case E.

Species pairs	unity exponent	optimal exponent
$\text{HCO} \times \text{OH}$	197%	23%
$\text{CO} \times \text{HCO}$	57%	48%
$\text{CO} \times \text{OH}$	67%	65%

All the test cases previously mentioned are two-dimensional. The structure of the resulting turbulent flames may not be perfectly realistic, since turbulence is intrinsically a three-dimensional phenomenon. Thus, a 3D DNS case with conditions identical to Case A has been performed (Case F) to check the generality of the conclusions, keeping the same domain side length and spatial resolution. Corresponding results are shown and discussed later.

### Choice of optimal exponents

Since the combination  $\text{HCO} \times \text{OH}$  with exponents is the clear winner of this contest, it is now important to check if the obtained, optimal exponents vary noticeably, or remain almost the same. The obtained optimal exponents are listed in Table 4.5 for all the previous cases.

From Table 4.5, it can be concluded that the optimal exponents for the best LIF-measurable combination,  $\text{HCO} \times \text{OH}$ , are nearly identical for all conditions,  $s_1 \simeq 1.5$  and  $s_2 \simeq 0.75$ . Using these recommended values,  $s_1 = 1.5$  and  $s_2 = 0.75$ , the last column of Table 4.5 demonstrates indeed that a very good reconstruction quality can be obtained for all cases considered.

TABLE 4.5. Obtained correlations for the best LIF-measurable species combination, HCO×OH.

Case	with optimal exponents	optimal exponent $s_1$	optimal exponent $s_2$	with recommended exponent pair ( $s_1 = 1.5; s_2 = 0.75$ )
A	30%	1.55	0.83	32%
B	25%	1.46	0.74	26%
C	25%	1.47	0.68	25%
D	38%	1.57	0.83	46%
E	23%	1.39	0.81	29%

### Impact of kinetic scheme

All the previous test cases used the syngas kinetic mechanism of Davis et al. [113]. Using a different mechanism may lead to noticeable changes in the prediction. This is why, starting with Case G, the USC Mech version II [115] is used to verify the robustness of the findings. The mixture composition in Case G is identical to Case B. A noticeable difference is that species CH<sub>2</sub>O is included in the USC Mech version II, while it does not exist in the mechanism of Davis et al. [113]. The best LIF-measurable correlations in Case G are listed in Table 4.6.

TABLE 4.6. Best LIF-measurable correlations in Case G.

Species pairs	unity exponent	optimal exponent	$s_1$	$s_2$
CH <sub>2</sub> O × OH	80%	14%	0.30	0.65
HCO × OH	136%	21%	1.46	0.71
HCO × CH <sub>2</sub> O	71%	27%	1.00	0.03
CO × HCO	58%	27%	0.09	1.01

Two new findings must be discussed when looking at Table 4.6. First, the best correlation measured by LIF still involves OH, but now CH<sub>2</sub>O as partner, as found indeed in the original work of Paul et al. [100]. This reveals the potential interest of measuring this species to track heat release. One advantage is that the signal-to-noise ratio for LIF of CH<sub>2</sub>O is generally higher compared to that of HCO, which means that CH<sub>2</sub>O can be more accurately measured using LIF than HCO. However, CH<sub>2</sub>O is usually considered as a negligible side product in syngas flames and its real involvement is very low. The species combination HCO×OH with

optimal exponents still remains second-best for LIF-measurable species, and is only slightly poorer (OH with  $\text{CH}_2\text{O}$ : 14%; with HCO: 21%; both being excellent values). A parity plot is shown in Fig. 4.1 describing the local, pixel-by-pixel correlations based on the species combination  $\text{HCO}\times\text{OH}$  and  $\text{CH}_2\text{O}\times\text{OH}$  with optimal exponents. As only the high heat release region ( $0.5 \leq \overline{H}_r \leq 1$ ) is of interest to reconstruct the flame and its thickness, the parity plot is limited to this range. From the parity plot in Fig. 4.1, it can be seen that the reconstruction quality of the correlation  $\text{CH}_2\text{O}\times\text{OH}$  with optimal exponents does not appear to be noticeably better than that involving HCO. While  $\text{HCO}\times\text{OH}$  quite often leads to an underestimation of the real heat release, the opposite is true for  $\text{CH}_2\text{O}\times\text{OH}$ , in which case the heat release is often overestimated. If, for some particular reason perhaps connected to the experimental setup or available hardware,  $\text{CH}_2\text{O}$  can be measured with a noticeably higher accuracy, the correlation  $\text{CH}_2\text{O}\times\text{OH}$  can be preferred. However, in the general case and looking again at Fig. 4.1, the reconstruction of heat release based on  $\text{HCO}\times\text{OH}$  can be further recommended as a very robust estimator of HRR. This is confirmed by the fact that the optimal exponents in Case G with USC Mech version II [115],  $s_1 = 1.46$  and  $s_2 = 0.71$  are very close to that discussed previously when using the mechanism of Davis et al. [113] (compare Tables 4.6 and 4.5). As a consequence, the previous recommendation ( $s_1 = 1.5$  and  $s_2 = 0.75$ ) still holds independently from the employed reaction scheme.

To further check the generality of these findings, Cases H, I and J have been computed using USC Mech version II for different species compositions. The best correlations measurable by LIF are listed in Table 4.7, confirming the previous statements. Collecting the information of Tables 4.6 and 4.7, generally valid exponents for the alternative correlation  $\text{CH}_2\text{O}\times\text{OH}$  can be recommended with exponents  $s_1 = 0.32$  and  $s_2 = 0.8$ .

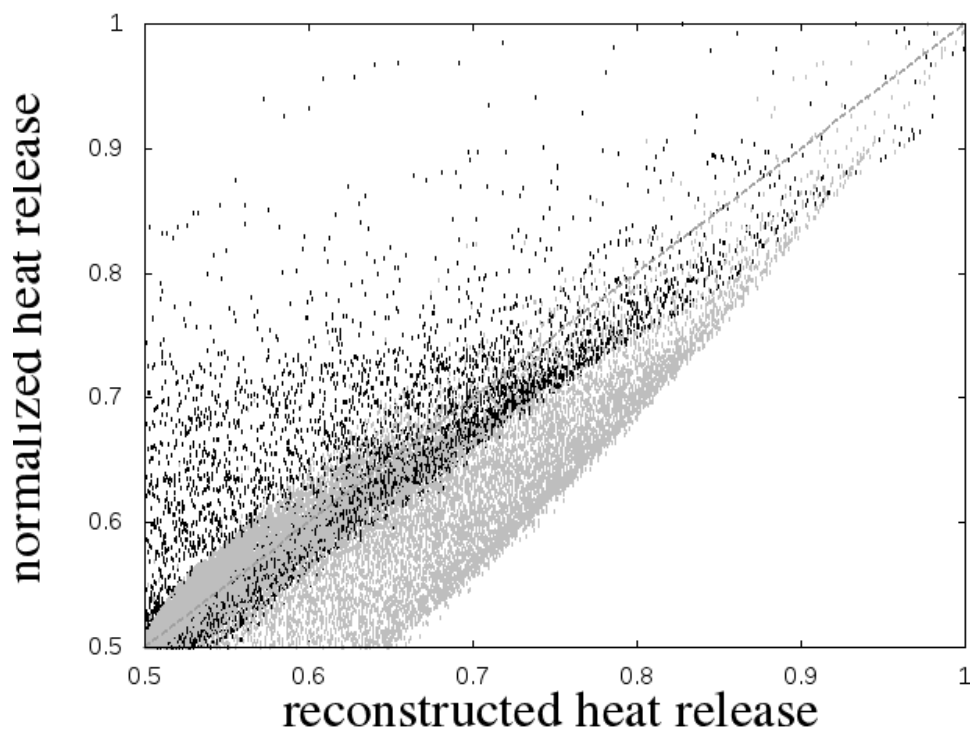


FIGURE 4.1. Parity plot between the normalized heat release and the reconstruction based on  $\bar{c}_{HCO}^{1.46} \times \bar{c}_{OH}^{0.71}$  (black points), or  $\bar{c}_{CH_2O}^{0.3} \times \bar{c}_{OH}^{0.65}$  (gray points).

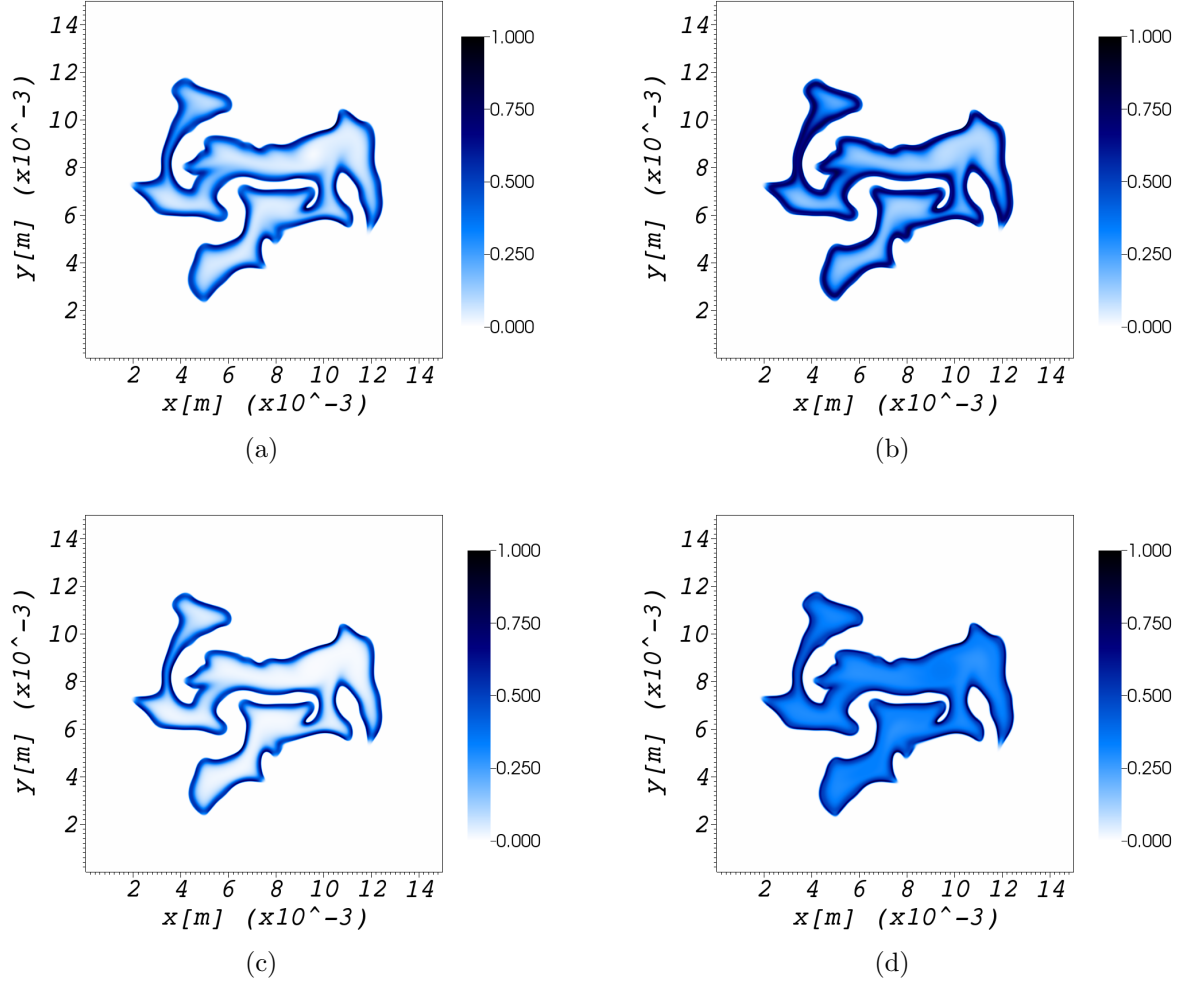


FIGURE 4.2. Example of instantaneous (a) normalized heat release distribution  $\overline{H}_r$  at dimensionless time  $\tau = 1.5$ ; (b) normalized heat release distribution reconstructed by  $\overline{c}_{\text{HCO}} \times \overline{c}_{\text{OH}}$ ; (c) normalized heat release distribution reconstructed by  $\overline{c}_{\text{HCO}}^{1.5} \times \overline{c}_{\text{OH}}^{0.75}$  and (d) normalized heat release distribution reconstructed by  $\overline{c}_{\text{CH}_2\text{O}}^{0.32} \times \overline{c}_{\text{OH}}^{0.8}$  at dimensionless time  $\tau = 1.5$ . All these results correspond to Case G.



TABLE 4.7. Best correlations in Case H, I and J for LIF-measurable species.

Case	Species pairs	unity exp.	optimal exp.	$s_1$	$s_2$
H	$\text{CH}_2\text{O} \times \text{OH}$	68%	27%	0.32	0.98
	$\text{HCO} \times \text{OH}$	290%	31%	1.51	0.86
	$\text{CO} \times \text{HCO}$	66%	45%	0.76	1.96
	$\text{HCO} \times \text{CH}_2\text{O}$	57%	48%	1.94	0.31
I	$\text{CH}_2\text{O} \times \text{OH}$	79%	9%	0.32	0.68
	$\text{HCO} \times \text{OH}$	102%	21%	1.4	0.65
	$\text{CO} \times \text{HCO}$	58%	27%	0.03	0.87
	$\text{HCO} \times \text{CH}_2\text{O}$	74%	27%	0.85	0.01
J	$\text{CH}_2\text{O} \times \text{OH}$	83%	22%	0.33	0.85
	$\text{HCO} \times \text{OH}$	239%	32%	1.57	0.77
	$\text{CO} \times \text{HCO}$	60%	45%	0.34	1.79
	$\text{HCO} \times \text{CH}_2\text{O}$	70%	46%	1.64	0.15

### Reconstruction tests

Comparisons between the reconstructed heat release distributions using  $\text{HCO} \times \text{OH}$  with unity exponents or using  $\bar{c}_{\text{HCO}}^{1.5} \times \bar{c}_{\text{OH}}^{0.75}$  are presented in Fig. 4.2, showing the advantage of introducing the optimal exponents. The instantaneous distribution of heat release rate for a turbulent premixed syngas flame obtained by DNS in Case G at the dimensionless time  $\tau=1.5$  is shown in Fig. 4.2(a). The distribution for reconstructed heat release using  $\bar{c}_{\text{HCO}} \times \bar{c}_{\text{OH}}$  is shown in Fig. 4.2(b), the distribution for reconstructed heat release using  $\bar{c}_{\text{HCO}}^{1.5} \times \bar{c}_{\text{OH}}^{0.75}$  is shown in Fig. 4.2(c) and the distribution for reconstructed heat release using  $\bar{c}_{\text{CH}_2\text{O}}^{0.32} \times \bar{c}_{\text{OH}}^{0.8}$  is shown in Fig. 4.2(d). While both Fig. 4.2(b) and Fig. 4.2(c) deliver suitable approximations, it is obvious from the high heat release regions that the original profile is more closely reconstructed using the heat release marker with optimal exponents. Comparing now Fig. 4.2(c) with Fig. 4.2(d), it is confirmed that the correlation  $\text{HCO} \times \text{OH}$  with optimal exponents leads to an underestimation of the real heat release, while  $\text{CH}_2\text{O} \times \text{OH}$  noticeably overestimates the real heat release.

To check a posteriori the reconstruction quality of the proposed heat release marker, the instantaneous distribution of heat release rate for a turbulent premixed syngas flame

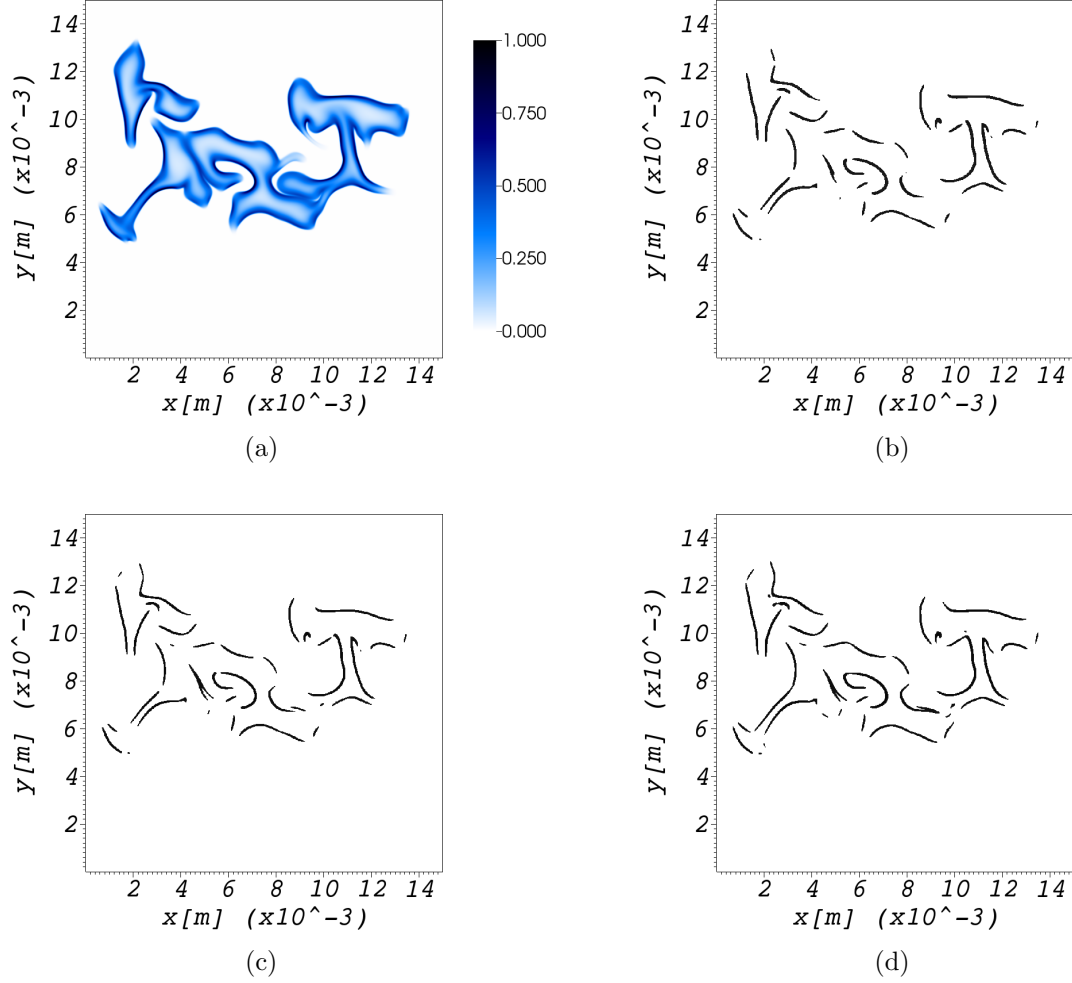
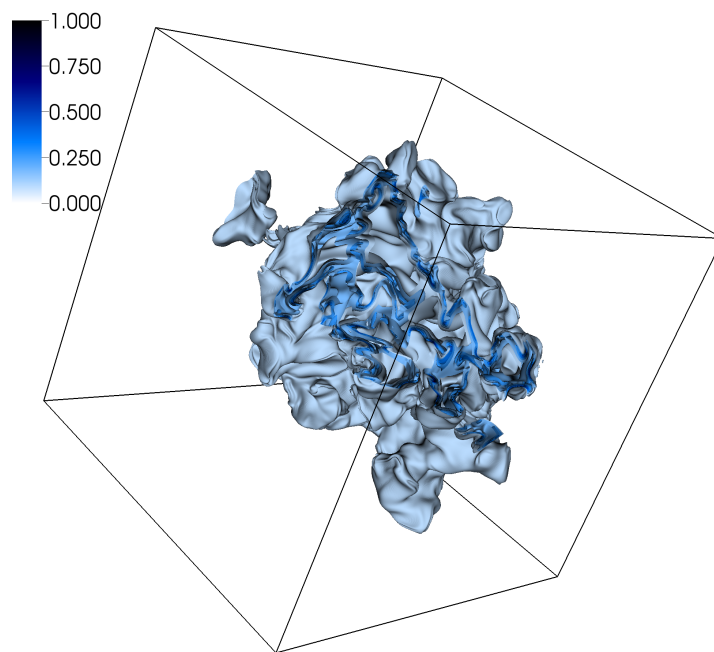
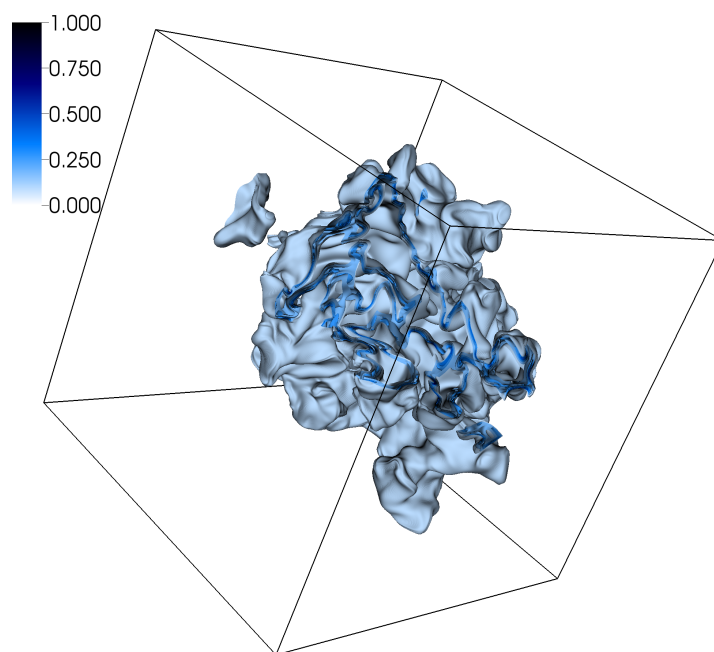


FIGURE 4.3. Example of instantaneous (a) normalized heat release distribution  $\bar{H}_r$  at dimensionless time  $\tau = 1.5$ ; (b) binarized heat release distribution after thresholding (a) at half of the peak value (black pixels corresponding to  $0.5 \leq \bar{H}_r \leq 1$ ); (c) binarized heat release distribution after thresholding normalized heat release distribution reconstructed by  $\bar{c}_{\text{HCO}}^{1.5} \times \bar{c}_{\text{OH}}^{0.75}$  at half of the peak value and (d) binarized heat release distribution after thresholding normalized heat release distribution reconstructed by  $\bar{c}_{\text{CH}_2\text{O}}^{0.32} \times \bar{c}_{\text{OH}}^{0.8}$  at half of the peak value. All these results correspond to Case H.



(a)



(b)

FIGURE 4.4. Case F (3D DNS): (a) normalized heat release and (b) reconstruction using  $\bar{c}_{HCO}^{1.5} \times \bar{c}_{OH}^{0.75}$ .

obtained by DNS in Case H at the dimensionless time  $\tau=1.5$  is shown in Fig. 4.3(a). The binarized heat release distribution corresponding to Fig. 4.3(a) is shown in Fig. 4.3(b). The corresponding binarized distribution for reconstructed heat release using the proposed generic heat release marker  $\bar{c}_{HCO}^{1.5} \times \bar{c}_{OH}^{0.75}$  is shown in Fig. 4.3(c). As a possible alternative, Fig. 4.3(d) shows the binarized distribution for reconstructed heat release using the heat release marker  $\bar{c}_{CH_2O}^{0.32} \times \bar{c}_{OH}^{0.8}$ . By comparing these figures, it can be seen that these two species combinations deliver almost exactly the profiles of HRR. All the high heat release regions are obtained with excellent accuracy. The flame topology (thickness, curvature) is also well approximated.

Similar comparisons have been successfully done for all cases considered in the analysis, but will not be shown here in the interest of space. This applies not only to the two-dimensional cases, but to three-dimensional flames as well (Case F, see Fig. 4.4). The position and thickness of all regions with high heat release are properly approximated.

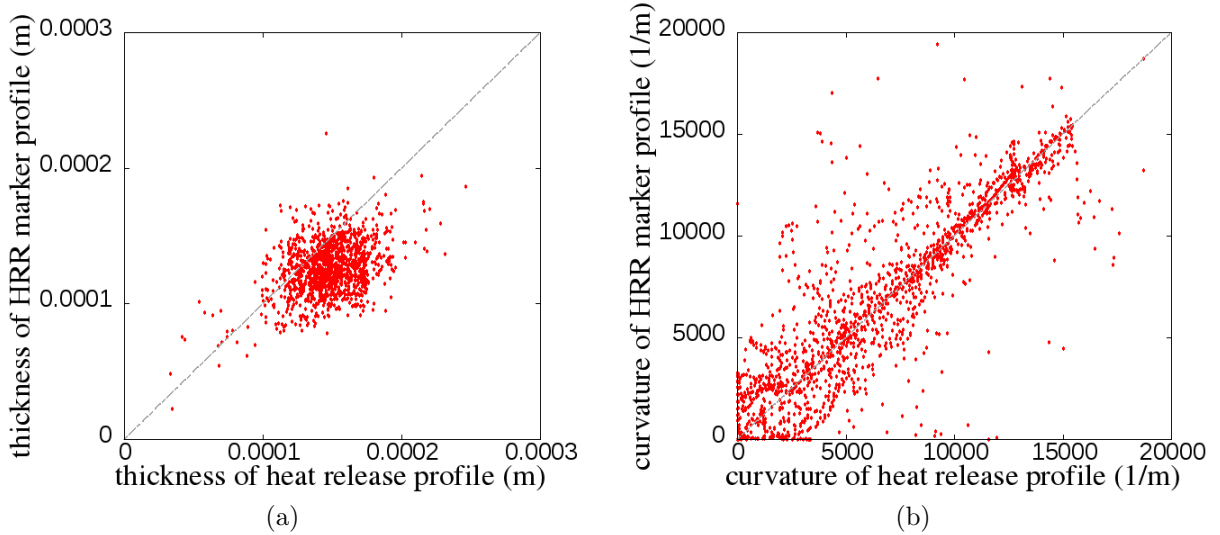


FIGURE 4.5. (a) Parity plot of flame thickness, showing the comparison between the values derived from the actual heat release profile, and from the proposed heat release reconstruction marker  $\bar{c}_{HCO}^{1.5} \times \bar{c}_{OH}^{0.75}$  and (b) Parity plot of flame curvature, showing the comparison between the values derived from the actual heat release profile, and from the proposed heat release reconstruction marker,  $\bar{c}_{HCO}^{1.5} \times \bar{c}_{OH}^{0.75}$ .

To quantitatively check that the identified heat release marker describes correctly the flame curvature as well, Case G has been retained. The flame front in Case G (shown in Fig. 4.2(a)) is taken into account for this detailed analysis. The flame front is first defined as the ridge line (or crest line) of heat release [85]. Then, the local unit normal vector to the flame front,  $\mathbf{n}$ , is computed, and the unit tangent vector,  $\mathbf{t}$ , is thus obtained. The flame curvature is computed as  $\|\frac{d\mathbf{t}}{ds}\|$ , where  $s$  is the arc length. Finally, the flame thickness is computed as the width of the high heat release region (corresponding as usual to  $0.5 \leq \bar{H}_r \leq 1$ ) when following the local direction of  $\mathbf{n}$  (normal to the flame). Figure 4.5(b) shows the flame curvature computed on the discrete points in the same curvilinear coordinate 1) along the real flame front, and 2) along the reconstructed flame front using the proposed heat release marker ( $\bar{c}_{HCO}^{1.5} \times \bar{c}_{OH}^{0.75}$ ). Figure 4.5(a) shows the flame thickness computed on the discrete points along the real flame front and along the reconstructed flame front. In both cases, most parts of the flame fronts have flame thickness around 0.15 mm. This figure demonstrates that flame thickness and flame curvature can be represented well by the proposed heat release marker,  $\bar{c}_{HCO}^{1.5} \times \bar{c}_{OH}^{0.75}$ .

### 4.1.5 Conclusions for syngas flames

In this work, the method originally proposed by Najm, Paul and co-workers [99, 100] for an indirect determination of the location of high heat release in turbulent flames has been reconsidered and extended. It now includes information concerning the thickness of the zones contributing mostly to heat release, and not only the peak locations. Moreover, exponents have been associated with each species pairs in order to improve the correlation. This last change can lead to a considerable improvement in the comparison between the original and reconstructed fields. Different equivalence ratios, H<sub>2</sub>/CO ratios and turbulence intensities were taken into account in 2D and 3D cases to derive a generally valid marker of heat release.

Two different reaction mechanisms were considered in order to check further the robustness of the findings.

It is found that a combination involving species  $O \times HO_2$  leads in principle to the best agreement in most cases. Unfortunately, these species cannot be properly measured yet in turbulent flames. Considering that only CO, HCO,  $CH_2O$  and OH can be obtained by LIF with a sufficient accuracy, the combination  $HCO \times OH$  is finally the best species pair found in general. The obtained agreement can be considerably improved using additional exponents. Finally, it is recommended to approximate the heat release rate using the normalized concentrations of HCO and OH with  $\bar{c}_{HCO}^{1.5} \times \bar{c}_{OH}^{0.75}$ . In this manner, not only the location of high heat release, but also information on flame topology (thickness, curvature) can be retrieved in an accurate manner.

If the concentration of species  $CH_2O$  can be measured with a noticeably higher accuracy than HCO, another excellent correlation is found to be  $\bar{c}_{CH_2O}^{0.32} \times \bar{c}_{OH}^{0.8}$ . Looking back at Table 4.3, a combination involving CO and OH would also be possible and deliver an acceptable reconstruction quality.

## 4.2 Application to Premixed Hydrogen Flames

Parts of the results presented in this section have been published in the VDI Berichte [119].

### 4.2.1 Introduction

Being carbon-free, hydrogen is especially interesting for mankind. Accurate measurements of heat release in turbulent hydrogen flames would be a key advantage both for our fundamental understanding and for practical applications. This is why the approach described in Section

4.1 is now applied to hydrogen flames.

Previous studies on heat release measurements in hydrogen flames mostly relied on OH-PLIF imaging [120, 121]. It is almost impossible to measure any other species by LIF in hydrogen flames. However, it has been shown recently that major species such as  $O_2$  and  $H_2$  can be measured in turbulent hydrogen flames using Raman scattering line imaging technique [122]. Though this technique is currently limited to 1D-lines, it might be extended to two or three dimensions in the future. Hence, it is assumed in the present study that OH,  $O_2$  and  $H_2$  are measurable in turbulent hydrogen flames (which is already true along lines). For the theoretical analysis, all 8 reacting species appearing in the detailed reaction schemes are first tested in a systematic manner.

### 4.2.2 Numerical setups

Here again, premixed turbulent hydrogen flames are computed by DNS using the in-house low-Mach solver *DINO* [7]. The flame starts from a spherical shape, as could be obtained for instance after ignition by an electrical spark, and expands into a turbulent environment. Two hydrogen mechanisms have been tested, in order to check how robust the obtained correlations might be: 1) the recent hydrogen mechanism of Boivin et al. [123], which contains 12 elementary reactions and 9 species ( $H_2$ ,  $O_2$ ,  $H_2O$ ,  $H$ ,  $O$ ,  $OH$ ,  $HO_2$ ,  $H_2O_2$  &  $N_2$ ); 2) the well-established hydrogen mechanism by Warnatz [124], which contains 19 elementary reactions and the same 9 species. In both cases, nitrogen is considered as an inert species. The thermo-diffusion effect (or Soret effect) [125] is taken into account as light radicals such as  $H$  or  $H_2$  are very important in hydrogen flames [126].

In order to identify heat release markers that can be generally applied to different conditions, the DNS simulations have been carried out for different equivalence ratios (Cases A, B and C), for different turbulence levels (Case D), and for either atmospheric or slightly

elevated pressures (Cases E and F), comparing results obtained in 2D or 3D configurations (Case G). For all these test cases (A - G), the recent mechanism of Boivin et al. [123] is used. In order to check the impact of the retained chemical scheme, Cases H, I and J correspond to a repetition of Cases A, B, and C, now using Warnatz’s hydrogen mechanism. More information concerning all test cases are shown in Table 4.8.

TABLE 4.8. Considered DNS cases for hydrogen flames.

	Mechanism	$\Phi$	P (bar)	$u_{rms}/s_l$	$l_{int}/\delta$	$Re_t$	Ka
A	Boivin	1.0	1	2.39	56.8	831	0.298
B	Boivin	1.2	1	2.30	59.6	839	0.273
C	Boivin	0.8	1	2.56	53.7	851	0.337
D	Boivin	1.0	1	3.34	56.8	1620	0.417
E	Boivin	1.0	1.5	2.40	84.9	1857	0.199
F	Boivin	1.0	2	2.41	113	3286	0.150
G(3D)	Boivin	1.0	1	2.37	90.5	1895	0.194
H	Warnatz	1.0	1	2.39	56.7	829	0.299
I	Warnatz	1.2	1	2.30	59.5	838	0.273
J	Warnatz	0.8	1	2.56	53.6	849	0.338

All these quantities have been clearly explained in connection with Table 4.1.

The DNS is carried out in a box with length of 1.5 cm on each side, and discretized with uniform mesh grid size of  $18.75 \mu\text{m}$ . This spatial resolution is necessary to resolve the smallest vortical structures and stiff intermediate radicals like  $\text{H}_2\text{O}_2$ . All the boundary conditions are periodic, the simulations being stopped well before the flame reaches any boundary. The initial spherical flame has a radius  $r = 1.2 \text{ mm}$  and is placed at the center of the numerical domain, with burned gas corresponding to the fresh gas compositions of Table 4.8 initialized within the kernel.

The simulation results are analyzed using the imaging method introduced in the previous section.



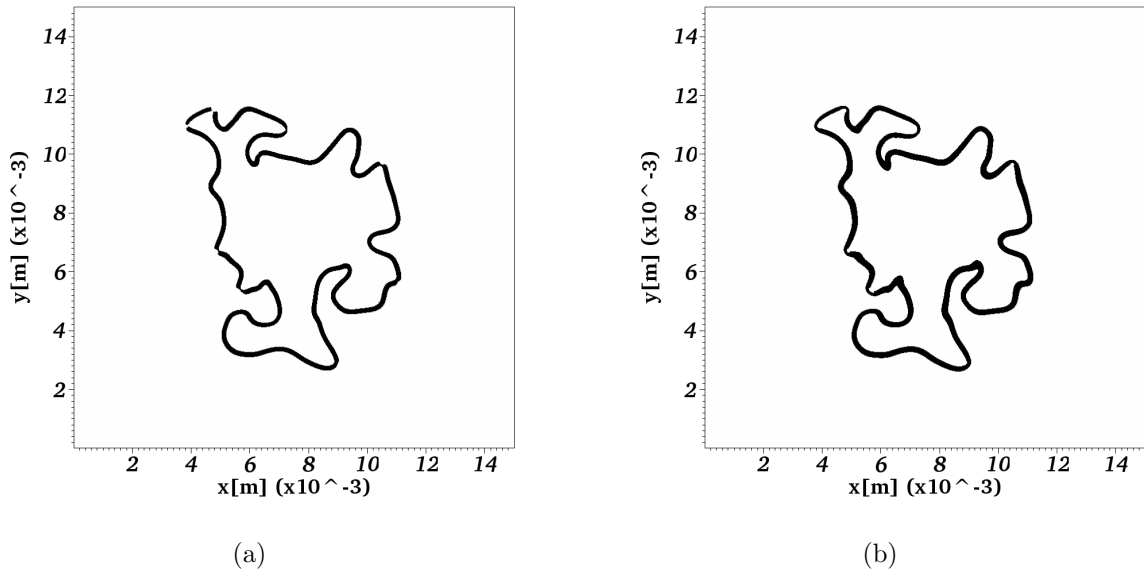


FIGURE 4.6. Example of instantaneous (a) binarized heat release distribution (black pixels corresponding to  $0.5 \leq \bar{H}_r \leq 1$ ) and (b) binarized heat release distribution reconstructed by  $\bar{c}_{\text{O}_2}^{0.46} \times \bar{c}_{\text{OH}}^{0.4}$  at dimensionless time  $\tau = 1.5$  in Case A.

### 4.2.3 Results and discussion

First, Case A is considered and used to exemplify the procedure. The two binarized images (Fig. 4.6(a) and Fig. 4.6(b)) are obtained by thresholding the normalized heat release distribution and the normalized reconstruction distribution at half-peak value. To get the difference between the two images, the objective function is then calculated. Table 4.9 shows the objective function  $q$  for all possible species combinations with optimal exponents (upper-right part of the table), or using unity exponents (lower-left part of the table) in Case A.

It is obvious from Table 4.9 that the reconstructions with optimal exponents again lead to lower objective functions  $q$  and, thus, to better approximations compared with the species combinations relying on unity exponents. Especially, the best reconstruction  $\text{H} \times \text{HO}_2$  shows only 5% difference when involving optimal exponents, while it shows 39% difference with

TABLE 4.9. Objective function  $q$  (to be minimized) for all possible species combinations in Case A; lower-left when using unity exponents, upper-right when using optimal exponents. The symbol – indicates no acceptable solution (value of  $q$  above 1000%). Along the diagonal, the resulting objective function for a single species with optimal exponent is listed.

	H	H <sub>2</sub>	O	O <sub>2</sub>	OH	H <sub>2</sub> O	HO <sub>2</sub>	H <sub>2</sub> O <sub>2</sub>
H	203%	12%	102%	5%	126%	134%	5%	10%
H <sub>2</sub>	19%	–	10%	557%	25%	17%	63%	36%
O	139%	41%	158%	8%	102%	102%	7%	12%
O <sub>2</sub>	24%	557%	59%	–	32%	10%	62%	35%
OH	291%	89%	148%	86%	519%	126%	31%	15%
H <sub>2</sub> O	209%	32%	182%	17%	546%	496%	11%	13%
HO <sub>2</sub>	39%	120%	40%	120%	95%	72%	116%	35%
H <sub>2</sub> O <sub>2</sub>	67%	106%	69%	107%	44%	69%	111%	101%

unity exponents. However, this best reconstruction is currently not accessible to experimental measurements in turbulent flames.

In Table 4.10, the four best correlations and the best experimentally-measurable correlations are listed. Again, the advantage of introducing optimal exponents is obvious. Assuming that only OH, H<sub>2</sub> and O<sub>2</sub> can be measured with sufficient accuracy in turbulent hydrogen flames, it is found that two corresponding correlations, H<sub>2</sub> × OH and O<sub>2</sub> × OH, lead to a very high reconstruction quality, with the objective function  $q$  below 40%. Now, examining the optimal exponents in these three test cases: for H<sub>2</sub> × OH,  $s_1$  is within the range of 0.39 – 0.45 and  $s_2$  is within the range of 0.45 – 0.51; for O<sub>2</sub> × OH,  $s_1$  is within the range of 0.41 – 0.53 and  $s_2$  is within the range of 0.40 – 0.43. The corresponding variation is limited to a small range. Considering that larger amounts of O<sub>2</sub> are present in the flow, leading in principle to easier and more accurate measurements, the best combination appears to be  $\bar{c}_{O_2}^{0.46} \times \bar{c}_{OH}^{0.40}$  and is valid for different conditions around stoichiometry.

For comparison, the objective function  $q$  obtained when using OH alone is very poor, around 500% in all three cases. This will be discussed again later considering Fig. 4.7(b).

To check further the generality of the proposed heat release marker, Case D now cor-

TABLE 4.10. Four best correlations for Cases A, B and C (from top to bottom), followed by best results for experimentally-measurable correlations.

Case A				
Species pairs	unity exponent	optimal exponent	exponent $s_1$	exponent $s_2$
H $\times$ HO <sub>2</sub>	39%	5%	0.71	0.56
H $\times$ O <sub>2</sub>	24%	5%	0.56	0.71
O $\times$ HO <sub>2</sub>	40%	7%	0.56	0.73
O $\times$ O <sub>2</sub>	59%	8%	0.37	0.77
H <sub>2</sub> $\times$ OH	89%	25%	0.43	0.5
O <sub>2</sub> $\times$ OH	86%	32%	0.46	0.4
Case B				
Species pairs	unity exponent	optimal exponent	exponent $s_1$	exponent $s_2$
H $\times$ O <sub>2</sub>	29%	11%	0.56	0.74
O $\times$ HO <sub>2</sub>	44%	11%	0.55	0.72
O $\times$ O <sub>2</sub>	67%	12%	0.36	0.78
H $\times$ HO <sub>2</sub>	39%	12%	0.74	0.59
H <sub>2</sub> $\times$ OH	92%	30%	0.39	0.45
O <sub>2</sub> $\times$ OH	90%	31%	0.41	0.4
Case C				
Species pairs	unity exponent	optimal exponent	exponent $s_1$	exponent $s_2$
H $\times$ HO <sub>2</sub>	37%	6%	0.72	0.58
H <sub>2</sub> $\times$ O	38%	6%	0.91	0.55
H $\times$ H <sub>2</sub>	26%	7%	0.62	0.64
H $\times$ O <sub>2</sub>	17%	8%	0.61	0.76
H <sub>2</sub> $\times$ OH	88%	24%	0.45	0.51
O <sub>2</sub> $\times$ OH	84%	38%	0.53	0.43

responds to a higher turbulence intensity. The best experimentally-measurable correlations are listed in Table 4.11. The results are nearly identical to those obtained for Case A (same case at lower turbulence level), highlighting the robustness of the corresponding predictions; the combination O<sub>2</sub>  $\times$  OH is still excellent.

TABLE 4.11. Best experimentally-measurable correlations in Case D.

Species pairs	unity exponent	optimal exponent	exponent $s_1$	exponent $s_2$
H <sub>2</sub> $\times$ OH	88%	26%	0.43	0.49
O <sub>2</sub> $\times$ OH	85%	33%	0.46	0.41

All the previous test cases have considered combustion under atmospheric pressure, as

already done for syngas flames in [84] and for hydrogen flames in [127]. However, hydrogen flames burning at elevated pressure are also commonly encountered and are thus interesting [128, 129]. Therefore, Cases E and F are conducted at slightly elevated pressures to check again the generality of the proposed heat release marker. Table 4.12 shows the best experimentally-measurable correlations. The same combinations are found to be optimal,  $\text{H}_2 \times \text{OH}$  and  $\text{O}_2 \times \text{OH}$ . However, the optimal exponents associated to all species increase with pressure. This is not unexpected, since flame thickness is strongly impacted by pressure, non-linear processes changing the exact position of the species profiles. To summarize, the same combinations are found to be optimal; but the optimal exponents associated to all species increase with pressure.

TABLE 4.12. Best experimentally-measurable correlations in Cases E and F.

Case E				
Species pairs	unity exponent	optimal exponent	exponent $s_1$	exponent $s_2$
$\text{H}_2 \times \text{OH}$	85%	16%	0.59	0.71
$\text{O}_2 \times \text{OH}$	83%	25%	0.57	0.59
Case F				
Species pairs	unity exponent	optimal exponent	exponent $s_1$	exponent $s_2$
$\text{H}_2 \times \text{OH}$	81%	16%	0.73	0.88
$\text{O}_2 \times \text{OH}$	79%	23%	0.71	0.83

As different chemical mechanisms involve different reaction pathways, the obtained distribution in space of species and radicals might be different as well. Therefore, it is interesting to check if the correlations are different when the DNS results rely on another reaction mechanism. For this purpose, Cases H, I and J (identical to Cases A, B and C) have been simulated again using the well-established hydrogen mechanism of Warnatz [124]. The best experimentally-measurable correlations are shown in Table 4.13.

Looking at Table 4.13, it is observed that this second reaction mechanism leads exactly to the same optimal species combinations,  $\text{H}_2 \times \text{OH}$  and  $\text{O}_2 \times \text{OH}$ . Even the optimal exponents

TABLE 4.13. Best experimentally-measurable correlations in Cases H, I and J.

Case H				
Species pairs	unity exponent	optimal exponent	exponent $s_1$	exponent $s_2$
H <sub>2</sub> × OH	87%	21%	0.48	0.64
O <sub>2</sub> × OH	84%	29%	0.47	0.45
Case I				
Species pairs	unity exponent	optimal exponent	exponent $s_1$	exponent $s_2$
H <sub>2</sub> × OH	92%	26%	0.42	0.52
O <sub>2</sub> × OH	89%	30%	0.43	0.44
Case J				
Species pairs	unity exponent	optimal exponent	exponent $s_1$	exponent $s_2$
H <sub>2</sub> × OH	88%	23%	0.52	0.67
O <sub>2</sub> × OH	81%	33%	0.61	0.62

found with the mechanism of Warnatz [124] are close to the values listed previously, only slightly larger. Hence, it appears that the proposed species combinations are valid independently from the employed reaction mechanism; almost 30 years separate the two kinetic mechanisms considered in our study.

In Fig. 4.7, the instantaneous normalized heat release distribution and some reconstructed distributions for Case A are compared. As it is seen, the reconstruction using both optimal heat release marker combinations  $\bar{c}_{\text{H}_2}^{0.43} \times \bar{c}_{\text{OH}}^{0.5}$  (Fig. 4.7(c)) and  $\bar{c}_{\text{O}_2}^{0.46} \times \bar{c}_{\text{OH}}^{0.4}$  (Fig. 4.7(d)) are much better than the conventional approximation based on OH only (reconstruction from  $\bar{c}_{\text{OH}}$  shown in Fig. 4.7(b)). Especially, the location of peak OH is only poorly associated to the region with high heat release; only the boundaries of both regions coincide in some sense. Similarly, the reconstruction by  $\bar{c}_{\text{H}_2}^{0.43} \times \bar{c}_{\text{OH}}^{0.5}$  appears to correlate less with heat release in a quantitative manner compared to the second proposed correlation  $\bar{c}_{\text{O}_2}^{0.46} \times \bar{c}_{\text{OH}}^{0.4}$ . Since, additionally, the amount of O<sub>2</sub> in the gas mixture is larger than hydrogen, facilitating accurate measurements, the reconstruction by  $\bar{c}_{\text{O}_2}^{0.46} \times \bar{c}_{\text{OH}}^{0.4}$  is probably preferable.

Summarizing all comparisons, the recommended heat release marker is finally  $\bar{c}_{\text{O}_2}^{0.46} \times \bar{c}_{\text{OH}}^{0.40}$  for turbulent hydrogen flames at atmospheric pressure. At elevated pressure, the optimal

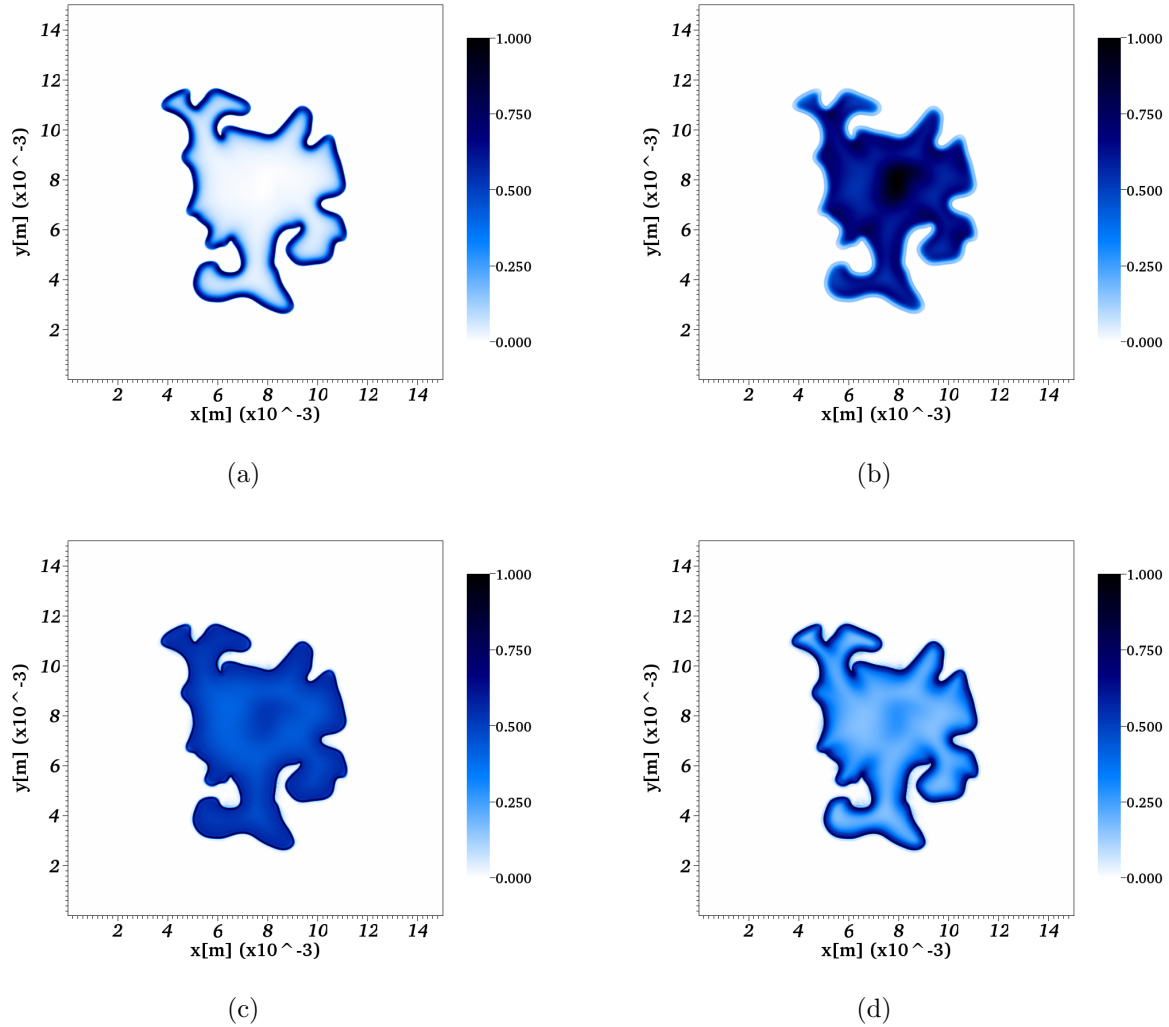


FIGURE 4.7. Example of instantaneous (a) normalized heat release distribution  $\overline{H}_\tau$  at dimensionless time  $\tau = 1.5$ ; (b) normalized heat release distribution reconstructed by  $\overline{c}_{\text{OH}}$ ; (c) normalized heat release distribution reconstructed by  $\overline{c}_{\text{H}_2}^{0.43} \times \overline{c}_{\text{OH}}^{0.5}$  and (d) normalized heat release distribution reconstructed by  $\overline{c}_{\text{O}_2}^{0.46} \times \overline{c}_{\text{OH}}^{0.4}$  at dimensionless time  $\tau = 1.5$ . All these results correspond to Case A.

exponents should be increased accordingly for the same pair of species.

As a final check, and considering that real turbulent flames show of course a three-dimensional structure, a turbulent flame has been simulated in 3D (Case G). Results are shown in Fig. 4.8. Comparing the 3D iso-surfaces, it is clear that the heat release region is much better approximated by reconstruction  $\bar{c}_{\text{O}_2}^{0.46} \times \bar{c}_{\text{OH}}^{0.40}$  than by OH only.

#### 4.2.4 Conclusions for hydrogen flames

The heat release profile in turbulent hydrogen-air flames has been investigated systematically by Direct Numerical Simulations. By post-processing the DNS results, an excellent solution is identified as heat release marker,  $\bar{c}_{\text{O}_2}^{0.46} \times \bar{c}_{\text{OH}}^{0.40}$ , leading to a robust and accurate approximation of the heat release distribution in the flame. This approximation is much better than that obtained only from OH. However, in order to use this correlation, measurements of O<sub>2</sub> are needed, which currently are typically limited to line measurements.

This correlation is not strongly sensitive to stoichiometry, does not depend on the turbulence level, and applies as well to flames at slightly elevated pressures (with increased exponents). Additionally, this same correlation has been obtained from two different reaction mechanisms. As a consequence, it seems to be valid in a very general sense.

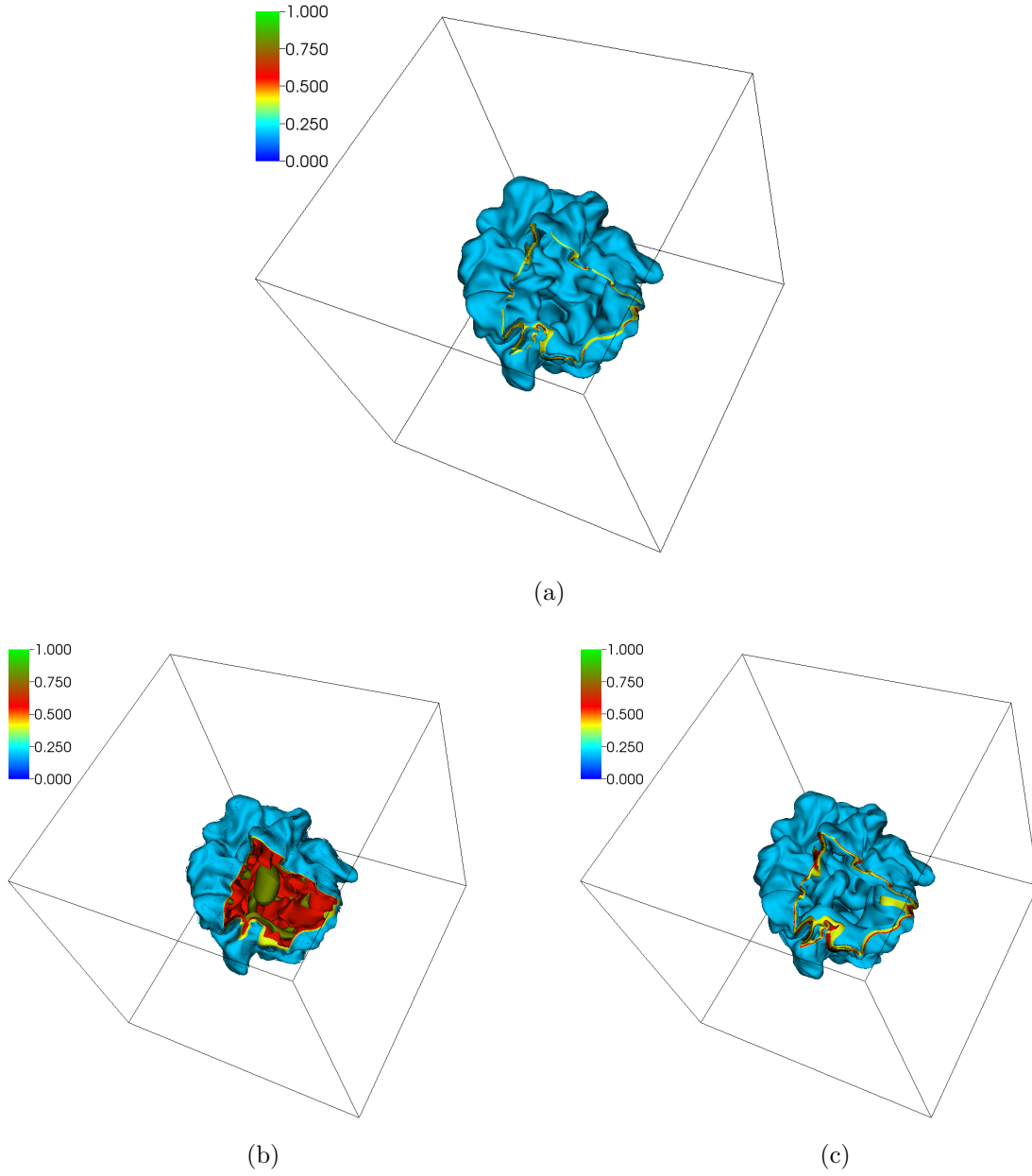


FIGURE 4.8. Case G (3D DNS): Clipped iso-surface of (a) normalized heat release; (b) conventional reconstruction by OH only; (c) reconstruction by  $\bar{c}_{\text{O}_2}^{0.46} \times \bar{c}_{\text{OH}}^{0.40}$ .



## 4.3 Application to Premixed Methane Flames

Parts of the results presented in this section have been published in the Proceedings of the Combustion Institute [130].

### 4.3.1 Introduction

Methane, being also the main component of natural gas, is used as a fuel in an uncountable number of applications. Therefore, characterizing heat release by a robust experimental procedure would be particularly useful.

To obtain the heat release reconstruction for methane flames in experiments, Paul and Najm [100] proposed a pixel-by-pixel product of the OH and CH<sub>2</sub>O PLIF images. In contrast to the HCO signal, the (OH × CH<sub>2</sub>O) images show a good quality and relatively intense signals in both laminar and turbulent flames. and can be obtained rather easily. This interesting method has, since then, been used and validated by many different authors for a wealth of applications [101, 103–107]. Nikolaou and Swaminathan [109] later reexamined the validity of the reaction rate of OH + CH<sub>2</sub>O ⇌ HCO + H<sub>2</sub>O as a reliable heat release rate marker for lean methane-air and preheated stoichiometric multicomponent mixtures (involving CO, H<sub>2</sub>, H<sub>2</sub>O, CO<sub>2</sub>, and CH<sub>4</sub>). For lean mixtures, it was found that the HRR correlates stronger with the rate of reaction OH + CH<sub>2</sub>O ⇌ HCO + H<sub>2</sub>O at higher heat release. For near-stoichiometric mixtures, the HRR correlates better with the reaction H + CH<sub>2</sub>O ⇌ HCO + H<sub>2</sub>. The performance of (H × CH<sub>2</sub>O) was recently compared with the conventional marker (OH × CH<sub>2</sub>O) [110]. It was found that both (H × CH<sub>2</sub>O) and (OH × CH<sub>2</sub>O) are suitable markers for methane-air flames with equivalence ratio  $\phi = 0.8$ -1.1, but that (H × CH<sub>2</sub>O) is less sensitive to the equivalence ratio. Even more recently, Wei et al. [131] studied the impact of equivalence ratio on HRR markers. They found that the

correlations ( $\text{H} \times \text{CH}_2\text{O}$ ) and ( $\text{OH} \times \text{CH}_2\text{O}$ ) are sensitive to the mixture equivalence ratio, resulting in a large prediction uncertainty for specific conditions, such as stratified flames. They proposed ( $\text{O} \times \text{CH}_3$ ) to be the best correlation for a wide range of equivalence ratios; however, O-atom LIF is very challenging [132] and  $\text{CH}_3$  LIF is even impossible in turbulent flames using the current diagnostic techniques.

In this study, a systematic evaluation of all possible HRR marker combinations is done for species measurable by LIF in methane-air flames. Direct Numerical Simulations of turbulent flames have been carried out for a variety of equivalence ratios. Building on top of our previous studies for simpler fuels described in the previous sections, a direct pixel-by-pixel comparison is proposed to identify optimal HRR markers measurable by LIF for turbulent methane flames, while minimizing the sensitivity toward the equivalence ratio. This is also the first time that so many different configurations have been considered in the analysis for methane flames, ensuring robustness of the predictions. A more detailed analysis has been introduced, involving additionally joint probability density functions (PDFs). Most importantly, the current study is the first time that a separate analysis is done for different regions of heat release. In this manner, it is observed that a generally valid HRR marker can be used to track simultaneously the highly active reaction zone and extinction events. Additionally, a feasibility study concerning the proposed marker is discussed for LIF experiments.

### 4.3.2 Numerical setups

Direct Numerical Simulations of premixed turbulent flames have been again performed using the in-house low-Mach reacting flow solver DINO [7, 133]. Starting from an initially spherical reaction zone, a premixed flame propagates into a turbulent environment.

To check the robustness of the obtained predictions, two detailed reaction mechanisms for methane flames have been employed: 1) GRI Mech 3.0 [134], and 2) the San Diego mechanism

[135]. Both mechanisms have been widely used for methane combustion. Additionally, the reduced mechanism of Smooke [136] has been employed in 3D (Case M in Table 4.14) to check the validity of the results obtained in two-dimensional DNS-simulations (Cases A-I0 in Table 4.14). All chemical kinetics, thermodynamic, and transport coefficients are systematically computed using Cantera 1.8 [15]. These flames span from thin reaction zones to corrugated-flamelet regimes in the turbulent premixed combustion diagram of Peters [137].

TABLE 4.14. Investigated DNS cases for methane flames.

Case	Mech	$\phi$	$s_l$ (m/s)	$u_{rms}/s_l$	$l_{int}/\delta$	Re	$\eta$ ( $\mu\text{m}$ )
A	GRI 3.0	0.6	1.52	3.51	21.6	92.9	49.2
B	GRI 3.0	0.7	1.84	2.89	25.9	93.2	49.3
C	GRI 3.0	0.8	2.10	2.52	29.5	91.5	49.5
D	GRI 3.0	0.9	2.26	2.35	32.4	93.4	49.7
E	GRI 3.0	1.0	2.33	2.28	31.4	90.1	49.5
F	GRI 3.0	1.1	2.30	2.31	33.4	94.2	49.9
G	GRI 3.0	1.2	2.16	2.47	31.0	94.0	49.7
H	GRI 3.0	1.3	1.91	2.79	27.6	94.4	49.9
I	GRI 3.0	1.4	1.59	3.35	22.0	90.0	49.5
J	GRI 3.0	1.0	2.33	1.55	23.2	43.9	60.7
K	GRI 3.0	1.0	2.33	3.19	44.4	173.4	41.5
A0	San Diego	0.6	1.54	3.45	21.9	91.9	49.1
B0	San Diego	0.7	1.91	2.79	26.2	92.8	49.3
C0	San Diego	0.8	2.13	2.50	29.7	92.5	49.3
D0	San Diego	0.9	2.27	2.35	33.0	93.6	49.6
E0	San Diego	1.0	2.35	2.26	32.3	93.1	49.5
F0	San Diego	1.1	2.32	2.29	33.6	94.2	49.9
G0	San Diego	1.2	2.16	2.47	31.3	93.7	49.5
H0	San Diego	1.3	1.89	2.82	26.5	91.4	49.2
I0	San Diego	1.4	1.57	3.39	22.6	90.4	49.4
M	Smooke	1.0	2.32	2.26	166.8	461	32.9

The computational domain has a side length  $L = 1$  cm. The domain is discretized by  $1024 \times 1024$  grid points, resulting in a resolution of  $9.8 \mu\text{m}$ . This resolution is fine enough to resolve both stiff radical species like  $\text{CH}_2\text{O}$  or  $\text{H}_2\text{O}_2$ , and the Kolmogorov length scale. An initial hot kernel with a temperature  $T_r = 1900$  K and a radius  $r = 1.5$  mm is initialized at the center of the domain and used to ignite the surroundings, set at a temperature  $T_u = 800$

K like in [109]. The initial pressure is  $p = 1$  atm. All the domain boundaries are periodic. The simulations have been continued up to  $t = 1.5\tau_t$  in order to reach a proper equilibrium between turbulence and chemistry [117], where  $\tau_t = l_{int}/u_{rms}$  is the characteristic time scale of the time-decaying turbulence. The simulation results at  $t = 1.5\tau_t$  are used to identify optimal HRR markers.

### 4.3.3 Identifying markers of heat release

As explained previously, it is necessary to obtain HRR markers that are able to predict heat release for a wide range of equivalence ratios. Species measurable by LIF are considered to be H, OH, CH<sub>2</sub>O, and HCO, like in [109]. As in all our previous studies [84, 119], species have been combined with exponents in order to improve the accuracy of the prediction.

From the fluorescence signal modeling in [138], the normalized distribution of the LIF signal intensity  $[S_f]$  reads

$$[S_f] = f(T, p, \chi_p)[\chi_{abs}], \quad (4.3)$$

$[\chi_{abs}]$  is the normalized distribution of the molar concentration of the excited species, and  $f(T, p, \chi_p)$  contains the combined effects of temperature  $T$ , pressure  $p$ , and mole fraction of perturbing species  $\chi_p$ . In the present study, all flames are atmospheric and the pressure is nearly constant within the flame, so that pressure-dependency is not an issue. The net influence of the perturbing species correlates with the temperature and has an inverse power-law dependence [110, 139]. Therefore, this effect can be lumped together with the temperature. The temperature dependence appears through the quenching rate coefficient and the Boltzmann population. When selecting properly the excited transition line, the Boltzmann population is insensitive to temperature. For OH LIF, The quenching rate depends only weakly on temperature [140]. The quenching rate of H LIF can be assumed to be proportional to  $T^{-1}$  [141], while CH<sub>2</sub>O LIF is assumed to be proportional to  $T^{-0.75}$  [110].

Regardless of the specific temperature-dependence model, the overall effect at the condition of two-photon overlap is given by  $f(T)$ ,

$$[S_{f1}] \times [S_{f2}] = f(T)[\chi_1] \times [\chi_2]. \quad (4.4)$$

where  $[S_{f1}]$ ,  $[S_{f2}]$ ,  $[\chi_1]$  and  $[\chi_2]$  are the normalized distribution of LIF signal intensity of species 1 and species 2, and normalized concentration of species 1 and species 2 respectively. Knowing the details of the experimental setup, it is usually not difficult to obtain the correct model for  $f(T)$  [142]. Since the model depends on the setup, a specific modeling for  $f(T)$  will not be discussed in the present study, relying purely on numerical simulations. For two species LIF, the two camera views (LIF signals) are overlapped on a pixel-by-pixel basis to evaluate HRR. As the distribution of the fluorescence signal is directly related to the distribution of the molar concentration of the excited species, a pixel-by-pixel computation involving species combinations is straightforward.

All possible two-species combinations ( $A_1, A_2$ ) associated to corresponding exponents ( $s_1, s_2$ ) have been evaluated. The objective is again to find a HRR marker ( $[A_1]^{s_1} \times [A_2]^{s_2}$ ) (where  $[A_i]$  denotes the normalized molar concentration of species number  $i$ ) that minimizes the difference between the real heat release profile and the reconstructed profile based on the marker combination.

To quantify the difference between the heat release profile and the reconstructed profile, the direct pixel-counting method described in [84] is used. First, the binarized image of normalized heat release  $[H_r]$  obtained by DNS is thresholded between two user-chosen critical values  $cr_{min}$  and  $cr_{max}$  (with  $0 \leq cr_{min} < cr_{max} \leq 1$ ). Then, all pixels with  $cr_{min} \leq [H_r] \leq cr_{max}$  have a value of 1, all other pixels are set to 0. The binarized image for the reconstructed profile is also treated in exactly the same way; the pixels of the normalized field of ( $[A_1]^{s_1} \times [A_2]^{s_2}$ ) with a value between  $cr_{min}$  and  $cr_{max}$  are set to 1, and the others to 0. Finally the

number of pixels with a different value at the same location in both images are counted, leading to a value  $n_{pix1}$ . The number of pixels with a value of 1 in the heat release images are counted as  $n_{pix2}$ . The objective function – to be minimized – is finally defined as  $q = n_{pix1}/n_{pix2}$ , and is a non-dimensional quantity describing the difference between both images. A value of  $q = 0$  means a perfect agreement.

The user-defined critical thresholds  $cr_{min}$  and  $cr_{max}$  are used to decide which heat release region is of particular interest for the comparison. In what follows, the low heat release region and the high heat release region are considered separately. First, the high heat release region is investigated, choosing  $cr_{min} = 0.5$  and  $cr_{max} = 1.0$ , as in the previous sections. In most practical applications, the objective is to maximize heat release, and regions with high heat release are obviously of particular interest. High heat release is also used to define the flame front [85]. On the other hand, the region of low heat release (defined here using  $cr_{min} = 0.1$  and  $cr_{max} = 0.3$ ) can be of particular interest when investigating flame quenching, and is considered in a second step.

Finally, the objective is to find the best combinations of species measurable by LIF, and the associated exponents, leading to a minimum value of the objective function  $q$  for either high (HHRR) or low heat release rate (LHRR). All possible exponent values  $s_1$  and  $s_2$  between 0 and 3 are systematically tested considering two digits, following again [84].

#### 4.3.4 Results and discussion

First, only the high heat release region ( $0.5 \leq [H_r] \leq 1$ ) is considered.

Looking at Fig. 4.9, it can be seen that the reconstruction quality can be improved by introducing additional exponents for a given species combination. For instance, the objective function  $q$  for the conventional marker combination ( $[OH] \times [CH_2O]$ ), corresponding to unity exponents, is 5.9% (lower arrow in Fig. 4.9), while it drops down to 3.0% for optimal

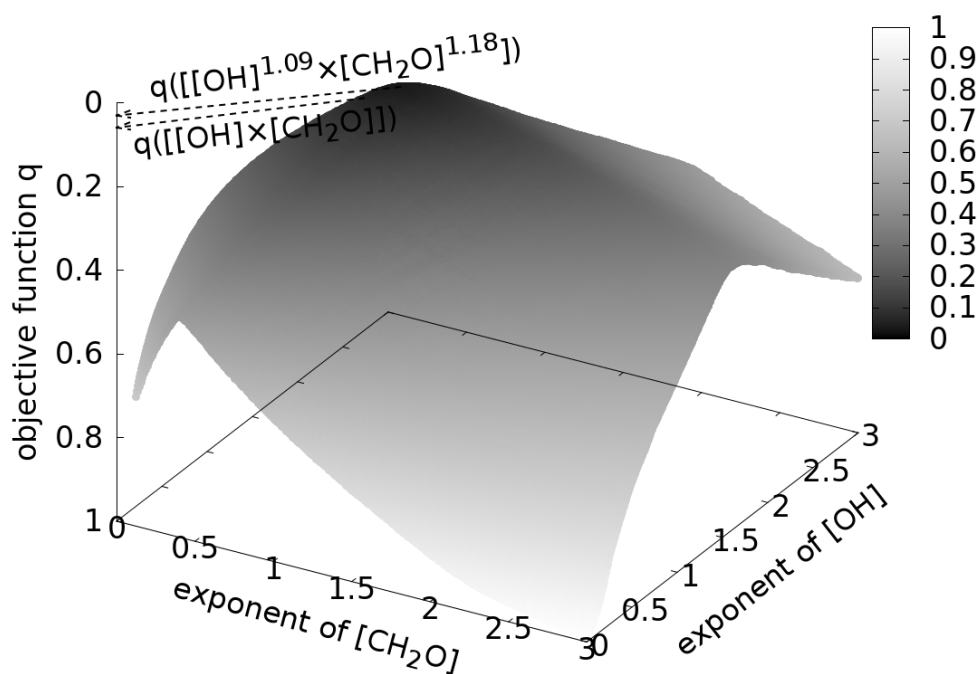


FIGURE 4.9. Objective function  $q$  evaluated for  $\text{OH} \times \text{CH}_2\text{O}$  with all possible exponents in Case F (for HRR). Note that the  $z$ -axis is inverted, so that the best possible reconstruction (minimizing  $q$ ) appears as a peak.

exponents, ( $[\text{OH}]^{1.09} \times [\text{CH}_2\text{O}]^{1.18}$ ). The superiority of markers involving optimal exponents is also obvious in Fig. 4.10, as a function of the equivalence ratio. There, it is shown that the reconstruction quality of conventional markers (unity exponents, dashed curves) varies a lot as function of the equivalence ratio. It is critical to obtain a generally valid marker of HRR with a low sensitivity towards equivalence ratio.

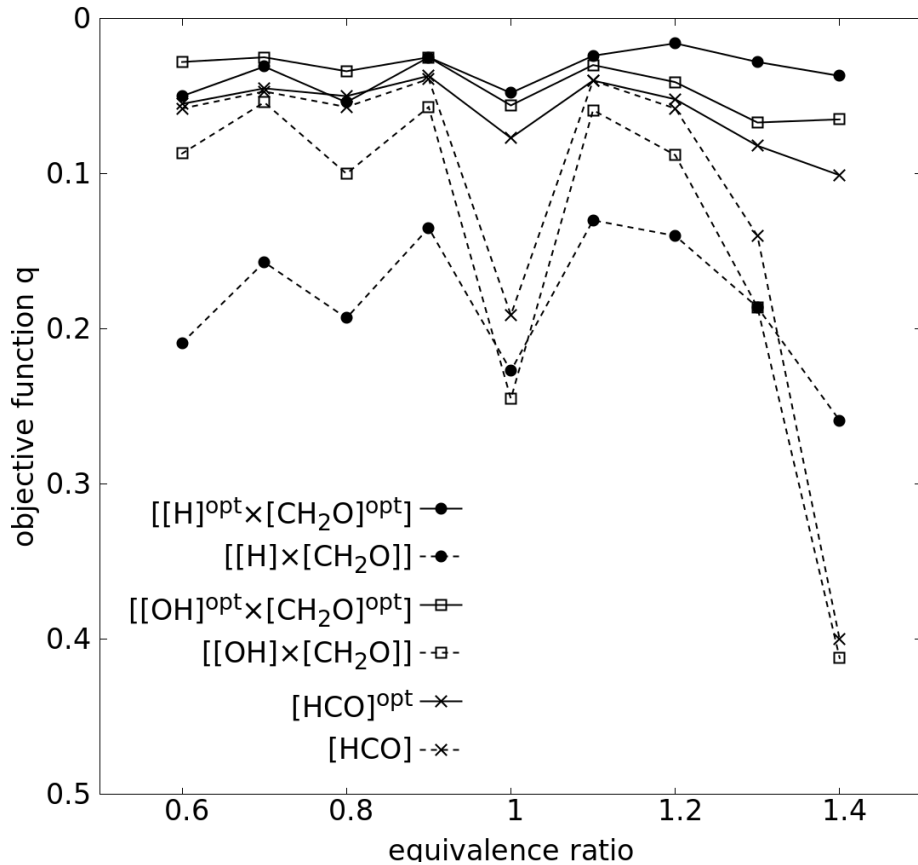


FIGURE 4.10. Objective function  $q$  evaluated for conventional HRR markers with unity or with optimal exponents for Cases A to I (for HHRR). Note that the  $z$ -axis is inverted, so that the best possible reconstruction (minimizing  $q$ ) appears as a peak. The optimal exponents (denoted “opt”) are always those found for a specific equivalence ratio, and may thus vary from point to point.

For this purpose, a fitting function is introduced to obtain the best exponents ( $s_1, s_2$ ) for all flames at different equivalence ratios ranging from 0.6 to 1.4, by maximizing:



$$f(s_1, s_2) = \sum_{x=0.6}^{1.4} \frac{1 - q(s_1, s_2)|_{\phi=x}}{1 - q_{min}|_{\phi=x}}, \quad (4.5)$$

where  $q_{min}|_{\phi=x}$  is the lowest objective function obtained at a given equivalence ratio  $\phi = x$ . This procedure also covers the case of single species (like HCO), when  $s_2 = 0$ .

The HCO-based markers (including [HCO], ([HCO]  $\times$  [OH]), ([HCO]  $\times$  [CH<sub>2</sub>O]) and ([HCO]  $\times$  [H])) are first checked. Unfortunately, it is found for the last three combinations that the best exponents for the second member of the combination (either [OH], [CH<sub>2</sub>O], or [H]) are close to 0 and vary in a stochastic manner for different equivalence ratios. This shows that [HCO] alone is indeed a better marker than in any combination. The next candidates are [HCO] (kept in the analysis), ([H]  $\times$  [CH<sub>2</sub>O]) and ([OH]  $\times$  [CH<sub>2</sub>O]). Finally, considering the GRI Mech 3.0 mechanism, the best HRR markers at all equivalent ratios are found to be [HCO]<sup>1.09</sup>, closely followed by ([H]<sup>1.13</sup>  $\times$  [CH<sub>2</sub>O]<sup>0.84</sup>) and ([OH]<sup>1.2</sup>  $\times$  [CH<sub>2</sub>O]<sup>1.24</sup>). For the San Diego mechanism, the best markers are [HCO]<sup>0.96</sup>, ([H]<sup>1.09</sup>  $\times$  [CH<sub>2</sub>O]<sup>0.89</sup>) and ([OH]<sup>0.93</sup>  $\times$  [CH<sub>2</sub>O]<sup>1.09</sup>). It can be seen that the optimal exponents for all optimal combinations are not identical for both reaction mechanisms, but quite similar. Involving now in the analysis all results obtained for all different equivalence ratios and both reaction mechanisms (Cases A - I and A0 - I0), the best solutions in general are finally found to be:

$$\begin{aligned} &[\text{HCO}]^{1.01}, \\ &([\text{H}]^{1.11} \times [\text{CH}_2\text{O}]^{0.86}), \\ &([\text{OH}]^{1.07} \times [\text{CH}_2\text{O}]^{1.17}). \end{aligned}$$

The first one is basically simply [HCO], as originally identified in the seminal work of [99, 100]. It is known that it is very difficult to measure this quantity, and it will not be discussed further.

Now, Cases J (with lower turbulence intensity) and K (with higher turbulence intensity) are performed to investigate the possible influence of varying turbulence intensity on the identified markers. Exactly the same optimal combinations are found in the same order for both cases, demonstrating again the robustness of these indicators. Checking now quantitatively the performance of the proposed combinations, for Case J,  $q([H]^{1.11} \times [CH_2O]^{0.86}) = 6.5\%$  and  $q([OH]^{1.07} \times [CH_2O]^{1.17}) = 2.8\%$ ; while for Case K,  $q([H]^{1.11} \times [CH_2O]^{0.86}) = 7.3\%$  and  $q([OH]^{1.07} \times [CH_2O]^{1.17}) = 3.8\%$ . These are excellent results, documenting the quality of the reconstruction of HHRR.

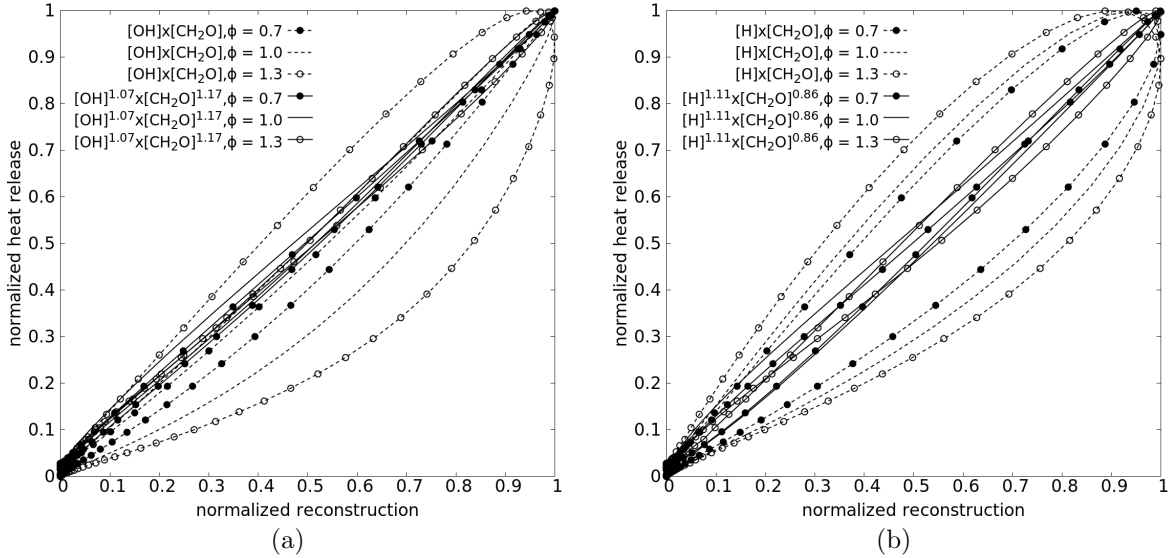


FIGURE 4.11. Normalized HRR vs. reconstruction from (a)  $[OH] \times [CH_2O]$  and (b)  $[H] \times [CH_2O]$ , with unity or with optimal exponents for laminar flames at different equivalence ratios.

Going one step further concerning a possible impact of turbulence, laminar methane flames have been considered additionally for equivalence ratios of 0.7, 1.0 and 1.3 in Fig. 4.11. These laminar flames are simulated using GRI Mech 3.0 with the same 2D spherical flame configuration, but without turbulence. The established marker ( $[OH] \times [CH_2O]$ ) (unity exponents, dashed lines) is highly sensitive to the equivalence ratio, much more than the

alternative combination  $[H] \times [CH_2O]$ , confirming the findings of [110]. Introducing now our optimal exponent combinations, it is observed that the reconstructions are always better, increasingly so for increasing equivalence ratio, and are much less sensitive to the equivalence ratio (solid lines in Fig. 4.11). Overall,  $[OH]^{1.07} \times [CH_2O]^{1.17}$  is slightly superior for these laminar flames.

The difficulty of finding an accurate and generally-valid HRR marker is again obvious when looking at Fig 4.11; the additional exponents are helpful for this purpose. For a laminar flame with  $\phi = 1.0$ , the reconstruction  $[H] \times [CH_2O]$  (dashed line without symbols in Fig 4.11(b)) shows a relatively poor reconstruction quality; the objective function is here  $q = 16\%$ . The reconstruction does not predict correctly the location of the peak HRR region, with a deviation exceeding 10%. The proportionality is also poor, the dashed line being quite far from the diagonal. However, the same reconstruction with optimal exponents  $[H]^{1.11} \times [CH_2O]^{0.86}$  shows a much better correlation, with  $q = 7.5\%$  (solid line without symbols in Fig 4.11(b)). The corresponding prediction lies very close the diagonal, and is thus a good approximation. Comparing these two cases, a reconstruction with an objective function  $q < 10\%$  is considered in this study as the necessary threshold for high-quality reconstruction, with even lower values of  $q$  indicating higher reconstruction accuracy.

Turning back to turbulent flames, the joint probability density functions (PDF) of the correlations between the normalized HRR and the reconstructions are shown in Fig. 4.12. The joint PDF is calculated using all the simulation results obtained with GRI Mech 3.0, for an equivalence ratio  $\phi = 0.6 - 1.4$  (Cases A to I). This figure demonstrates again the positive impact of the exponents introduced together with the species combinations. The joint PDF in Fig. 4.12(b) and Fig. 4.12(d) lie much closer to the diagonal compared with the conventional markers involving unity exponents (shown in Figs. 4.12(a) and 4.12(c)).

All the previous studies relied on 2D DNS. It is still impossible to carry out such a

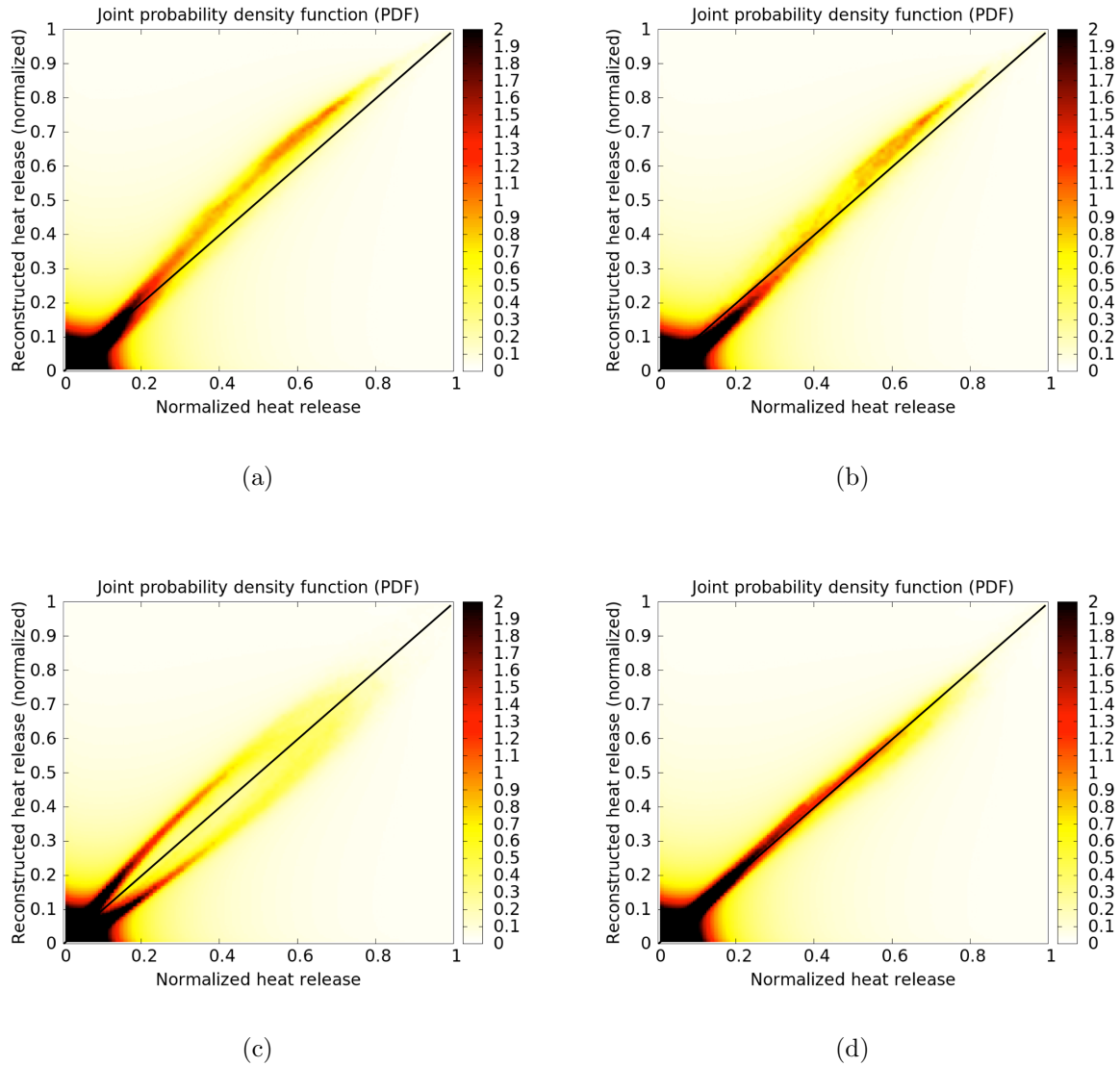


FIGURE 4.12. Joint PDF of the correlation between normalized HRR and (a) reconstruction from  $([\text{OH}] \times [\text{CH}_2\text{O}])$ ; (b) reconstruction from  $([\text{OH}]^{1.07} \times [\text{CH}_2\text{O}]^{1.17})$ ; (c) reconstruction from  $([\text{H}] \times [\text{CH}_2\text{O}])$  or (d) reconstruction from  $([\text{H}]^{1.11} \times [\text{CH}_2\text{O}]^{0.86})$ .

systematic study in 3D with the available computing power. Nevertheless, a single 3D case has been computed with the reduced methane mechanism of Smooke [136] (Case M), in order to check possible 3D effects. As shown by Fig. 4.13, the reconstruction of heat release using the optimal marker combinations and exponents proposed previously (see Figs. 4.13(c)

and 4.13(d)) reproduce perfectly the high heat release region (Fig. 4.13(a)). Using unity exponents (see Fig. 4.13(b)), noticeable discrepancies appear in the high heat release region.

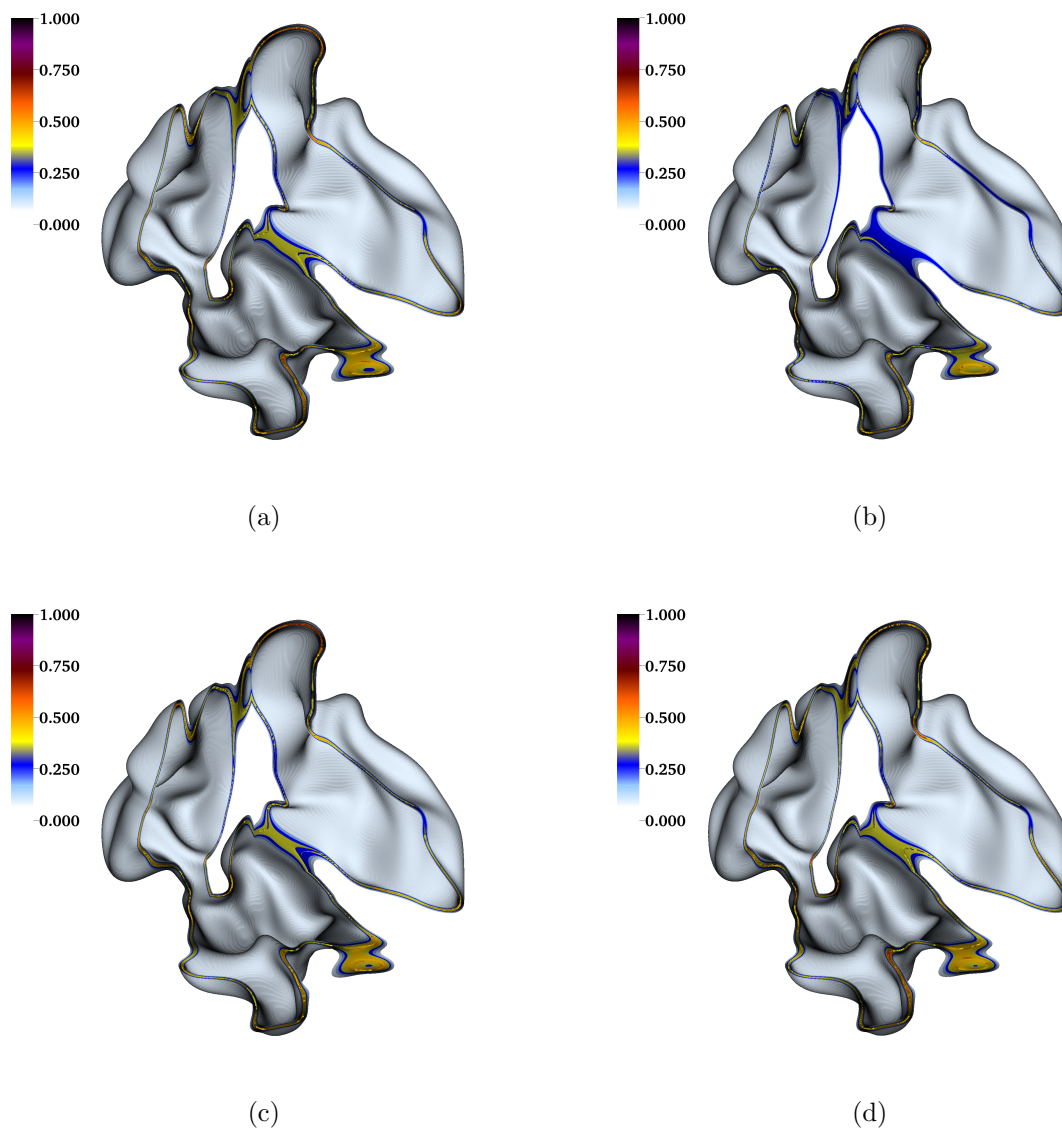


FIGURE 4.13. Case M (3D DNS): Clipped iso-surface of (a) normalized heat release; (b) conventional reconstruction by  $([\text{OH}] \times [\text{CH}_2\text{O}])$  with unity exponents; (c) reconstruction by  $([\text{OH}]^{1.07} \times [\text{CH}_2\text{O}]^{1.17})$ ; (d) reconstruction by  $([\text{H}]^{1.11} \times [\text{CH}_2\text{O}]^{0.86})$ . The iso-surfaces are clipped with 3 cut-planes normal to  $x$ ,  $y$  and  $z$  directions respectively.

Finally, it is possible to apply exactly the same analysis to the low heat release region

(LHRR). This would be particularly useful for analyzing extinction processes, or quenching followed by re-ignition. Using a similar analysis, the optimized marker combinations for the low heat release region ( $0.1 \leq [H_r] \leq 0.3$ ) are found to be:

$$\begin{aligned} & [\text{HCO}]^{0.89}, \\ & ([\text{H}]^{1.14} \times [\text{CH}_2\text{O}]^{0.86}), \\ & ([\text{OH}]^{0.95} \times [\text{CH}_2\text{O}]^{1.0}). \end{aligned}$$

It is interesting to see that these three combinations, and their order of appearance, are identical to that found for HHRR. Even the exponents do not change much. Overall, the indicators derived to describe the high heat release region can be used to investigate as well extinction phenomena.

### 4.3.5 Conclusions for methane flames

In the present study, premixed spherical methane-air flames have been simulated by Direct Numerical Simulations. A pixel-to-pixel image comparison is used to quantify the reconstruction quality of different HRR markers and obtain optimal combinations, taking also into account an exponent for each species concentration. Optimal HRR markers have been found, able to describe premixed flames at an equivalence ratio ranging from 0.6 to 1.4, either laminar or turbulent, both in 2D and 3D configurations, using two different reaction mechanisms, and describing both high and low heat release levels.

Apart from  $[\text{HCO}]$  used as single species, but barely measurable, the optimal marker combinations measurable by LIF are  $([\text{OH}]^{1.07} \times [\text{CH}_2\text{O}]^{1.17})$  and  $([\text{H}]^{1.11} \times [\text{CH}_2\text{O}]^{0.86})$ . Those are found to be noticeably better than the same species combinations with unity exponents.

The combination ( $[H]^{1.11} \times [CH_2O]^{0.86}$ ) is a slightly better choice to predict heat release over its whole range, even for quenching flames. However,  $[H]$  can currently only be measured with the two-photon excitation process. As an alternative, ( $[OH]^{1.07} \times [CH_2O]^{1.17}$ ) is a very good compromise, allowing relatively easy measurements while still leading to a very good prediction.

## 4.4 Conclusions

For syngas flames, the optimal HRR markers are found to be ( $[HCO]^{1.5} \times [OH]^{0.75}$ ) and ( $[CH_2O]^{0.32} \times [OH]^{0.8}$ ); for hydrogen flames, the optimal HRR marker is found to be ( $[O_2]^{0.46} \times [OH]^{0.4}$ ); for methane flames, the optimal HRR markers are identified to be ( $[OH]^{1.07} \times [CH_2O]^{1.17}$ ) and ( $[H]^{1.11} \times [CH_2O]^{0.86}$ ). In all these light-fuel flames, OH is found to be important for the markers. While, in hydrocarbon fuel flames, HCO and  $CH_2O$  are also important. This indicates the importance of the oxidation reaction  $CH_2O + OH = HCO + H_2O$  for heat release in those flames. The different optimal exponents also indicate largely different reaction pathways involved in those flames.

Typical combustion process generally involves three steps: ignition, flame development and/or propagation, and extinction. Systematic DNS studies have been used in this chapter to track heat release during flame propagation, and possibly extinction (low heat release region). In the next chapter, the same DNS tool will be used to investigate ignition process.





# Chapter 5

## Hotspot Ignition of a Turbulent Gas Flame

Parts of the results presented in this chapter have been published in the Journal Flow, Turbulence & Combustion [143].

### 5.1 Introduction

Ignition is an important and complex issue, which has been extensively investigated during many decades. Early studies on ignition for safety analysis mostly relied on experimental measurements and simplified theoretical models, as reported by Lewis and von Elbe [2] (first published in 1951). Numerical studies are difficult since the underlying processes (chemical kinetics, turbulent transport, heat exchange) are fully coupled. It is very demanding to take into account all aspects simultaneously in the same numerical analysis. Hence, in the past, many authors have isolated one specific aspect and have concentrated their analysis on that point. Main challenges concerning chemistry are the poorly known chemical pathways and the large number of individual reactions for complex fuels. That is why the present study only considers stoichiometric hydrogen-air mixtures, for which accurate and validated

physicochemical data are available [3]. Simulating turbulent flows is a challenge of its own. This is why the present study relies exclusively on Direct Numerical Simulations. Finally, the central challenge underlying heat exchange processes consists in modeling accurately all relevant paths (convection, diffusion, radiation). In order to obtain results independent from a specific geometry or confinement, only convection and diffusion are retained in the present study.

Ignition was first studied for laminar, non-premixed flames [144, 145] using simple chemistry. Later, kinetic effects have been taken into account, e.g. [146–149]. Due to the dominating combustion mode at that time and to associated simplifications, ignition has been mostly investigated for non-premixed flames, as reviewed for instance in [150].

In the early nineties, numerical studies on ignition under turbulent conditions became possible due to the progress in computing power. A two-dimensional (2D) turbulent flow was considered in [151, 152] with simplified chemical kinetics. The results were discussed further in [8, 153], demonstrating in particular the interest of DNS to investigate such configurations. Further aspects, like composition inhomogeneities impact as well the auto-ignition process [154]. Later works considered more realistic kinetics in 2D flows (e.g., [155]) or looked at three-dimensional (3D) flows but with simplified kinetics (like in [156–158]). For example, Reddy *et al.* [159] conducted 2D numerical simulations of lean premixed natural gas-air combustion and studied the critical ignition energy and the influence of equivalence ratio, kernel temperature and size. It was found that as long as the available ignition energy is greater than a prescribed minimum value, the duration in which a steady flame speed is achieved is a strong function of kernel temperature; it is not a function of kernel size. A parametric study of auto-ignition scenarios for lean n-heptane/air [160] and hydrogen/air [161] mixtures with thermal stratification at constant volume and high pressure have been later conducted using 2D DNS, concentrating on the influence of imposed initial temperature

fluctuations  $T'$  and of the ratio of turbulence to ignition delay timescale. Further DNS studies indeed considered 3D flames with complex kinetic schemes (see e.g., [162]) but did not investigate specifically the ignition mechanism. The recent study in [163] investigated autoignition of DME/air turbulent mixtures, using a 2D parametric study and a single 3D case to check the possible effect of 3D turbulence. Zhou *et al.* [164] performed parametric 3D DNS with a skeletal chemistry for auto-ignition of a turbulent n-heptane spray. However, only 5 DNS cases have been actually considered, since a large number of 3D DNS realizations are impossible with current computer resources.

The present study is based on DNS with detailed chemical and transport models. A parametric investigation is carried out concerning ignition events induced by a hotspot in homogenous  $H_2$ -air pre-mixtures at ambient temperature and pressure. An ignition diagram is first obtained to determine the critical combinations of hotspot temperature and radius leading to successful ignition or misfire. The same configurations are afterwards perturbed by adding turbulent fluctuations of increasing intensity. By repeating independent realizations for each turbulence level, the impact of turbulence on ignition probability and ignition delay is quantified in a statistically meaningful manner. To reveal the underlying mechanism controlling ignition, the ignition spot is identified and tracked in a Lagrangian frame. Unlike previous flame tracking studies [165–167], flame surface and flame structure are not of primary interest here, since a “flame” still does not exist as an established structure yet; thus, the tracking algorithm is governed only by fluid motion and turbulent fluctuations, and is used to compute the balance of the different physicochemical terms leading to ignition or misfire.

As 3D DNS involving accurate models for chemical, diffusion and thermodynamic processes are still not practical for systematic studies, the present work is mainly focused on 2D configurations, as done also for instance in [160, 161, 163, 168–170]. Yu and Bai [171]

compared 2D and 3D DNS of auto-ignition of a lean  $\text{H}_2/\text{air}$  mixture, and concluded that 3D turbulence results in faster heat transfer rate than 2D. In the present study, several 3D cases have been computed as well in order to check the possible influence of 3D turbulence on ignition delay. Due to vortex stretching, which leads to a wider range of turbulent scales in 3D cases, the results might differ.

In Section 5.2, the problem configuration (including numerics, chemical kinetics, molecular transport, and initialization) and post-processing techniques are briefly outlined, followed by a discussion of the numerical results in Section 5.3. Results from homogeneous laminar configurations are first presented (Sect. 5.3.1) to validate the employed numerical models with corresponding experimental data, and then obtain a laminar ignition diagram. The influence of turbulence intensity on the ignition probability and ignition delay is then discussed (Sect. 5.3.2). Finally, the findings obtained by tracking the hotspot in a Lagrangian frame are presented (Sect. 5.3.3), before concluding the chapter.

## 5.2 Problem configuration and initialization

### 5.2.1 Direct numerical simulations

In the present chapter, the parallel DNS flame solver *DINO* [7] is again used. It solves the low-Mach Navier-Stokes system coupled with detailed physicochemical models. The spatial derivatives are computed using a six-order centered explicit scheme. An explicit fourth-order Runge-Kutta time integrator is employed for temporal integration. All further details have been presented in the previous chapters.

Chemical reactions are solved by Cantera [15] in *DINO*. For the results presented later, a  $\text{H}_2/\text{O}_2$  chemical scheme suitable to investigate ignition phenomena [123] has been systematically employed. It involves 12 elementary reactions and 9 species ( $\text{H}_2$ ,  $\text{O}_2$ ,  $\text{H}_2\text{O}$ ,  $\text{H}$ ,  $\text{O}$ ,  $\text{OH}$ ,

$\text{HO}_2$ ,  $\text{H}_2\text{O}_2$ ,  $\text{N}_2$ ); reactions involving nitrogen are not considered.

As light radicals such as  $\text{H}$  or  $\text{H}_2$  play a noticeable role in hydrogen combustion [126], the thermo-diffusion effect (Soret effect) [125] is of significant importance and is always taken into account in the present DNS simulations. Full multicomponent diffusion may be numerically quite expensive [13]. Therefore, the Hirschfelder-Curtiss approximation [172] (also called mixture-averaged diffusion) is employed in the present study.

### 5.2.2 Flame configurations and initialization

According to dimensionality, the initial flame configurations in this study are categorized into: 0D homogeneous pre-mixture with uniform temperature (referred hereafter as setup *S0D*); 1D homogeneous pre-mixture with a pulse in temperature (referred hereafter as setup *S1D*); 2D homogeneous pre-mixture with a circular hotspot at higher temperature (referred hereafter as setup *S2D*); and finally 3D homogeneous pre-mixture with a spherical hotspot at higher temperature (referred hereafter as setup *S3D*).

The first configuration *S0D* is used to validate the numerical and physicochemical models, specifically for premixed ignition studies. In this first instance, uniform initial profiles for all variables are imposed at  $t = 0$  and allowed to iterate in a zero-dimensional simulation. In this way, the ignition delay  $\tau$  is obtained as a function only of the mixture composition (described by the equivalence ratio  $\Phi$ ), and of the initial mixture temperature  $T_0$  and pressure  $p_0$ .

The second configuration *S1D* is illustrated in Fig. 5.1. Here, initial profiles are prescribed as *S0D* but in a one-dimensional configuration and this time with a pulse in temperature (and hence in density considering initially isobaric conditions at atmospheric pressure) in the middle of the domain. The third and fourth configurations *S2D* and *S3D* are similar to *S1D*, but in two and three dimensions respectively. In all *S1D*, *S2D* and *S3D* cases, the homogeneous pre-mixture is consisting of  $Y_{\text{H}_2} = 0.029$ ,  $Y_{\text{O}_2} = 0.233$  and  $Y_{\text{N}_2} = 0.738$

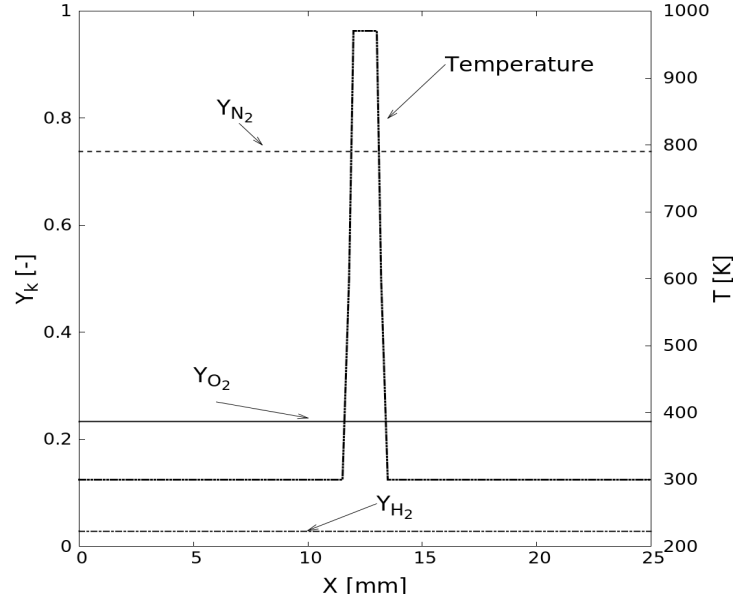


FIGURE 5.1. Typical computational domain and flame configuration showing *S1D* case – one-dimensional hotspot (initial configuration).

(equivalence ratio  $\Phi = 1$  in air). The ignition induction time is investigated as a function of the initial temperature  $T_0$  within the hotspot and of the radius  $R_0$  of the initial hotspot (half-width of the initial hot temperature zone for *S1D*). The surrounding mixture has temperature  $T_u = 300$  K. The step in temperature profile is approximated by a hyperbolic tangent function  $\psi$ , involving a stiffness parameter  $\epsilon$  and the distance from the center  $r$

$$\begin{aligned}
 r &= \sqrt{(x - 0.5 \cdot L_x)^2 + (y - 0.5 \cdot L_y)^2 + (z - 0.5 \cdot L_z)^2}, \\
 \psi &= 0.5 \left( 1 + \tanh \left( \frac{\epsilon \cdot (r - R_0)}{R_0} \right) \right),
 \end{aligned} \tag{5.1}$$

where  $\epsilon$  is the stiffness parameter, systematically set to 50 in this study. The parameters  $L_x$ ,  $L_y$  and  $L_z$  are the domain length in  $x$ ,  $y$  and  $z$ -direction respectively. Preliminary studies have shown that the choice of the stiffness parameter leads to a negligible impact on the obtained results in the range considered, confirming observations of previous studies [173].

The domain is consisting of a line (for *S1D*), square (for *S2D*), cube (for *S3D*) of side length  $L = 1.6$  cm discretized with a uniform grid ( $1024$ ,  $1024^2$  and  $1024^3$  points, respectively), leading to a grid spacing of  $15.625 \mu\text{m}$ . Such a fine grid is necessary for DNS to resolve correctly stiff intermediate radicals like  $\text{H}_2\text{O}_2$ , and simultaneously the smallest vortical structures in the highest turbulence case in the present study (see later Table 5.1). The "SuperMuc" supercomputer located in Munich (see <https://www.lrz.de/services/compute/supermuc/systemdescription/> for more information) is used for all computations. For 2D cases, each run takes 30 minutes using 256 cpu cores; for 3D cases, each run takes almost five days using 1024 cpu cores in parallel. All the boundary conditions are periodic. Simulations are always stopped well before the reaction front reaches the boundary.

For the turbulent cases, the initial laminar profiles are superimposed with a homogeneous isotropic turbulent field at  $t = 0$ , generated based on an Inverse Fast Fourier Transform (IFFT) with an analytically prescribed turbulence spectrum following von Kármán with Pao correction (VKP spectrum). Overall, 13 turbulence levels have been considered, ultimately spanning a wide range in turbulence intensities ( $0.25 \leq u'/s_L \leq 1.53$ ) and integral-scale Reynolds number  $\text{Re}_t = u'l_t/\nu$  ( $22.8 \leq \text{Re}_t \leq 848.9$ ), where  $u'$ ,  $s_L$ ,  $l_t$  and  $\nu$  are the root-mean-square (rms) of velocity fluctuations, laminar flame speed, integral length scale and mixture viscosity respectively. The laminar flame speed for the condition considered is  $s_L = 2.43$  m/s. All turbulent cases are located in the turbulent premixed combustion diagram of [137] as shown in Fig. 5.2. The Damköhler number  $\text{Da} = s_L^2 l_t / u' \nu$  and further information concerning all simulated cases are gathered in Table 5.1. In this table,  $\eta$  denotes the Kolmogorov length scale,  $\tau_f$  is the characteristic time of turbulence,  $\text{Ka}$  is the Karlovitz number. It is observed that the cases lie in the wrinkled or corrugated flamelet regimes. However, the reader should keep in mind that the current project considers the ignition process, not an established flame.

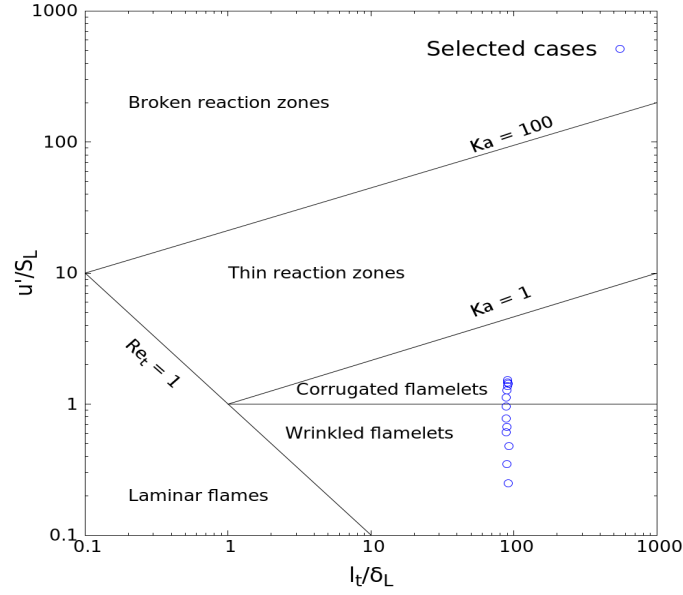


FIGURE 5.2. All the considered cases in the Borghi-Peters turbulent premixed combustion diagram [137].

TABLE 5.1. Initial turbulence parameters for all simulated cases.

Cases	$u'/s_L$	$l_t$ (mm)	$\tau_f$ (ms)	$Re_t$	Da	Ka	$\eta$ (mm)
1	0.25	0.902	0.99	22.8	363.8	0.013	0.07
2	0.35	1.293	1.01	45.6	256.6	0.026	0.06
3	0.48	1.727	1.00	82.1	196.3	0.046	0.052
4	0.61	2.213	0.99	136.2	144.8	0.081	0.045
5	0.67	2.442	1.00	164.9	131.9	0.097	0.043
6	0.78	2.860	1.00	224.8	114.1	0.131	0.038
7	0.96	3.387	0.97	327.7	93.0	0.195	0.036
8	1.13	4.057	0.95	462	78.4	0.274	0.033
9	1.28	4.323	0.95	557.7	70.4	0.335	0.031
10	1.37	4.914	0.99	678.5	66.1	0.394	0.03
11	1.43	5.199	1.01	749.3	64.7	0.423	0.03
12	1.47	5.364	1.01	794.6	61.9	0.455	0.029
13	1.53	5.505	1.00	848.9	59.8	0.487	0.029



TABLE 5.2. Really obtained  $Re_t$  for all runs of all simulated cases.

Runs	C1	C2	C3	C4	C5	C6	C7	C8	C9	C10	C11	C12	C13
1	22.8	45.6	82.1	136.2	164.9	224.8	327.7	462.0	557.7	678.5	749.3	794.6	848.9
2	23.1	43.3	79.7	132.3	161.9	216.1	323.7	479.8	592.3	658.5	708.2	795.6	858.0
3	22.6	44.9	80.2	128.5	162.3	220.5	336.7	475.3	613.9	681.1	739.8	786.7	846.4
4	23.0	44.5	77.6	134.9	160.0	216.8	322.3	446.9	573.8	694.1	696.0	789.6	856.8
5	21.5	45.7	79.3	131.7	162.0	214.3	327.3	459.6	568.5	641.1	736.1	776.4	828.0
6	23.9	45.6	80.3	133.8	164.6	226.6	333.9	477.2	565.6	675.3	722.5	780.7	848.6
7	23.5	44.1	78.5	132.3	166.3	209.2	333.1	475.7	595.1	669.8	720.5	787.1	823.9
8	23.4	43.9	78.2	137.4	168.2	219.5	329.7	475.3	580.9	673.6	701.2	797.3	801.1
9	22.8	44.4	81.9	137.4	166.3	221.2	332.7	452.6	588.4	674.2	693.9	790.2	814.5
10	22.6	45.7	78.7	133.1	162.8	217.7	323.7	466.7	577.4	666.1	738.1	799.8	840.0
11	22.6	44.4	81.5	136.0	162.3	214.0	336.4	450.1	572.7	683.0	733.2	754.6	857.0
12	22.8	44.8	82.0	135.1	163.4	222.4	342.0	466.8	575.0	680.0	713.9	759.9	832.5
13	23.8	43.4	80.4	131.9	163.2	216.3	338.5	468.8	606.2	674.4	756.0	799.6	836.9
14	22.7	44.7	79.1	137.7	164.1	220.0	333.8	472.7	577.2	677.4	746.1	798.0	826.5
15	22.8	43.4	81.2	139.2	161.8	209.2	335.6	465.2	557.2	641.1	742.2	778.8	850.1

To obtain statistically meaningful results, an average over a sufficient number of independent realizations is needed, as already discussed for instance in [174]. For this reason, fifteen realizations have been finally considered for those turbulence intensities. Since a random number generator is involved, each DNS is associated with the same global properties of turbulence (spectrum, correlations, fluctuations...) but corresponds to a different initial condition in space, and thus to a different realization. Finally, this study relies on  $13 \times 15$  independent DNS runs in two dimensions, complemented by selected three-dimensional simulations. As shown in Table 5.2, the really obtained integral-scale Reynolds number  $Re_t$  for all those fifteen realizations of all cases have been checked, and show slight variations around the targeted values.

### 5.2.3 Postprocessing and particle tracking

There are many criterias with which the auto- and/or hotspot-ignition delay,  $\tau$ , of a flammable mixture can be defined: for instance based on the moment of fastest temper-

ature rise, fastest gas expansion, fastest pressure rise, fastest reaction rate rise, fastest rise in a given species [175, 176]... All these definitions have convincing justifications depending on the particular focus of the study, although a disparity of up to 20% in the obtained delay times might be observed [173]. When considering detailed chemistry simulations, the ignition delay computed as the time of fastest temperature rise is often recommended for simple kinetic systems like hydrogen [173] and is used systematically in the present study. If ignition does not occur within 5 ms and the peak temperature is decreasing, the case is classified as misfire and the simulation is stopped.

In previous studies tracking a premixed flame (e.g., [166]), the position of a flame particle vs. time is typically described by,

$$\frac{d\mathbf{x}^p(t)}{dt} = \mathbf{u}(\mathbf{x}^p(t), t) + S_d(\mathbf{x}^p(t), t)\mathbf{n}, \quad (5.2)$$

where  $\mathbf{x}^p(t)$  is the flame particle position,  $\mathbf{u}(\mathbf{x}^p(t), t)$  is the flow velocity at position  $\mathbf{x}^p(t)$ ,  $S_d(\mathbf{x}^p(t), t)$  is the local displacement speed of the flame isosurface with  $\mathbf{n}$  being the unit vector normal to the flame front.

However, in the present study, the “ignition spot” (and not the surface of a burning flame) is the target considered for tracking. This ignition spot is defined as the Lagrangian fluid particle that ignites first within the computational domain, in case of successful ignition. The local movement of this ignition spot does not correspond to the propagation of a flame front. Though a flame front would later develop, we are only interested in the initial (ignition) phase, before the establishment of any flame. Thus, instead of Eq. 5.2, tracking corresponds in the present case simply to,

$$\frac{d\mathbf{x}^p(t)}{dt} = \mathbf{u}(\mathbf{x}^p(t), t), \quad (5.3)$$

as would be the case for a non-reacting flow. For the tracking algorithm, the initial position of

the later ignition spot is required, but it is at first unknown. This is why the DNS simulations used for tracking purposes are repeated twice with exactly the same initial turbulence. The first DNS simulation delivers the overall ignition delay  $\tau$  and the position at which ignition takes place. During this first simulation, the Lagrangian pathlines of massless flow tracers placed at all grid points within the hot kernel or at a distance smaller than  $0.5R_0$  from its initial boundary are tracked using standard tools implemented in DINO. Considering the large number of such points, only the starting position (at  $t = 0$ ) and the current position (always overwritten) of the corresponding pathlines are kept in memory.

Using this approach, at the end of the first simulation, the initial position of the ignition spot (in a purely Lagrangian sense, Eq. 5.3) is known. Now, in the second DNS (with exactly the same field of turbulence), only the history of this specific point is tracked in time, now storing at each time-step of the DNS all parameters needed for the later analysis.

For cases that do not ignite (misfire), the initial candidate point which will lead to the highest temperature at the final simulation time is tracked using again the previous technique. Finally, both for cases leading to successful ignition or to misfire, all the relevant quantities (composition, temperature...) are stored along these trajectories in space and time for a later analysis.

### 5.3 Numerical results and discussion

First, results in the laminar regime are discussed and an ignition chart involving critical ignition parameters in the absence of turbulence is derived. Then, by introducing turbulent fluctuations in the domain, the influence of turbulence intensity is discussed. Results are presented in a statistical manner towards characterizing successful ignition (or misfire) events relevant to safety issues. Finally, the underlying mechanism leading to successful ignition is analyzed by tracking the ignition spot in a Lagrangian frame.

### 5.3.1 Ignition/misfire events under laminar conditions

DNS in laminar conditions have been carried out for a wide range of initial hotspot temperatures ( $910 \leq T_0 \leq 1500$  K, for homogenous zero-dimensional cases *S0D* to three-dimensional spherical hotspots, *S3D*) and kernel radius ( $0.2 \leq R_0 \leq 3.0$  mm, for two-dimensional circular hotspots, *S2D*). In Fig. 5.3(a), the ignition induction time  $\tau$  is plotted as a function of  $T_0$ . The induction times are found to decrease strongly with increasing initial mixture temperature. This result is expected in zero-dimensional cases since the ignition delay in such a configuration is governed only by the rate-limiting elementary reactions [177]. Strong competition between the chain branching and chain terminating reactions at higher temperatures leads to earlier ignition. With the other setups, a fixed half-width (*S1D*) or hotspot radius (*S2D, S3D*) of  $R_0 = 1.0$  mm is used. From Fig. 5.3(a), it is obvious that all these cases show the same ignition delay at high temperatures. However, the critical temperature (denoted hereafter as  $T_{0,c@R_0=1mm}$ ) for successful ignition is larger in *S2D* and in *S3D* than in *S1D* case; and that in *S1D* case is larger than for *S0D* case. The different critical temperature between *S0D* and *S1D* is due to heat diffusion to the cold surroundings in *S1D* case, which does not exist in *S0D* and obviously impacts noticeably ignition delay. The difference between *S1D*, *S2D*, and *S3D* cases is due to the associated change in the surface-to-volume ratio of the hot initial region. However, for sufficiently large values of  $T_0$  and  $R_0$ , laminar ignition delays collapse together for all setups.

The variation of ignition delay with mixture equivalence ratio  $\Phi$  for three initial temperatures ( $T_0 = 950, 1000, \text{ and } 1100$  K) for setup *S0D* is shown in Fig. 5.3(b). Unlike the strong dependence of  $\tau$  on  $T_0$ , there is no striking effect of  $\Phi$  on  $\tau$ , which is consistent with experimental findings [146]. At higher temperature (1100 K), ignition is very slightly faster for mixtures approaching stoichiometry from below. At lower temperatures (e.g., 950 K), the ignition delay first drops noticeably on the lean side before rising steadily till stoichiometry.

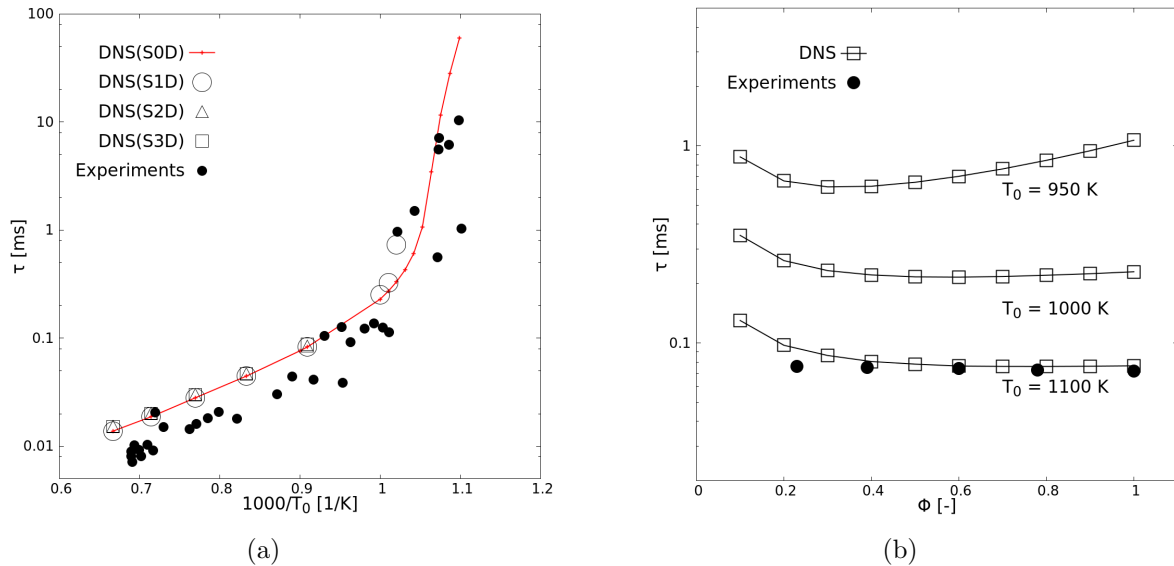


FIGURE 5.3. Ignition delay ( $\tau$ ) versus (a) initial temperature  $T_0$  for  $\Phi = 1.0$  (and  $R_0 = 1$  mm for setups  $S1D$ ,  $S2D$ ,  $S3D$ ) and (b) mixture equivalence ratio ( $0.1 \leq \Phi \leq 1.0$  for setup  $S0D$ ) of  $H_2$ -air mixtures under laminar conditions, with corresponding experimental data from the literature [146, 178].

As a whole, clear variations in ignition induction times across  $\Phi$  are more visible at lower temperature values.

Experimental self-ignition delay data from the literatures [146, 178] for different  $T_0$  and  $\Phi$  within the limits considered in the simulations have been included as well in Fig. 5.3 for setup  $S0D$ . Note that for the experimental data, different groups used different criteria to define ignition. Therefore, direct comparisons are more difficult. Nevertheless, this figure shows that the numerical predictions and experimental data are in good agreement over the whole range of considered conditions. Since the ignition delay is purely kinetically controlled in homogeneous systems, the suitability of the employed reaction mechanism is confirmed as well by this study.

In Fig. 5.4, the dependence of the ignition delay  $\tau$  on the hotspot radius  $R_0$  for setup  $S2D$  is plotted. The minimum hotspot radius needed at a given hotspot temperature  $T_0$  to

ignite the pre-mixture successfully is denoted here as the critical radius  $R_{0,c@T_0}$ . Starting from this critical radius, the hotspot-ignition delay first decreases rapidly with increasing initial size of the hotspot (via  $R_0$ ), before becoming constant for a sufficiently large value of  $R_0$ . It is indeed expected that the ignition delay will not change when radius  $R_0$  is large enough, because at such condition the ignition delay is purely governed by the rate-limiting elementary reactions [177], leading to conditions similar to the zero-dimensional case. A hot region with a radius smaller than the critical radius  $R_{0,c}$  for a given  $T_0$  value does not lead eventually to a stable flame, since it does not harbor enough energy to trigger the chain reactions and compensate for heat loss to the surroundings. When radius  $R_0$  is larger than the critical radius  $R_{0,c@T_0}$ , the ignition delay is shorter for higher hotspot temperature. The relationship between ignition delay  $\tau$  and hotspot temperature  $T_0$  at constant radius  $R_0$  is indirectly confirmed in Fig. 5.4.

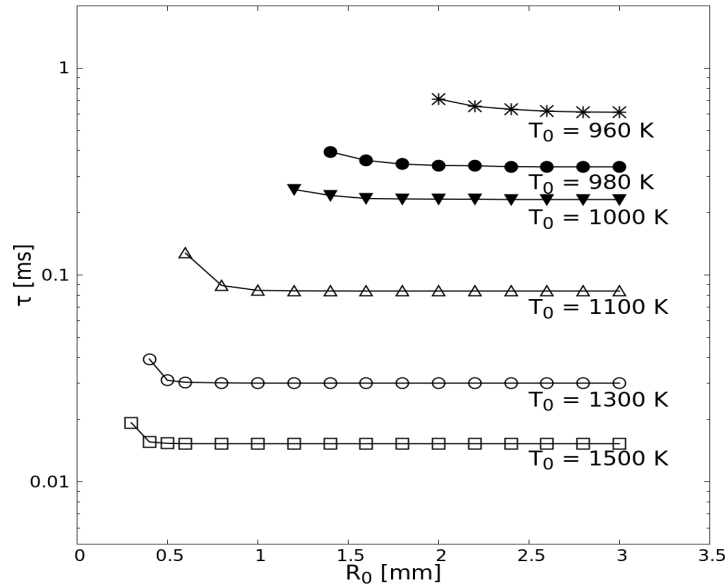


FIGURE 5.4. Hotspot ignition delay versus initial radius of hot kernel  $R_0$  for stoichiometric  $H_2$ -air mixtures in setup *S2D*.

As discussed above, there is a critical temperature  $T_{0,c@R_0}$  and a critical radius  $R_{0,c@T_0}$

corresponding to the limit case for successful ignition. The entire spectrum of  $(T_0, R_0)$  combinations that lead to a successful ignition or misfired event for laminar, stoichiometric hydrogen-air pre-mixtures are plotted in Fig. 5.5. This ignition diagram shows successful ignition with circles and misfires with dots. A boundary curve separating ignition from misfire is shown in black. For this purpose, small variations in  $R_0$  down to 0.05 mm have been considered in order to obtain a better resolution around the ignition/misfire interface. Now combining Fig. 5.3(a) and Fig. 5.4, it is concluded that the ignition delay will decrease as the sample case moves from the lower boundary curve to the top side of the diagram and first rapidly decrease, then keep constant as the case moves from the left boundary curve to the right side of the diagram.

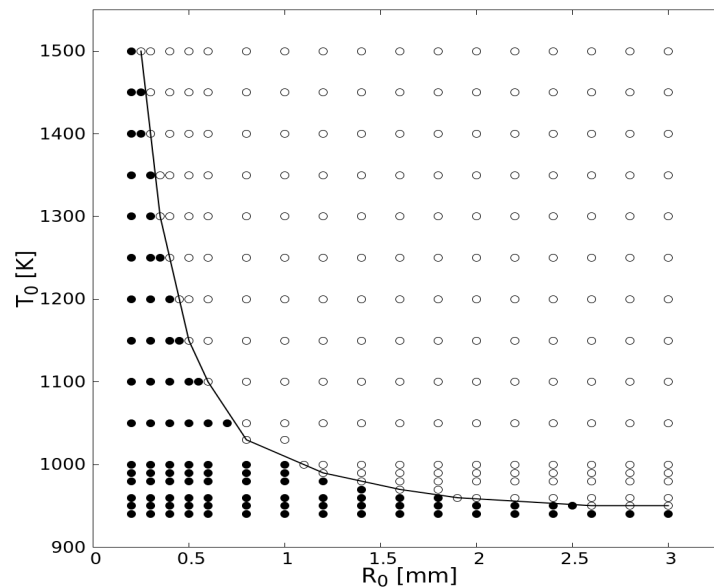


FIGURE 5.5. Hotspot-induced ignition diagram as a function of  $(T_0, R_0)$  for stoichiometric  $H_2$ -air mixtures under laminar conditions in setup *S2D*. Successful ignition is shown with circle, misfire with dot.

For what follows, a single point ( $T_0 = 1000$  K,  $R_0 = 1.2$  mm) near the boundary curve at the ignition side of Fig. 5.5 has been chosen to check the impact of turbulence on ignition

probability and ignition delay.

### 5.3.2 Ignition or misfire events under turbulent conditions

Adding now time-decaying isotropic turbulence at various turbulence intensities, the influence of turbulence on the probability of hotspot-ignition events for premixed hydrogen-air mixtures can be quantified. As mentioned in the previous section, the hotspot is chosen with temperature  $T_0 = 1000$  K and radius  $R_0 = 1.2$  mm. This size is much larger than the Kolmogorov scale for all cases considered.

The typical structure of the reaction zone is shown in Fig. 5.6, where the temperature fields are displayed at three different time instances for two selected realizations from Case 6 ( $u'/s_L = 0.78$ ) and Case 8 ( $u'/s_L = 1.13$ ), respectively. The impact of turbulence on the initially laminar kernel is very clear. In the first scenario (Fig. 5.6 - left column), the turbulence intensity is relatively mild. A smooth and quite homogeneous increase in heat release rate and consequently temperature is observed, resulting ultimately in a successful ignition event. In the second scenario (Fig. 5.6 - right column), it is a more hostile turbulent environment whose direct impact on the initial mixture leads to a misfire. Here, the turbulence intensity is considerably higher, resulting in enhanced mixing and diffusion of hot pockets within the surrounding cold mixture. The maximum temperature in the domain drops from 1000 K to well below 600 K with increasing time as the turbulence increasingly wrinkles the kernel. In this case, transport supersedes chemical reactions, ultimately leading to a complete quenching of the reactions. Remember that here, there are no initial temperature fluctuations in the hot region, which, if present, could have enabled the hot pockets to ignite earlier [179–181].

For a given turbulence intensity, each of the simulated turbulent cases has been finally repeated fifteen times, corresponding to independent realizations for a fixed value of  $u'/s_L$ .



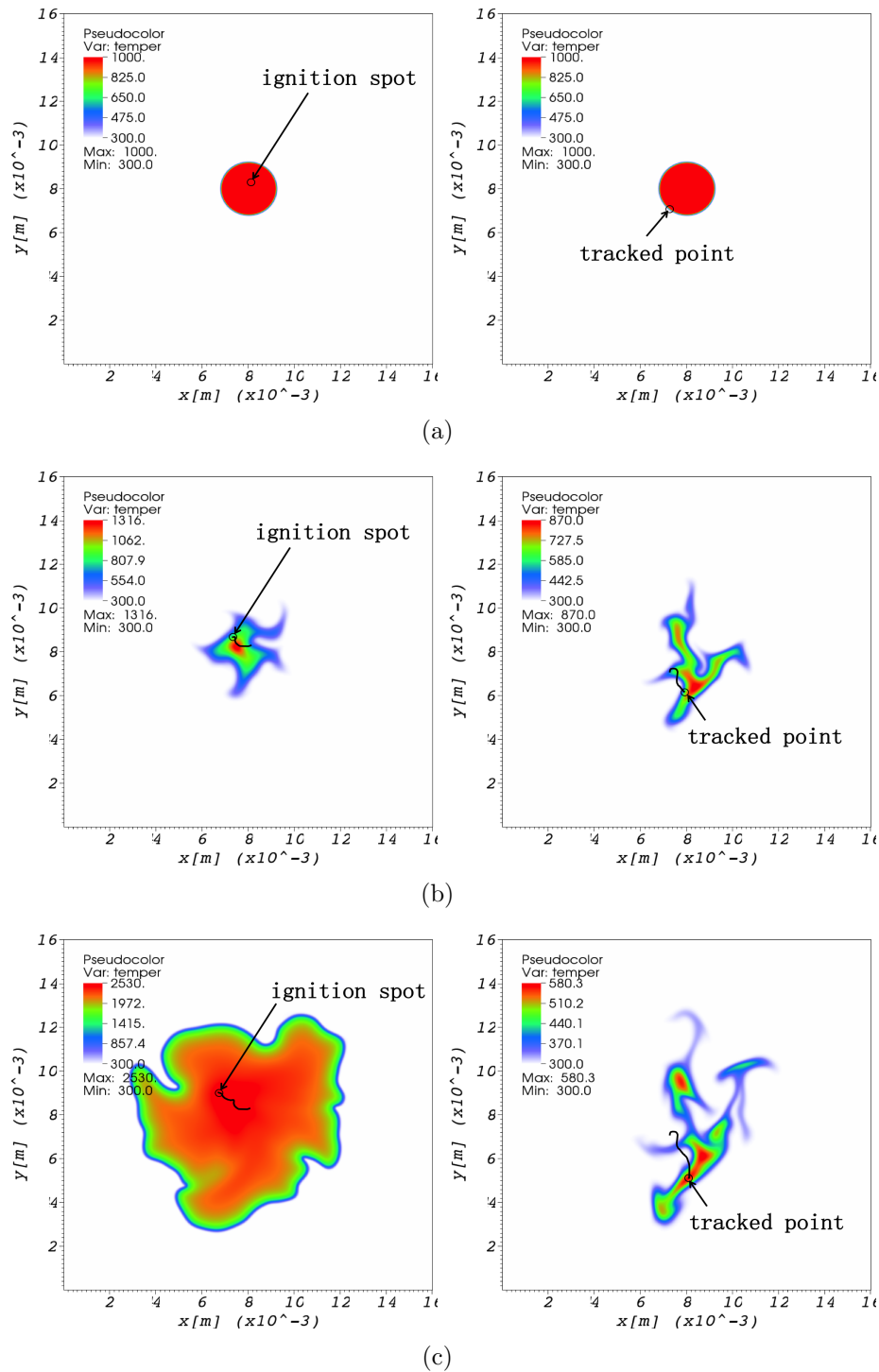


FIGURE 5.6. Exemplary temporal evolution of the temperature field during a successful (left column:  $u'/s_L = 0.78$ ) and misfire (right column:  $u'/s_L = 1.13$ ) event in a hotspot-induced ignition simulation of stoichiometric  $\text{H}_2$ -air pre-mixtures under turbulent conditions for  $T_0 = 1000$  K and  $R_0 = 1.2$  mm. (a)  $t/\tau_f = 0.0$ , (b)  $t/\tau_f = 0.3$  and (c)  $t/\tau_f = 0.6$ . The color scale is always a min-max scale and is therefore different for each subfigure.

The obtained ignition delays are listed in Table 5.3 for nine from the 13 cases presented in Table 5.1, selected to illustrate the typical trend in ignition delay under the influence of increasing turbulence stirring from left to right. Also included in Table 5.3 is the mean value of the ignition delay for the fifteen realizations. Note that this mean is obtained only from all successful ignition events. For these initial conditions, the corresponding 2D laminar case will always ignite at  $\tau_0 = 0.259$  ms, which is hereby taken as a reference for comparisons.

TABLE 5.3. Hotspot ignition times (in ms) of atmospheric, stoichiometric H<sub>2</sub>-air mixtures with initially  $T_0 = 1000$  K,  $R_0 = 1.2$  mm for nine of the thirteen different turbulent conditions. Fifteen realizations are presented for each turbulence intensity. Entries with a hyphen (–) refer to a misfire event.

Cases	1	3	4	6	8	9	10	11	13
Run 1	0.264	0.278	0.298	0.304	–	–	–	–	–
Run 2	0.268	0.273	0.298	0.343	0.354	–	–	–	–
Run 3	0.267	0.283	0.284	0.314	0.314	–	–	–	–
Run 4	0.267	0.323	0.279	0.293	–	–	–	–	–
Run 5	0.268	0.278	0.283	–	–	–	–	–	–
Run 6	0.267	0.279	0.302	0.279	0.342	–	–	–	–
Run 7	0.268	0.269	0.323	–	–	–	–	0.369	–
Run 8	0.263	0.273	–	0.289	–	–	–	–	–
Run 9	0.264	0.278	0.288	0.648	–	–	–	–	–
Run 10	0.264	0.283	0.303	0.287	–	–	–	–	–
Run 11	0.267	0.268	0.283	–	–	–	0.324	–	–
Run 12	0.269	0.268	0.299	0.278	0.313	–	–	–	–
Run 13	0.264	0.278	0.279	0.304	–	0.427	–	–	–
Run 14	0.264	0.278	0.334	–	–	–	–	–	–
Run 15	0.268	0.274	0.274	–	–	–	–	–	–
Average	0.266	0.279	0.295	0.334	0.331	0.427	0.324	0.369	–

By checking the results in Table 5.3, the dependence of hotspot-induced ignition delay  $\tau$  and ignition probability  $P_i$  on the increasing turbulence intensity is obtained as in Fig. 5.7. In these 15 realizations, when turbulence intensity is lower than 0.484 (corresponding to  $Re_t \leq 82.1$ , Cases 1 to 3), all runs are leading to successful ignition. Increasing further turbulence intensity, ignition is not always observed any more; for Case 13 (corresponding to  $Re_t = 848.9$ ), no ignition is observed at all. It is interesting to see that the ignition delay in all turbulent realizations is longer than the laminar ignition delay  $\tau_0 = 0.259$  ms under

same initial conditions (except turbulence), without exception. This confirms the school of thought that turbulence alone delays ignition of flammable mixtures compared to the corresponding case under laminar conditions, and never the other way round. However, this applies obviously only to cases with fully homogeneous initial conditions; the picture might be far more complicated when adding for instance inhomogeneities in dilution or equivalence ratio.

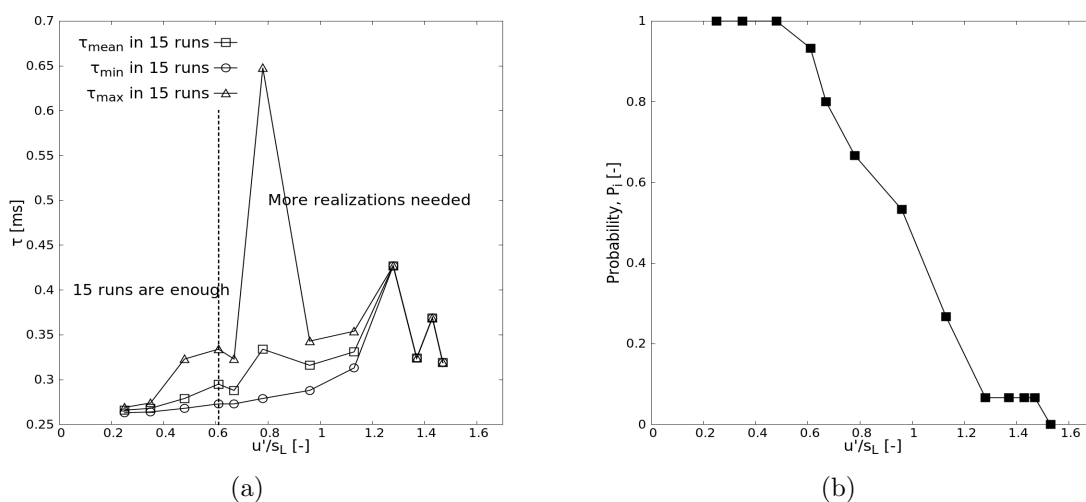


FIGURE 5.7. Hotspot-induced ignition: (a) ignition delay  $\tau_{mean}$  and (b) ignition probability,  $P_i$  versus turbulence intensity ( $u'/s_L$ ) of atmospheric stoichiometric  $H_2$ -air pre-mixtures computed for  $T_0 = 1000$  K,  $R_0 = 1.2$  mm.

It is obvious from Fig. 5.7(b) that the probability of successful ignition is decreasing monotonically with the increasing turbulence intensity, from 1 (always ignites, for laminar conditions) to 0 (never ignites, at very high turbulence intensity). Starting first with Case 9, at most one successful ignition event happens in all 15 realizations; the "mean" value for ignition delay is then a single value, and cannot be used for any statistics. At very high turbulence intensity, more realizations would be needed to obtain a statistical mean value of the ignition delay. This would also smooth out the probability curve. As shown

in Fig. 5.7(a), when  $u'/s_L > 0.61$ , the number of statistical samples becomes insufficient to calculate a proper mean ignition delay with a sufficient accuracy. Starting with Case 4, the mean ignition delay starts to oscillate around increasing values as the turbulence intensity increases. This is an indication that for Case 4 upwards, more realizations would be needed. Nonetheless, the monotonic increase of the ignition delay with turbulence intensity can still be guessed, and is clearer when looking at the shortest ignition time required in fifteen realizations, at least for those cases with  $u'/s_L \leq 1.28$ .

Since these results have been obtained in 2D DNS, the possible impact of three-dimensional features should be checked once again. For this purpose, several 3D runs have been simulated with hotspot radius at  $R_0 = 1.2$  mm and  $T_0 = 1100$  K. This slightly higher temperature ensures that the 2D results deliver a nearly constant ignition delay for multiple realizations, even at high turbulence. For such conditions, the possible impact of three-dimensional features on ignition can be investigated separately from the effect of turbulence. As shown in Fig. 5.8, the ignition delay for S2D and S3D cases are completely identical at low turbulence intensity. This similarity between 2D and 3D is expected since the ignition delay  $\tau$  is for these conditions much lower than the characteristic time scale of turbulence  $\tau_f$ , which means that the rate-limiting process is only chemical reaction; for such conditions, 3D turbulent features should show only little effect [182]. However, the same comparison reveals visible differences in the high-turbulence range, starting around Case 8. Under such conditions, the ignition delay in 3D is found to be systematically longer than that in 2D, and increases toward values close to  $\tau_f$ . This finding supports the idea that the mixing process becomes rate-limiting when the size of the large turbulent eddies (represented by the integral length scale  $l_t$ ) are sufficiently large [182]. In the present case, the corresponding critical ratio between integral length scale and hot spot diameter is  $l_t/(2R_0) \approx 1.7$ . Vortex stretching in 3D strongly increases the scalar dissipation rate compared to 2D [182]. As will

be shown in the next section, faster scalar dissipation rate results in longer time for  $\text{HO}_2$  to accumulate, leading finally to a longer ignition delay. Accordingly, successful ignition becomes less probable, as heat transfer rate is faster in 3D, dissipating the hotspot, as already discussed for instance in [171].

However, since a three-dimensional DNS takes roughly 1000 times as long as the same computation in 2D for the same number of computing cores, statistical studies involving a large number of realizations are still not feasible in 3D. Remembering that the main focus of this work is set on safety applications, this is not a major problem, since 2D DNS always deliver a conservative estimate, overestimating the rapidity and the probability of ignition at high turbulence intensity. Using predictions from 2D DNS, corresponding safety guidelines would be always on the safe side.

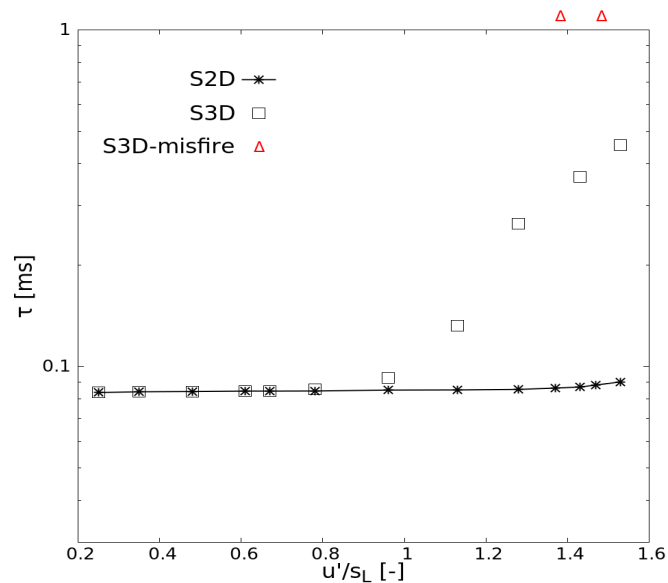


FIGURE 5.8. Hotspot ignition delay  $\tau$  versus turbulence intensity ( $u'/s_L$ ) of atmospheric stoichiometric  $\text{H}_2$ -air pre-mixtures computed for both 2D and 3D configurations. The hot kernel has an initial radius  $R_0 = 1.2$  mm and initial temperature  $T_0 = 1100$  K.

### 5.3.3 Ignition point tracking and analysis

To figure out what controls successful ignition or misfire, the two runs corresponding to Case 6 and to Case 8 already shown in Fig. 5.6 have been analyzed further using Lagrangian tracking. The tracking trajectories have been plotted as black lines in Fig. 5.6.

For Case 6, the ignition point is selected as the point with the highest heat release rate at ignition time. The contribution of heat diffusion, mass diffusion and reaction to the temperature rise in the transport equation for temperature are computed respectively using Einstein summation convention as

$$T'_{\text{heat diffusion}} = \frac{1}{\rho C_p} \frac{\partial}{\partial x_j} \left( \lambda \frac{\partial T}{\partial x_j} \right), \quad (5.4)$$

$$T'_{\text{mass diffusion}} = -\frac{1}{\rho C_p} \frac{\partial T}{\partial x_j} \sum_{k=1}^{N_s} \rho C_{p,k} Y_k V_{k,j}, \quad (5.5)$$

$$T'_{\text{reaction}} = -\frac{1}{\rho C_p} \sum_{k=1}^{N_s} h_k \dot{\omega}_k, \quad (5.6)$$

and are shown for the tracked point in Fig. 5.9(a). Here,  $C_p$ ,  $h_k$ ,  $\dot{\omega}_k$ ,  $\lambda$ ,  $V_{k,j}$  represent the specific heat capacity at constant pressure, specific enthalpy, mass reaction rate, heat diffusion coefficient and  $j$ -th component of the  $k$ -species molecular diffusion velocity, respectively. Variable  $N_s$  denotes the total number of species. The evolution in time of the mass fraction of all radicals and species have also been tracked for the ignition point, and are shown in Fig. 5.9(b).

In Fig. 5.9(a), a standard ignition picture is observed, as discussed in textbooks; temperature rises because of heat release produced by the chemical reactions, competing (successfully in this case) with heat diffusion as dominating sink term. The temperature change associated to mass diffusion is negligibly small in comparison to the other two contributions. By

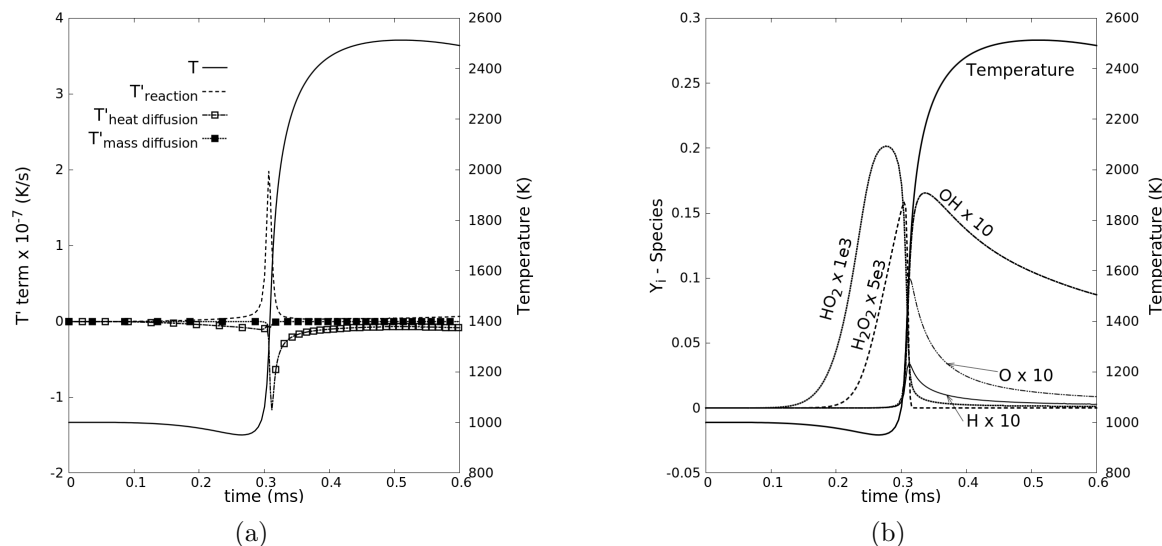


FIGURE 5.9. Temporal evolution of (a) the relevant contributions in the temperature transport equation and (b) the mass fractions of all intermediate species at the ignition point for one realization of Case 6, tracked in a Lagrangian frame, and leading to successful ignition.

checking the evolution of each intermediate species in Fig. 5.9(b), it is interesting to see radicals  $\text{HO}_2$ , then  $\text{H}_2\text{O}_2$ , reach peaks just before the ignition starts, and radicals  $\text{OH}$  and  $\text{O}$  start to gain after  $\text{HO}_2$  and  $\text{H}_2\text{O}_2$  are consumed. As is known, fast production of radical  $\text{OH}$  is the typical characteristics for ignition of hydrogen-air mixtures. It is confirmed that reactive radical  $\text{OH}$  is mostly generated by the chain branching reactions  $\text{HO}_2 + \text{H} = \text{OH} + \text{OH}$ , and  $\text{HO}_2$  is produced by initial reaction  $\text{H} + \text{O}_2 (+\text{M}) = \text{HO}_2 (+\text{M})$ . The chain branching reactions  $\text{H} + \text{O}_2 = \text{OH} + \text{O}$  and  $\text{O} + \text{H}_2 = \text{OH} + \text{H}$  are not the major pathways in generating radical  $\text{OH}$  for the thermodynamic conditions in this study. This finding matches well with [176] and the recent work in [183]. As a conclusion, the local accumulation of radical  $\text{HO}_2$  is the real clue for successful ignition.

As seen from Fig. 5.9, the temperature at the ignition point does not drop too much from the hot initial temperature before ignition, due to the low level of heat diffusion  $T'_{\text{heat diffusion}}$  close to the kernel center under mild turbulent fluctuations. There are two reasons for the

quick rise of  $\text{HO}_2$  in this case: (1) the temperature is high enough for fast initial reactions producing  $\text{HO}_2$ ; (2) the transport of  $\text{HO}_2$  away from this region is slow, due to low turbulence. This statement can be confirmed by comparing with the results in the quenching case (Case 8), as shown in Fig. 5.10.

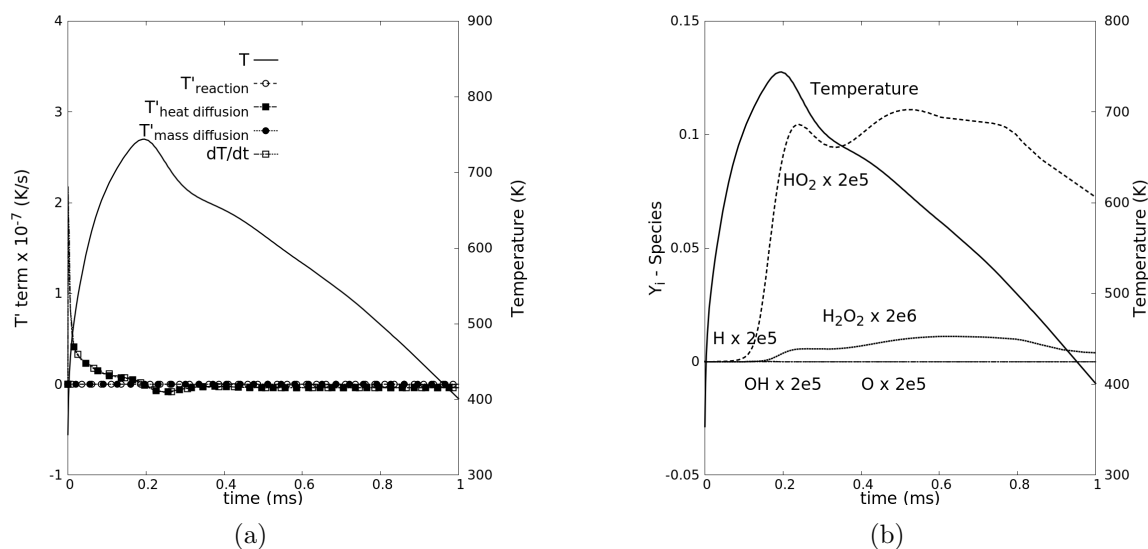


FIGURE 5.10. Temporal evolution of (a) the relevant contributions in the temperature transport equation and (b) the mass fractions of all intermediate species at the point that will reach highest temperature at the end of the simulation for one realization of Case 8, tracked in a Lagrangian frame, and leading to misfire.

For the selected realization in Case 8, as already seen in Fig. 5.6 (right column), the point that will reach maximum temperature at the end of the simulation is not well within the kernel (as in Case 6), but at its boundary; hence, it is initially associated only to an intermediate temperature level, slightly above 350 K. The following temperature rise is largely dominated by heat diffusion from the hot kernel. After this rise in temperature, the radical  $\text{HO}_2$  starts to gain because of initial reaction, leading to peak temperature of almost 750 K, before dropping back. A noticeable production of OH is not observed. The small quantity of  $\text{HO}_2$  initially generated diffuses away due to intensive turbulent fluctuations. To summarize, there is not enough  $\text{HO}_2$  for starting the following chain-branching reactions for



radical OH, and the mixture will not get ignited. Due to the very fast destruction of the hot kernel by intense turbulence, the conditions found within this kernel are even less favorable than at its boundary.

## 5.4 Concluding remarks

A systematic study has been done concerning the probability of successful hotspot-induced ignition of atmospheric H<sub>2</sub>-air pre-mixtures using Direct Numerical Simulations. Besides the slight influence of the mixture equivalence ratio, the ignition probability and ignition induction time are found to be mainly function of the initial hotspot temperature  $T_0$ , hotspot radius  $R_0$ , and turbulence intensity. An ignition diagram has been obtained for laminar conditions, allowing to determine regimes of successful ignition. Starting from the boundary curve in the ignition diagram, the ignition delay decreases as the initial kernel temperature  $T_0$  increases; the ignition delay first decreases, and then keep constant as the hotspot radius  $R_0$  increases. All the spherical kernels with initial  $(T_0, R_0) \leq (T_{0,c}, R_{0,c})$  will lead to misfire, even without any turbulence. The critical combination  $(T_{0,c}, R_{0,c})$  is shown as a separation curve in the ignition diagram. With the increase of turbulence intensity, the probability of successful ignition is decreasing, the ignition induction time is becoming longer. For all turbulent realizations, the ignition delay is always larger than the laminar one, without exception.

The impact of three dimensional features has been checked by several 3D DNS realizations. The importance of the relative scale of ignition delay  $\tau$  compared to the characteristic time scale of turbulence  $\tau_f$  is confirmed. When the ignition delay  $\tau$  is much lower than the characteristic time scale of turbulence  $\tau_f$ , corresponding here to a mild turbulent environment, the ignition delays of the 2D and 3D DNS are similar. At very high turbulence intensity, the ignition delay becomes longer in 3D DNS, and the ignition probability decreases

due to stronger and faster dissipation.

The ignition point has been tracked in a Lagrangian frame to understand the ignition behavior, quantifying the trade-off between transport processes and chemical reactions. Initial reaction  $\text{H} + \text{O}_2 (+\text{M}) = \text{HO}_2 (+\text{M})$  followed by chain-branching reaction  $\text{HO}_2 + \text{H} = \text{OH} + \text{OH}$  are found to be critical for successful ignition at temperatures near 1000 K. When turbulence intensity is low, the mixing of the hotspot with cold surroundings is slow, the temperature around the ignition spot within the kernel remains high enough for the initial reaction to generate enough  $\text{HO}_2$ . The diffusion of  $\text{HO}_2$  to the surroundings is also slow, which results in  $\text{HO}_2$  accumulation at the ignition spot. When  $\text{HO}_2$  reaches a certain level (typically a local mass fraction of the order of  $10^{-4}$  in this study), the chain-branching reaction producing OH becomes intensive, finally leading to successful ignition. When increasing turbulence intensity, the mixing becomes intensive, for both heat and active radicals such as  $\text{HO}_2$ . Then, it becomes more difficult or even impossible to accumulate enough  $\text{HO}_2$  at any specific spot. The probability of successful ignition becomes lower. It may ignite for some realizations, but it will take more time for radicals  $\text{HO}_2$  to reach a sufficient level, leading to longer ignition times, and lowering the probability of a successful ignition.

It is now possible to bring all building blocks of this work together, and consider ignition in a turbulent reacting flow with a complex geometry in the final chapter of this thesis.

# Chapter 6

## Simulations of turbulent reacting flows in complex geometry

### 6.1 General introduction

The ultimate objective of this work is the simulation of turbulent gaseous flows and combustion by DNS in complex geometries, with a particular emphasis on Internal Combustion Engine burning methane. In that case, a safe and reliable ignition is of central importance.

Regarding engine simulations, the geometry is closed. With piston movement (volume changes) and thermodynamic state changes, the thermodynamic pressure will change accordingly. The previous governing equations in Chapter 2 assumed the thermodynamic pressure to be constant. Thus, the following equation is now introduced to compute the change in thermodynamic pressure [184]:

$$\frac{1}{p} \frac{dp}{dt} = \sum \left( \frac{1}{T} \frac{DT}{Dt} + \bar{W} \sum_{k=1}^{N_s} \frac{1}{W_k} \frac{DY_k}{Dt} \right) - \sum dV, \quad (6.1)$$

where  $\bar{W}$  is the mixture mean molecular weight and  $\sum dV$  is the volume change rate.  $D/Dt$  is the material derivative. After considering the change of the thermodynamic pressure, the

temperature equation Eq. 2.3 becomes:

$$\frac{\partial T}{\partial t} = -\frac{1}{\rho C_p} \sum_{k=1}^{N_s} h_k \dot{\omega}_k + R_T + \frac{1}{\rho C_p} \frac{\gamma}{\gamma - 1} \frac{dp}{dt}, \quad (6.2)$$

where  $\gamma$  is the heat capacity ratio. In this way, the pressure and temperature coupling is correctly considered in the governing equations for closed domain.

In the following simulations, Section 6.2 discusses the turbulent hot jet ignition mimicking a pre-chamber/main chamber system; Section 6.3 introduces the simulations in a simplified internal combustion engine geometry; Finally, Section 6.4 discusses simulations in a real, industrial pre-chamber geometry.

## 6.2 Pre-chamber hot jet ignition

### 6.2.1 Introduction

Pre-chamber turbulent hot jet ignition systems are becoming increasingly popular for lean gas engines. The multiple ignition spots initiated by the hot jet promote burning of leaner mixtures in the main chamber, thus increasing thermal and fuel efficiency [5]. A review of pre-chamber hot jet ignition techniques can be found in [185].

To figure out the resulting jet structures and to identify the conditions critical for successful ignition by a hot jet, many experimental and numerical studies have been done in the last decades. It was first found in [186] that the nozzle diameter and the pre-chamber to main chamber volume ratio strongly influence the structure of the jet. Later, Wallesten and Chomiak [187] found that a spark location in the pre-chamber farther away from the orifice promotes ignition in the main chamber. The important influence of the hot jet temperature and speed of mixing on the jet ignition process has been investigated in [188]. Malé et al.

[189] extended the work of [188] with 3D DNS and proved that the jet injection speed and temperature directly govern ignition. Carpio et al. [190] studied numerically the laminar  $\text{H}_2/\text{air}$  jet ignition/extinction. The influence of injection velocity and mixture equivalence ratio on the critical orifice radius (resulting in successful jet ignition) has been discussed. To understand further the ignition mechanism, Ghorbani et al. [191] found that the turbulent jet ignition (ignition probability, ignition delay time, and ignition location) is strongly influenced by the mixing process and the chemical kinetics employed in the numerical simulations. Biswas et al. [192] conducted experiments in a pre-chamber configuration and identified two ignition mechanisms: 1) jet ignition and 2) flame ignition, depending on the relative diameter of the jet orifice compared to the laminar flame thickness. A global Damköhler number was defined; the limiting Damköhler number for a  $\text{CH}_4/\text{air}$  flame is found to be around 140, below which ignition probability is almost 0. To reveal the details of the flow and flame through the orifice, both experiments and Large-Eddy Simulations (LES) were conducted in [193]. It was found that the jet flow is composed of a column of hot products surrounded by an annulus of unburnt pre-chamber gases. An estimate of  $2\delta_L/d$  was proposed to classify the jet ignition ( $2\delta_L/d > 1$ ) and flame ignition ( $2\delta_L/d < 1$ ) cases, where  $\delta_L$  is the laminar flame thickness and  $d$  is the orifice diameter. More recently, Sidey and Mastorakos [194] simplified the practical configuration and studied the strained layer between a reactive mixture and hot combustion products. The ignition time as a function of strain rate and degree of reaction completion in the stream of hot products have been investigated. Qin et al. [195] studied the ignition mechanism in a simplified constant-volume divided-chambers system using Direct numerical simulations (DNS). The effect of pre-chamber hot jet on ignition was divided into chemical effect (involving intermediate radicals), thermal effect (high temperature), or enrichment effect (unburned rich mixture issuing from pre-chamber). Allison et al. [196] investigated the effect of fuel type, orifice diameter and ignition location in the pre-chamber

by experiments and LES and found that the strain rate and effective orifice size determine the local quenching of radical species at the orifice. Wang et al. [197] found that moving the ignition spark farther from the orifice reduces the 1–10% mass fraction burning period. They identified three regions in the hot jet: 1) extinction region; 2) just-ignition region and 3) combustion region. In a follow-up study, Wang et al. [198] studied the effect of pre-chamber syngas reactivity on hot jet ignition and found that incomplete fuel conversion in the orifice results in a lower hot jet temperature. Malé et al. [199] used LES to investigate pre-chamber ignition behavior in a real engine. Three regimes were identified in the main chamber: 1) ignition by hot gas ejection; 2) combustion sustained by hot gas ejection; 3) combustion unsustained by hot gas ejection. These results correspond quite well to the original picture of [186]. Benekos et al. [200] conducted a parametric 2D DNS study on the effects of wall boundary condition, initial temperature and main chamber composition on pre-chamber ignition. It was found that turbulent jet ignition is associated to two characteristic times: one for ignition of the most reactive mixture fraction, and the second one for ignition of all states created through mixing of the pre-chamber gases with the main chamber mixtures.

These previous studies confirm the importance of orifice diameter, spark location, fuel type, and turbulence on ignition of the main chamber mixtures. Additionally, wall heat losses are quite important for the outcome of the ignition process. Since so many different parameters affect the ignition, the central question is still not completely clarified: What is the interplay between all these phenomena during the transient ignition process? As proposed in [192], a global Damköhler number could be used to combine the effect of orifice diameter and turbulence on ignition; this Damköhler number quantifies the competition between turbulent mixing and chemical reactions. However, the connection to other parameters such as spark location, fuel type, pre-chamber mixtures are still unknown. In this study, direct numerical simulations (DNS) have been done in a simplified pre-chamber/ main chamber system with

a systematically reduced C/H/O kinetic mechanism to describe methane/air chemistry. The hot jet characteristics in the orifice and the transient ignition process have been investigated in a detailed manner. The underlying physics determining ignition in different setups are then discussed, with consequences regarding the interplay between the features affecting the transient ignition process. The jet time scales (for cold jet and hot jet), as well as the relative intensities of different jet effects (enrichment effect, chemical effect, and thermal effect) are found to determine the success of the transient ignition process, which is composed of near-orifice local just-ignition and global ignition. Turbulence is found to have different effects on local just-ignition and global ignition. Note that per definition (see [197, 198]) a local, just-ignition event does not necessarily lead to global combustion, though it shows all features of a successful ignition event. Global ignition corresponds to the development of a self-sustained flame in the main chamber.

### 6.2.2 Numerical simulations and configurations

The simulations in this section are also performed using the in-house low-Mach DNS flame solver *DINO* [7]. An implicit Williamson third-order Runge-Kutta time integrator with analytic Jacobian inversion (PyJAC [20]) is employed for temporal integration. The mixture-averaged diffusion coefficients have been used in the transport equations. The methane/air mechanism from [201] has been used, which contains 14 solved and 15 steady-state species with 141 reactions.

The numerical configuration has been set up as shown in Fig. 6.1. The orifice diameter  $d$  is chosen to be comparable to twice of the laminar flame thickness  $\delta_L$  of the pre-chamber mixtures, as shown in Table 6.1. The geometry is resolved by the novel immersed boundary method from [29]. A uniform grid size of  $9.76 \mu\text{m}$  has been used, which is sufficient to resolve correctly the thermal boundary layer and the detailed flame structure (with almost 28 grid

points across the laminar flame thickness), especially in the orifice. The minimal value of  $\delta_L = 0.09$  mm has been calculated for a pressure  $p = 10$  bar for stoichiometric mixtures. The maximum  $\Delta y^+$  value ( $\Delta y^+ = \frac{\Delta y u_\tau}{\nu}$  where  $u_\tau$  is the friction velocity computed at the wall-adjacent node and  $\nu$  is the kinematic viscosity) at the first wall-adjacent node during the jet flow is 0.787. All the boundaries are cold walls with initial temperature of 300 K including isothermal wall condition (written ISOT in Case A - G, Case A3D and B3D in Table 6.1) or adiabatic wall condition (denoted ADIA in Case H in Table 6.1). The initial ambient temperature is also 300K. The initial pressure is atmospheric, as has also been used in the pre-chamber study of [198]. The 2D simplified geometry shown in Fig. 6.1(a) resembles the previous DNS study in [195] with a slightly smaller main chamber volume (volume ratio between pre-chamber and main chamber is 54%), while the 3D geometry shown in Fig. 6.1(b) has a volume ratio of 5% between the pre-chamber and main chamber, which is comparable to a practical gas engine [202]. Detailed dimensions of the 2D and 3D geometries are shown in Fig. 6.1. The choice of these dimensions was dictated by the best possible compromise between numerical feasibility and connection to practical configurations. The differences in dimensions and ratio between 2D and 3D geometries are due to the different objectives: 1) in 2D, to set up fast DNS simulations for a detailed parametric study; in 3D, going toward more realistic conditions for a few cases. Keeping the same orifice diameter, the surface/volume ratio of the 3D orifice is twice of that in the 2D orifice, resulting in more intensive wall heat losses in 3D. The effect of wall heat losses is studied in Section "Radical quenching in orifice". It has to be emphasized that the current study intends to reveal the underlying physicochemical mechanisms related to different parameters affecting the transient ignition process. Even though most of the analysis is based on 2D results, the obtained physicochemical mechanism for transient ignition process is validated finally by 3D simulations, confirming its value for realistic pre-chamber combustion system studies.



Further 3D simulations are currently running.

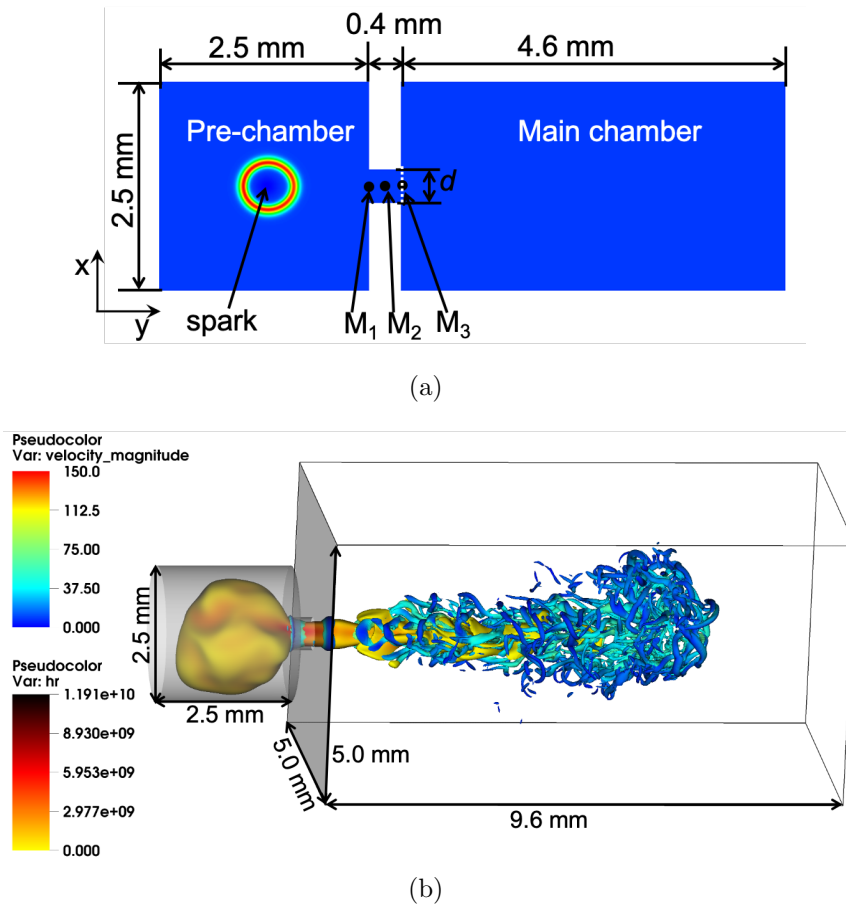


FIGURE 6.1. Schematic of the computational domain: (a) 2D domain showing also the three points  $M_1$ ,  $M_2$ ,  $M_3$  used for a quantitative analysis of the process as well as the location of the orifice outlet used to compute mass fluxes (white dashed line); (b) 3D domain showing the iso-surface of  $Q$ -criterion at  $3 \times 10^{10}$  ( $1/s^2$ ) colored by velocity magnitude and iso-surface of temperature at 800 K colored by heat release rate at  $t = 0.5$  ms.

The spark is numerically modeled using the energy deposition model from [203], where the energy source is modeled as a Gaussian distribution in both time and space:

$$\dot{Q} = \frac{\epsilon}{4\pi^2 \delta_s^3 \delta_t} \exp^{-\frac{1}{2} \left( \frac{r}{\delta_s} \right)^2} \exp^{-\frac{1}{2} \left( \frac{t-t_0}{\delta_t} \right)^2}. \quad (6.3)$$

In the above equation,  $r$  is the radial distance to the spark center,  $t$  is the current time and

$t_0$  is the time instant when the power density function reaches its maximum. The spark is controlled by 3 parameters: the energy deposition  $\epsilon$ ,  $\delta_s = \Delta_s/a$  and  $\delta_t = \Delta_t/a$  where  $\Delta_s$ ,  $\Delta_t$  and  $a$  are characteristic size, time duration of the spark and deposited coefficient, respectively. The value  $a = 4\sqrt{\ln(10)}$  is chosen so that 98% of the deposited energy is within the domain  $\Delta_s^3 \cdot \Delta_t$  [203]. For 2D simulations, the spark distribution equation has been adapted accordingly to

$$\dot{Q} = \frac{\epsilon}{(2\pi)^{3/2} \delta_s^2 \delta_t} \exp^{-\frac{1}{2} \left(\frac{r}{\delta_s}\right)^2} \exp^{-\frac{1}{2} \left(\frac{t-t_0}{\delta_t}\right)^2}. \quad (6.4)$$

In this study the spark parameters are chosen as:  $\Delta_s = 0.6$  mm,  $\Delta_t = 0.05$  ms,  $t_0 = 0.05$  ms and  $\epsilon = 0.12$  mJ, ensuring a stable ignition of the pre-chamber for all conditions considered, and also avoiding local super-adiabatic temperature at the spark.

TABLE 6.1. The investigated DNS cases

Case	$\phi$ (pre-chamber)	$\phi$ (main chamber)	$d$ (mm)	$u'/s_L$	$\tau_f$ ( $\mu$ s)	$\delta_L$ (mm)	$\eta$ ( $\mu$ m)	spark location (mm)	wall cond.
A	1.0	0.5	0.4	0	-	0.24	N/A	(1.25,1.25)	ISOT
B	1.0	0.5	0.4	0	-	0.24	N/A	(1.25,0.75)	ISOT
C	0.7	0.5	0.4	0	-	0.28	N/A	(1.25,1.25)	ISOT
D	0.7	0.5	0.6	0	-	0.28	N/A	(1.25,1.25)	ISOT
E	0.7	0.7	0.4	0	-	0.28	N/A	(1.25,1.25)	ISOT
F	0.7	0.5	0.4	41.6	5.12	0.28	13.3	(1.25,1.25)	ISOT
G	0.7	0.7	0.4	15.1	5.14	0.28	17.0	(1.25,1.25)	ISOT
H	1.0	0.5	0.4	0	-	0.24	N/A	(1.25,1.25)	ADIA
A3D	1.0	0.5	0.4	0	-	0.24	N/A	(1.25,1.25,1.25)	ISOT
B3D	1.0	0.5	0.4	21.9	12.87	0.24	14.3	(1.25,1.25,1.25)	ISOT

The details of the investigated cases in this study are shown in Table 6.1, where  $\phi$  is the equivalence ratio of the mixture,  $u'$  is the rms velocity of the initial turbulence,  $\tau_f$  is the characteristic time of turbulence,  $s_L$  is the laminar flame speed of the pre-chamber mixtures,  $\delta_L$  is laminar flame thickness, and  $\eta$  is the Kolmogorov length scale (larger than the grid resolution for turbulent cases, 9.76  $\mu$ m). The turbulence parameters correspond to the initial

turbulence. The initial  $\phi$  in the orifice is a step function from pre-chamber to main-chamber. As is seen,  $2\delta_L/d > 1$  in Cases A - C and Cases E - G. They should thus correspond to the "jet ignition"-regime according to [193], while Case D corresponds to the "flame ignition"-regime. In Table 6.1, Case A is a reference configuration to investigate the effect of different parameters; Case B is chosen to study the effect of a different spark location; Case C is setup to study the effect of varying pre-chamber mixture equivalence ratio  $\phi$ ; Case D is chosen to study the effect of orifice diameter, compared to Case C; Case E is retained to study the effect of main chamber mixture equivalence ratio  $\phi$ , compared to Case C; by comparison between Case C and Case F, as well as between Case E and Case G, the effect of turbulence is revealed; Case H is chosen to study the effect of the wall condition; Finally, Case A3D and Case B3D are used to check the 3D turbulence effect, and also to validate the 2D results. The normalized power spectrum densities of the initial turbulence as a function of frequency are compared for Case G and Case B3D in Fig. 6.2, together with the theoretical slope of  $-5/3$ . As expected, differences are seen, but the spectra are sufficiently similar to allow for meaningful comparisons.

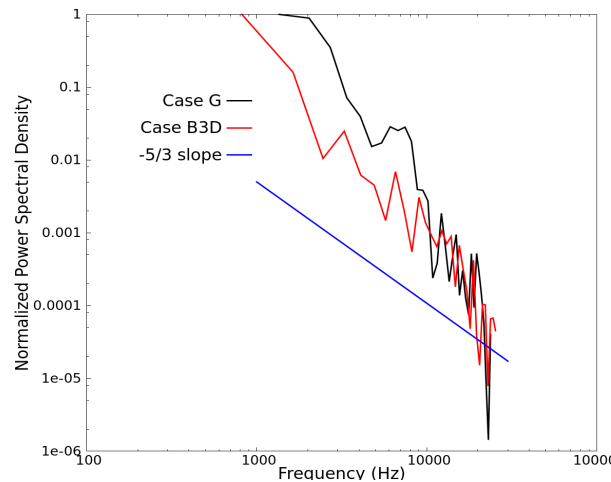


FIGURE 6.2. Comparison of the normalized power spectrum density of the initial turbulence as a function of frequency in Case G and Case B3D.

As mentioned previously, a low-Mach solver has been used for all simulations. Though no strict rule applies, it is commonly accepted that such solvers should be used for  $Ma \leq 0.3$ . For this reason, the Mach number has been systematically monitored. The peak Mach number has been measured as  $Ma = 0.78$  (in Case A3D), close to the outlet of the orifice. However, the total time duration showing local values of  $Ma > 0.3$  never exceeded  $60 \mu s$ , which is a very short time compared to the whole simulation; the high-Mach region was limited to a very small area close to the orifice; no instabilities were observed on any fields. For all those reasons, using a low-Mach solver to keep acceptable numerical costs is considered acceptable for this study.

### 6.2.3 Results and Discussion

The following results and discussion are first presented for 2D parametric studies (Case A - H). In Section "3D validation", 3D results will be presented and analyzed to validate the conclusions obtained by 2D studies.

#### Phases identification

To clearly identify and distinguish different ignition and combustion phases in the pre-chamber/main chamber systems, the time evolution of the progress variable  $\bar{c}$  based on  $c = Y_{CO_2} + Y_{H_2O}$  [204] at three points in the orifice ( $M_1$ ,  $M_2$  and  $M_3$  shown in Fig. 6.1) has been plotted in Fig. 6.3, exemplarily for Case A. The local value of  $\bar{c}$  at each point is obtained by normalizing  $c$  between 0 and 1 using the spatially and temporally peak value in the whole domain over time. After a detailed analysis, four phases have been identified during ignition for all configurations. For a quantitative analysis, these different phases have

been finally defined as follows:

$$\text{Phase} = \begin{cases} 1 & \text{if } \bar{c}_{M_1} < 1 \times 10^{-5} \\ 2 & \text{if } \bar{c}_{M_1} \geq 1 \times 10^{-5} \text{ and } d\bar{c}_{M_3}/dt \geq 0 \text{ and } \bar{c}_{M_1} > \bar{c}_{M_3} \\ 4 & \text{if } \bar{c}_{M_3} > \bar{c}_{M_2} > \bar{c}_{M_1} \text{ and } d\bar{c}_{M_1}/dt \geq 0 \\ 3 & \text{otherwise} \end{cases}$$

under the condition that phase 1, 2, 3, and 4 are in sequence and continuous.

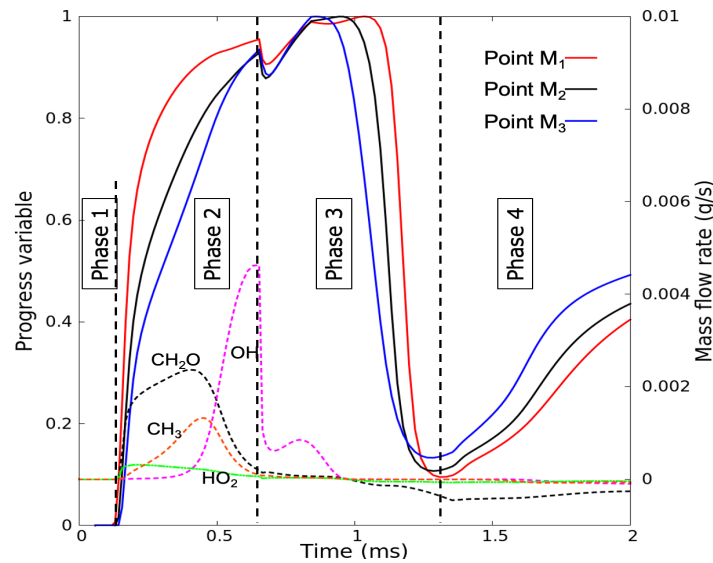


FIGURE 6.3. Time evolution of the normalized progress variable  $\bar{c}$  at point  $M_1$ ,  $M_2$  and  $M_3$  (solid lines) and mass flow rate of  $\text{CH}_2\text{O}$ ,  $\text{CH}_3$ ,  $\text{HO}_2$  and  $\text{OH}$  (dashed lines) through the orifice outlet for Case A. A positive mass flux is from pre-chamber to main chamber.

To analyze in more detail these four characteristic phases, the fields of velocity, OH mass fraction and temperature have been plotted in Fig. 6.4. Figure 6.4(a) shows the velocity field at 0.13 ms, corresponding to the end of Phase 1 (see again Fig. 6.3). Figure 6.4(b), Fig. 6.4(c) and Fig. 6.4(d) present the OH mass fraction distribution at 0.58 ms, 1.0 ms and 1.7 ms, corresponding to Phase 2, 3, and 4, respectively.

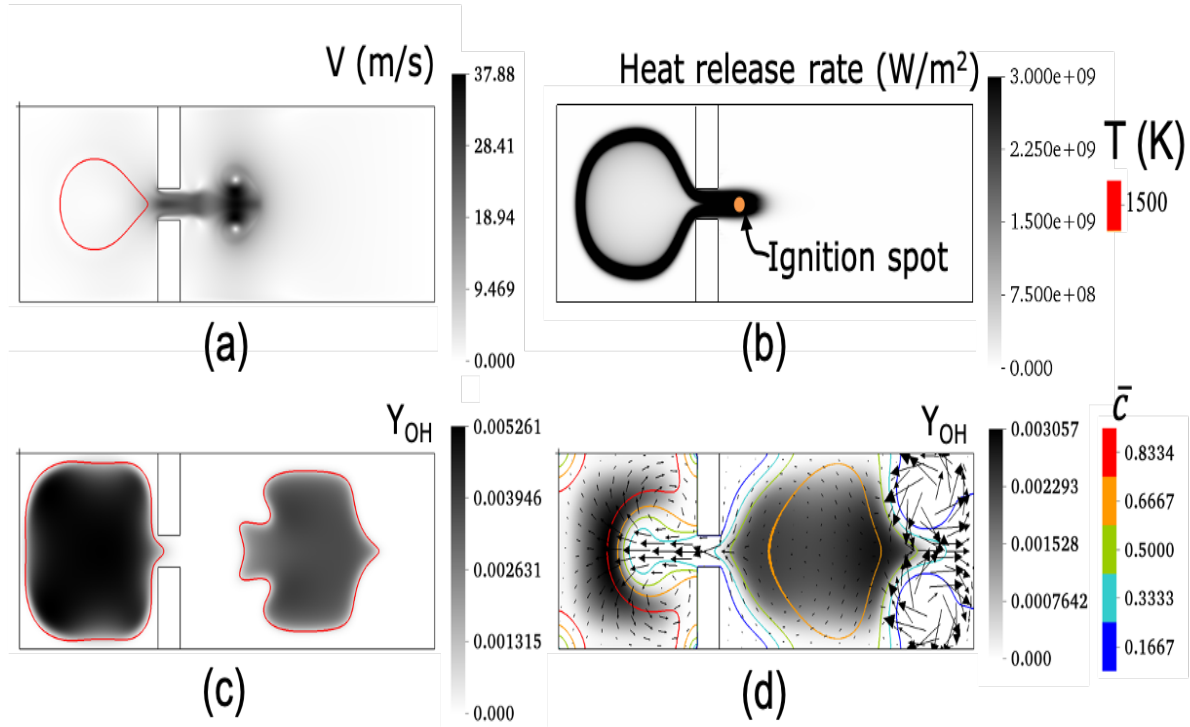


FIGURE 6.4. (a) Velocity field (gray colour scale) with single temperature isolevel (red, 1500 K) at 0.13 ms, corresponding to the end of Phase 1; (b) Heat release rate (gray colour scale) at 0.58 ms, close to the end of Phase 2; (c) OH mass fraction (gray colour scale) with single temperature isolevel (red, 1500 K) at 1.0 ms, Phase 3; and (d) OH mass fraction (gray colour scale) with isolevels of normalized progress variable  $\bar{c}$  (solid coloured lines) and velocity vectors (scaled proportional to magnitude, peak velocity 6.15 m/s) at 1.7 ms, Phase 4. All these results correspond to Case A.

Combining the data shown in Figs. 6.3 and 6.4, the four different phases can be described as follows:

1. Phase 1: spark ignition leading to stable flame development in pre-chamber. The spark ignites the mixtures, leading to the establishment of a flame. As a consequence, the pressure increases in the pre-chamber. The cold mixtures in the pre-chamber are driven toward the main chamber through the orifice. This leads to the formation of a cold-jet structure, as shown in Fig. 6.4(a).
2. Phase 2: hot jet propagates through the orifice. The flame in the pre-chamber has now reached the orifice. This leads to the generation of a hot jet, penetrating in the main chamber, as shown in Fig. 6.4(b) (note the different structures of the red temperature isolevel between Fig. 6.4(a) and Fig. 6.4(b)). This hot jet soon leads to the ignition of the gas located in the main chamber near the orifice. The ignition delay of the main chamber mixtures is defined as the time duration between the hot jet injection (start of Phase 2) and the rapid increase of OH mass fraction ( $dY_{\text{OH}}/dt > 0.1 \text{ ms}^{-1}$ ) [205] due to reaction in the main chamber. Detailed identification of the ignition delay time will be introduced in Section "Characteristic time-scales of the jet flow".
3. Phase 3: radicals quench within the orifice. As the combustion in the pre-chamber is almost completed, the velocity of the hot jet through the orifice decreases. As has been mentioned in [193], this hot jet in the orifice is composed of a column of hot products surrounded by an annulus of unburnt pre-chamber gases. Due to excessive heat loss to the cold wall (a constant temperature of 300 K is imposed there), the hot jet structure is broken, as shown in Fig. 6.4(c), leading to two disconnected high-temperature regions. Chemical reaction rates decrease rapidly [198], leading to a rapid decay of  $\bar{c}$  (see Fig. 6.3). Ultimately, the transport of radicals and heat from pre-

chamber to main chamber through the orifice stops. This will be discussed in more details in Section "Radical quenching in orifice".

4. Phase 4: back-propagation from main chamber to pre-chamber. As the flame develops significantly in the main chamber while pre-chamber combustion is almost completed, the pressure in the main chamber becomes higher than in the pre-chamber (see later Fig. 6.9 in Section "Radical quenching in orifice"). This leads to a back-flow through the orifice from main chamber to pre-chamber, as clearly visible in Fig. 6.4(d). Obviously, the occurrence of this last phase and the time at which it starts strongly depend on the relative volume of main chamber and pre-chamber.

These four phases have been found for all cases listed in Table 6.1. They are consistent with previously published studies, e.g. [193, 195], which confirms the representativity of the present numerical configurations. However, the classification and the distinction between the different phases are different. In the present study, a clear distinction based on the normalized progress variable in the orifice has been proposed, as explained at the beginning of this section. Thanks to the different cases listed in Table 6.1, it is now possible to check the influence of different parameters on the ignition process and on the four phases underlying it.

The state of the fluid at the orifice is of crucial importance for the pre-chamber/ main chamber system. Figure 6.5 shows the temperature, axial velocity, mass fraction of OH, and heat release rate profile across the orifice at the level of point  $M_3$  at different time instants. As is seen, the profiles in the orifice are smooth and symmetric. The time evolution of the profiles confirms the previous statements concerning the 4 phases. From Fig. 6.4(a) and Fig. 6.5(b), it is observed that the jet structure is symmetric in the orifice and in the main chamber. This symmetric structure can obviously be broken by initializing asymmetric fluctuations. Later, the spontaneous transition to turbulence also leads to a rupture of symmetry. This



issue is considered later in more details for 3D cases.

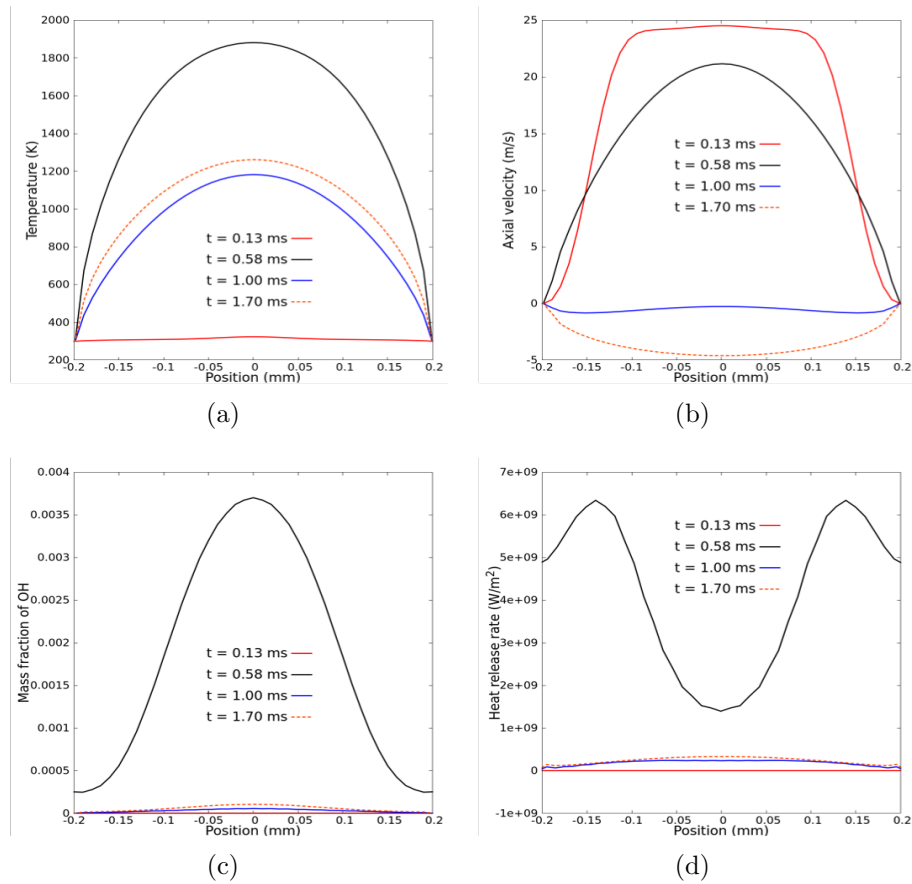


FIGURE 6.5. (a) Temperature, (b) axial velocity, (c) mass fraction of OH and (d) heat release rate profile across the orifice at the level of point  $M_3$  at  $t = 0.13$  ms, 0.58 ms, 1.00 ms and 1.70 ms in Case A.

### Contributions of the hot jet from pre-chamber to main chamber on ignition

According to [195], the effect of the hot jet on main-chamber ignition can be subdivided into 1) enrichment effect, 2) chemical effect, and 3) thermal effect. All three effects are coupled together during the overall ignition process. In the following, these effects are analyzed quantitatively in more details. Compared to the successful ignition in Case A, shown in in Figs. 6.3 and 6.4 and discussed in the previous section, Case C is using a leaner mixture in

the pre-chamber. As a consequence, the resulting hot jet cannot ignite the main-chamber mixture. These two cases are now compared to check the hot jet effects on ignition.

To quantify the hot jet effects on overall ignition delineate between chemical and thermal aspects, the relative contribution of each species  $i$  to the total heat release rate is calculated as follows:

$$H_i = \dot{\omega}_i h_i / \sum_{j=1}^{N_s} \dot{\omega}_j h_j \quad (6.5)$$

where  $\dot{\omega}_i$  and  $h_i$  are the mass production rate and the specific enthalpy of the species  $i$  respectively, and  $N_s$  is the total number of species. Per definition,  $H_i$  is a non-dimensional quantity that can be positive (exothermic) or negative (endothermic), with  $\sum_{i=1}^{N_s} H_i = 1$ . The contributions of each species at the ignition spot (the Eulerian point with most heat release at the ignition time, shown in Fig. 6.4(b)) exemplarily for Case A, are plotted with time in Fig. 6.6. As is seen, production of  $\text{H}_2\text{O}$ ,  $\text{CH}_3$  and  $\text{CH}_2\text{O}$  are contributing most (together more than 90%) to the heat release just before ignition (at  $t = 0.52$  ms). Production of  $\text{CH}_3$  and  $\text{CH}_2\text{O}$  (mostly by reaction  $\text{CH}_4 + \text{O} = \text{CH}_3 + \text{OH}$  (R89 in [201]) and  $\text{CH}_3 + \text{O} = \text{CH}_2\text{O} + \text{H}$  (R67 in [201])) generate more than 40% of the total heat release. This means that the local amounts of  $\text{CH}_4$ ,  $\text{CH}_3$  and  $\text{O}$  are important for initiating the ignition process. Meanwhile, the chain-branching reaction  $\text{HO}_2 + \text{H} = \text{OH} + \text{OH}$  (R6 in Lindstedt's mechanism [201]) is critical for the production of  $\text{OH}$  radicals [143], which are in turn essential for the subsequent high heat release reactions generating  $\text{H}_2\text{O}$ . Thus, the local amount of  $\text{HO}_2$  is an important indicator for the final successful ignition. Figure 6.7 shows the scatter plot of selected species mass fractions ( $\text{CH}_4$ ,  $\text{CH}_3$  and  $\text{HO}_2$ ) vs. temperature in the whole main chamber for Case C at  $t = 0.7$  ms (until the end of Phase 2) and Case A at  $t = 0.52$  ms (just before ignition). The corresponding premixed 1D flames under the same conditions (the same initial temperature and pressure as the main chamber in the 2D DNS) for different mixtures equivalence ratios  $\phi$  are also plotted in Fig. 6.7 as reference.

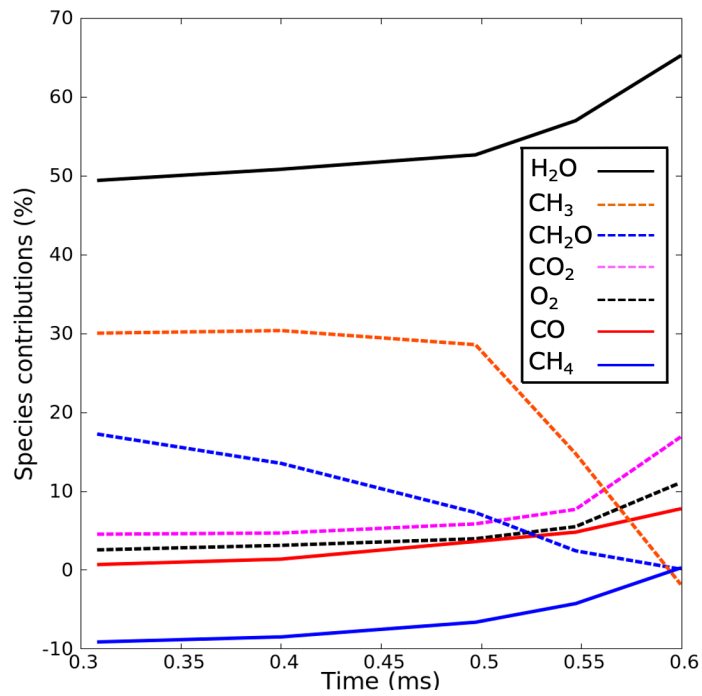


FIGURE 6.6. Time-evolution of relative heat release  $H_i$  associated to different species at ignition spot (point shown in Fig. 6.4(b)) until ignition by the hot jet, exemplarily for Case A. Species with negligible contributions are not shown.

The fuel enrichment effect is obvious from both Fig. 6.7(a) for Case A and Fig. 6.7(b) for Case C. The scatter points show local  $\text{CH}_4$  mass fractions considerably higher than the corresponding laminar 1D premixed flame with  $\phi = 0.5$  at the same temperature, while the initial main chamber mixture corresponds to  $\phi = 0.5$  in both cases. Due to an initially even richer mixture in pre-chamber for Case A, the enrichment effect is more intensive in Case A than in Case C, with a scatter plot of  $\text{CH}_4$  mass fraction exceeding the corresponding laminar 1D premixed flame with  $\phi = 0.7$  at most points. The thermal effect can be observed from Fig. 6.4(b). The hot jet brings high temperature gas (transporting heat) into the main chamber, which helps to ignite the initially cold mixtures there. The chemical effect is obvious from Fig. 6.7(c) and Fig. 6.7(d). In both cases, the  $\text{HO}_2$  mass fraction can be locally higher than in the corresponding reference premixed flame at  $\phi = 0.5$ . In Fig. 6.7(c), the  $\text{HO}_2$  mass fraction is even higher than for reference premixed flame corresponding to initial mixture in the pre-chamber ( $\phi = 1.0$ ) in the temperature range 600 K - 1300 K. This accumulation of  $\text{HO}_2$  promotes the ignition process. It is less pronounced for Case C.

Checking now the coupling of these effects, the fuel enrichment effect brings more  $\text{CH}_4$  into the main chamber lean mixtures, promoting the reaction R89:  $\text{CH}_4 + \text{O} = \text{CH}_3 + \text{OH}$ . The chemical effect also transports  $\text{CH}_3$  toward the main chamber with the hot jet. Both effects promote the high heat release reaction R67:  $\text{CH}_3 + \text{O} = \text{CH}_2\text{O} + \text{H}$ , generating enough heat to support the ignition process. In Fig. 6.7(e), the distribution of the scatter points representing  $\text{CH}_3$  in the main chamber shows the same trend as the reference premixed flame corresponding to pre-chamber conditions ( $\phi = 1.0$ ). Especially, the peak  $\text{CH}_3$  mass fraction locates at the same temperature ( $\approx 1600$  K). This indicates that the  $\text{CH}_3$  distribution in the main chamber is dominated by the chemical and thermal effects induced by the hot jet.

For Case C, as discussed previously, the enrichment effect has also transported some additional  $\text{CH}_4$  toward the main chamber, promoting again reaction R89. However, due to

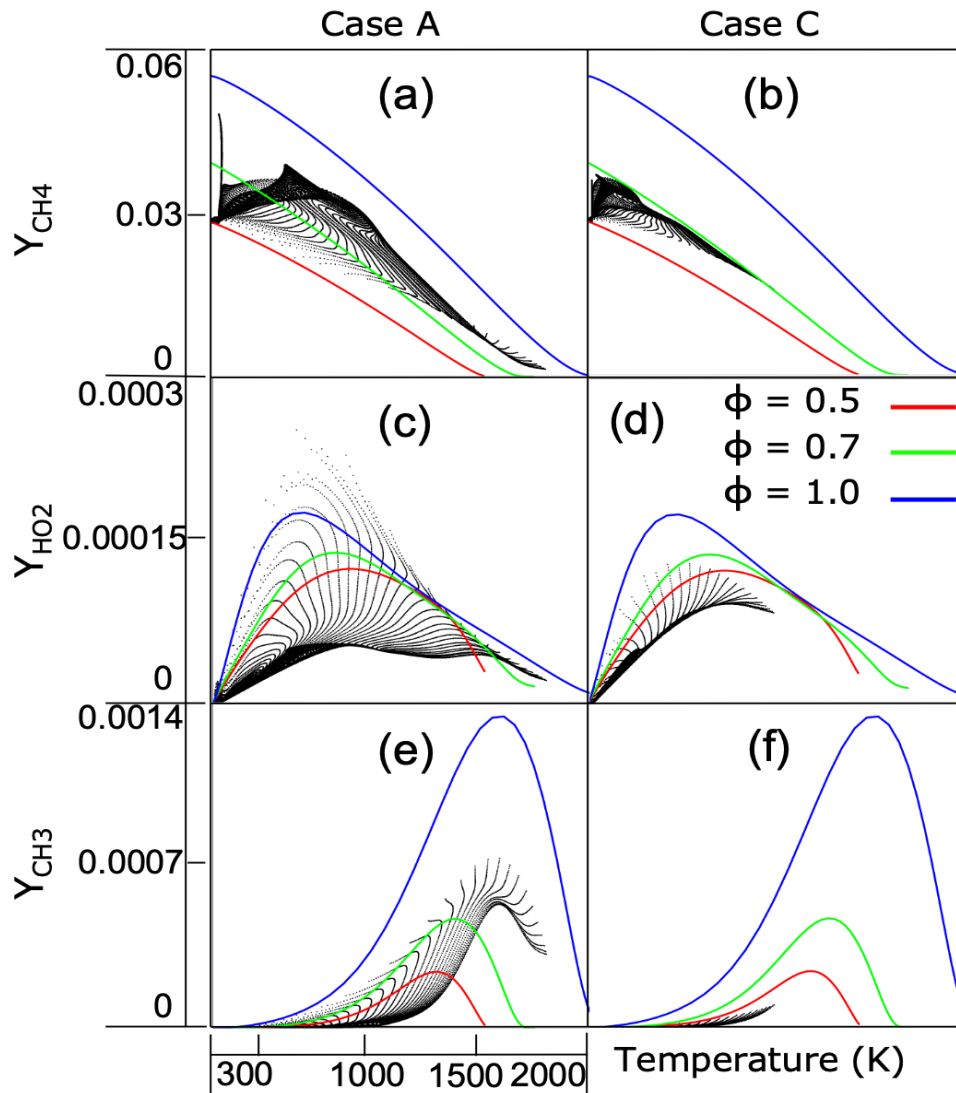


FIGURE 6.7. Scatter plot (black dots) of  $\text{CH}_4$  mass fraction (a and b),  $\text{HO}_2$  mass fraction (c and d) and  $\text{CH}_3$  mass fraction (e and f) vs. temperature in the whole main chamber at time  $t = 0.52$  ms for Case A (a, c and e) and at time  $t = 0.7$  ms for Case C (b, d and f). Corresponding premixed 1D flames under the same conditions (the same initial temperature and pressure as the main chamber in the 2D DNS) for different mixtures equivalence ratios  $\phi$  are also plotted for comparison (coloured solid lines). The scatter plots show all the grid points in the main chamber.

lower chemical effect and thermal effect, the  $\text{CH}_3$  mass fraction and temperature range is quite low in the main chamber (see Fig. 6.7(f)), even lower than the reference 1D flame with  $\phi = 0.5$ . Therefore, it can be concluded that chemical effect and thermal effect are more important than enrichment effect for Case A and Case C, determining ultimately successful ignition (for Case A) or quenching (for Case C) in the main chamber.

As the enrichment effect is associated to the cold jet flow, while the chemical and thermal effects come with the hot jet flow, the time duration of the cold vs. hot jet flow is critical in this regard, as discussed in the next section.

### Characteristic time-scales of the jet flow

To quantify the duration of the cold jet and hot jet in the main chamber, the characteristic time-scales of the cold jet  $\tau_{cj}$  and hot jet  $\tau_{hj}$  are defined as the time duration of Phase 1 and Phase 2 discussed in Section "Phases identification", respectively. Even if the hot jet continues after Phase 2, its contribution to ignition rapidly becomes negligible: for 1) Chemical effect, the mass flow rates of the radicals decrease to a very low level, as can be seen in Fig. 6.3; regarding 2) Thermal effect: heat convection by the hot jet from the orifice to the main chamber stops rapidly, as will be discussed in Section "Radical quenching in orifice". Table 6.2 lists the characteristic time-scales of the cold jet  $\tau_{cj}$  and hot jet  $\tau_{hj}$  for the seven cases in Table 6.1. By comparing all these cases, it can be assumed that ignition or misfire in the main chamber depends on the combination of four factors:

1. Main chamber equivalence ratio  $\phi$  (Case C vs. Case E);
2. Intensity of chemical enrichment and thermal effects (controlled by orifice diameter in Case C vs. Case D, or by pre-chamber equivalence ratio  $\phi$  in Case A vs. Case C);
3. Hot-jet characteristic time-scale  $\tau_{hj}$  (controlled by spark location in Case A vs. Case

B);

4. Turbulence intensity (comparing Case G to Case E, and Case F to Case C).

The main chamber usually contains leaner mixtures in real engines, in order to enhance fuel efficiency. Thus, the first important factor in this list is not really a free parameter, since it is process-oriented. By increasing the orifice diameter, the hot jet width is larger, bringing more heat into the main chamber, and promoting thermal effect. On the other hand, a too large orifice diameter will ultimately destroy the pre-chamber/main chamber system, resulting in no hot jet generation. Using a richer pre-chamber mixture enhances the enrichment effect. And the pre-chamber flame (determined by its equivalence ratio  $\phi$  and fuel type) affects both chemical effect and thermal effect. Finally, orifice diameter and pre-chamber mixtures determine if ignition or misfire will occur by changing the intensity of the transfer processes between pre-chamber and main chamber. The spark location, on the other hand, can impact ignition by changing the hot-jet characteristic time-scale. A spark location farther away from the orifice decreases the hot-jet characteristic time-scale, and can thus lead to misfire. Note that the main chamber volume would also affect the characteristic time-scales and influence ignition, but this parameter has not been varied in the present study. Finally, turbulence is also known to influence ignition [143], and its effect will be discussed in Section "Turbulence effect".

As mentioned, the ignition delay time is associated with the OH radical generation by reaction in the main chamber. To distinguish whether the OH mass fraction is increasing because of reaction or of advection, Fig. 6.8 has been plotted, which shows the maximum OH mass fraction over all vertical cross-sections from pre-chamber (left boundary) to main chamber (right boundary) as a function of time, exemplarily for Case A and Case G. In Fig. 6.8(a), local just-ignition can be observed at time  $t = \tau_{cj} + \tau = 0.52$  ms, when the OH mass fraction increases rapidly ( $dY_{\text{OH}}/dt > 0.1 \text{ ms}^{-1}$ ) at location  $y = 3.4$  mm. This is even

TABLE 6.2. Time-scales and global Damköhler number for Cases A - G considered in this study. The value of Da is computed at  $t = \tau_{cj} + \tau$  for ignition cases and at  $t = \tau_{cj} + \tau_{hj}$  for misfire cases at the exit of the orifice (white dashed line in Fig. ??). Remember that the ignition delay is computed after the end of the cold-jet phase, so that ignition takes place indeed at  $\tau_{cj} + \tau$ .

Case	$\tau_{cj}$ (ms)	$\tau_{hj}$ (ms)	ignition delay $\tau$ (ms)	local just-ignition	global ignition	Da
A	0.13	0.53	0.39	✓	✓	110.8
B	0.27	0.42	0.41	✓	×	89.8
C	0.15	0.55	-	×	×	70.2
D	0.15	0.56	0.41	✓	✓	91.0
E	0.15	0.50	0.43	✓	✓	87.9
F	0.26	0.62	0.34	✓	×	56.6
G	0.14	0.51	0.49	✓	✓	72.1

more obvious in Fig. 6.8(b) for Case G, where local just-ignition happens at  $t = \tau_{cj} + \tau = 0.63$  ms near location  $y = 3.8$  mm. Soon after, a region with local flame quenching appears at  $t = 0.67$  ms, with a decrease in OH mass fraction. Finally, slightly after  $t = 0.7$  ms, global ignition happens leading to self-sustained combustion. The corresponding ignition delay  $\tau$  (computed using the time instant of the first local just-ignition after end of the cold-jet phase) is listed in Table 6.2 for Case A - G. The global Damköhler number is computed at the orifice exit (white dashed line in Fig. 6.1) as defined in [192]. It is computed for the ignition cases at  $t = \tau_{cj} + \tau$ , and for the misfire cases at  $t = \tau_{cj} + \tau_{hj}$ , using:

$$\text{Da} = \frac{s_L l}{u' \delta_L}, \quad (6.6)$$

where  $s_L$  and  $\delta_L$  are respectively computed as the laminar flame speed and laminar flame thickness for the laminar premixed flame corresponding to the initial main-chamber mixtures and pressure found there at the time when Da is computed, while the velocity fluctuations  $u'$  and the integral length scale  $l$  are estimated as in [192] at the orifice exit.



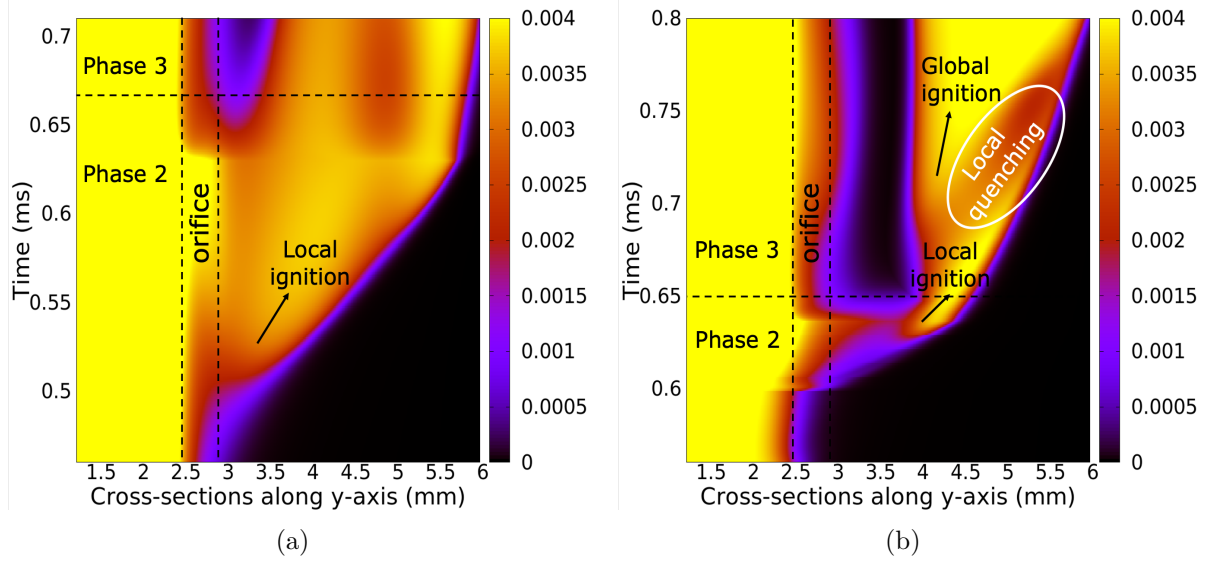


FIGURE 6.8. Time evolution of maximum OH mass fraction along all vertical cross-sections (from left – pre-chamber – to right – main chamber –, the two vertical dashed lines marking the position of the orifice), exemplarily for (a) Case A and (b) Case G. For a better visibility, the beginning of the process is not shown, and the time-scales vary.

### Radical quenching in orifice

Radical quenching is observed in the orifice during Phase 3. Figure 6.9 shows the time evolution of the different terms controlling heat balance in the orifice: reaction, advection and diffusion, exemplarily for Case A. The axial velocities at points  $M_1$  and  $M_3$  and the pressure difference between these two points are also plotted. The different terms of the heat balance in the orifice are computed as (using Einstein summation convention):

$$H_{\text{diffusion}} = \sum_V^{in\ orifice} \left[ \frac{\partial}{\partial x_j} \left( \lambda \frac{\partial T}{\partial x_j} \right) - \frac{\partial T}{\partial x_j} \rho C_{p,k} Y_k V_{k,j} \right] dV, \quad (6.7)$$

$$H_{\text{advection}} = - \sum_V^{in\ orifice} \rho C_p u_j \frac{\partial T}{\partial x_j} dV, \quad (6.8)$$

$$H_{\text{reaction}} = - \sum_V^{\text{in orifice}} h_k \dot{\omega}_k dV. \quad (6.9)$$

Here,  $C_p$ ,  $h_k$ ,  $\dot{\omega}_k$ ,  $\lambda$ ,  $V_{k,j}$  represent the specific heat capacity at constant pressure, specific enthalpy, mass reaction rate, heat diffusion coefficient and  $j$ th component of the species molecular diffusion velocity, respectively. From Fig. 6.9, it can be seen that the flow velocity increases as the hot jet enters the orifice (due to thermal expansion, as discussed in [206]); heat accumulation by advection is dominating at this early stage. Later on, the heat generation by reaction strongly increases, until the end of Phase 2. It is interesting that the velocity at the inlet of the orifice (point  $M_1$ ) is slightly smaller than that at the outlet (point  $M_3$ ) during the hot jet injection process, due to the establishment of the boundary layer in the orifice, resulting in higher axial velocity at the centerline. After Phase 2, the hot jet velocity decreases, resulting in decreased supply of radicals and hot gases from the pre-chamber. The heat generation by reaction also decreases rapidly due to reactions' quenching.

To check the effect of the cold wall on radical quenching in the orifice, Case H has been simulated. Figure 6.10 shows the time evolution of the progress variables  $\bar{c}$  at points  $M_1$ ,  $M_2$  and  $M_3$  for Case H. Heat generation by reaction has also been plotted. As can be seen from the evolution of the progress variable in Fig. 6.10, the reaction front is not interrupted in the orifice for adiabatic wall condition ( $\bar{c}_{M_1} > \bar{c}_{M_2} > \bar{c}_{M_3}$ ), compared to the case considering a cold isothermal wall (with  $\bar{c}_{M_2} < \bar{c}_{M_3}$  immediately after Phase 2 in Fig. 6.3). Additionally, heat generation by reaction does not show a very rapid decrease, indicating that reactions are not completely quenched in the orifice, confirming the importance of wall heat loss to explain radical quenching. The decrease in heat generation seen in the right part of Fig. 6.10 simply represents the passage of the flame front through the orifice outlet. As a conclusion, radical quenching in the orifice is explained by two effects, mostly combined: 1) reduced radical supply from the pre-chamber, and 2) quenching of the reactions in the orifice mostly

due to wall heat loss. In reality, the orifice wall is neither adiabatic nor isothermal. The wall heat loss might not be enough for radical quenching. A detailed wall heat transfer model is critical for practical investigation on the radical quenching event in industrial chambers. Apart from the above two effects, radical destruction at the walls also plays a crucial role for radical quenching in a realistic orifice. To simulate accurately such a process, a detailed wall reaction model would be necessary. This is the subject of future studies.

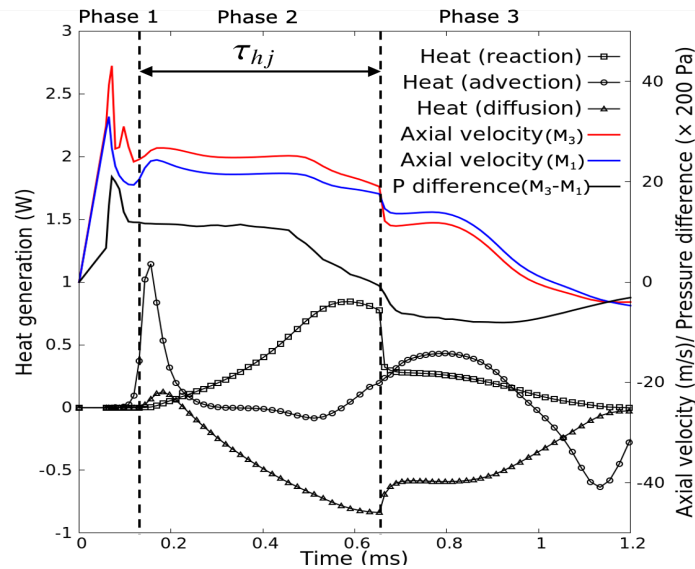


FIGURE 6.9. Time evolution of the different terms controlling heat balance in the orifice (left scale, lines with markers), together with (right scale) axial velocity at points  $M_3$  (red) and  $M_1$  (blue) as well as pressure difference between  $M_3$  and  $M_1$  (black). The different phases are labelled on the top. All these results are shown exemplarily for Case A.

### Transient ignition process

Figure 6.11 shows the time evolution of the maximum OH mass fraction in the main chamber for Case A - G. For each curve, the time is normalized by the characteristic time-scale of the jet ( $\tau_{cj} + \tau_{hj}$ ) in order to facilitate comparisons. As is seen in Fig. 6.11, confirming previous discussions connected to Fig. 6.8, the global ignition process in the main chamber can be divided into: 1) near-orifice local just-ignition (first rapid increase of OH mass fraction due

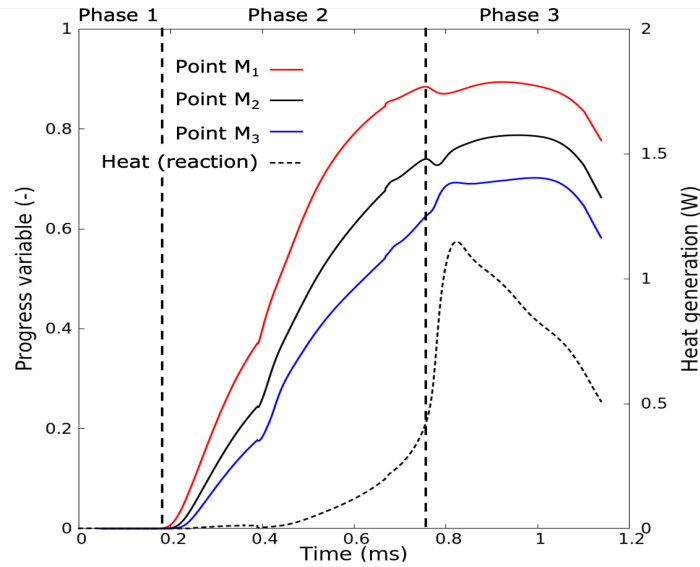


FIGURE 6.10. Time evolution of the progress variable  $\bar{c}$  at points  $M_1$ ,  $M_2$ ,  $M_3$  and contribution of reaction to heat balance within the orifice for Case H. The different phases are labelled on the top.

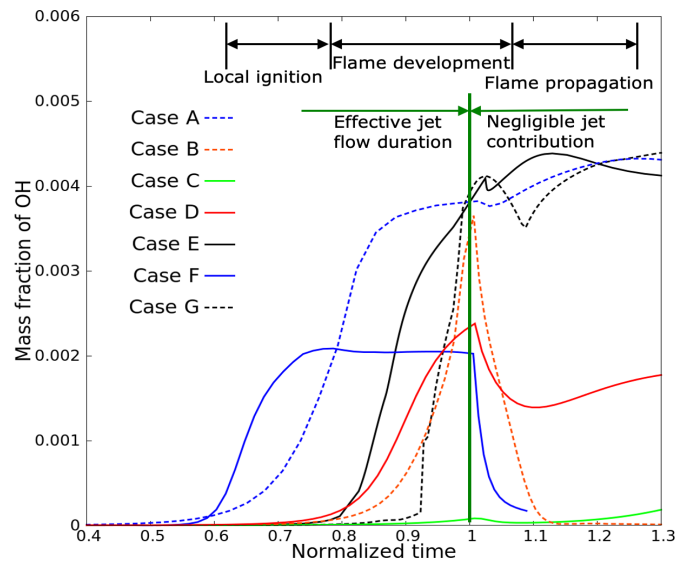


FIGURE 6.11. Time evolution of the maximum OH mass fraction in the main chamber for Case A - G. For each curve, the time is normalized by the characteristic time-scale of the jet ( $\tau_{cj} + \tau_{hj}$ ), so that normalized time 1 corresponds to the end of the jet flow from pre-chamber to main chamber.

to reaction); 2) flame development supported by the jet flow (OH mass fraction increases slowly and propagates downstream); 3) development of a self-sustained flame, independent from the hot jet (OH mass fraction increases further or stays at a high level after the hot jet stopped). These three steps are consistent with the recent findings in [199], where a real engine geometry was simulated by LES. All three steps must be successful to achieve overall ignition in the main chamber. The start of the third process is called “global ignition”, distinguishing it from the local just-ignition in the initial stage [191].

It is interesting to note that local just-ignition is observed in Cases B and F; however, global ignition does not happen. For Case B, the increase in OH mass fraction shows at first qualitatively a similar shape to Case A, but shifted toward a later normalized time (remember that the horizontal scale in Fig. 6.11 is normalized by  $(\tau_{cj} + \tau_{hj})$ ). However, the hot jet characteristic time  $\tau_{hj}$  is much shorter for Case B, resulting in less radicals and hot gases penetrating into the main chamber; for this reason, global ignition cannot be initiated. Concerning Case F,  $\tau_{hj}$  becomes longer due to intense turbulent mixing compared with Case C. Chemical effect and thermal effect become more prominent, resulting in local just-ignition near the orifice (at the difference of Case C, where no ignition at all as found). However, global ignition still does not happen, because of turbulent quenching in the main chamber. The impact of turbulence is discussed in more detail in the next section.

### **Turbulence effect**

Different from previous studies [192, 197] where there is no initial turbulence, the present work investigates as well the impact of initial turbulence on hot jet ignition. As already mentioned in Table 6.1, a homogeneous isotropic turbulence has been initially super-imposed on the flow field in Case G (to be compared to Case E) and in Case F (to be compared to Case C).

By comparing Case E and Case G in Table 6.2 and Fig. 6.11, the ignition delay in Case G (with initial turbulence) is longer, while the characteristic jet scales  $\tau_{cj}$ ,  $\tau_{hj}$  are almost unchanged, the sum ( $\tau_{cj} + \tau_{hj}$ ) being exactly the same. After this effective jet flow duration, local quenching (indicated by the decrease of maximum OH mass fraction in Fig. 6.11) is more intense in Case G. This result matches well with the observations discussed in [143] regarding the influence of turbulence on ignition. A stronger turbulence (due to initial, homogeneous turbulence as well as jet-induced turbulence) results in faster mixing, so that hot-jet radicals diffuse more rapidly; as a consequence, local quenching is observed shortly after the effective jet duration ( $\tau_{cj} + \tau_{hj}$ ). When the turbulence intensity increases further, local quenching ultimately becomes global quenching, since all local ignition kernels are quickly dissipated. This is consistent with the critical Damköhler number concept for successful hot jet ignition proposed in [192, 197]. From Table 6.2, it is observed that higher global Damköhler numbers result in easier local ignition and shorter ignition delay times. This is reasonable since the global Damköhler number is computed using the turbulence characteristics near the orifice exit [192]. However, the Damköhler number limit for ignition (estimated as 140 for CH<sub>4</sub>/air in [192]) is not the same as in the present study. This confirms that the critical Damköhler number is a useful concept but is not the only parameter determining ignition or misfire.

Comparing now Case C and Case F (same as Case C, adding initial turbulence) in Fig. 6.11, no ignition appears at all in Case C, while local just-ignition is observed in Case F with the assistance of turbulence. Turbulence is expected to dissipate the reactive radicals and species from the pre-chamber jet flow into the main chamber more efficiently, thus generating local spots with more reactive conditions for ignition events.

Therefore, under the investigated conditions, it is observed that: 1) a more intense turbulence will lead to more intensive local quenching of the flame, which is defavorable for global ignition; while 2) a higher turbulence intensity enhances the near-orifice local

just-ignition probability, and plays therefore a positive role.

### 3D validation

Since the energy cascade and the generation of fluctuations are indeed different for real 3D turbulence, the validity of the previous conclusions should be checked using 3D DNS. Cases A3D and B3D in Table 6.1 are proposed for this purpose.

Figure 6.12 shows the scatter plots of reactive species ( $\text{CH}_3$  and  $\text{HO}_2$ ) vs. progress variable from the 2D and 3D DNS cases at the local just-ignition time. Since the geometry is different, quantitative differences are expected and are clearly observed. In particular, the reactive species are at a lower level in 2D compared to 3D. Still, the shapes of the profiles remain similar.

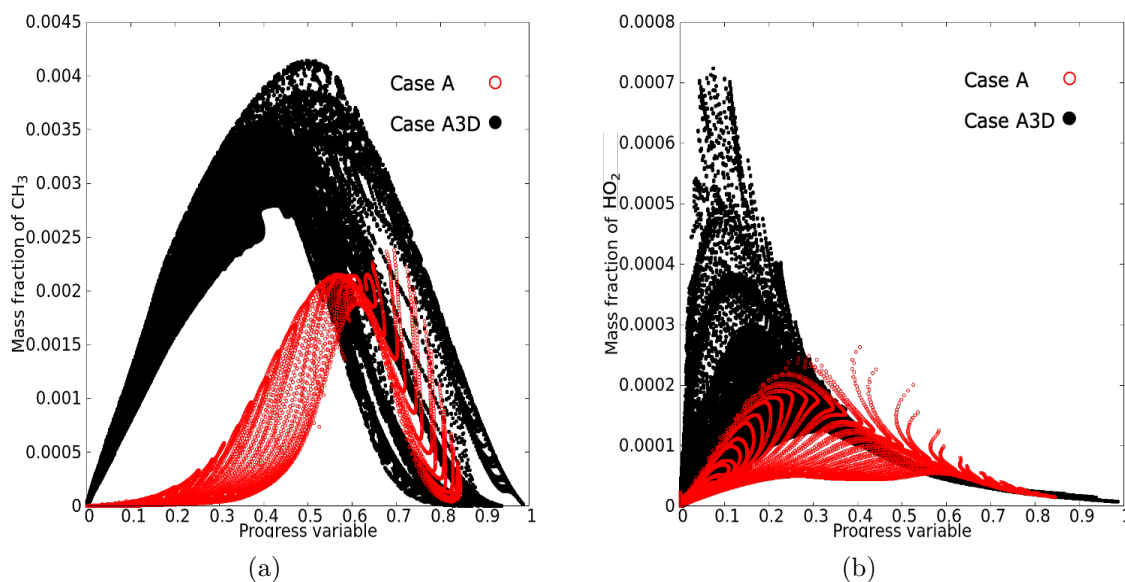


FIGURE 6.12. Scatter plot of (a) mass fraction of  $\text{CH}_3$  vs. progress variable and (b) mass fraction of  $\text{HO}_2$  vs. progress variable in the main chamber for Case A (red circles) at  $t = 0.52$  ms and Case A3D (black dots) at  $t = 0.545$  ms.

Figure 6.13 shows the flame evolution represented by the OH mass fraction equal to 0.001 for Case B3D at 3 sequential time instants. As is seen, at  $t = 0.545$  ms, there is a local

just-ignition spot in the main chamber. Later at  $t = 0.755$  ms, the flame develops further with the support of the hot jet flow. At  $t = 0.864$  ms, the hot jet flow entering the main chamber starts to be quenched, but the flame is self-sustained and propagates further in the main chamber. This results confirm the transient ignition process observed in the 2D simulations.

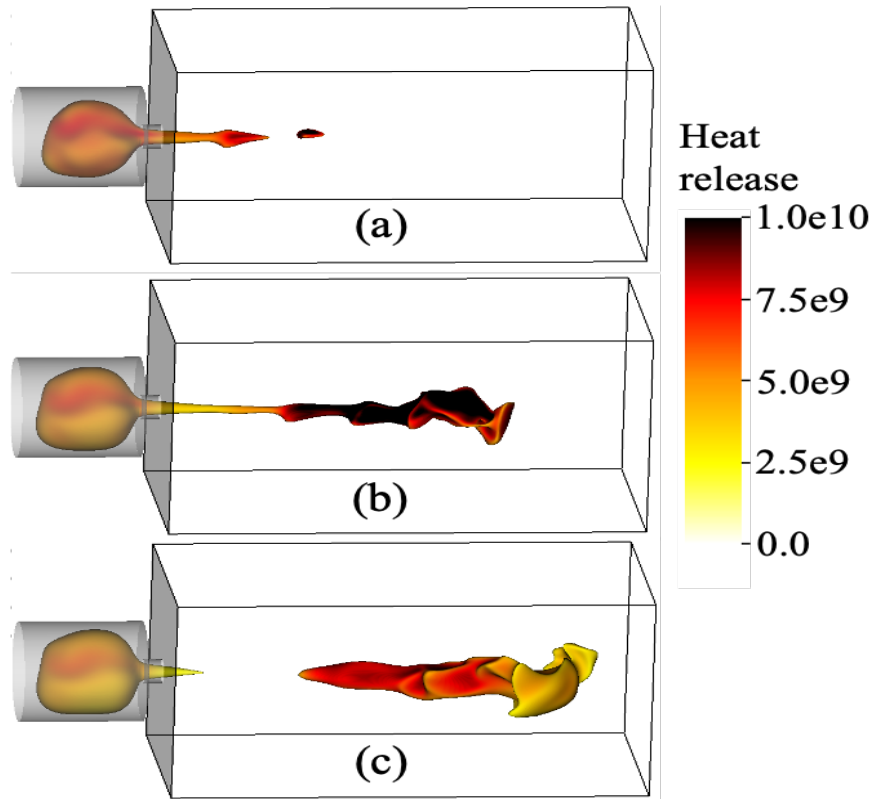


FIGURE 6.13. Iso-surface of OH mass fraction at 0.001 colored by heat release rate for Case B3D at 3 different time instants (a)  $t = 0.545$  ms, (b)  $t = 0.755$  ms, and (c)  $t = 0.864$  ms.

The 3D turbulence effect on local just-ignition has also been investigated. Figure 6.14(a) shows the scatter plot between temperature and  $\text{HO}_2$  mass fraction for Case A3D and Case B3D at  $t = 0.545$  ms, when local just-ignition happens. As is seen, the  $\text{HO}_2$  mass fraction is distributed more broadly in Case B3D, especially at higher temperature. This indicates that a more intensive turbulence transports more efficiently the reactive radicals from the



hot jet flow into the main chamber mixtures. As is known, local just-ignition is determined by the most reactive mixtures [200]. Thus, turbulence leads to an easier local just-ignition. Figure 6.14(b) shows the scatter plot between temperature and local equivalence ratio. As is seen, the local equivalence ratio is also distributed much more broadly in Case B3D. More spots exist where there is a rich mixture at high temperature, leading to easier local just-ignition in Case B3D. This finding confirms the previous 2D analysis based on comparisons between Case C and Case F. It can be concluded that a higher turbulence intensity will enhance the chemical effect (by transporting more efficiently the reactive radicals into the main chamber) and the enrichment effect (by mixing more efficiently the richer mixtures from the pre-chamber jet flow with the lean gases in the main chamber), resulting in easier local just-ignition in the main chamber.

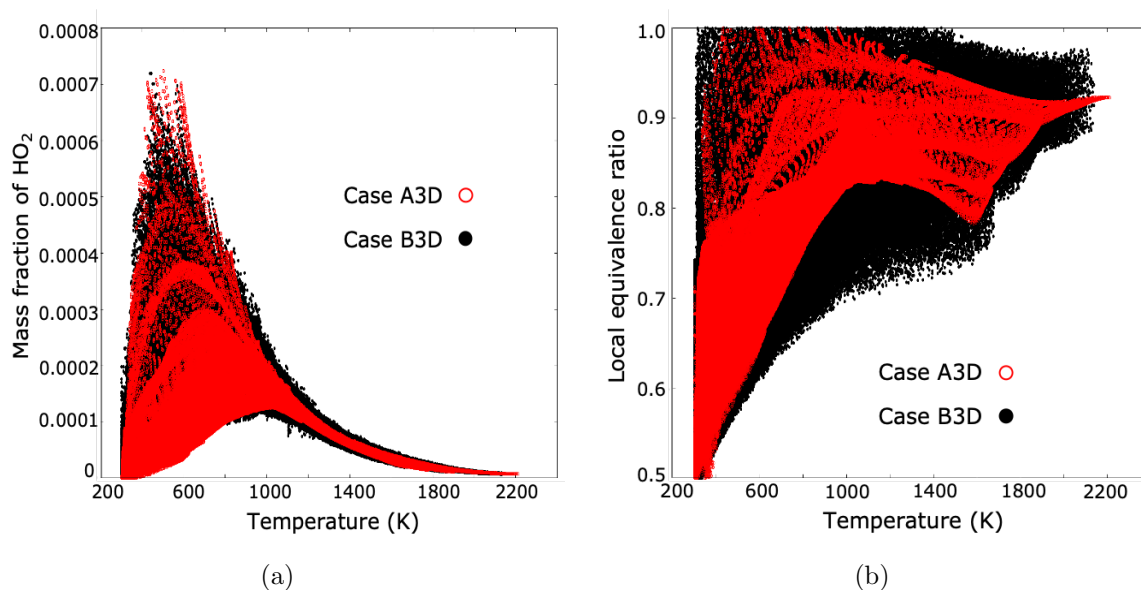


FIGURE 6.14. Scatter plot of (a) mass fraction of  $\text{HO}_2$  vs. temperature and (b) local equivalence ratio vs. temperature in the main chamber for Case A3D (red circles) and Case B3D (black dots) at  $t = 0.545$  ms.

Finally, the 3D turbulence effect on global ignition has been investigated. Figure 6.15 shows the time evolution of the volume in the main chamber where the OH mass fraction

is larger than 0.001. As is seen, there are two rapid increases of the OH volume for both Case A3D and Case B3D. The first rapid increase indicates the injection of the pre-chamber hot jet flow into the main chamber, while the second rapid increase indicates the global ignition event (stable flame propagation). Compared to Case A3D, in Case B3D, the global ignition delay is longer. In Case B3D, more and stronger fluctuations of the signal reveal local quenching events. A higher turbulence intensity results in faster dissipation of some local just-ignition spots, leading to a longer global ignition delay. This result confirms the 2D analysis based on comparisons between Case E and Case G. Thus, the turbulence effect on the transient ignition process is consistent for both 2D and 3D DNS simulations: turbulence facilitates local just-ignition, but delays – or could even hinder – global ignition.

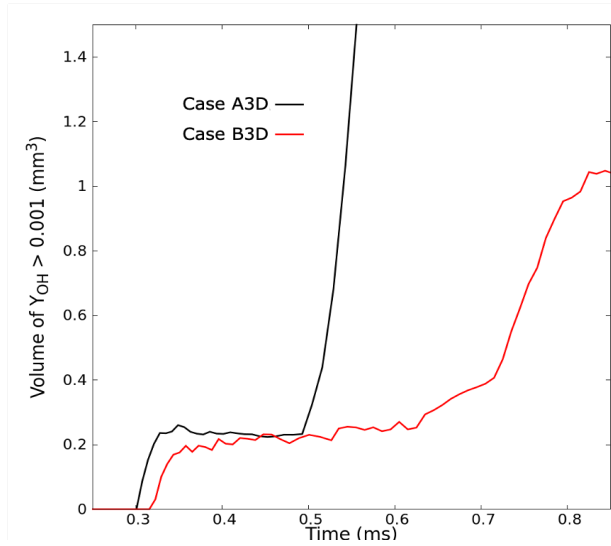


FIGURE 6.15. Time evolution of the volume in the main chamber where OH mass fraction is larger than 0.001 in Case A3D and Case B3D.

In realistic, 3D turbulence, the aerodynamic strain rates and the flame-strain rate alignment in the main chamber are particularly interesting. These quantities are shown in Fig. 6.16. The strain rate tensor  $s_N$  can be decomposed in 3 principal directions  $s_N = s_1 \cos^2 \theta_1 + s_2 \cos^2 \theta_2 + s_3 \cos^2 \theta_3$ , where  $s_1, s_2$ , and  $s_3$  are the most extensive, inter-

mediate and most compressive principal strain rates, respectively, and  $\theta_1, \theta_2$ , and  $\theta_3$  are the corresponding angles between the flame normal unit vector and the eigenvectors related to  $s_1, s_2$  and  $s_3$ . Figure 6.16(a) shows the PDFs of the most extensive and compressive strain rates ( $s_1$  and  $s_3$ ) and the strain rate tensor norm ( $|s_N|$ ) in Case A3D at  $t = 0.9$  ms. As expected,  $s_1$  and  $s_3$  are positive and negative respectively, characterizing the extensive and compressive strain rates. The peaks of strain rate tensor norm lies within  $100 - 600 \text{ s}^{-1}$ , with a decreasing magnitude at higher strain rates. Figure 6.16(b) shows the PDFs of the angle  $\theta_1$  between the most extensive strain rate eigenvectors and the flame normal unit vectors at the flame front for both Case A3D and Case B3D at the same time,  $t = 0.9$  ms. As can be seen, the PDFs of the alignment have a large peak at  $\cos(\theta_1) \simeq 1$  for both cases, which indicates that the extensive strain rate eigenvectors are preferentially aligned with the flame normal, as also found in [207]. Compared to Case A3D, the preferential alignment (PDF near  $\cos(\theta_1) = 1$ ) is somewhat reduced in Case B3D. Since Case B3D has stronger turbulent fluctuations and lower Damköhler number, this confirms that the preferential alignment is reduced when the Damköhler number is decreased [208, 209].

#### 6.2.4 Intermediate conclusions

The transient ignition process in a pre-chamber/main chamber system has been investigated by DNS. Four phases have been identified controlling the ignition process in the system: 1) Spark ignition and stable flame development in the pre-chamber; 2) Hot jet flow propagating through the orifice and igniting the main-chamber mixtures; 3) Radical quenching within the orifice; 4) Back-propagation from the main chamber to the pre-chamber. This last step depends strongly on the volumes of pre-chamber and main chamber, and is therefore not universal; it is also less relevant for the present study, since it takes place after ignition. The pre-chamber jet flow effects on the ignition of the main-chamber mixtures have been

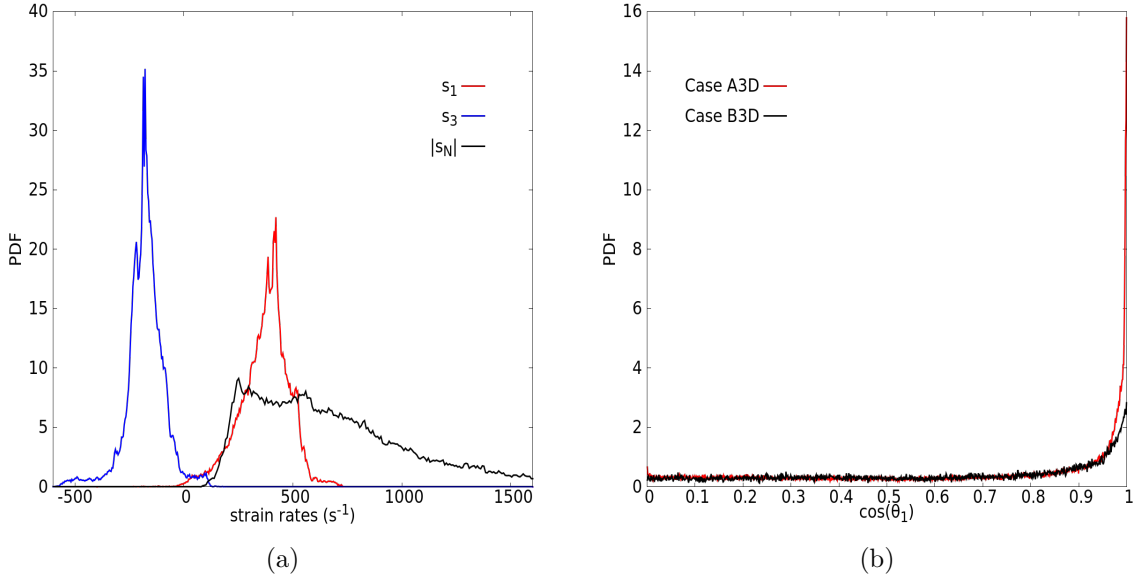


FIGURE 6.16. (a) PDFs of the most extensive and most compressive strain rates ( $s_1$  and  $s_3$ ) and strain rate tensor norm ( $|s_N|$ ) in Case A3D at  $t = 0.9$  ms; (b) PDFs of the extensive strain rate eigenvector alignment with the flame normal unit vector at the flame front in Case A3D and Case B3D at  $t = 0.9$  ms.

analyzed. The characteristic time-scales of the hot jet are important to successfully initiate ignition in the main chamber. Radical quenching in Phase 3 is mainly due to 1) lack of radical supply from the pre-chamber, and 2) quenching of the elementary reactions in the orifice due to excessive wall heat loss. Finally, it is found that the transient ignition process is composed of 1) near-orifice local just-ignition; 2) flame development supported by the jet flow, and 3) flame propagation independently from the hot jet (global ignition). Turbulence effects have also been checked. It appears that turbulence enhances the chemical and enrichment effect at local spots in the main chamber, leading to easier local just-ignition. On the other hand, local just-ignition spots are more easily dissipated away by a higher turbulence intensity, thus resulting in a longer global ignition delay. 3D DNS have also been carried out, confirming the transient ignition process and the turbulence effect on this process. The present findings support the concept of a critical Damköhler number to delineate between ignition and misfire,

but not as a standalone parameter.

The geometry considered in this first investigation is obviously extremely simplified, and is very far from a real system. It must now be checked if DINO is able to consider as well a more realistic configuration.

## 6.3 DNS simulation in generic internal combustion engine without combustion

Before the hot jet ignition process can start in a real engine, 1) a suitable mixture must be provided, and 2) a stable flame must be established thanks to a suitable spark. These two points can only be accurately checked by taking into account the real ICE geometry in a realistic manner. For this purpose, it will first be checked that DINO is able to reproduce the features found in a generic ICE geometry. Finally, a real configuration will be considered.

### 6.3.1 Introduction

Fluid structures, heat and mass transfer, and turbulence/wall interaction have huge effects on the performance of ICE, together with cycle-to-cycle variations (CCVs). To reveal the underlying physics of the complex flow in ICE, both experimental studies and numerical studies have been done previously. We want to check here that DINO could be used as well for that purpose.

Morse et al. [210] first used Laser Doppler Velocimetry (LDV) to investigate the fluid fields in a valve-piston assembly. Later, Reeves et al. [211] applied Particle Image Velocimetry (PIV), instead of LDV, for the measurement of the velocity field in a generic ICE. Alharbi et al. [212] and Jainski et al. [213] studied the velocity boundary layer in ICE using PIV. High speed Laser-Induced Fluorescence (LIF) can be used to measure the temperature and

species fields by tracing the different fluorescence of gases. A recent study by Peterson et al. [214] delivered flow and temperature fields in a gasoline engine by combined toluene-LIF and PIV measurements. In spite of the improvement of measurement techniques for flows in ICE, it is still difficult to experimentally measure every relevant quantities during the fast motion of the piston, especially near the engine walls.

On the other hand, numerical simulations of the ICE may deliver all fields. At the very beginning, simple RANS with a  $k - \epsilon$  model was employed to simulate the flow in a diesel engine, e.g. [215]. The first LES of an ICE was probably performed by Haworth et al. [216], who simulated an axial symmetric piston/cylinder geometry. Since turbulence is important in the ICE geometry, leading to large CCVs, both RANS and LES suffer from the limited accuracy related to turbulence and turbulent combustion models used in such simulations. DNS in ICE becomes increasingly important, giving a high-fidelity representation of the flow field in the ICE, even near the wall. However, due to the large dimensions, complex geometry, moving boundary, high rotating speed, and high pressure in real engines, DNS in such configurations is incredibly challenging. As previously done by Schmitt et al. [217, 218], DNS in a simplified ICE might first give a good representation of the flow characteristics in real engines. Hence, the present DNS study also concentrates on the simplified geometry considered in [210, 217, 218]. All simulations are again carried out with the DNS solver *DINO* [7]. Our novel ghost-cell IBM (see Chapter 3) has been used to represent all walls of the complex ICE geometry.

#### 6.3.2 Incompressible simulation of the intake stroke

DNS of the first cycle intake stroke in this simplified ICE is first investigated, using the incompressible formulation of *DINO* for maximal stability. The geometry is shown in Fig. 6.17. The main chamber cylinder has diameter  $B = 75$  mm, the bottom piston moving length

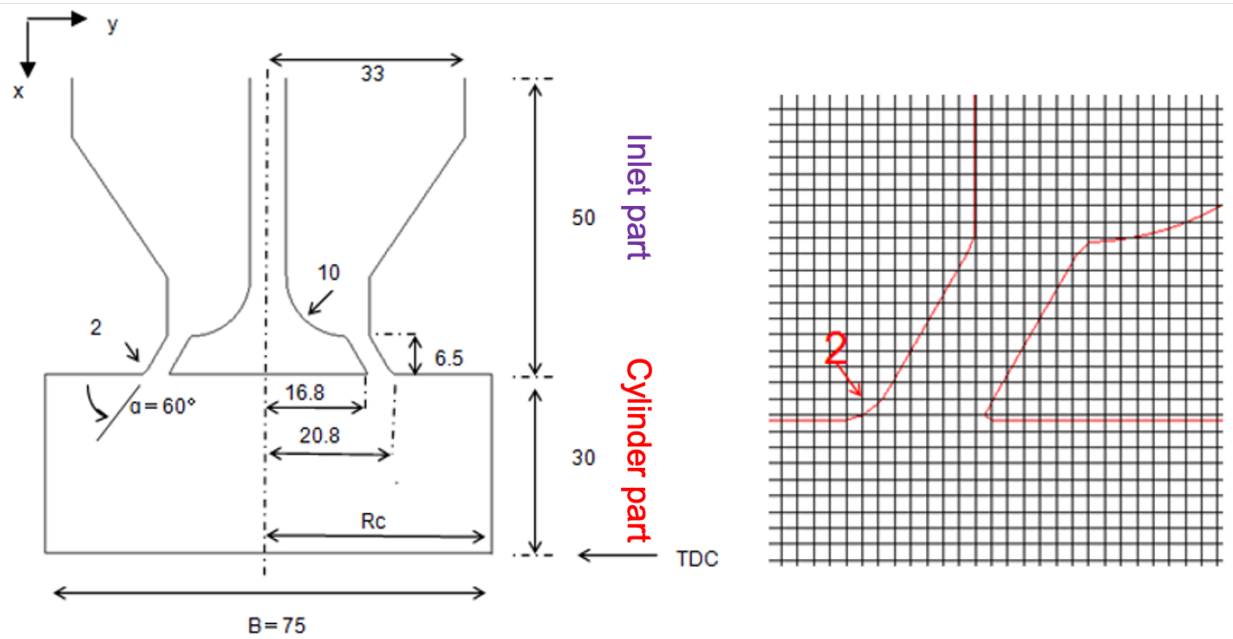


FIGURE 6.17. Schematic of the geometry (in mm, left) and mesh structure near the valve part (right).

is  $S = 60$  mm, the clearance heights from the cylinder head to Top Dead Center (TDC) and Bottom Dead Center (BDC) are 30 mm and 90 mm respectively, allowing a compression ratio of 3. The valve angle is  $30^\circ$  with respect to the cylinder head. The width of the valve is 4 mm. Pure air has been tested first with constant kinematic viscosity  $\nu = 1.846 \times 10^{-5}$  Pa·s and constant density  $\rho = 1.17$  kg/m<sup>3</sup> under conditions of 300 K and 1 bar. The piston speed is 200 rpm, which is just high enough to develop turbulent flow in the main chamber cylinder. The piston velocity is prescribed as  $V_p = 0.2\pi \sin(\frac{\pi t}{0.15})$  in m/s, leading to a mean velocity  $V_{p,mean} = 0.4$  m/s. The whole intake stroke takes 0.15 s. The domain is discretized using regular Cartesian grids, as shown in Fig. 6.17 (right), composed of 0.52 million grid points in two dimensions and 268 million grid points in three dimensions. The Reynolds number at the time when the piston velocity reaches maximum is  $Re_{max} = \frac{V_{p,max}B}{\nu} = 3070$ . The grid resolution is enough to resolve the Kolmogorov length scale. All the wall boundaries are isothermal (constant temperature  $T = 300$  K). The bottom boundary is imposed as a

moving boundary condition, with velocity given by the piston velocity.

2D simulation has been first carried out in this configuration. Figure 6.18 shows the plots of the instantaneous velocity field and vorticity field with time. At the beginning stage (36 °CA), jets are formed and vortex rings are generated. Later, at 77 °CA, many more vortices are created because of the interactions between the jet flows and the bottom wall (moving piston). Kelvin-Helmholtz instabilities can be observed. At 90 °CA, the flow symmetry is already broken because of turbulence. At 135 °CA, a fully turbulent flow has developed within the cylinder.

Then 3D simulation has been done, to provide a more realistic turbulent field. Figure 6.19 shows the comparison of  $V_x/V_{p,mean}$  profile between the experiment [210] and the current DNS at 36 °CA at different axial locations below the cylinder head.  $V_x$  is the axial velocity. It is obvious that the numerical simulation matches quite well the experimental results.

Figure 6.20 shows a three-dimensional view of the intake process. At 45 °CA, gas is pushed in, and jet structure is forming. At 90 °CA, velocity of the bottom piston reaches maximum. The jet flow goes to the side wall and separates. At 135 °CA, the interaction of the jet with walls generates many smaller structures. Finally at 180 °CA, the piston reaches bottom position, and the flow structure becomes complex because of the interaction between recirculation vortices and small-scale turbulence.

#### 6.3.3 Low Mach simulation of the intake stroke

After this first successful test with DINO and the new IBM approach to represent the geometry, the more suitable low-Mach solver in DINO is activated, and the simulation is repeated to check stability. To assess also the proper function of the mixing modules, the inlet region (above the cylinder head) contains now an initial mixture composed of N<sub>2</sub>, O<sub>2</sub> and H<sub>2</sub> with mass fraction of 0.7412, 0.2251 and 0.0375 respectively. This mixture corresponds to



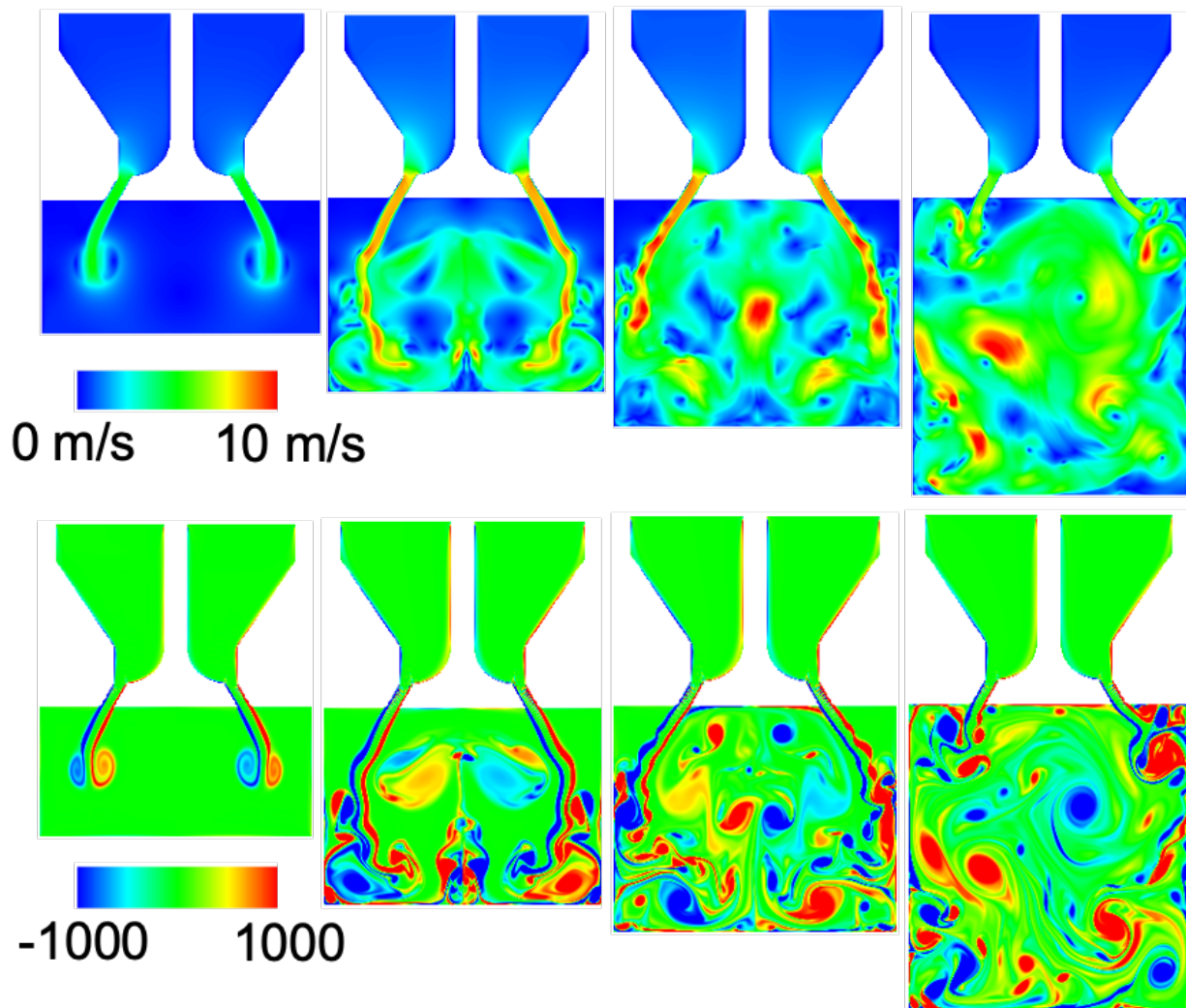


FIGURE 6.18. Instantaneous velocity magnitude (top) and vorticity magnitude (bottom) profile at different time instants (36 °CA, 77 °CA, 90 °CA, 135 °CA from left to right) for the 2D simulation.

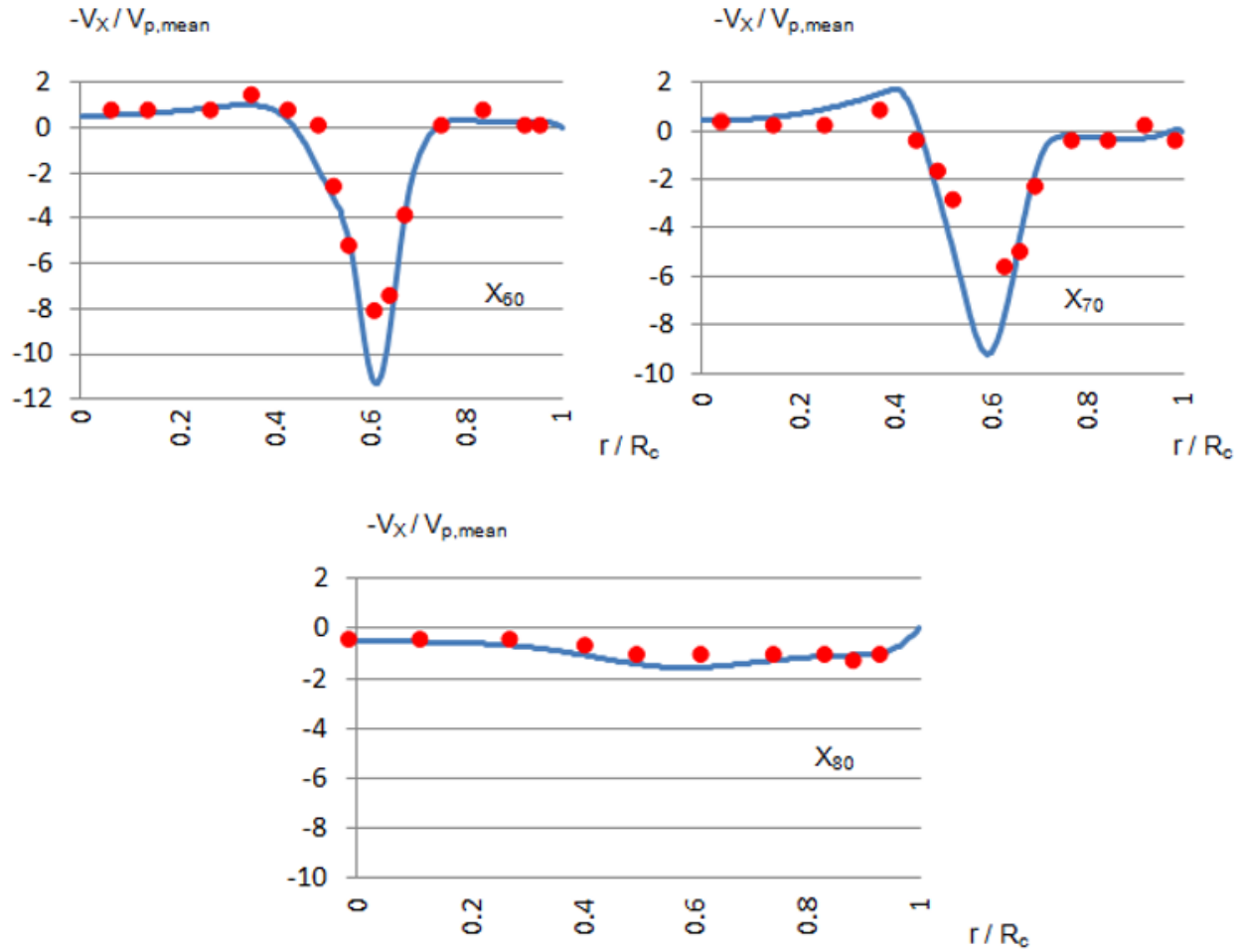


FIGURE 6.19. Comparison of  $V_x/V_{p,mean}$  between experiment and the 3D DNS at 36 °CA at different axial locations below the cylinder head (solid line: DNS, symbols: experiment).  $X_{60}$ ,  $X_{70}$  and  $X_{80}$  represents 10 mm, 20 mm, and 30 mm below the cylinder head, respectively.

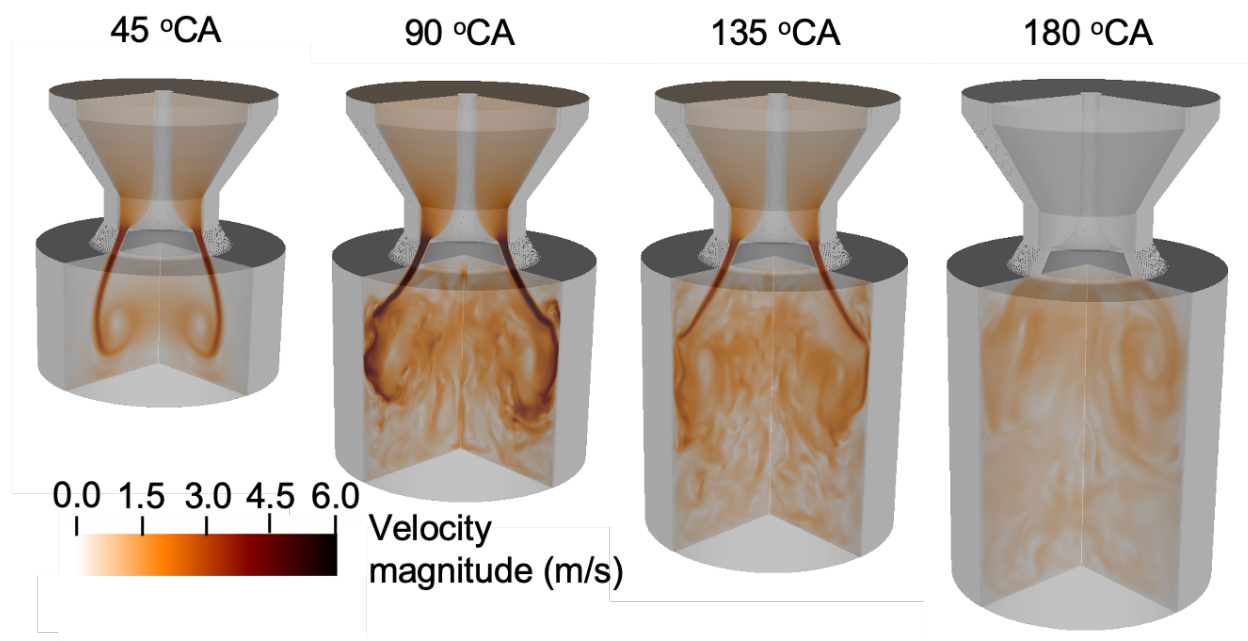


FIGURE 6.20. 3D profiles of the velocity magnitude at 45 °CA, 90 °CA, 135 °CA, 180 °CA.

the mole fraction ratio 2:1 of hydrogen and air. The initial gas temperature in the inlet region is 500 K. The main chamber contains an initial mixture of  $N_2$ ,  $O_2$  and  $H_2O$  with mass fraction of 0.7791, 0.1353 and 0.0855 respectively, which corresponds to the complete combustion of the inlet mixture. The gas here has initial temperature of 900 K. The isothermal wall has constant temperature of 500 K everywhere. All other dynamic conditions (piston speed, compression ratio...) are the same as in the incompressible simulation. A uniform Cartesian grid (composed of 2.1 million grid points) with grid size of 0.073 mm is used to resolve all scales in this two-dimensional simulation.

Figure 6.21 shows the velocity, temperature and  $O_2$  species fields at 16 °CA, 63 °CA, 90 °CA, 120 °CA and 180 °CA, respectively. With the piston movement, the hydrogen/air mixture is drawn into the cylinder. Starting from 120 °CA, the flow fields do not remain symmetrical due to the interaction among the vortex rings. The maximum temperature inside the cylinder decreases from 900 K to almost 700 K because of the turbulent mixing

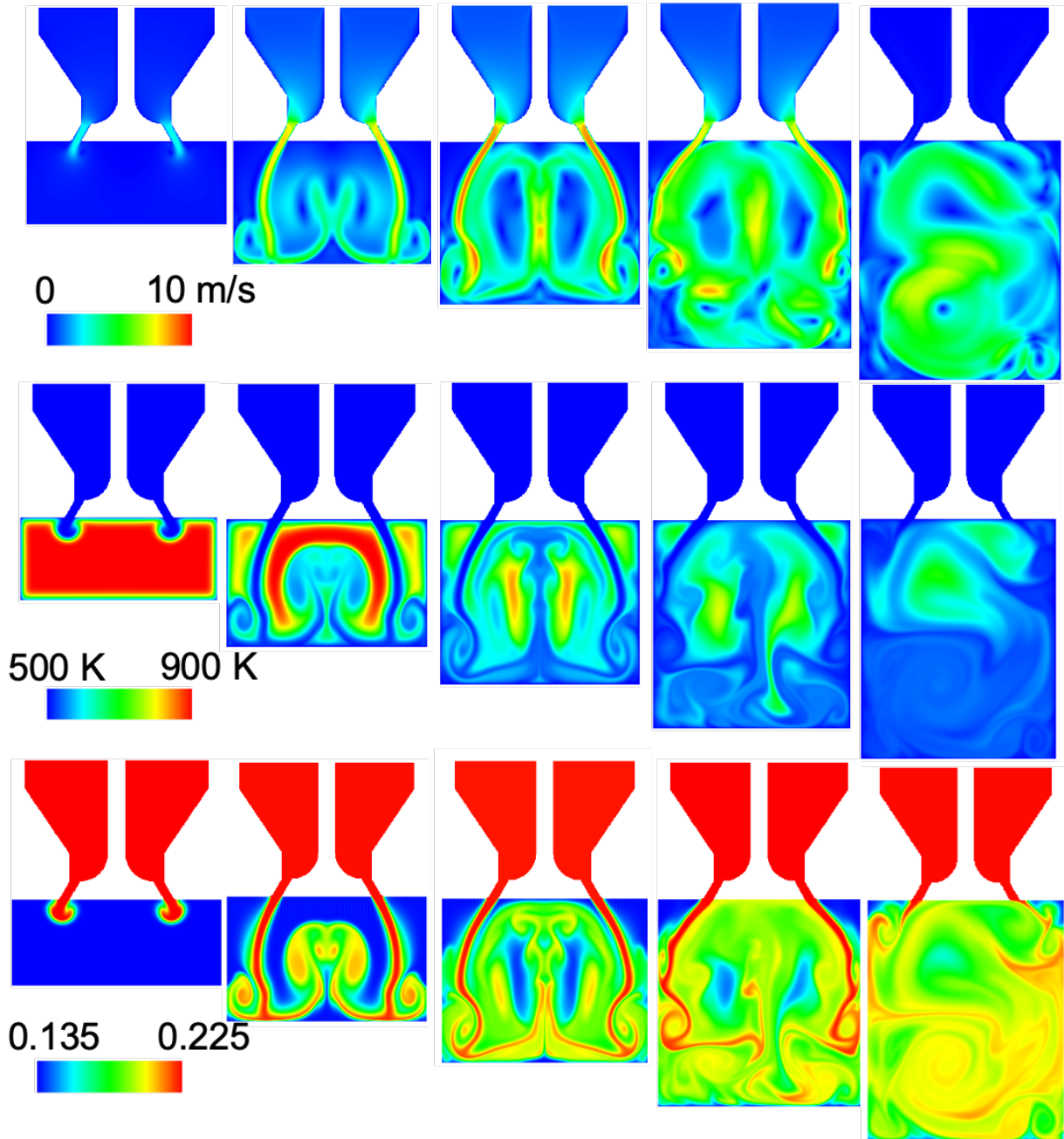


FIGURE 6.21. Velocity magnitude (top), temperature (middle) and  $O_2$  mass fraction (bottom) profile at 16 °CA, 63 °CA, 90 °CA, 120 °CA and 180 °CA (from left to right).

of the hot gases with the inlet cold flows and due to heat losses to the cylinder walls. The species mixing is quite efficient, and tends to generate a homogeneous field, already during intake stroke.

### 6.3.4 Conclusions and perspectives

In this first ICE study using DINO, DNS has been applied to a simplified engine-like geometry. The first cycle intake stroke has been simulated by two different solvers: the incompressible solver (for pure air flow), and the low-Mach solver (for multi-species turbulent mixing), in either 2D or 3D configurations. In the incompressible simulation, the flow characteristics in the intake stroke have been successfully compared with experimental results. The expected development of turbulence during intake can be clearly observed. In the low Mach simulation, the thermal and chemical mixing processes proceed as expected. Since this very academic configuration is not of particular interest, the last part of this chapter will consider instead a real pre-chamber geometry for an ICE burning methane. This is the last and most challenging application of the developed solver.

## 6.4 DNS simulations in real pre-chamber geometry

The pre-chamber geometry, provided by industrial partners, has been finally simulated using DNS. The obtained results are compared to URANS simulations. The current DNS simulation has been setup to verify the accuracy of the URANS models in this configuration and to provide detailed flow characteristics in the real pre-chamber system under engine-like operation conditions.

### 6.4.1 Numerical setup

The 3D pre-chamber geometry is represented by the level-set method with signed distance field. The novel immersed boundary method of Chapter 3 has been used to resolve the boundary conditions. All the DNS simulations are performed by DINO [7]. The reduced methane/air mechanism from [136] has been used, which contains 17 species and 25 reactions. Figure 6.22 shows the schematic of the 3D pre-chamber geometry. Confidentially, the real dimensions of the geometry are not mentioned.

### 6.4.2 Engine operating conditions

The investigated engine has operating speed at 1800 rpm. The exhaust stroke starts from 180 °CA until 360 °CA. Then, the following intake stroke ends at 540 °CA. Finally, the compression stroke lasts from 540 °CA to 720 °CA. In the exhaust stroke, the exhaust gases are pushed out from the main chamber. And starting from 270 °CA, fuel is injected into the pre-chamber. In the intake stroke, fuel is still flowing from the pre-chamber to the main chamber, mixing with the fresh air there. And starting from 645 °CA in the compression stroke, well-mixed lean gases in the main chamber begin to flow back into the pre-chamber, though there is still fuel injection into the pre-chamber. From 710 °CA, there is spark ignition in the pre-chamber, followed by hot jet ignition in the main chamber. Therefore, in the following study, 3 separate DNS have been done for the pre-chamber flow: 1) fuel injection phase (270 °CA - 297 °CA); 2) back-flow phase (645 °CA - 710 °CA) and 3) spark ignition phase (start from 710 °CA).

### 6.4.3 Fuel injection phase

DNS has been firstly carried out for the fuel injection phase from 270 °CA to 297 °CA. At this time, the obtained filling level with methane can be assessed. All walls are isothermal at a

temperature of 393 K. Pure methane is injected into the system through the 8 thin capillaries, with diameter less than 1 mm. The injection speed is 354 m/s. The initial gas inside the pre-chamber is pure air, with pressure around 3 bar. These initial conditions correspond to the quasi-steady state in the injection process, as predicted by URANS. The 5 bottom outlet pipes are connecting to the main chamber and are approximated with zero-gradient pressure condition in this simulation. A total of 60 million grid points have been used with mesh size of 0.04 mm, which is enough to resolve the Kolmogorov scale (the smallest value of the Kolmogorov scale during the simulation is 0.058 mm.). The simulation takes almost 1 million CPU hours on supercomputers in Munich (SuperMUC).

In Fig. 6.22, the iso-surface of methane mass fraction at 0.01 is plotted at different crank angles. At 270 °CA, the methane gas begins to flow into the pre-chamber volume through the 8 thin capillaries. At 276 °CA, the methane flow has already mixed and propagated through the 6 pipes connecting the top and bottom part of the pre-chamber volume. At 282 °CA, the flow goes to the cylinder wall of the bottom pre-chamber and spreads out. Until 295 °CA, the pre-chamber volume is full of methane with mass fraction larger than 0.01. The iso-surface profile is highly turbulent during the whole process and a lot of small structures can be observed. The mixing between the injected methane and the initial air in the pre-chamber is very efficient.

Figure 6.23 shows the comparison of the methane mass fraction iso-surface ( $Y_{CH_4} = 0.01$ ) between DNS and URANS at different crank angles from the bottom perspective view. All the URANS results shown in this Chapter have been obtained by a partner group (V. Sazonov, group of Prof. H. Rottengruber) using AVL FIRE. It is seen that the corresponding iso-surface in DNS has much more small turbulent structures while URANS predicts a smoother iso-surface. However, the overall propagation of the iso-surface is very similar at different crank angles. One obvious difference between DNS and URANS is the

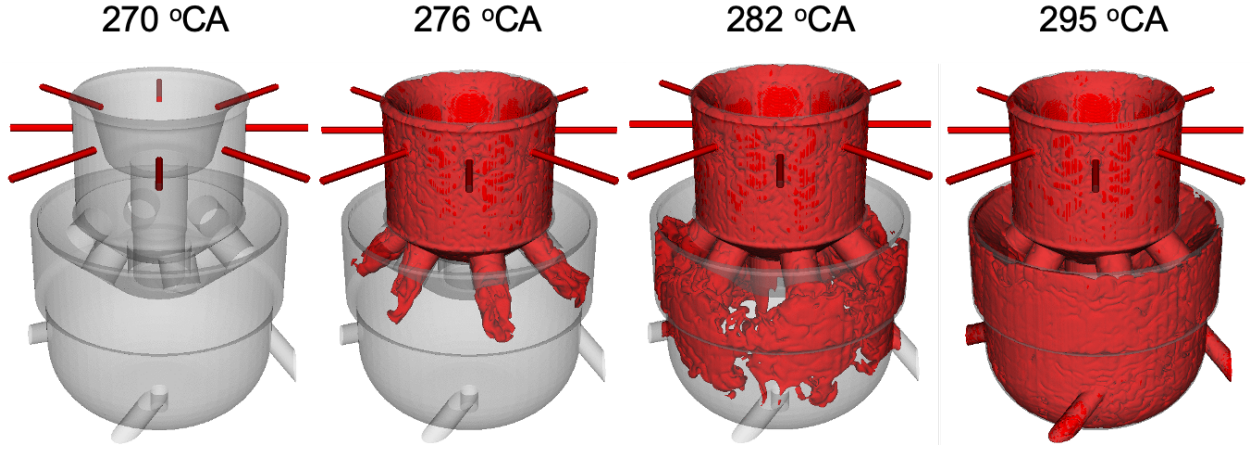


FIGURE 6.22. Iso-surface of methane mass fraction ( $Y_{CH_4} = 0.01$ ) at 270 °CA, 276 °CA, 282 °CA, and 295 °CA (from left to right).

propagation of the methane iso-surface in the central annular gap. As is seen at crank angle 278.2 °CA, and more obvious at 281.8 °CA, the mass flow rate of the methane gas through the central annular gap is much larger in URANS than in DNS.

The difference between URANS and DNS results for methane mass flow is more obvious in Fig. 6.24, showing the vertical cut plane of the methane mass fraction distribution. The turbulent structure of the methane gas in DNS is clearer. The amount of methane flow through the central annular gap is obviously much more in URANS. At 278 °CA, the methane mass fraction near the inner cylinder wall above the central gap is relatively low in DNS, which will directly affect the methane mass flow rate in the central gap, explaining the differences.

To check further whether the methane mass fraction distribution is dominated by convection or diffusion, the right-hand-side term of the species equation for  $CH_4$  has been computed for the convection and diffusion term as follows:

$$R_{\text{convection}} = -u_j \frac{\partial Y_{CH_4}}{\partial x_j}, \quad (6.10)$$



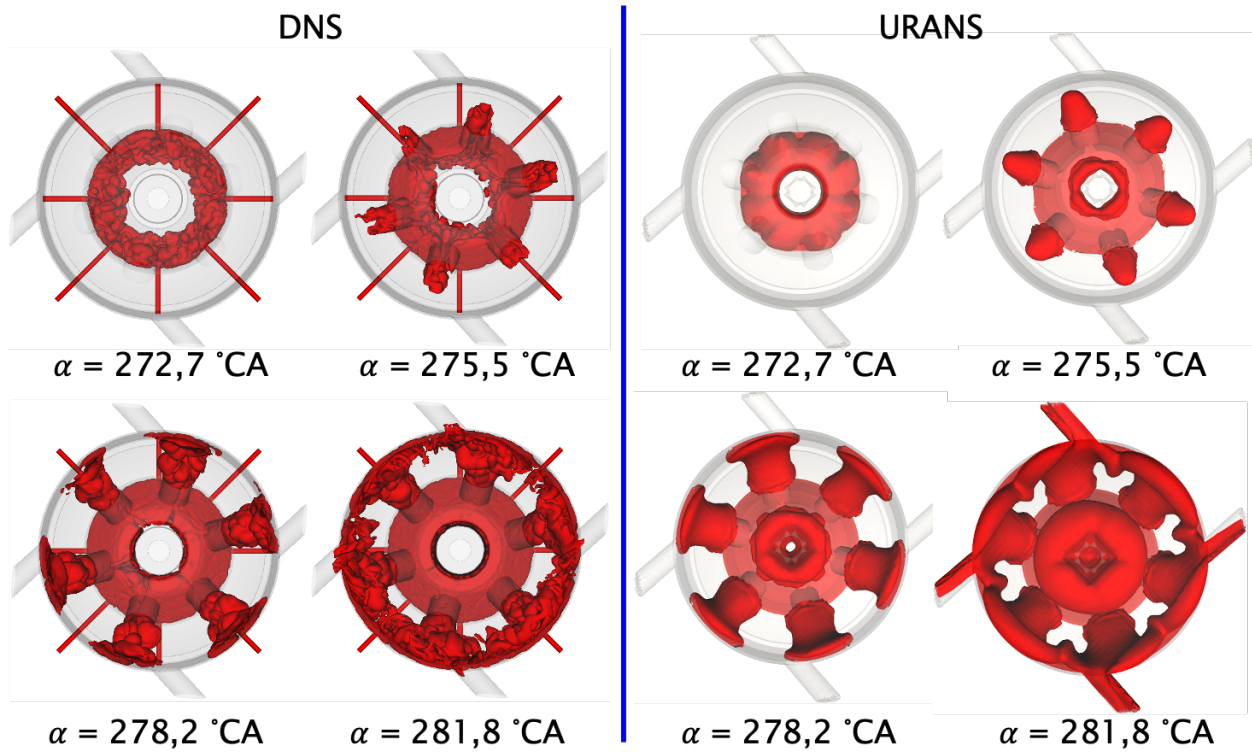


FIGURE 6.23. Iso-surface of methane mass fraction ( $Y_{CH_4} = 0.01$ ) at  $272.7^\circ\text{CA}$ ,  $275.5^\circ\text{CA}$ ,  $278.2^\circ\text{CA}$ , and  $281.8^\circ\text{CA}$ : comparison between DNS (left) and URANS (right).

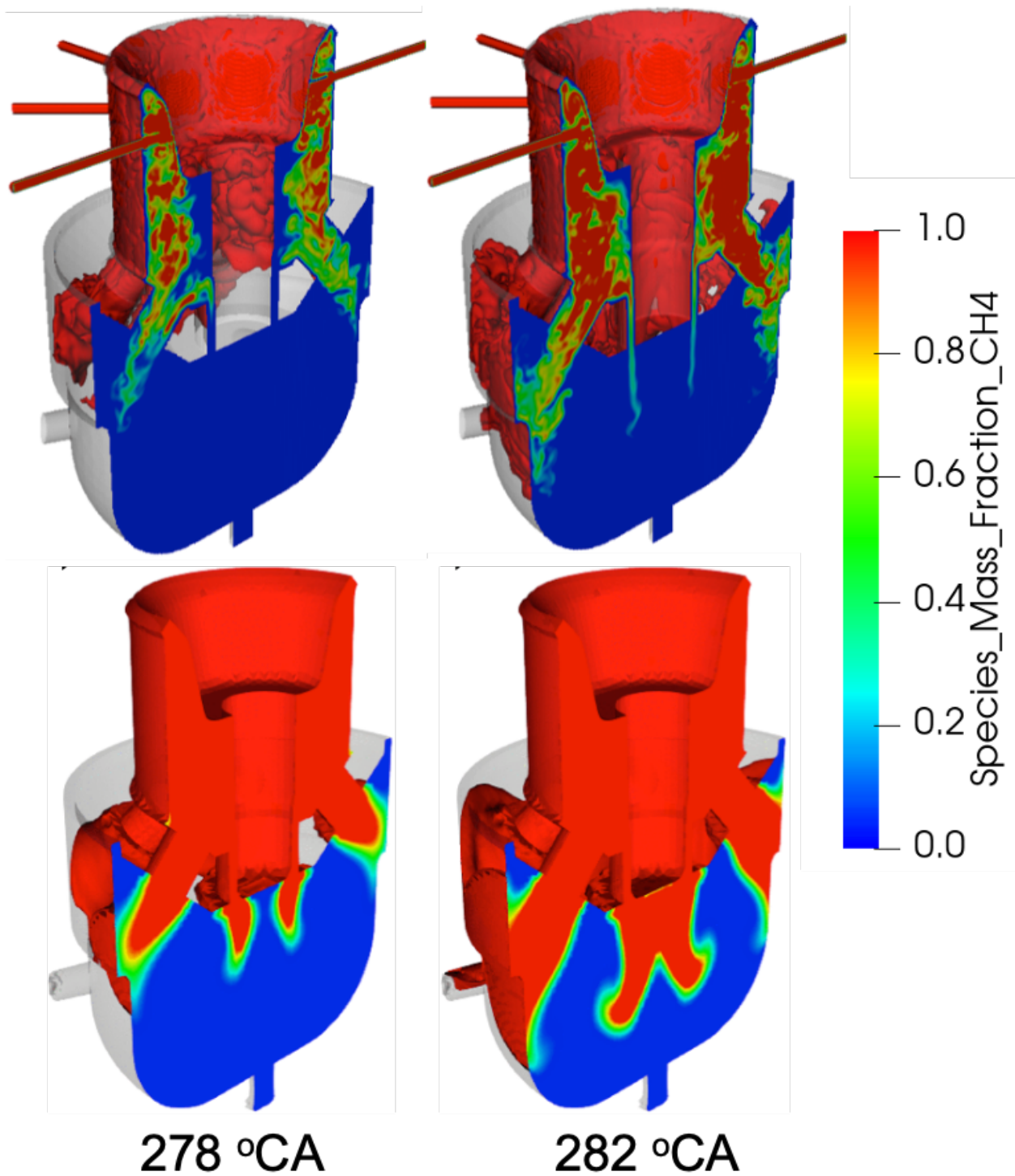


FIGURE 6.24. Vertical cut plane showing the methane mass fraction distribution with iso-surface of the methane mass fraction at 0.01: comparison between DNS (top) and URANS (bottom) at 278 °CA (left) and 282 °CA (right).

$$R_{\text{diffusion}} = -\frac{1}{\rho} \frac{\partial \rho Y_{\text{CH}_4} V_j}{\partial x_j}, \quad (6.11)$$

where  $V_j$  represent the  $j$ th component ( $j = 1, 2, 3$ ) of methane molecular diffusion velocity. Figure 6.25 shows the methane mass contribution by convection and diffusion in the central 2D cut plane at 282 °CA. It is clear that the mass flow of methane is mostly dominated by convection. Thus, getting properly the turbulent velocity field is essential to predict the distribution of methane mass fraction.

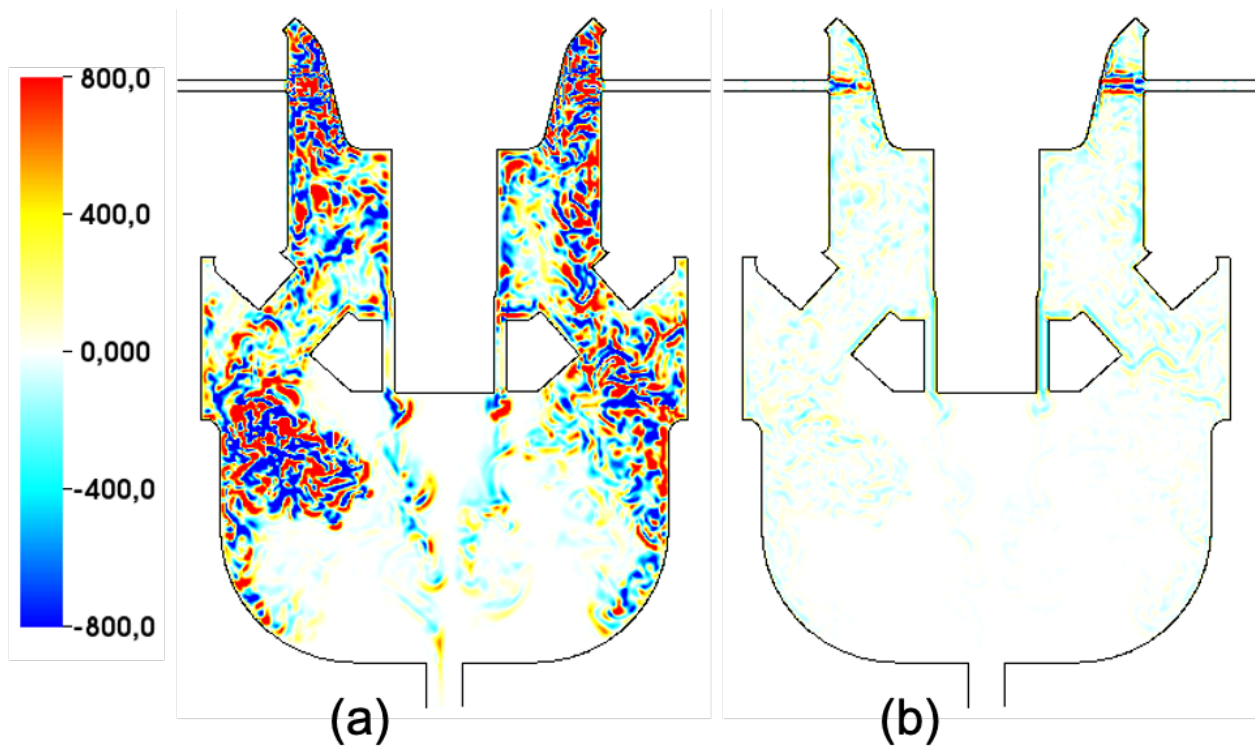


FIGURE 6.25. 2D central cut plane showing the contribution of (a) convection and (b) diffusion at 282 °CA regarding methane mass fraction.

Figure 6.26 shows the 2D cut plane of the velocity field for DNS and URANS at 277 °CA, 282 °CA, and 290 °CA. As is seen in DNS results, at 277 °CA, the velocity magnitude is lower near the inner cylinder wall above the central gap, resulting in lower methane mass fraction there as clearly shown in Fig. 6.24. At 282 °CA, though the velocity in the central

gap is large, the methane mass fraction near the upper inlet of the central gap is relatively low. Thus the convected methane mass through the gap is less. Until 290 °CA, the flow convection through the connecting pipes is large, resulting in large CH<sub>4</sub> mass fraction near the outer cylinder wall of the lower pre-chamber. For URANS, the velocity magnitude is large near the inner cylinder wall above the central gap, which combined to the larger methane mass fraction there, leads to a much larger methane mass flow rate through the central gap. The difference between DNS and URANS for the velocity field near the inner cylinder wall is mainly due to turbulence-wall interaction, which highly depends on how the turbulence is resolved. In DNS, the flow is highly turbulent and the interaction between the high-speed jets and the wall generates more small structures.

#### 6.4.4 Back-flow phase

The back-flow phase has been simulated from 645 °CA to 720 °CA. The back-flow gas from the 5 bottom pipes (1 vertical and 4 tangential pipes connecting the bottom chamber surface to the main cylinder) is a methane/air mixture with equivalence ratio of 0.5, which corresponds to the fully-mixed gas in the main chamber at the beginning of the compression phase, as estimated from URANS simulations. The initial gas inside the pre-chamber is pure methane. All walls are isothermal at temperature of 393 K and the initial pre-chamber gas temperature is 417 K. The initial pressure in the pre-chamber is 8.52 bar. The time-varying inlet gas velocity and thermodynamic pressure is following the curve in Fig. 6.27, which has been pre-computed in 1D by V. Sazonov. A total of 80 million grid points have been used with mesh size of 0.03 mm. In total, 2.11 million CPU hours have been consumed for this compression simulation.

In Fig. 6.28, the iso-surface of methane mass fraction at 0.6 is plotted at different crank angles. At 645 °CA, the lean mixture from the main chamber begin to flow into the pre-

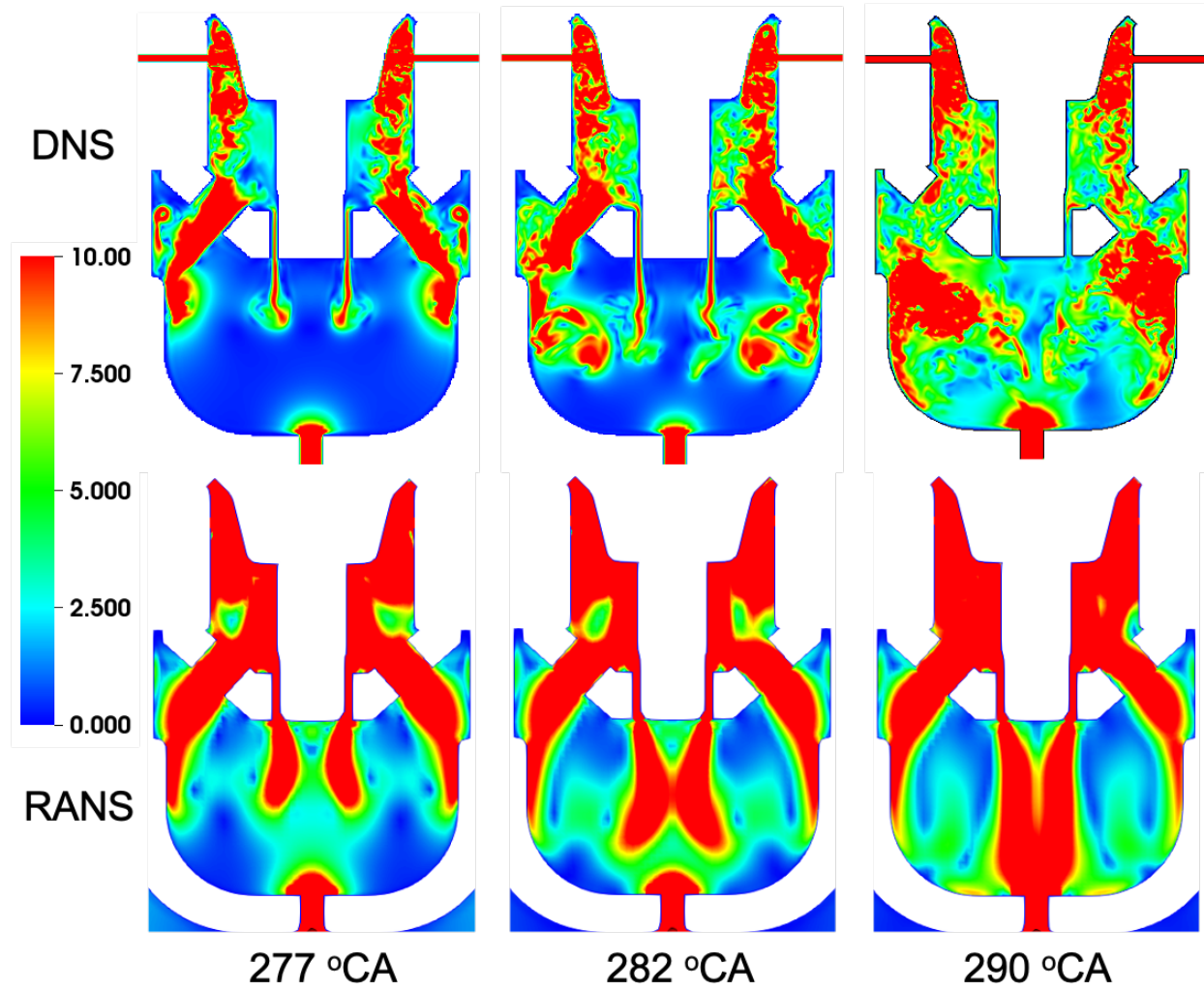


FIGURE 6.26. 2D central cut plane showing the velocity magnitude profile for DNS (top) and URANS (bottom) at 277 °CA, 282 °CA, and 290 °CA.

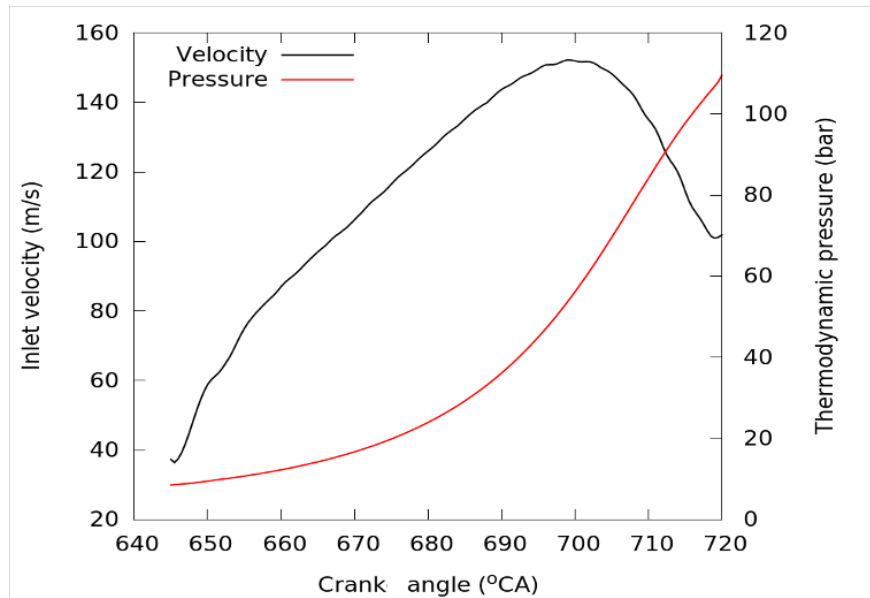


FIGURE 6.27. Temporal evolution of inlet velocity and thermodynamic pressure in the pre-chamber, as obtained in a partner group (V. Sazonov, Prof. H. Rottengruber) from 1D simulation.

chamber through the 5 inlet pipes. At 650 °CA, turbulent jet structures are formed, and begin to interact. At 657 °CA, the jets are mixed together and lead to a swirling flow in the bottom part of the pre-chamber. At 663 °CA, the injected leaner mixture fills the whole bottom part and starts flowing toward the top part of the pre-chamber.

The DNS results are compared with URANS results at 680 °CA in Fig. 6.29 regarding velocity profile. From the comparison, it is seen that the overall distribution of velocity matches fairly well, while the details are different. In both simulations, high-speed flows appear in the jet inflow region and near the outer cylinder wall of the bottom pre-chamber. Obviously, the resulting turbulent structures are far more complex in DNS.

Figure 6.30 shows a comparison of the temperature profile between DNS and URANS. The overall temperature distributions are also similar. The profile is more turbulent and the heat of the hot jet is transported away more rapidly in DNS, while the jet temperature



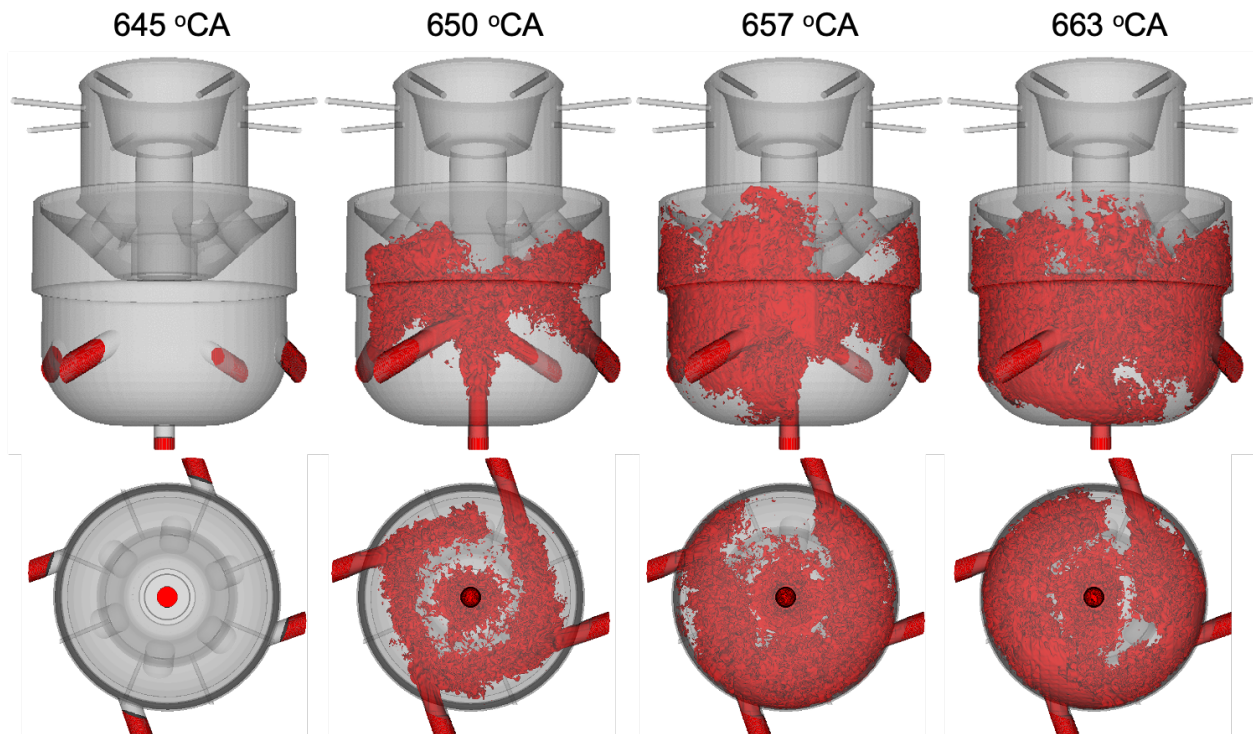


FIGURE 6.28. Iso-surface of methane mass fraction ( $Y_{CH_4} = 0.6$ ) at 645 °CA, 650 °CA, 657 °CA, and 663 °CA (from left to right).

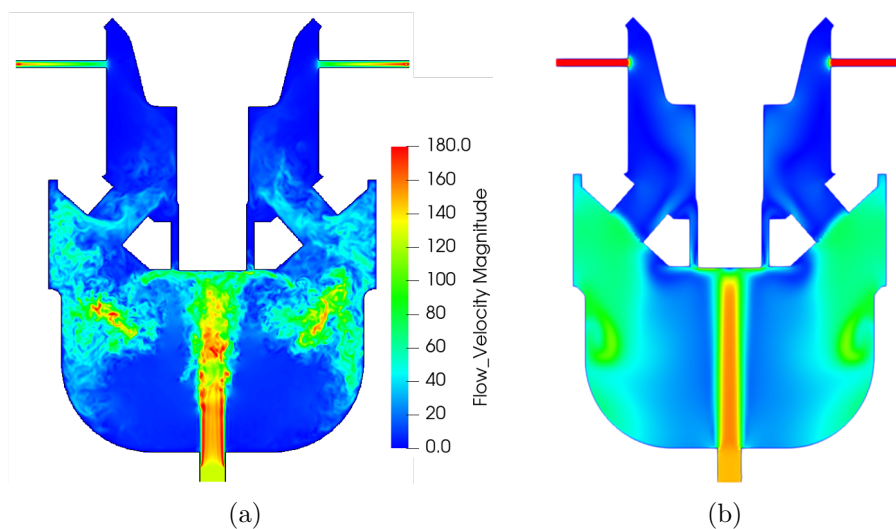


FIGURE 6.29. 2D central cut profile of velocity magnitude at 680 °CA (a) using DNS and (b) using URANS.

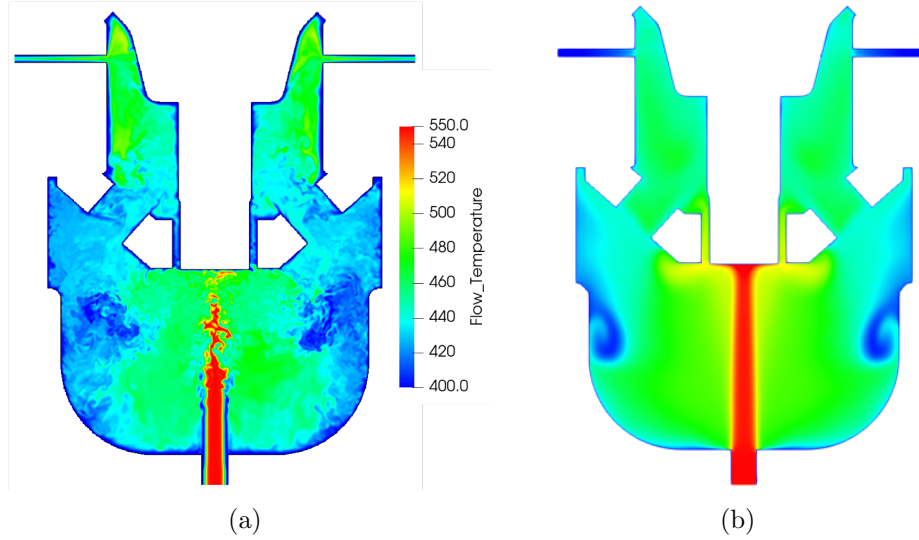


FIGURE 6.30. 2D central cut profile of temperature at 680 °CA (a) using DNS and (b) using URANS.

remains high until it collides with the wall in URANS.

Turbulent fluctuations are very important for the practical process, and can only be accurately estimated in DNS. Figure 6.31 shows the mean velocity profile and the velocity fluctuations in the central 2D cut-plane of the pre-chamber at 710 °CA. The mean profile and fluctuations are computed by averaging over 20 crank angles (from 690 °CA to 710 °CA). Looking at Fig. 6.31(b), the absolute velocity fluctuations are quite high in some local regions, exceeding the level of the mean profile by up to a factor 5, which is considerable.

Figure 6.32 shows the time evolution of the peak Reynolds number ( $Re$ ) computed in the whole pre-chamber (left), and in the central gap (right). The peak  $Re$  in the pre-chamber is computed based on the peak velocity in the turbulent, high-speed jet flow, while the peak  $Re$  in the central gap is computed based on the thin gap flow. The peak Reynolds number in the thin gap is relatively low and the flow is not so turbulent, which should facilitate the



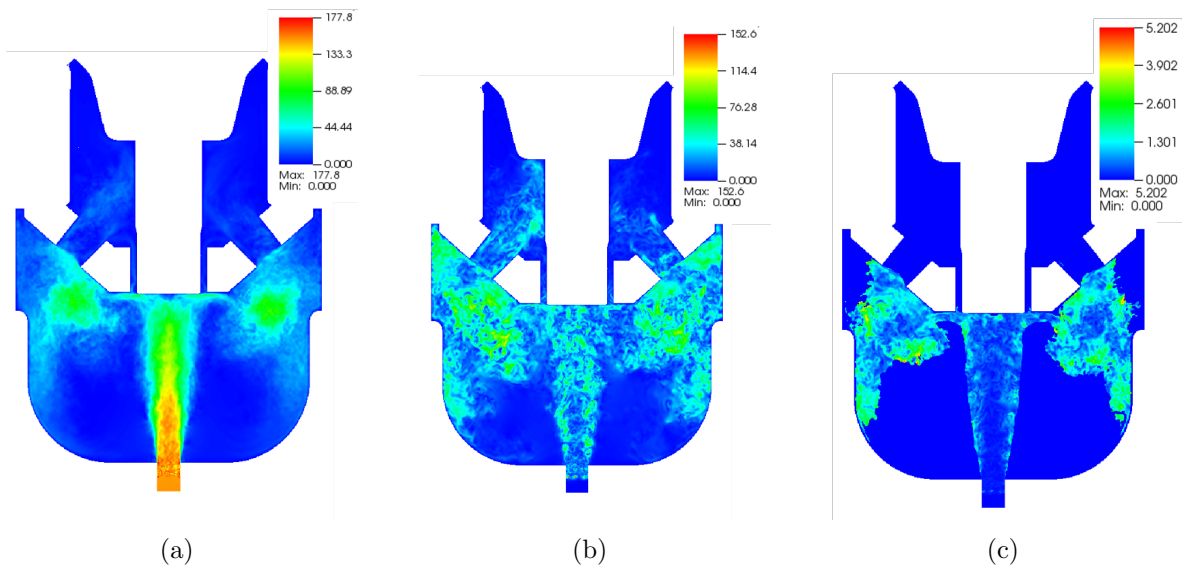


FIGURE 6.31. (a) Mean velocity profile (in m/s); (b) absolute velocity fluctuations (in m/s) and (c) relative velocity fluctuations in the 2D pre-chamber central cut plane at 710 °CA.

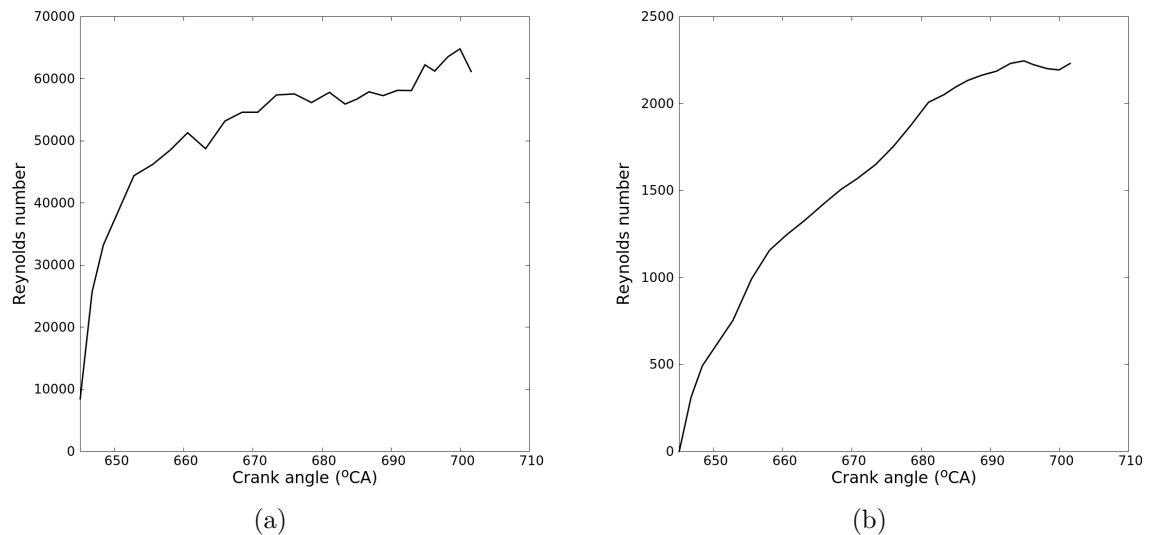


FIGURE 6.32. Peak Reynolds number vs. time (a) in the whole pre-chamber and (b) in the central gap connecting both parts of the pre-chamber.

future ignition in that region.

### 6.4.5 Spark ignition phase

Ignition is initiated in DNS by placing a numerical spark. The spark is placed at the bottom inlet of the central gap. The spark configuration is similar to that discussed in Section 6.2, with energy deposition as a Gaussian distribution in both time and space.

Since the combustion DNS simulation would be too expensive in such a large geometry and high pressure up to about 100 bar, the domain has to be reduced to enable DNS simulations. Thus, the region near the spark location is extracted for the combustion simulation. The domain is reduced to a few mm in each direction, including the whole central gap geometry. The reduced geometry is shown in Fig. 6.33.

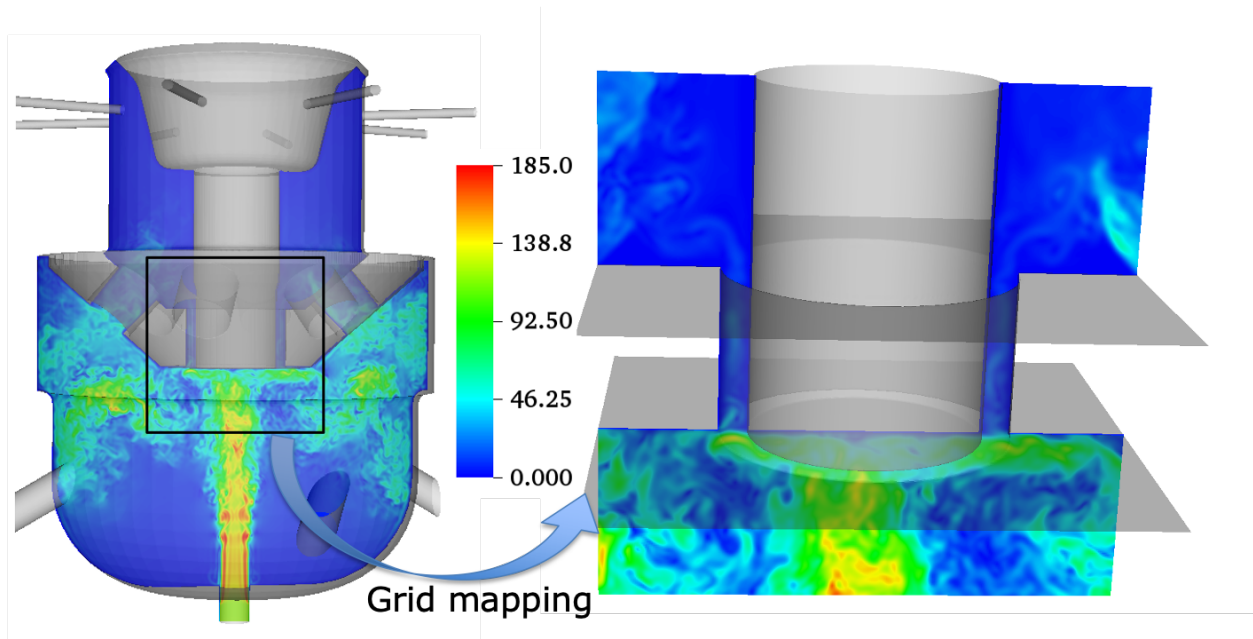


FIGURE 6.33. Turbulent velocity profile in the compression simulation at 710 °CA (left), and derived initial profile for ignition simulation (right).

The turbulent profile at the end of the compression simulation (at 710 °CA) is read as the initial profile for the ignition simulation. The compression simulation relies on a grid with

$618 \times 480 \times 480$ , while the ignition simulation employs  $1024 \times 1024 \times 1024$  grid points in a smaller domain. Mapping of the turbulent profile from the old grid to the new grid is done using a trilinear interpolation. The initial pressure is 88 bar. Since the temperature profile near the spark region is almost homogeneous at the end of the compression phase, the average temperature (550 K) is used as the initial temperature for the gas mixtures. The isothermal wall temperature is 393 K. A homogeneous mixture composition with equivalence ratio of 0.83 is employed. The initial velocity profile, mapped from the compression simulation, is shown in Fig. 6.33.

Figure 6.34 shows first simulation results with spark parameters:  $\Delta_s = 3$  mm,  $\Delta_t = 0.5$  ms,  $t_0 = 0$  ms and  $\epsilon = 1.2$  J. The OH mass fraction and temperature profiles are plotted at different time instants. As is seen, the ignition spot of the spark is highly influenced by the turbulent flow field. The high-speed flow brings the ignition spot toward the lower-right region, preventing propagation into the central gap. This confirms findings from Chapter 5: the turbulent flow strongly affects the ignition delay and ignition probability. Comparisons between the characteristic time of the turbulent flow and the ignition delay time under laminar condition will determine how much the turbulent flow conditions will affect the ignition delay. Future study will concentrate on analyzing the key features of ignition and initial flame propagation in the pre-chamber.

### 6.4.6 Conclusions and perspectives

DNS has been carried out to simulate the reacting gas flow inside an industrial pre-chamber geometry for a selected range of crank angles during the intake stroke and the compression stroke. Highly turbulent, complex flow structures are observed in the process. The DNS results have been compared with URANS results under the same conditions. The overall distribution of the profiles are in good agreement, but DNS shows as expected more turbulent

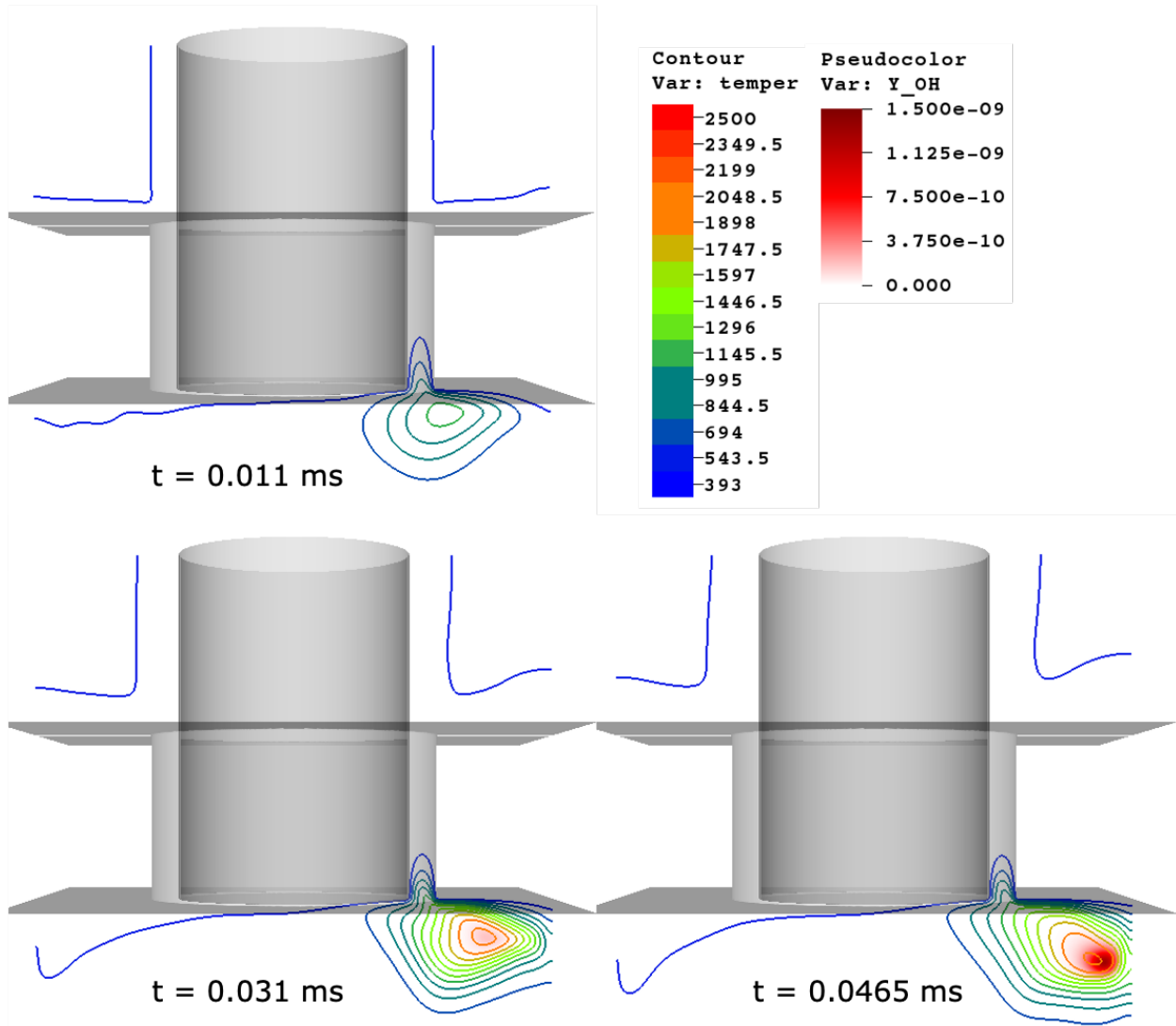


FIGURE 6.34. OH mass fraction (color plot) and temperature contours (isolines) at the 2D central cut plane through the initial spark location at  $t = 0.011$  ms,  $t = 0.031$  ms, and  $t = 0.0465$  ms revealing the progress of ignition below the central gap in the pre-chamber.

structures. Even qualitative differences are observed, for instance regarding the flow structures obtained after impingement of a high-speed jet on a wall. This has consequences regarding mixing quality.

Finally, the results from the compression stroke are used to investigate spark-induced ignition in the resulting flow. Due to the tremendous complexity of this problem, only a smaller part of the pre-chamber can be simulated with DNS. This is, however, sufficient to check that ignition is indeed possible under such conditions. Unfortunately, it is not possible to show and discuss all the results obtained in this configuration due to confidentiality issues. However, the results shown demonstrate clearly that DNS is now mature for real-life applications, but obviously require highly efficient numerical procedures and high-performance computers.



# Chapter 7

## Conclusions and Outlook

### 7.1 Conclusions

In this dissertation, tools for direct numerical simulations have been developed with the final objective of investigating ignition and flame propagation in a complex geometry like e.g. ICE. Our in-house combustion solver DINO has been used for all the simulations.

To extend DINO for flow simulations in complex geometry, a novel ghost-cell immersed boundary method has been first developed. This IBM is computationally more efficient than classical methods. It is also flexible and can be combined with different time iteration and spatial discretization methods. Implementation and parallelization of this IBM is straightforward. Validation reveals an accuracy close to second order with smaller absolute truncation errors. This IBM is able to deal with complex 3D geometries as well as moving geometries.

To enable later validations by comparison with experimental data, heat release, as the most important quantity for combustion research, has been assessed by DNS. Heat release markers, that can be used to reconstruct the heat release profile in experiments, have been found by systematic DNS studies for different fuels. For premixed syngas flames, two markers are identified ( $\bar{c}_{HCO}^{1.5} \times \bar{c}_{OH}^{0.75}$  and  $\bar{c}_{CH_2O}^{0.32} \times \bar{c}_{OH}^{0.8}$ ) that can accurately represent the location of high heat release and also the flame topology (thickness, curvature). For premixed hydrogen

---

flames, the marker  $\bar{c}_{O_2}^{0.46} \times \bar{c}_{OH}^{0.40}$  is identified to give a robust and accurate approximation of the heat release distribution. Finally, for premixed methane flames, two markers are identified ( $\bar{c}_{OH}^{1.07} \times \bar{c}_{CH_2O}^{1.17}$  and  $\bar{c}_H^{1.11} \times \bar{c}_{CH_2O}^{0.86}$ ). The latter combination is slightly better to predict heat release over its whole range, even for quenching flames. The proposed markers would enable a more accurate comparison between experiments and simulations regarding heat release. Unfortunately, the experiments planned in the final project have been delayed and have not started when writing this thesis.

Ignition itself is a very complicated process. Systematic DNS have been done to investigate the relationship between hot-spot ignition probability and turbulence intensity for hydrogen/air mixtures. An ignition diagram was first obtained for laminar conditions. The ignition delay decreases as the initial kernel temperature increases, and first decreases, then keep constant as the kernel radius increases. Higher turbulence intensity results in longer ignition delay time and lower ignition probability. The importance of the relative scale of ignition delay compared to the characteristic time scale of turbulence is confirmed.

Finally, the turbulent flow and ignition in engine-related geometries are investigated. Firstly, pre-chamber hot jet ignition characteristics have been studied, and 3 transient ignition processes have been identified. The factors affecting ignition or misfire events in the main chamber have been analyzed. It is found that the characteristic time-scales of the hot jet are important to successfully initiate ignition. Turbulence enhances the chemical and enrichment effect at local spots in the main chamber, leading to easier local just-ignition. On the other hand, local just-ignition spots are more easily dissipated away by a higher turbulence intensity, thus resulting in a longer global ignition delay. Then, the first cycle stroke in a simplified internal combustion engine geometry has been simulated using DINO, confirming that DNS is possible in such configurations. Finally, a real pre-chamber geometry has been fully represented in DINO. The relevant part of the intake and of the compression



process have been simulated and the resulting features have been analyzed in terms of mixing and turbulent fluctuations. At the end, a numerical spark has been implemented, and ignition studies have been started using DINO.

## 7.2 Outlook

The current work concentrates on

1. Pursuing the DNS study regarding ignition and flame development in the industrial pre-chamber geometry. The ignition and combustion simulation will follow the current non-reacting flow simulation, using the obtained turbulent flow field. To enable full simulation, chemistry tabulation techniques will be used. The final DNS results will be compared with the RANS results and experimental results in a quantitative manner. Turbulence statistics and flame dynamics in the prechamber will be analyzed in detail.
2. Investigating the NO<sub>x</sub> emission in ammonia/hydrogen/air flames. Detailed diffusion models are checked for NH<sub>3</sub>/H<sub>2</sub>/air flame simulations. The optimal HRR marker for such flame is being analyzed through artificial neural networks (ANN).
3. Using machine learning techniques for chemistry tabulation and flame tabulation. On-the-fly artificial neural network has been implemented to replace the ODE integration in chemistry computation. Further work are being done to tabulate the flame with well designed ANN.
4. Studying large-scale turbulence structures in channel flow. Data-driven methods are being applied to analyze scale separation and mode decomposition in high Re turbulent flows.

# Bibliography

- [1] B. Looney. Statistical review of world energy. Technical report, The British Petroleum Company Limited, 2020.
- [2] B. Lewis and G. von Elbe. *Combustion, Flames and Explosions of Gases*. Academic Press Inc, 3rd edition, 1987.
- [3] C.K. Law. A compilation of experimental data on laminar burning velocities. In N. Peters and B. Rogg, editors, *Reduced Kinetic Mechanisms for Applications in Combustion Systems*, volume 15 of *Lecture Notes in Physics monographs*. Springer-verlag, 1993.
- [4] C. Müller, B. Morcinkowski, C. Schernus, K. Habermann, and T. Uhlmann. Development of a pre-chamber for spark ignition engines in vehicle applications. In *Ignition Systems for Gasoline Engines: 4th International Conference, 2018, Berlin, Germany.*, pages 261–274, 2018.
- [5] P.L. Pitt, J.D. Ridley, and R.M. Clements. An ignition system for ultra lean mixtures. *Combust. Sci. Technol.*, 35(5-6):277–285, 1983.
- [6] C. Chi, B.J. Lee, and H.G. Im. An improved ghost-cell immersed boundary method for compressible flow simulations. *Int. J. Numer. Meth. Fluids*, 83(2):132–148, 2017.
- [7] A. Abdelsamie, G. Fru, T. Oster, F. Dietzsch, G. Janiga, and D. Thévenin. Towards direct numerical simulations of low-Mach number turbulent reacting and two-phase flows using immersed boundaries. *Comp. Fluids*, 131:123–141, 2016.
- [8] T. Poinso and D. Veynante. *Theoretical and Numerical Combustion*. R. T. Edwards, 2nd edition, 2005.
- [9] J. de Charentenay, D. Thévenin, and B. Zamuner. Comparison of direct numerical simulations of turbulent flames using compressible or low-mach number formulation. *Int. J. Numer. Meth. Fluids*, 39:497–515, 2002.

## Bibliography

- 
- [10] G. Fru. *Direct numerical simulation of turbulent flames on parallel computers*. PhD thesis, Otto-von-Guericke-Universität Magdeburg, 2012.
- [11] A. Abdelsamie. *Direct numerical simulations of turbulent flow and spray combustion*. PhD thesis, Otto-von-Guericke-Universität Magdeburg, 2017.
- [12] A. Majda and J. Sethian. The derivation and numerical solution of the equation for zero Mach number combustion. *Combust. Sci. Technol.*, 42:185–205, 1985.
- [13] R. Hilbert, F. Tap, H. El-Rabii, and D. Thévenin. Impact of detailed chemistry and transport models on turbulent combustion simulations. *Prog. Energy Combust. Sci.*, 30:165–193, 2004.
- [14] A. Ern and V. Giovangigli. *Multicomponent Transport Algorithms*, volume 24. Lecture Notes in Physics Monographs, Springer, 1994.
- [15] D.G. Goodwin, H.K. Moffat, and R.L. Speth. available at <http://www.cantera.org>, 2015.
- [16] W.H. Press, S.A. Teukolsky, W.T. Vetterling, and B.P. Flannery. *Numerical Recipes in FORTRAN*. Cambridge University Press, New York, 2nd edition, 1992.
- [17] J. Kim and P. Moin. Application of a fractional-step method to incompressible Navier-Stokes equations. *J. Comput. Phys.*, 59(2):308–323, 1985.
- [18] D.L. Brown, R. Cortez, and M.L. Minion. Accurate projection methods for the incompressible Navier–Stokes equations. *J. Comput. Phys.*, 168(2):464–499, 2001.
- [19] F. Lucci, A. Ferrante, and S. Elghobashi. Modulation of isotropic turbulence by particles of Taylor length-scale size. *J. Fluid Mech.*, 650:5–55, 2010.
- [20] K.E. Niemeyer, N.J. Curtis, and C. Sung. pyJac: Analytical Jacobian generator for chemical kinetics. *Comput. Phys. Commun.*, 215:188–203, 2017.
- [21] S. Laizet, E. Lamballais, and J.C. Vassilicos. A numerical strategy to combine high-order schemes, complex geometry and parallel computing for high resolution DNS of fractal generated turbulence. *Comp. Fluids*, 39(3):471–484, 2010.

## Bibliography

- 
- [22] S. Laizet and N. Li. Incompact3d: A powerful tool to tackle turbulence problems with up to  $O(10^5)$  computational cores. *Int. J. Numer. Meth. Fluids*, 67(11):1735–1757, 2011.
- [23] J.W. Cooley, P.A.W. Lewis, and P.D. Welch. The fast Fourier transform algorithm: Programming considerations in the calculation of sine, cosine and Laplace transforms. *Journal of Sound and Vibration*, 12(3):315–337, 1970.
- [24] P. N. Swarztrauber. Symmetric FFTs. *Mathematics of Computation*, 47(175):323–346, 1986.
- [25] N. Li and S. Laizet. 2DECOMP&FFT - a highly scalable 2D decomposition library and FFT interface. In *Cray User’s Group 2010 Conference*, 2010.
- [26] D. Thévenin, O. Gicquel, J. de Charentenay, R. Hilbert, and D. Veynante. Two- versus three-dimensional direct simulations of turbulent methane flame kernels using realistic chemistry. *Proc. Combust. Inst.*, 29:2031–2039, 2002.
- [27] D. Thévenin, F. Behrendt, U. Maas, B. Przywara, and J. Warnatz. Development of a parallel direct simulation code to investigate reactive flows. *Comput. Fluids*, 25(5):485–496, 1996.
- [28] A. Abdelsamie, G. Lartigue, C. E. Frouzakis, and D. Thévenin. The taylor–green vortex as a benchmark for high-fidelity combustion simulations using low-Mach solvers. *Comput. Fluids*, 223:104935, 2021.
- [29] C. Chi, A. Abdelsamie, and D. Thévenin. A directional ghost-cell immersed boundary method for incompressible flows. *J. Comput. Phys.*, 404:109122, 2020.
- [30] C.S. Peskin. Numerical analysis of blood flow in the heart. *J. Comput. Phys.*, 25(3):220–252, 1977.
- [31] C.S. Peskin. The immersed boundary method. *Acta Numer.*, 11:479–517, 2002.
- [32] R. Mittal and G. Iaccarino. Immersed boundary methods. *Annu. Rev. Fluid Mech.*, 37(1):239–261, 2005.
- [33] G. Iaccarino and R. Verzicco. Immersed boundary technique for turbulent flow simulations. *Appl. Mech. Rev.*, 56(3):331–347, 2003.

## Bibliography

- 
- [34] S. Marella, S. Krishnan, H. Liu, and H.S. Udaykumar. Sharp interface Cartesian grid method I: An easily implemented technique for 3D moving boundary computations. *J. Comput. Phys.*, 210(1):1–31, 2005.
- [35] M. Uhlmann. An immersed boundary method with direct forcing for the simulation of particulate flows. *J. Comput. Phys.*, 209(2):448–476, 2005.
- [36] T. Kempe and J. Fröhlich. An improved immersed boundary method with direct forcing for the simulation of particle laden flows. *J. Comput. Phys.*, 231(9):3663–3684, 2012.
- [37] C.S. Peskin. Flow patterns around heart valves: A numerical method. *J. Comput. Phys.*, 10(2):252–271, 1972.
- [38] R. Mittal, H. Dong, M. Bozkurttas, F.M. Najjar, A. Vargas, and A. von Loebbecke. A versatile sharp interface immersed boundary method for incompressible flows with complex boundaries. *J. Comput. Phys.*, 227(10):4825–4852, 2008.
- [39] J. Mohd-Yusof. Combined immersed-boundary/B-spline methods for simulations of flow in complex geometries. *CTR Annual Research Briefs*, pages 317–327, 1997.
- [40] J. Kim, D. Kim, and H. Choi. An immersed-boundary finite-volume method for simulations of flow in complex geometries. *J. Comput. Phys.*, 171(1):132–150, 2001.
- [41] E.A. Fadlun, R. Verzicco, P. Orlandi, and J. Mohd-Yusof. Combined immersed-boundary finite-difference methods for three-dimensional complex flow simulations. *J. Comput. Phys.*, 161(1):35–60, 2000.
- [42] R.P. Fedkiw. Coupling an Eulerian fluid calculation to a Lagrangian solid calculation with the ghost fluid method. *J. Comput. Phys.*, 175(1):200–224, 2002.
- [43] S. Majumdar, G. Iaccarino, and P. Durbin. RANS solver with adaptive structured boundary non conforming grids. *Annual Research Briefs, Center for Turbulence Research, Stanford University*, pages 353–466, 2001.
- [44] Y.-H. Tseng and J.H. Ferziger. A ghost-cell immersed boundary method for flow in complex geometry. *J. Comput. Phys.*, 192(2):593–623, 2003.

## Bibliography

- 
- [45] R. Ghias, R. Mittal, and H. Dong. A sharp interface immersed boundary method for compressible viscous flows. *J. Comput. Phys.*, 225(1):528–553, 2007.
- [46] D. K. Clarke, H. A. Hassan, and M. D. Salas. Euler calculations for multielement airfoils using Cartesian grids. *AIAA J.*, 24(3):353–358, 1986.
- [47] R.B. Pember, J.B. Bell, P. Colella, W.Y. Curtchfield, and M.L. Welcome. An adaptive Cartesian grid method for unsteady compressible flow in irregular regions. *J. Comput. Phys.*, 120(2):278–304, 1995.
- [48] T. Ye, R. Mittal, H.S. Udaykumar, and W. Shyy. An accurate Cartesian grid method for viscous incompressible flows with complex immersed boundaries. *J. Comput. Phys.*, 156(2):209–240, 1999.
- [49] P. Colella, D.T. Graves, B.J. Keen, and D. Modiano. A Cartesian grid embedded boundary method for hyperbolic conservation laws. *J. Comput. Phys.*, 211(1):347–366, 2006.
- [50] T. Gao, Y.-H. Tseng, and X.-Y. Lu. An improved hybrid Cartesian/immersed boundary method for fluid–solid flows. *Int. J. Numer. Meth. Fluids*, 55(12):1189–1211, 2007.
- [51] D. Pan and T.-T. Shen. Computation of incompressible flows with immersed bodies by a simple ghost cell method. *Int. J. Numer. Meth. Fluids*, 60(12):1378–1401, 2009.
- [52] P.A. Berthelsen and O.M. Faltinsen. A local directional ghost cell approach for incompressible viscous flow problems with irregular boundaries. *J. Comput. Phys.*, 227(9):4354–4397, 2008.
- [53] E. Balaras. Modeling complex boundaries using an external force field on fixed Cartesian grids in large-eddy simulations. *Comp. Fluids*, 33(3):375–404, 2004.
- [54] F. Gibou, R. P. Fedkiw, L.-T. Cheng, and M. Kang. A second-order-accurate symmetric discretization of the Poisson equation on irregular domains. *J. Comput. Phys.*, 176(1):205–227, 2002.
- [55] J. Lee and D. You. An implicit ghost-cell immersed boundary method for simulations of moving body problems with control of spurious force oscillations. *J. Comput. Phys.*, 233:295–314, 2013.

## Bibliography

- 
- [56] Y. Gorse, A. Iollo, H. Telib, and L. Weynans. A simple second order Cartesian scheme for compressible Euler flows. *J. Comput. Phys.*, 231(23):7780–7794, 2012.
- [57] A. Mark and B. van Wachem. Derivation and validation of a novel implicit second-order accurate immersed boundary method. *J. Comput. Phys.*, 227(13):6660–6680, 2008.
- [58] A.F. Shinn, M.A. Goodwin, and S.P. Vanka. Immersed boundary computations of shear- and buoyancy-driven flows in complex enclosures. *Int. J. Heat Mass Transf.*, 52(17):4082–4089, 2009.
- [59] J.H. Williamson. Low-storage Runge-Kutta schemes. *J. Comput. Phys.*, 35(1):48–56, 1980.
- [60] S. Osher and J.A. Sethian. Fronts propagating with curvature-dependent speed: Algorithms based on Hamilton-Jacobi formulations. *J. Comput. Phys.*, 79(1):12–49, 1988.
- [61] J.A. Sethian. *Level Set Methods and Fast Marching Methods*. Cambridge University Press: Cambridge, 1999.
- [62] J.A. Sethian. Evolution, implementation, and application of level set and fast marching methods for advancing fronts. *J. Comput. Phys.*, 169(2):503–555, 2001.
- [63] S. Osher and J.A. Sethian. *Level Set Methods and Dynamic Implicit Surfaces*. Springer-Verlag: New York, 2003.
- [64] R. Mittal and S. Balachandar. Effect of three-dimensionality on the lift and drag of nominally two-dimensional cylinder. *Phys. Fluids*, 7(8):1841–1865, 1995.
- [65] C.H.K. Williamson. Vortex dynamics in the cylinder wake. *Annu. Rev. Fluid Mech.*, 8:477–539, 1996.
- [66] D. Barkley and R.D. Henderson. Three-dimensional Floquet stability analysis of the wake of a circular cylinder. *J. Fluid Mech.*, 322:215–241, 1996.
- [67] M.-C. Lai and C.S. Peskin. An immersed boundary method with formal second-order accuracy and reduced numerical viscosity. *J. Comput. Phys.*, 160(2):705–719, 2000.
- [68] L. Baranyi. Computation of unsteady momentum and heat transfer from a fixed circular cylinder in laminar flow. *J. Comput. Appl. Mech.*, 4(1):13–25, 2003.

## Bibliography

- 
- [69] C.H.K. Williamson. Oblique and parallel modes of vortex shedding in the wake of a circular cylinder at low Reynolds numbers. *J. Fluid Mech.*, 206:579–627, 1989.
- [70] H. Dütsch, F. Durst, S. Becker, and H. Lienhart. Low-Reynolds-number flow around an oscillating circular cylinder at low Keulegan–Carpenter numbers. *J. Fluid Mech.*, 360:249–271, 1998.
- [71] S. Cai, A. Ouahsine, J. Favier, and Y. Hoarau. Moving immersed boundary method. *Int. J. Numer. Meth. Fluids*, 85(5):288–323, 2017.
- [72] Z.J. Wang. Two dimensional mechanism for insect hovering. *Phys. Rev. Lett.*, 85(10):2216–2219, 2000.
- [73] S. Xu and Z.J. Wang. An immersed interface method for simulating the interaction of a fluid with moving boundaries. *J. Comput. Phys.*, 216(2):454–493, 2006.
- [74] J. Yang and F. Stern. A simple and efficient direct forcing immersed boundary framework for fluid–structure interactions. *J. Comput. Phys.*, 231(15):5029–5061, 2012.
- [75] R. Clift, J.R. Grace, and M.E. Weber. *Bubbles Drops and Particles*. Academic Press, New York, 1978.
- [76] H. Sakamoto and H. Haniu. The formation mechanism and shedding frequency of vortices from a sphere in uniform shear flow. *J. Fluid Mech.*, 287:151–171, 1995.
- [77] D. Ormières and M. Provansal. Transition to turbulence in the wake of a sphere. *Phys. Rev. Lett.*, 83:80–83, 1999.
- [78] R. Mittal. A Fourier–Chebyshev spectral collocation method for simulating flow past spheres and spheroids. *Int. J. Numer. Meth. Fluids*, 30(7):921–937, 1999.
- [79] T.A. Johnson and V.C. Patel. Flow past a sphere up to a Reynolds number of 300. *J. Fluid Mech.*, 378:19–70, 1999.
- [80] S. Taneda. Experimental investigation of the wake behind a sphere at low Reynolds numbers. *J. Phys. Soc. Jpn.*, 11(10):1104–1108, 1956.
- [81] G. Janiga, P. Berg, S. Sugiyama, K. Kono, and D.A. Steinman. The computational fluid dynamics rupture challenge 2013—Phase I: Prediction of rupture status in intracranial aneurysms. *Am. J. Neuroradiol.*, 36(3):530–536, 2015.



## Bibliography

- 
- [82] S.L. Curtis, M. Bradley, P. Wilde, J. Aw, S. Chakrabarti, M. Hamilton, R. Martin, M. Turner, and A.G. Stuart. Results of screening for intracranial aneurysms in patients with coarctation of the aorta. *Am. J. Neuroradiol.*, 33(6):1182–1186, 2012.
- [83] P. Berg, C. Roloff, O. Beuing, S. Voss, S. Sugiyama, N. Aristokleous, A.S. Anayiotos, N. Ashton, A. Revell, N.W. Bressloff, A.G. Brown, B. Jae Chung, J.R. Cebra, G. Copelli, W. Fu, A. Qiao, A.J. Geers, S. Hodis, D. Dragomir-Daescu, E. Nordahl, Y. Bora Suzen, M. Owais Khan, K. Valen-Sendstad, K. Kono, P.G. Menon, P.G. Albal, O. Mierka, R. Münster, H.G. Morales, O. Bonnefous, J. Osman, L. Goubergrits, J. Pallares, S. Cito, A. Passalacqua, S. Piskin, K. Pekkan, S. Ramalho, N. Marques, S. Sanchi, K.R. Schumacher, J. Sturgeon, H. Švihlová, J. Hron, G. Usera, M. Mendina, J. Xiang, H. Meng, D.A. Steinman, and G. Janiga. The computational fluid dynamics rupture challenge 2013—Phase II: Variability of hemodynamic simulations in two intracranial aneurysms. *J. Biomech. Eng.*, 137(12):121008/1–13, 11 2015.
- [84] C. Chi, G. Janiga, A. Abdelsamie, K. Zähringer, T. Turányi, and D. Thévenin. DNS study of the optimal chemical markers for heat release in syngas flames. *Flow Turbul. Combust.*, 98(4):1117–1132, 2017.
- [85] C. Zistl, R. Hilbert, G. Janiga, and D. Thévenin. Increasing the efficiency of postprocessing for turbulent reacting flows. *Comput. Vis. Sci.*, 12:383–395, 2009.
- [86] W. Hubschmid, R. Bombach, A. Inauen, F. Güthe, S. Schenker, N. Tylli, and W. Kreutner. Thermoacoustically driven flame motion and heat release variation in a swirl-stabilized gas turbine burner investigated by LIF and chemiluminescence. *Exp. Fluids*, 45(1):167–182, 2008.
- [87] K. Zähringer, D. Durox, and F. Lacas. Helmholtz behavior and transfer function of an industrial fuel swirl burner used in heating systems. *Int. J. Heat Mass Transf.*, 46:3539–3548, 2003.
- [88] C.S. Panoutsos, Y. Hardalupas, and A.M.K.P. Taylor. Numerical evaluation of equivalence ratio measurement using OH\* and CH\* chemiluminescence in premixed and non-premixed methane-air flames. *Combust. Flame*, 156:273–291, 2009.
- [89] T. Leitgeb, T. Schuller, D. Durox, F. Giuliani, S. Köberl, and J. Woisetschläger. In-

## Bibliography

- 
- terferometric determination of heat release rate in a pulsated flame. *Combust. Flame*, 160:589–600, 2013.
- [90] A. Gazi, G. Vourliotakis, G. Skevis, and M.A. Founti. Assessment of chemical markers for heat-release rate correlations in laminar premixed flames. *Combust. Sci. Tech.*, 185:1482–1508, 2013.
- [91] N.B. Anikin, R. Suntz, and H. Bockhorn. Tomographic reconstruction of 2D-OH-chemiluminescence distributions in turbulent diffusion flames. *Appl. Phys. B*, 107:591–602, 2012.
- [92] J. Floyd, P. Geipel, and A.M. Kempf. Computed Tomography of Chemiluminescence (CTC): Instantaneous 3D measurements and phantom studies of a turbulent opposed jet flame. *Combust. Flame*, 158(2):376–391, 2011.
- [93] M. Stöhr, R. Sadanandan, and W. Meier. Experimental study of unsteady flame structures of an oscillating swirl flame in a gas turbine model combustor. *Proc. Combust. Inst.*, 32(2):2925–2932, 2009.
- [94] C. Hirsch, J. Wäsle, A. Winkler, and T. Sattelmayer. A spectral model for the sound pressure from turbulent premixed combustion. *Proc. Combust. Inst.*, 31(1):1435–1441, 2007.
- [95] B. Janus, A. Dreizler, and J. Janicka. Experiments on swirl stabilized non-premixed natural gas flames in a model gasturbine combustor. *Proc. Combust. Inst.*, 31(2):3091–3098, 2007.
- [96] A. Matynia, J. Molet, C. Roche, M. Idir, S. de Persis, and L. Pillier. Measurement of OH concentration profiles by laser diagnostics and modeling in high-pressure counterflow premixed methane/air and biogas/air flames. *Combust. Flame*, 159:3300–3311, 2012.
- [97] J.M. Donbar, J.F. Driscoll, and C.D. Carter. Reaction zone structure in turbulent nonpremixed jet flames – from CH-OH PLIF images. *Combust. Flame*, 122(1-2):1–19, 2000.
- [98] J. Kiefer, Z.S. Li, J. Zetterberg, X.-S. Bai, and M. Aldén. Investigation of local flame structures and statistics in partially premixed turbulent jet flames using simultaneous

## Bibliography

- 
- single-shot CH and OH planar laser-induced fluorescence imaging. *Combust. Flame*, 154(4):802–818, 2008.
- [99] H.N. Najm, P.H. Paul, C.J. Mueller, and P.S. Wyckoff. On the adequacy of certain experimental observables as measurements of flame burning rate. *Combust. Flame*, 113:312–332, 1998.
- [100] P.H. Paul and H.N. Najm. Planar laser-induced fluorescence imaging of flame heat release rate. *Proc. Combust. Inst.*, 27:43–50, 1998.
- [101] A. Fayoux, K. Zähringer, O. Gicquel, and J.C. Rolon. Experimental and numerical determination of heat release in counterflow premixed laminar flames. *Proc. Combust. Inst.*, 30:251–257, 2005.
- [102] B. O. Ayoola, R. Balachandran, C. F. Kaminski, and E. Mastorakos. Measurements of local heat release rates in a turbulent premixed bluff body stabilised flame with acoustic forcing. In *European Combustion Meeting*, pages 111/1–111/5. Louvain-la-Neuve, Belgium, 2005.
- [103] R.L. Gordon, A.R. Masri, and E. Mastorakos. Heat release rate as represented by  $[\text{OH}] \times [\text{CH}_2\text{O}]$  and its role in autoignition. *Combust. Theory Model.*, 13(4):645–670, 2009.
- [104] S. Pfadler, F. Beyrau, and A. Leipertz. Flame front detection and characterization using conditioned particle image velocimetry (CPIV). *Opt. Expr.*, 15(23):15444–15456, 2007.
- [105] M. Röder, T. Dreier, and C. Schulz. Simultaneous measurement of localized heat-release with OH/CH<sub>2</sub>O-LIF imaging and spatially integrated OH\* chemiluminescence in turbulent swirl flames. *Appl. Phys. B*, 107(3):611–617, 2012.
- [106] M. Röder, T. Dreier, and C. Schulz. Simultaneous measurement of localized heat-release with OH/CH<sub>2</sub>O-LIF imaging and spatially integrated OH\* chemiluminescence in turbulent swirl flames. *Proc. Combust. Inst.*, 34:3549–3556, 2013.
- [107] S. Böckle, J. Kazenwadel, T. Kunzelmann, D.-I. Shin, C. Schulz, and J. Wolfrum. Simultaneous single-shot laser-based imaging of formaldehyde, OH, and temperature in turbulent flames. *Proc. Combust. Inst.*, 28:279–286, 2000.

## Bibliography

- 
- [108] R. Yuan, J. Kariuki, A. Dowlut, R. Balachandran, and E. Mastorakos. Reaction zone visualisation in swirling spray n-heptane flames. *Proc. Combust. Inst.*, 35(2):1649–1656, 2015.
- [109] Z.M. Nikolaou and N. Swaminathan. Heat release rate markers for premixed combustion. *Combust. Flame*, 161(12):3073–3084, 2014.
- [110] I.A. Mulla, A. Dowlut, T. Hussain, Z.M. Nikolaou, S.R. Chakravarthy, N. Swaminathan, and R. Balachandran. Heat release rate estimation in laminar premixed flames using laser-induced fluorescence of CH<sub>2</sub>O and H-atom. *Combust. Flame*, 165:373–383, 2016.
- [111] O. Gicquel, L. Vervisch, G. Joncquet, B. Labegorre, and N. Darabiha. Combustion of residual steel gases: laminar flame analysis and turbulent flamelet modeling. *Fuel*, 82:983–991, 2003.
- [112] T. Lieuwen, V. Yang, and R. Yetter. *Synthesis Gas Combustion: Fundamentals and Applications*. CRC Press, Dordrecht, 2009.
- [113] S.G. Davis, A.V. Joshi, H. Wang, and F. Egolfopoulos. An optimized kinetic model of H<sub>2</sub>/CO combustion. *Proc. Combust. Inst.*, 30:1283–1292, 2005.
- [114] C. Olm, I.Gy. Zsély, T. Varga, H.J. Curran, and T. Turányi. Comparison of the performance of several recent syngas combustion mechanisms. *Combust. Flame*, 162:1793–1812, 2015.
- [115] H. Wang, X. You, A.V. Joshi, S.G. Davis, A. Laskin, F. Egolfopoulos, and C.K. Law. available at [http://ignis.usc.edu/USC\\_Mech\\_II.htm/](http://ignis.usc.edu/USC_Mech_II.htm/), 2007.
- [116] H. Shalaby, A. Laverdant, and D. Thévenin. Direct numerical simulation of a realistic acoustic wave interacting with a premixed flame. *Proc. Combust. Inst.*, 32:1473–1480, 2009.
- [117] C.J. Rutland and A. Trouvé. Direct simulations of premixed turbulent flames with nonunity Lewis numbers. *Combust. Flame*, 94(1-2):41–57, 1993.
- [118] C. Solomon and T. Breckon. *Fundamentals of digital image processing: A practical approach with examples in Matlab*. Wiley, 2011.

## Bibliography

- 
- [119] C. Chi, G. Janiga, K. Zähringer, and D. Thévenin. Indirect measurement of heat release in hydrogen flames using species correlations. *VDI Ber.*, 2302:625–636, 2017.
- [120] A. C. Eckbreth. *Laser Diagnostics for Combustion Temperature and Species*. Gordon and Beach Publishers, Amsterdam, 1996.
- [121] K. Kohse-Höinghaus and J.B. Jeffries. *Applied Combustion Diagnostics*. Taylor & Francis, New York, 2002.
- [122] K.N. Gabet, N. Jiang, W.R. Lempert, and J.A. Sutton. Demonstration of high-speed 1D Raman scattering line imaging. *Appl. Phys. B*, 101(1):1–5, 2010.
- [123] P. Boivin, C. Jiménez, A.L. Sánchez, and F.A. Williams. An explicit reduced mechanism for H<sub>2</sub>-air combustion. *Proc. Combust. Inst.*, 33(1):517–523, 2011.
- [124] J. Warnatz. *Combustion chemistry*. Springer-Verlag, 1985.
- [125] V. Giovangigli. *Multicomponent Flow Modeling*. Birkhäuser, Boston, 1999.
- [126] A. Ern and V. Giovangigli. Thermal diffusion effects of hydrogen-air and methane-air flames. *Combust. Theory Model.*, 2:345–372, 1998.
- [127] C. Chi, A. Abdelsamie, T. Oster, and D. Thévenin. Probability of hotspot ignition and ignition spot tracking in turbulent hydrogen-air mixtures using direct numerical simulations. In *Proceedings of the 8th European Combustion Meeting*, pages 925–930, 2017.
- [128] K.K.J. Ranga Dinesh, H. Shalaby, K.H. Luo, J.A. van Oijen, and D. Thévenin. High hydrogen content syngas fuel burning in lean premixed spherical flames at elevated pressures: Effects of preferential diffusion. *Int. J. Hydrog. Energy*, 41(40):18231–18249, 2016.
- [129] K.K.J. Ranga Dinesh, H. Shalaby, K.H. Luo, J.A. van Oijen, and D. Thévenin. Effects of pressure on cellular flame structure of high hydrogen content lean premixed syngas spherical flames: A DNS study. *Int. J. Hydrog. Energy*, 41(46):21516–21531, 2016.
- [130] C. Chi, G. Janiga, K. Zähringer, and D. Thévenin. DNS study of the optimal heat release rate marker in premixed methane flames. *Proc. Combust. Inst.*, 37(2):2363–2371, 2019.

## Bibliography

- 
- [131] Z.L. Wei, C.W. Leung, C.S. Cheung, and Z.H. Huang. Single-valued prediction of markers on heat release rate for laminar premixed biogas-hydrogen and methane-hydrogen flames. *Energy*, 133:35–45, 2017.
- [132] W.D. Kulatilaka, S. Roy, N. Jiang, and J.R. Gord. Photolytic-interference-free, femtosecond, two-photon laser-induced fluorescence imaging of atomic oxygen in flames. *Appl. Phys. B*, 122(2):26, 2016.
- [133] A. Abdelsamie and D. Thévenin. Direct numerical simulation of spray evaporation and autoignition in a temporally-evolving jet. *Proc. Combust. Inst.*, 36(2):2493–2502, 2017.
- [134] G.P. Smith, D.M. Golden, M. Frenklach, N.W. Moriarty, B. Eiteneer, M. Goldenberg, C.T. Bowman, R.K. Hanson, S. Song, W.C. Gardiner, V.V. Lissianski, and Z. Qin. available at  $\langle \text{http} : // \text{www.me.berkeley.edu/gri\_mech} \rangle$ , 2017.
- [135] Chemical-Kinetic Mechanisms for Combustion Applications, San Diego Mechanism web page, Mechanical and Aerospace Engineering (Combustion Research), University of California at San Diego, available at  $\langle \text{http} : // \text{combustion.ucsd.edu} \rangle$ , 2017.
- [136] M.D. Smooke and V. Giovangigli. Formulation of the premixed and non-premixed test problems. In M.D. Smooke, editor, *Reduced Kinetic Mechanisms and Asymptotic Approximations for Methane-Air Flames*, volume 384 of *Lecture Notes in Physics*, Berlin Springer Verlag, 1991.
- [137] N. Peters. *Turbulent combustion*. Cambridge University Press, Cambridge, 2000.
- [138] B.E. Battles and R.K. Hanson. Laser-induced fluorescence measurements of NO and OH mole fraction in fuel-lean, high-pressure (1-10 atm) methane flames: fluorescence modeling and experimental validation. *J. Quant. Spectrosc. Radiat. Transfer*, 54(3): 521–537, 1995.
- [139] P.H. Paul, J.A. Gray, J.L. Durant, and J.W. Thoman. A model for temperature-dependent collisional quenching of NO A2  $\sigma^+$ . *Appl. Phys. B*, 57(4):249–259, 1993.
- [140] N.L. Garland and D.R. Crosley. On the collisional quenching of electronically excited OH, NH and CH in flames. *21th Symposium (International) on Combustion*, pages 1693–1702, 1988.

## Bibliography

- 
- [141] W.D. Kulatilaka, J.H. Frank, and T.B. Settersten. Interference-free two-photon LIF imaging of atomic hydrogen in flames using picosecond excitation. *Proc. Combust. Inst.*, 32(1):955–962, 2009.
- [142] B. O. Ayoola, R. Balachandran, J. H. Frank, E. Mastorakos, and C. F. Kaminski. Spatially resolved heat release rate measurements in turbulent premixed flames. *Combust. Flame*, 144(1-2):1–16, 2006.
- [143] C. Chi, A. Abdelsamie, and D. Thévenin. Direct numerical simulations of hotspot-induced ignition in homogeneous hydrogen-air pre-mixtures and ignition spot tracking. *Flow Turbul. Combust.*, 101(1):103–121, 2018.
- [144] F. Marble and T. Adamson. Ignition and combustion in a laminar mixing zone. *Jet Propu.*, pages 85–94, 1954.
- [145] C.K. Law and H. Law. A theoretical study of ignition in the laminar mixing layer. *J. Heat Trans.*, 104:329–337, 1982.
- [146] I. Momtchiloff, E. Taback, and R. Buswell. Kinetics in hydrogen-air flow systems. I. calculation of ignition delays for hypersonic ramjets. *Proc. Combust. Inst.*, 9:220–230, 1962.
- [147] U. Maas and J. Warnatz. Ignition processes in carbon-monoxide-hydrogen-oxygen mixtures. *Proc. Combust. Inst.*, 22:1695–1704, 1988.
- [148] J. Warnatz. Numerical simulation of ignition processes. In A. Dervieux and B. Larrouturou, editors, *Numerical Combustion*, volume 351 of *Lecture Notes in Physics*. Springer-Verlag, 1989.
- [149] U. Maas and J. Warnatz. Simulation of chemically reacting flows in two-dimensional geometries. *Impact Comput. Sci. Eng.*, 1:394–420, 1989.
- [150] E. Mastorakos. Ignition of turbulent non-premixed flames. *Prog. Energy Combust. Sci.*, 35(1):57–97, 2009.
- [151] T. Hasegawa, A. Arai, S. Kadowaki, and S. Yamaguchi. Autoignition of a turbulent premixed gas. *Combust. Sci. Technol.*, 84:1–13, 1992.

## Bibliography

- 
- [152] M. Baum and T. Poinso. Effect of mean flow on premixed flame ignition. *Combust. Sci. Technol.*, 106:19–39, 1995.
- [153] T. Poinso, S. Candel, and A. Trouvé. Applications of direct numerical simulation to premixed turbulent combustion. *Prog. Energy Combust. Sci.*, 21:531–576, 1996.
- [154] T. Echekeki and J.H. Chen. Direct numerical simulation of autoignition in non-homogeneous hydrogen-air mixtures. *Combust. Flame*, 134(3):169–191, 2003.
- [155] C.F. Kaminski, J. Hult, M. Alden, S. Lindenmaier, A. Dreitzler, U. Maas, and M. Baum. Spark ignition of turbulent methane/air mixtures revealed by time-resolved planar laser-induced fluorescence and direct numerical simulations. *Proc. Combust. Inst.*, 28:399–405, 2000.
- [156] J. Hult, S. Gashi, N. Chakraborty, M. Klein, K. Jenkins, R. Cant, and C. Kaminski. Measurement of flame surface density for turbulent premixed flames using PLIF and DNS. *Proc. Combust. Inst.*, 31(1):1319–1326, 2007.
- [157] M. Klein, N. Chakraborty, and R. Cant. Effects of turbulence on self-sustained combustion in premixed flame kernels: a direct numerical simulation (DNS) study. *Flow Turbul. Combust.*, 81:583–607, 2008.
- [158] N. Chakraborty, E. Mastorakos, and S. Cant. Effects of turbulence on spark ignition in inhomogeneous mixtures: a direct numerical simulation (DNS) study. *Combust. Sci. Technol.*, 179:293–317, 2007.
- [159] H. Reddy and J. Abraham. Ignition kernel development studies relevant to lean-burn natural-gas engines. *Fuel*, 89(11):3262 – 3271, 2010.
- [160] C. Yoo, T. Lu, J.H. Chen, and C.K. Law. Direct numerical simulations of ignition of a lean n-heptane/air mixture with temperature inhomogeneities at constant volume: Parametric study. *Combust. Flame*, 158(9):1727–1741, 2011.
- [161] G. Bansal and H.G. Im. Autoignition and front propagation in low temperature combustion engine environments. *Combust. Flame*, 158(11):2105 – 2112, 2011.
- [162] R. Sankaran, E. Hawkes, C. Yoo, J.H. Chen, T. Lu, and C.K. Law. Direct numerical simulation of stationary lean premixed methane-air flames under intense turbulence. In *Fifth US Combustion Meeting, Paper B09*, 2007.



## Bibliography

- 
- [163] G. Bansal, A. Mascarenhas, and J.H. Chen. Direct numerical simulations of autoignition in stratified dimethyl-ether (DME)/air turbulent mixtures. *Combust. Flame*, 162(3):688–702, 2015.
- [164] T. Zhou, T. Ye, M. Zhu, M. Zhao, and J. Chen. Effect of droplet diameter and global equivalence ratio on n-heptane spray auto-ignition. *Fuel*, 187:137–145, 2017.
- [165] H. Schmidt and R. Klein. *Flexible Flame Structure Modelling in a Flame Front Tracking Scheme*. Springer Berlin Heidelberg, 2005.
- [166] H.A. Uranakara, S. Chaudhuri, H.L. Dave, P.G. Arias, and H.G. Im. A flame particle tracking analysis of turbulence–chemistry interaction in hydrogen–air premixed flames. *Combust. Flame*, 163:220–240, 2016.
- [167] A. Scholtissek, F. Dietzsch, M. Gauding, and C. Hasse. In-situ tracking of mixture fraction gradient trajectories and unsteady flamelet analysis in turbulent non-premixed combustion. *Combust. Flame*, 175:243–258, 2017.
- [168] P. Pal, M. Valorani, P.G. Arias, H.G. Im, M.S. Wooldridge, P.P. Ciottoli, and R.M. Galassi. Computational characterization of ignition regimes in a syngas/air mixture with temperature fluctuations. *Proc. Combust. Inst.*, 36(3):3705–3716, 2017.
- [169] M.B. Luong, G.H. Yu, S.H. Chung, and C.S. Yoo. Ignition of a lean PRF/air mixture under RCCI/SCCI conditions: A comparative DNS study. *Proc. Combust. Inst.*, 36(3):3623–3631, 2017.
- [170] T. Yao and K.H. Luo. Direct numerical simulation study of hydrogen/air auto-ignition in turbulent mixing layer at elevated pressures. In *Digital proceedings of the 8th European Combustion Meeting*, 2017.
- [171] R. Yu and X.-S. Bai. Direct numerical simulation of lean hydrogen/air auto-ignition in a constant volume enclosure. *Combust. Flame*, 160(9):1706–1716, 2013.
- [172] J. Hirschfelder, C. Curtiss, and R. Bird. *Molecular Theory of Gases and Liquids*. New York: Wiley, 1954.
- [173] R. Hilbert and D. Thévenin. Autoignition of turbulent non-premixed flames investigated using direct numerical simulations. *Combust. Flame*, 128(1-2):22–37, 2002.

## Bibliography

- 
- [174] H. Shalaby and D. Thévenin. Statistically significant results for the propagation of a turbulent flame kernel using direct numerical simulation. *Flow Turbul. Combust.*, 84(3):357–367, 2010.
- [175] E. Mastorakos, A. Pires da Cruz, T. Baritaud, and T. Poinso. A model for the effects of mixing on the autoignition of turbulent flows. *Combust. Sci. Technol.*, 125:243–282, 1997.
- [176] H.G. Im, J.H. Chen, and C.K. Law. Ignition of hydrogen-air mixing layer in turbulent flows. *Proc. Combust. Inst.*, 27:1047–1056, 1998.
- [177] U. Maas and J. Warnatz. Ignition processes in hydrogen-oxygen mixtures. *Combust. Flame*, 74:53–69, 1988.
- [178] W. Laster and E. Sojka. Autoignition of H<sub>2</sub>-air: the effect of NO<sub>x</sub> addition. *Jet Propu.*, 4:385–390, 1989.
- [179] Y.Z. Zhang, E.H. Kung, and D.C. Haworth. A PDF method for multidimensional modeling of HCCI engine combustion: effects of turbulence/chemistry interactions on ignition timing and emissions. *Proc. Combust. Inst.*, 30:2763–2771, 2005.
- [180] J.H. Chen, E.R. Hawkes, R. Sankaran, S.D. Mason, and H.G. Im. Direct numerical simulation of ignition front propagation in a constant volume with temperature inhomogeneities: I. fundamental analysis and diagnostics. *Combust. Flame*, 145:128–144, 2006.
- [181] E.R. Hawkes, R. Sankaran, P.P. Pébay, and J.H. Chen. Direct numerical simulation of ignition front propagation in a constant volume with temperature inhomogeneities: II. parametric study. *Combust. Flame*, 145:145–159, 2006.
- [182] S. Sreedhara and K.N. Lakshmisha. Autoignition in a non-premixed medium: DNS studies on the effects of three-dimensional turbulence. *Proc. Combust. Inst.*, 29:2051–2059, 2002.
- [183] J. Melguizo-Gavilanes, L.R. Boeck, R. Mével, and J.E. Shepherd. Hot surface ignition of stoichiometric hydrogen-air mixtures. *Int. J. Hydrog. Energy*, 42(11):7393–7403, 2017.

## Bibliography

- 
- [184] V. Daru, P. Le Quéré, M.-C. Duluc, and O. Le Maître. A numerical method for the simulation of low Mach number liquid–gas flows. *J. Comput. Phys.*, 229(23):8844–8867, 2010.
- [185] E. Toulson, H.J. Schock, and W.P. Attard. A review of pre-chamber initiated jet ignition combustion systems. *SAE Tech. Pap.*, 2010-01-2263, 2010.
- [186] S. Yamaguchi, N. Ohiwa, and T. Hasegawa. Ignition and burning process in a divided chamber bomb. *Combust. Flame*, 59(2):177–187, 1985.
- [187] J. Wallesten and J. Chomiak. Investigation of spark position effects in a small pre-chamber on ignition and early flame propagation. *SAE Tech. Pap.*, 2000-01-2839, 2000.
- [188] R. Sadanandan, D. Markus, R. Schießl, U. Maas, J. Olofsson, H. Seyfried, M. Richter, and M. Aldén. Detailed investigation of ignition by hot gas jets. *Proc. Combust. Inst.*, 31(1):719–726, 2007.
- [189] Quentin Malé, Olivier Vermorel, Frédéric Ravet, and Thierry Poinsot. Direct numerical simulations and models for hot burnt gases jet ignition. *Combust. Flame*, 223:407–422, 2021.
- [190] J. Carpio, I. Iglesias, M. Vera, A.L. Sánchez, and A. Liñán. Critical radius for hot-jet ignition of hydrogen–air mixtures. *Int. J. Hydrog. Energy*, 38(7):3105–3109, 2013.
- [191] A. Ghorbani, G. Steinhilber, D. Markus, and U. Maas. Ignition by transient hot turbulent jets: An investigation of ignition mechanisms by means of a PDF/REDIM method. *Proc. Combust. Inst.*, 35(2):2191–2198, 2015.
- [192] S. Biswas, S. Tanvir, H. Wang, and L. Qiao. On ignition mechanisms of premixed CH<sub>4</sub>/air and H<sub>2</sub>/air using a hot turbulent jet generated by pre-chamber combustion. *Appl. Therm. Eng.*, 106:925–937, 2016.
- [193] E. Mastorakos, P. Allison, A. Giusti, P. De Oliveira, S. Benekos, Y. Wright, C. Frouzakis, and K. Boulouchos. Fundamental aspects of jet ignition for natural gas engines. *SAE Int. J. Engines*, 10(5):2429–2438, 2017.

## Bibliography

- 
- [194] J.A.M. Sidey and E. Mastorakos. Pre-chamber ignition mechanism: Simulations of transient autoignition in a mixing layer between reactants and partially-burnt products. *Flow Turbul. Combust.*, 101(4):1093–1102, 2018.
- [195] F. Qin, A. Shah, Z.-W. Huang, L.-N. Peng, P. Tunestal, and X.-S. Bai. Detailed numerical simulation of transient mixing and combustion of premixed methane/air mixtures in a pre-chamber/main-chamber system relevant to internal combustion engines. *Combust. Flame*, 188:357–366, 2018.
- [196] P.M. Allison, M. de Oliveira, A. Giusti, and E. Mastorakos. Pre-chamber ignition mechanism: Experiments and simulations on turbulent jet flame structure. *Fuel*, 230:274–281, 2018.
- [197] N. Wang, J. Liu, W.L. Chang, and C.F. Lee. A numerical study of the combustion and jet characteristics of a hydrogen fueled turbulent hot-jet ignition (thji) chamber. *Int. J. Hydrog. Energy*, 43(45):21102–21113, 2018.
- [198] N. Wang, J. Liu, W.L. Chang, and C.F. Lee. A numerical study on effects of pre-chamber syngas reactivity on hot jet ignition. *Fuel*, 234:1–8, 2018.
- [199] Q. Malé, G. Staffelbach, O. Vermorel, A. Misdariis, F. Ravet, and T. Poinsot. Large eddy simulation of pre-chamber ignition in an internal combustion engine. *Flow Turbul. Combust.*, 103(2):465–483, 2019.
- [200] Sotirios Benekos, Christos E. Frouzakis, George K. Giannakopoulos, Michele Bolla, Yuri M. Wright, and Konstantinos Boulouchos. Prechamber ignition: An exploratory 2-d dns study of the effects of initial temperature and main chamber composition. *Combust. Flame*, 215:10–27, 2020.
- [201] R.P. Lindstedt and E.M. Vaos. Transported PDF modeling of high-Reynolds-number premixed turbulent flames. *Combust. Flame*, 145(3):495–511, 2006.
- [202] A. Shah, P. Tunestal, and B. Johansson. Effect of relative mixture strength on performance of divided chamber ‘Avalanche Activated Combustion’ ignition technique in a heavy duty natural gas engine. *SAE Tech. Pap.*, 2014-01-1327, 2014.
- [203] G. Lacaze, E. Richardson, and T. Poinsot. Large eddy simulation of spark ignition in a turbulent methane jet. *Combust. Flame*, 156(10):1993–2009, 2009.

## Bibliography

- 
- [204] C.D. Pierce and P. Moin. Progress-variable approach for large-eddy simulation of non-premixed turbulent combustion. *J. Fluid Mech.*, 504:73–97, 2004.
- [205] C. Zhou, Y. Li, U. Burke, C. Banyon, K. Somers, S. Ding, S. Khan, J. Hargis, T. Sikes, O. Mathieu, E. Petersen, M. Alabbad, A. Farooq, Y. Pan, Y. Zhang, J. Lopez, Z. Loparo, S. Vasu, and H.J. Curran. An experimental and chemical kinetic modeling study of 1,3-butadiene combustion: Ignition delay time and laminar flame speed measurements. *Combust. Flame*, 197:423–438, 11 2018.
- [206] M. Short and D.A. Kessler. Asymptotic and numerical study of variable-density premixed flame propagation in a narrow channel. *J. Fluid Mech.*, 638:305–337, 2009.
- [207] N. Swaminathan and R. W. Grout. Interaction of turbulence and scalar fields in premixed flames. *Phys. Fluids*, 18(4):045102, 2006.
- [208] N. Chakraborty and N. Swaminathan. Influence of the damköhler number on turbulence-scalar interaction in premixed flames. i. physical insight. *Phys. Fluids*, 19(4):045103, 2007.
- [209] P.E. Hamlington, Alexei Y. Poludnenko, and Elaine S. Oran. Interactions between turbulence and flames in premixed reacting flows. *Phys. Fluids*, 23(12):125111, 2011.
- [210] A. P. Morse, J. H. Whitelaw, and M. Yianneskis. Turbulent flow measurements by Laser-Doppler anemometry in motored piston-cylinder assemblies. *J. Fluid Eng.*, 101(2):208–216, 1979.
- [211] M. Reeves, C.P. Garner, J.C. Dent, and N.A. Halliwell. Particle image velocimetry analysis of IC engine in-cylinder flows. *Opt. Laser Eng.*, 25(6):415–432, 1996.
- [212] A. Y. Alharbi and V. Sick. Investigation of boundary layers in internal combustion engines using a hybrid algorithm of high speed micro-PIV and PTV. *Exp. Fluids*, 49(4):949–959, 2010.
- [213] C. Jainski, L. Lu, A. Dreizler, and V. Sick. High-speed micro particle image velocimetry studies of boundary-layer flows in a direct-injection engine. *Int. J. Engine Res.*, 14(3):247–259, 2013.

## Bibliography

- 
- [214] B. Peterson, E. Baum, B. Böhm, V. Sick, and A. Dreizler. Spray-induced temperature stratification dynamics in a gasoline direct-injection engine. *Proc. Combust. Inst.*, 35(3):2923–2931, 2015.
- [215] R. D. Reitz and C. J. Rutland. 3-D modeling of diesel engine intake flow, combustion and emissions. *SAE Int. J. Engines*, 100:1513–1520, 1991.
- [216] D. C. Haworth. Large-Eddy Simulation of in-cylinder flows. *Oil Gas Sci. Technol.*, 54(2):175–185, 1999.
- [217] M. Schmitt. *Direct numerical simulations in engine-like geometries*. PhD thesis, ETH Zürich, 2014.
- [218] M. Schmitt, C. E. Frouzakis, Y. M. Wright, A. Tomboulides, and K. Boulouchos. Direct numerical simulation of the compression stroke under engine relevant conditions: Local wall heat flux distribution. *Int. J. Heat Mass Transf.*, 92:718–731, 2016.